Philipps-Universität Marburg

Examining Uptake of Nanomaterials by Eukaryotic Cells with Digital Image Cytometry

Dissertation

zur Erlangung des Doktorgrades
der Naturwissenschaften
(Dr. rer. nat.)

dem
Fachbereich Physik
der Philipps-Universität Marburg
vorgelegt von

Raimo Hartmann

geboren in
Hoya

Marburg/Lahn, 2015

Vom Fachbereich Physik der Philipps-Universität Marburg (Hochschulkennziffer: 1180) als Dissertation angenommen am: 06.07.2015

Erstgutachter:	Prof. Dr. Wolfgang J. Parak
Zweitgutachter:	Prof. Dr. Peter Lenz
Prüfer:	Prof. Dr. Gregor Witte

Tag der mündlichen Prüfung: 16.07.2015

Die vorliegende Arbeit wurde am Fachbereich Physik
der Philipps-Universität Marburg unter Anleitung von

Herrn Prof. Dr. Wolfgang J. Parak

in der Zeit von November 2011 bis April 2015 angefertigt.

Zusammenfassung

Künstliche Nanomaterialien eignen sich aufgrund ihrer winzigen Größe und der damit verbundenen interessanten Eigenschaften für zahlreiche biologische und medizinische Anwendungen. Die Wechselwirkungen auf zellulärer Ebene hängen von einer Vielzahl unterschiedlicher Faktoren ab. Um die Wirksamkeit und Toxizität von Nanopartikeln einschätzen zu können, ist es notwendig, ihre zelluläre Aufnahme, ihren intrazellulären Transport und letztendlichen intrazellulären Verbleib sowie die durch sie ausgelöste Zellantwort zu verstehen. Die genannten Faktoren werden ihrerseits von den physikalisch-chemischen Parametern des eingesetzten Nanomaterials wie z.B. Größe, Oberflächenchemie, Oberflächenladung und Elastizität beeinflusst.

Durch Fluoreszenzmikroskopie lassen sich mit einer Vielzahl kommerziell erhältlicher, fluoreszierender Reporterfarbstoffe viele zelluläre Funktionen abbilden und auswerten. Zur bildbasierten Quantifizierung von Zellmerkmalen (engl. *Image Cytometry*) eignen sich Computer-basierte Algorithmen sehr gut, da Verfälschungen durch die subjektive Wahrnehmung und Beobachtungsperspektive des Experimentators vermieden werden können. Diese im folgenden als *Digital Image Cytometry* bezeichnete Methode profitiert von automatisierter Mikroskopie, da eine große Anzahl von Zellen abgebildet werden muss, um in der Lage zu sein, einzelne Populationen zu identifizieren und statistisch aussagekräftige Resultate zu erzielen.

Diese Methode wurde in der vorliegenden Arbeit zur Untersuchung der Auswirkung von plasmonischen Gold-Nanopartikeln (Au NP) auf die Morphologie und die Lebensfähigkeit von menschlichen Endothel- und Epithelzellen (HUVEC- und HeLa-Zellen) angewandt. Die verwendeten 4-5 nm großen Au NP sind mit Polymethacrylsäure umhüllt und ihre physikalisch-chemischen Eigenschaften sind nahezu vollständig beschrieben. Mehr oder weniger identische Gold-Nanopartikel sind bereits in mehreren zuvor durchgeführten und entsprechend dokumentierten Studien eingesetzt worden und bieten interessante Anwendungsmöglichkeiten im biomedizinischen Bereich. Die verwendeten Gold-Nanopartikel werden nach der Aufnahme in intrazellulären lysosomalen Strukturen angereichert. Als Ergebnis des ersten Teils der Arbeit lässt sich eine signifikante Auswirkung der eingesetzten Nanopartikel auf die Morphologie von Mitochondrien und Lysosomen sowie auf die Struktur des Aktinzytoskeletts und insbesondere auf die Teilungsfähigkeit der Zellen (Proliferationsfähigkeit) beobachten. Bemerkenswert ist die Tatsache, dass die dafür ausreichende Dosis um ein bis zwei Größenordnungen geringer ist als diejenige, bei der akute Zytotoxizität und erhöhte Werte von reaktiven Sauerstoffspezies (ROS) gemessen werden.

Der zweite Teil dieser Arbeit beruht auf Untersuchungen des Endozytose-

Vorgangs von Polymer-Mikrokapseln. Diese stellen ein interessantes Trägersystem dar, um Wirkstoffe in das Zellinnere zu transportieren und dort freizusetzen. Nach der Aufnahme durch *Lipid Raft*-vermittelte Phagozytose durchlaufen die Kapseln eine intrazelluläre Kaskade von immer azidischer werdenden Vesikeln. Durch das Einbringen eines pH-sensitiven Fluoreszenzfarbstoffs in die Kapseln kann ihr Aufnahmevorgang mittels der damit assoziierten Ansäuerung zeitaufgelöst abgebildet werden. Die Kinetik des Ansäuerungs-prozesses hängt dabei maßgeblich von der Elastizität der Kapseln ab. Weiche Partikel mit hoher Elastizität werden schneller in Lysosomen transportiert als weniger elastische. Außerdem wird mit diesem Sensorpartikelsystem die Relevanz der V_1G_1-Untereinheit der an der Ansäuerung lysosomaler Vesikel beteiligten vakuolären ATPase verifiziert.

Abstract

Due to their small size and related interesting properties, artificial nanomaterials are utilized for a great number of biological and medical applications. Cell entry routes, intracellular trafficking and processing of nanoparticles, which determine their fate, efficiency, and toxicity, are depending on various parameters of the specific nanomaterial, such as size, surface charge, surface chemistry and elasticity. Nanoparticle-cell interactions are typically elucidated by means of fluorescence microscopy. Cell functions can be observed by a multiplicity of commercially available probes. For the quantification of cell features from images (*image cytometry*), computer-based algorithms are favoured to avoid bias introduced by the subjective perception of the observer. By applying high throughput microscopy in combination with *digital image cytometry* the screening of high numbers of cells is made possible. With the large quantity of obtained data, cell populations can be identified and, in general, results that are statistically meaningful are obtained.

In the first part of this work this method is applied in order to examine the cellular responses upon exposure to plasmonic poly(methacrylic acid)-coated gold nanoparticles (Au NPs) with respect to morphology and viability of human endothelial and epithelial cells (HUVECs and HeLa cells). Au NPs of 4-5 nm size were chosen which had been thoroughly characterized in terms of their physico-chemical parameters. These particles bear interesting properties for biomedical applications and, for several years, have been in the focus of research. In this work significant impacts on mitochondrial and lysosomal morphology upon exposure to the Au NPs are reported. The alteration of the structure of the cytoskeleton and a dramatically reduced proliferation are described. Interestingly, the smallest dose inducing the described cellular responses was of one or two magnitudes lower than those, where acute cytotoxicity and an increase in the production of reactive oxygen species (ROS) were observed.

In the second part the process of endocytosis of polymer capsules is examined. These systems are seen as a promising tool for intracellular cargo delivery and release. After *lipid raft*-mediated phagocytosis, the capsules are transferred from the neutral extracellular medium to increasingly acidic intracellular vesicles. By embedding a pH-sensitive fluorescent dye into the cavity of the capsule the uptake process and the associated acidification can be monitored time-dependently. It is demonstrated that the kinetic of the acidification process strongly depends on the stiffness of the capsules. Soft particles with minor stiffness are transported faster into lysosomal structures than stiffer ones. Additionally, these sensor particles are used to confirm the importance of the V_1G_1-subunit of the vacuolar ATPase being responsible for vesicle acidification.

Table of Contents

1. Introduction

Nowadays nanotechnology is everywhere. Engineered nanomaterials can be found in everyday products but also in cutting-edge technology. Since the mid 80's, when the term "nanoparticle" (NP) first appeared, a completely new branch of science emerged. New tools were developed which allowed the systematic organization and manipulation of matter on the nanometer length scale. Today, nanomaterials are in the focus of research in several disciplines, including the application in molecular biology and medicine.[1–3]

Being reduced to several nanometers the physico-chemical properties of matter change. This can be related to the following aspects: (i) Surface-dependent properties of the bulk material such as chemical reactivity, soil-repellant features, or surface conductivity are becoming more dominant due to the dramatically increased surface-to-volume ratio. (ii) Size-dependent effects become visible, detectable for instance as superparamagnetism. (iii) Quantum mechanical properties are altered which can result in new optical characteristics, for example size-dependent changes in the absorption/emission spectra.[1,4,5]

Apart from interesting physico-chemical features for material sciences, nanomaterials bear superior properties for biomedical applications. They are small enough to be internalized by eukaryotic cells and can be targeted by surface modifications or external stimuli to some degree.[6–8] Superparamagnetic nanoparticles (*e.g.* from iron oxide) and plasmonic nanoparticles (*e.g.* from gold) can both be applied for hyperthermia, but due to different underlying phenomena.[9–12] With magnetic nanoparticles energy from alternating magnetic fields is converted into heat while plasmonic NPs convert UV/visible light into heat radiation. Apart from that, luminescent NPs, such as quantum dots (QDs), are suitable for labeling or tracking purposes in molecular biology and medical diagnosis. This is due to their excellent optical characteristics, such as narrow emission/excitation bands or high photostability.[13–15] In addition, nanoparticles are utilized for intracellular sensing and delivery,[16–18] and researchers are trying to target diseases such as cancer or Alzheimer's disease.[19–21]

Although nanoparticles are already applied *in vivo* since the early 90's, the interactions with biological systems are not entirely understood on the single cell level so far. During the last decade, huge efforts were spent to unravel the dependency between endocytic uptake and several parameters of the nanoparticulate material, such as size,[22,23] shape,[24] surface charge/chemistry[25–28] or stiffness[29–31] *in vitro*. Although this led to an improvement in the general understanding, most studies are lacking comparability, as the experimental conditions are extremely diverse. This applies to the selection of cells, the exposure conditions, different assay endpoints, or low significance of the studies carried out. Also, difficulties are the result of to the almost continuous creation of more

and more different nanomaterials and the fact, that the area of bionanotechnology is very interdisciplinary.[18]

Generally, once suspended in biological fluids, proteins and other biomolecules are adsorbed on the nanoparticle surface forming a layer called *protein corona*. It is assumed that the biological identity of the NP and the interaction with cells are defined by this corona.[32–34] Upon cellular internalization, which typically happens through energy-dependent endocytic pathways, NPs are mostly transported to lysosomes (degradative intercellular organelles), where they are enriched.[27,28,35,36] Regarding *in vitro* experiments lysosomal accumulation is often accompanied by increasing cytotoxicity.[28,37] In animal models accumulation of NPs was observed mainly in the liver, spleen, and kidneys.[38–40]

Cytometry describes the measurement of cell properties. Nanoparticle-cell interactions are commonly studied with microscopy-based methods. The method of determining characteristics of cells from microscope images is referred to as *image cytometry*. Many nanomaterials are intrinsically fluorescent or are designed to be functionalized easily with fluorescent dyes. Hence, fluorescence microscopy or variants of this method are typically used for imaging. Biological systems can have complex architecture, but the building blocks, *i.e.* individual cells, appear to be rather similar, as the same substructures (*i.e.* nucleus, outer plasma membrane, cytoskeleton, mitochondria, certain vesicles, *etc.*) can be found inside most of them. All of these unique substructures have unique properties (*e.g.* specific architecture or certain constituents). Based on these properties they can be recognized within any cell and thus, if stained and imaged appropriately, in any image representing a cell. Therefore, a visual model can be created, which describes how a cell, which was treated with certain dyes or exhibits certain fluorescent patterns, typically appears on a micrograph. Based on this model a computer is now able to "see" and identify any cell being similar to the proposed model, including its constituents. As a result, the examination process can be automated. The computer-aided process of assessing cell properties is referred to as *digital image cytometry* in the following. This kind of image analysis is not reflecting the subjective perception of the experimenter any more. Additionally, the analysis process is much faster and the number of analyzable cells is dramatically increased, together with the statistical significance of the obtained results.

This principle of digital image cytometry is utilized in high content analysis (HCA)[1]. HCA is used to describe the screening and examination of thousands of cells ("content") in microscope images generated usually by automated microscopes in high throughput. HCA is mostly applied in biotechnological research, drug discovery, and in the workflow of pharmaceutical industry. It is either used

[1] also referred to as high content screening (HCS)

to identify substances that trigger desired cellular responses, or for assessing cytotoxicity *in vitro*.[41–43] Generally, it is regarded as a "multiparametric interrogation of cellular processes in any format".[41] Important research fields where HCA-based assays were employed, are for instance neurobiology[44,45], oncology[46,47], cell signalling[48,49], or target identification and validation.[50,51]

In basic research in the field of nanobiotechnology, multiparametric response- and cytotoxicity studies are needed to be able to fully correlate cell functions with the parameters of the deployed nanomaterial in a systematic manner. Remarkably, such questions can often be answered with one HCA-based approach by multiplexing different assays with fluorescent probes spread across the visible spectrum.[41] In addition, this knowledge may help to estimate health and environmental hazards upon disposal of and exposure to certain potentially toxic nanomaterials.

So far, several published studies can be found utilizing HCA in a broader context for assessing nanoparticle-cell interactions: An extensive work about the cytotoxicity of cationic and anionic amine-modified polystyrene NPs ($d_h \approx 50$ nm)[2] including seven different cell lines[3] was performed by Anguissola *et al.* The analysis of the HCA data revealed that for cationic NPs, first (in terms of lowest concentration of NPs) lysosomal alkalinization occurs, which is followed by the loss of mitochondrial membrane potential, nuclear condensation, the increase of cytosolic calcium levels, and finally the disturbance of the integrity of plasma membranes. The effects were observed in a certain order but at similar concentrations, where viability (in terms of cell count) was decreased. For anionic particles these effects could not be observed in the investigated range of NP-concentrations.[28]

Similarly, but less well-performed, cellular responses were assessed upon exposure to L-cysteine-stabilized Au NPs[4] and 3 nm-sized cadmium telluride (CdTe) quantum dots using HCA by Jan *et al.* Interestingly, cellular proliferation and mitochondrial membrane potential were already reduced at concentrations almost two orders of magnitude lower (≈ 1 nM) than those where acute cytotoxicity was observed (> 50 nM) in terms of reduced cell count and loss of plasma membrane integrity.[52]

The cellular effects of gold nanoparticles were also investigated by Soenen *et al.* They reported that exposure to poly(methacrylic acid)-coated NPs of 4 nm in diameter and concentrations above 50 nM reduced cellular viability, cell size, cell proliferation, and differentiation in endothelial cells. Additionally, neurite outgrowth was impeded in neural progenitor cells. Furthermore, deformations in

[2] d_h = hydrodynamic diameter
[3] 1321N1, SH-SY5Y, Raw267.4, A549, hCMEC, HepG2, and HEK293 cells
[4] Jan *et al.*[52] did not provide any further characterization in their work

the actin and tubulin cytoskeleton were observed.[53]

Solmesky *et al.* utilized HCA for studying the toxicity of lipid-based nanoparticles in fibroblasts ($d_h \approx 100$ nm) depending on the nanoparticle surface charge at physiological pH.[54] Several parameters were assessed including viability, proliferation and morphological changes of mitochondria. Cationic nanoparticles turned out to be the most cytotoxic in terms of cell viability, which is also in line with previous findings.[25,55] In addition, a decrease in mitochondrial elongation was observed.[54]

These studies were selected because the benefits of the application of HCA, and such the benefit of digital image cytometry, are comprehensively demonstrated. Especially in the first article, the authors could reconstruct the cellular mechanisms, which eventually lead to cell death upon exposure to nanoparticles, in a very systematic manner.[28]

1.1. About this Thesis

Similar to industrial processes, many experimental tasks in the laboratory can be simplified or handled more efficiently by computer-based automatization. In particular, this applies to data processing as no complex machinery is required. In this work, it is described how the application of digital image cytometry can help to investigate the interaction of nanomaterials with cells, as well as, possibly answering many questions in this regard. From the point of computer science, this includes the application of autonomous image acquisition with automated microscopes, subsequent image processing of multidimensional data sets, identification of relevant structures (segmentation), measuring and/or tracking of certain properties, and finally data evaluation including the representation of the results. Many experiments involving imaging of biological samples can be set up in such a way that enables fast and efficient processing later on. Ideally, due to the bunch of different parameters generated by computer vision-based image analysis, more image details are accessible and more features can be quantified to draw statistically sound conclusions. In comparison to manual methods the throughput is dramatically higher.

This work is based on several studies with different focuses (Publications, § 6), which are already published or close to publication. They are dealing with cellular responses to nanoparticles and endocytic pathways of polymer-based sensor microcapsules. To create a coherent presentation of the results, the content of these studies is reassembled with respect to the application of digital image cytometry. It is illustrated how this technique can be used to study uptake rates, intracellular transport, and cellular responses to nanomaterials quantitatively. Formally, this thesis is a cumulative work.

In the second chapter the concept of digital image cytometry is introduced,

involving the prerequisites for the experimental design, image acquisition, image processing, image segmentation, and feature extraction. In the next chapter the cellular responses upon exposure to gold nanoparticles are addressed, which were investigated with this technique. Here, especially the detection of alterations in cellular/subcellular morphology is described. Finally, in the fourth chapter, the usage of polymer microcapsules for the exploration of the cellular endocytic machinery in a wider context of image cytometry is explained.

2. Digital Image Cytometry

In digital image cytometry, measurements of cell properties are derived from microscopic images (in 2D or 3D) by applying algorithms. This approach is closely linked to computer vision, as the automatic recognition (segmentation) of individual cells is required. All cellular features with unique morphometric, densiometric or textural properties can be investigated provided that their imaging is possible.[56,57] In combination with high-throughput microscopy, valuable data sets containing profiles of thousands of individual cells can be obtained within a short time. Digital image cytometry is the basis for high content analysis, which is used in biological research and drug discovery, to identify substances altering the cellular phenotype in a desired manner.[41,43]

Comparing the results from image cytometry with classical flow cytometry/imaging flow cytometry[58], discrepancies are present when applying the two techniques to similar cell samples.[59,60] In the case of flow cytometry, fluorescence-labeled cells pass a laser beam one by one. From the momentary pulse of emitted photons caused by single cell-crossing events the amount of fluorescence can be used to correlate the labeling efficiency with cellular functioning. Differences may be caused by the fact that the imaging conditions are completely different and thus, the results have to be carefully normalized to be comparable in absolute values.

The main advantage of imaging cytometry is the usage of digital microscopy and therefore the capability to "look into the cell" with high spatial resolution. Hundreds of parameters can be quantified which are not accessible by classical flow cytometry. Finally, the capability to analyze time-lapse image data lends itself to observations of the evolution of certain parameters over time, by following individual cells during movement or tracking particles during cellular uptake.[41,43]

2.1. Requirements

Digital image cytometry is typically performed on image sets gathered by fluorescence microscopy, as this microscopy technique allows for visualizing specific structures exclusively. However, for automated computer vision, it is mandatory to additionally obtain information of features of the cellular framework for cell identification (Image Segmentation, § 2.4).

In conventional absorption light microscopy, image contrast is generated by an inhomogeneous absorption or scattering profile of the specimen, which can be altered by introducing dyes. Distinct structures are only capable of being differentiated in case they bear different optical properties. All colors are usually

registered in the same image. In contrast, in fluorescence microscopy structures of interest are fluorescently labeled with dyes emitting at different wavelengths upon excitation. The fluorescence, *i.e.* the photon counts originating from specific cellular structures, is registered in different channels depending on the wavelength. The absolute fluorescence intensity is ideally proportional[5] to the amount of introduced dye, which, in turn, scales with the concentration of the labeled structures or the internalized fluorescent nanomaterial.

2.1.1. Visualizing the Cell

Fluorescent molecules can be specifically introduced into cells by selecting one method out of a great number of various established ones. Thereby, live-cell imaging requires different approaches in contrast to the observation of fixed (preserved) cells. For live-cell imaging cells can be transfected (*i.e.* modifying the genetic information) to induce transient or stable expression of fluorescent proteins linked to target structures.[61] As another approach, several fluorescently labeled compounds are commercially available, which can penetrate the outer cellular membrane and can either bind selectively to cellular organelles, or are enriched within intracellular environments being characterized by a low pH (*e.g.* lysosomes) or enhanced membrane potential (*e.g.* mitochondria). Immunofluorescence describes the usage of fluorescently-labeled antibodies to identify certain antigens in a very specific manner.[62] As antibodies cannot penetrate the outer cellular plasma membrane due to their large size (around 160 kDa), only antigens which are presented on the outer cellular plasma membrane are detectable in live-cell imaging. Nonetheless, for fixed tissue, immunofluorescence is a widely used method, as cellular plasma membranes can be permeabilized by detergents, which facilitate the use of antibodies.[63]

2.1.2. Nanomaterials

The interaction of nanomaterials with cells can either be measured directly (*e.g.* by tracing materials with fluorescent markers) or indirectly by studying cellular responses upon exposure. In image cytometry both approaches can be combined. Relative uptake rates can be determined, nanoparticle transport can be examined by correlating their fluorescence patterns spatially with the intracellular distributions of specific cellular structures (direct approaches), and in addition, changes in cellular morphology and functioning can be investigated (indirect approach).

[5] depending on the optical properties of the fluorescent complex and the instrumentation.

2.2. Image Acquisition and Image Resolution

The value of the data which are obtained by image cytometry, is strongly dependent on the capabilities of the optical system used for imaging. For meaningful interpretations of the results, one has to be aware of the capabilities and limits of the image acquisition system. Unfortunately, a perfect visual copy of the fluorophore distribution inside a specimen cannot be obtained. Every image obtained with an optical system without super-resolution capabilities is blurred due to the system's characteristic point spread function (PSF). The PSF describes how a single point source is seen by the detector in any optical system, influenced by the diffraction-limited nature of photon propagation.

Due to the relatively large spatial dimension of the PSF regarding a widefield fluorescence microscope, images acquired from any fluorophore in the specimen are blurred because many undesired photons from unfocussed optical sections are included. Hence, the detection volume in such a system can hardly be quantified.

This problem can be circumvented by acquiring several optical slices around the desired axial position. Subsequently, the blur is reassessed to its origin (location of the fluorophore) to inverse the effects of the PSF by means of numerical deconvolution of the image stack.

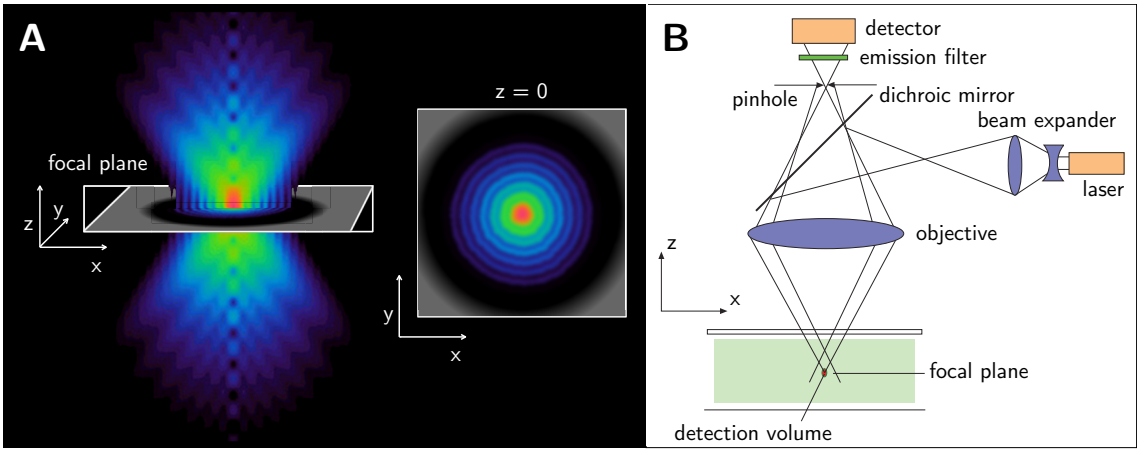

Figure 2.1: Point spread function (PSF) and light path of a confocal laser scanning microscope. A: *Cross-section of a three-dimensional PSF at* y = 0 *(left) and top-view of the same slice in the focal plane (*z = 0*). The detection volume is shaped as a rotational ellipsoid.* ***B:*** *Illustration of the light path inside a confocal laser scanning microscope. By adjusting the diameter of the confocal pinhole, ideally, only the first main maximum (red) of the PSF (shown in A) is detected with a confocal laser scanning microscope to ensure a high depth of sharpness. A was taken from* [64]*; B was taken from* [65]*.*

In a confocal laser scanning microscope (cLSM) the light not originating from the focus is suppressed, in contrast to a conventional widefield microscope.

Firstly, due to higher detection sensitivity (use of photomultipliers instead of CCD cameras), fluorophore-excitation outside of the focus is minimized by decreasing the illuminating light intensity. Secondly, photons which do not originate from the axial position defined through the focal plane, are depleted by a small pinhole within the emission light path. Thereby, only the central part of every fluorophore's PSF is "cropped" and additional axial resolution is gained. In such a setup, the recorded signal behind the pinhole is influenced by the illumination and the detection pathway. Both contribute to blur due to the combined effects of the PSF_{ex}, characterizing the illuminating light path of the instrument and the PSF_{em} of the optical path of the detection setup. If the dimensions or the full width at half maximum of the PSF_{ex} is larger, but in the same range as the PSF_{em}, then the resolving capability is governed mainly by the lateral and axial size of the PSF_{ex} and can be approximated as stated in Eq. 2.1 and Eq. 2.2.[66]

$$r_{lateral} = \frac{0.51\lambda_{ex}}{NA} \qquad \textbf{Eq. 2.1}$$

$$r_{axial} = 0.88\frac{\lambda_{ex}}{n - \sqrt{n^2 - NA^2}} \qquad \textbf{Eq. 2.2}$$

Here, λ_{ex} is the excitation wavelength, n corresponds to the refractive index of the surrounding medium, and NA is the numerical aperture of the used objective. The thickness of a single optical slice (d_{slice}), *i.e.* the slice which is contributing to one single image, can be estimated with the full width at half maximum of the PSF_{em} (Eq. 2.3).[65]

$$d_{slice} = \sqrt{r_{axial}^2 + \left(\frac{\sqrt{2}nd_{pinhole}}{NA}\right)^2} \qquad \textbf{Eq. 2.3}$$

In Eq. 2.3, r_{axial} was calculated based on Eq. 2.2, $d_{pinhole}$ is the back-projected, object-related, diameter of the confocal pinhole (*i.e.* the size of the pinhole as seen in the focal plane), n corresponds to the refractive index of the surrounding medium, and NA is the numerical aperture of the used objective.

Due to their small size classical optical imaging of nanomaterials is strongly limited by diffraction. In widefield or confocal laser scanning microscopy the integrated fluorescent intensity originating from a certain volume can be used to calculate intracellular concentrations, although distinct nanostructures might not be resolvable when lying adjacent to it. The fluorescence readout of nanomaterials equipped with sensing capabilities can often be used to characterize their intracellular environment. This often correlates with their intercellular location, although imaging is limited by diffraction.[67]

2.3. Image Processing

For image segmentation (Image Segmentation, § 2.4), uniform datasets are required. Therefore, appropriate handling of artifacts originating either from the optical imaging itself or from the digitizing of the underlying signals, is needed to minimize intensity non-uniformities. Possible error sources have to be identified and considered during image restoration. In case of confocal fluorescence laser scanning microscopy, images are only slightly blurred by out-of-focus information, but suffer from non-uniform illumination and noise.[68] In the latter case, especially Poisson-distributed shot noise originating from photon detection at low count rates is unavoidable. Examples of methods correcting for non-uniform illumination are (i) the morphological opening of the corresponding image for background extraction, (ii) the subtraction of a blurred version of the image from the original one, or (iii) the adaption of a parameterized surface or grid of cubic splines[6] to the image and normalization of the intensity values based on the computed fit (Figure 2.2).[69,70] All methods have advantages and disadvantages; especially the first approach requires knowledge about the size distribution of the structures to be segmented. Image restoration regarding shot noise is typically performed by deconvolution or filtering.[69,71] Noise reduction by deconvolution typically yields better results. While working with large image sets this approach requires excessive computational time and hence, Gaussian smoothing or especially median filtering is often favored.

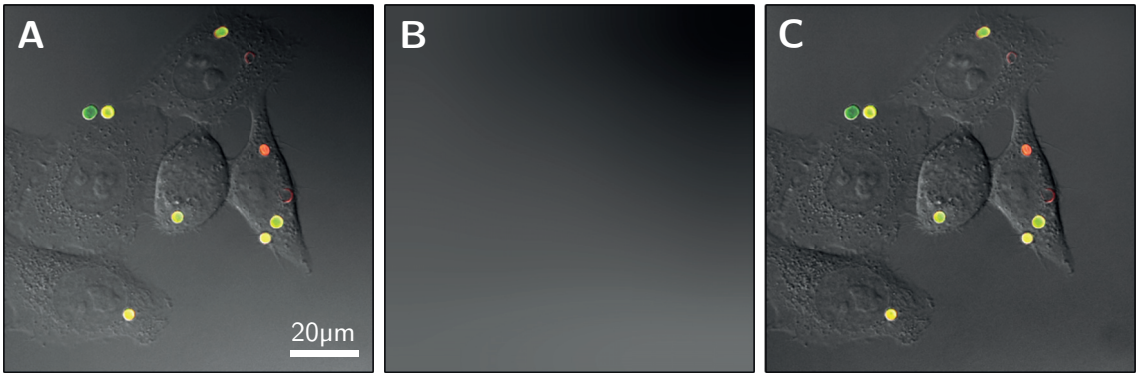

Figure 2.2: Correction of image non-uniformities due to misaligned illumination. ***A:*** *Fluorescence microscope image showing human cervical cancer cells (HeLa) cells with internalized microcapsules (green, red) and non-uniform background in the transmission channel.* ***B:*** *Spline-surface fit to the background.* ***C:*** *Corresponding image after background subtraction. This Figure was created by the author for the purpose of illustration.*

[6] Splines are piece-wise defined polynomial functions.

2.4. Image Segmentation

By means of image segmentation, a digital image is partitioned into its constituent regions to locate objects or certain patterns. Starting from early age, the visual cortex in our brain is trained to identify and allocate objects in the image stream generated by our visual system. Although the human brain can easily recognize the boundaries of an individual cell inside tissue under the microscope, segmentation remains the most difficult task in computer vision.[69] For each segmentation problem, the image constituents are modeled (*e.g.* stained nuclei are bright and round). Based on this model, the segmentation algorithms are selected. In the following paragraphs several segmentation methods most often used are briefly introduced. For practical application in image cytometry, a combination of several segmentation methods is typically used in combination with morphological image processing based on the theory of mathematical morphology. The latter case comprises the application of non-linear operations which alter shape (shrinking/expanding) or morphology (hole-filling, gap-closing, intersectioning) of features in an image.[69]

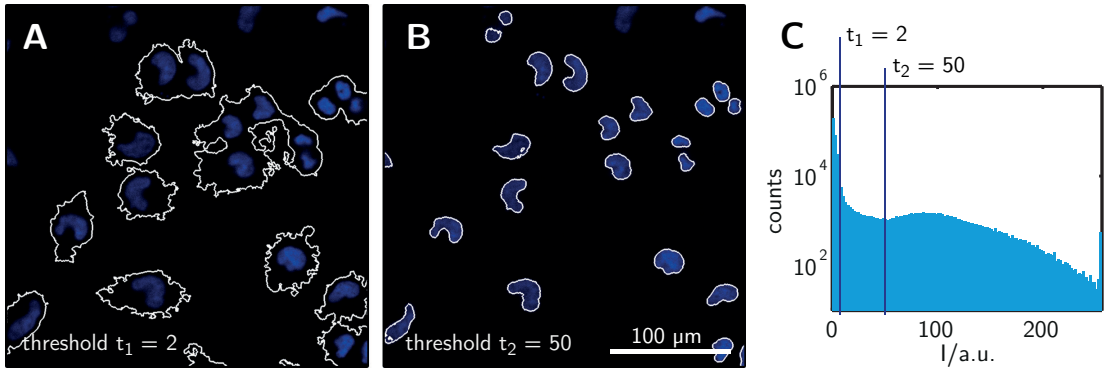

Figure 2.3: Segmentation by thresholding. A, B: *Different thresholds were applied to a fluorescence image showing cell nuclei.* ***C:*** *Histogram in logarithmic scale of the fluorescence image shown in A and B with the corresponding thresholds. This Figure was created by the author for the purpose of illustration.*

2.4.1. Thresholding

In the simplest case, image structures of interest (for instance particles or cell nuclei) are well-separated and brighter than the background. Segmentation is performed by finding all connected components brighter than a suitable threshold (Figure 2.3). Uniform image datasets are favored where all images were acquired under exactly the same conditions, and one global and manually-set threshold can be used to segment all structures of interest. For more complex problems several approaches exist in literature to determine appropriate thresholds locally.[72] Clumped objects are not separated by thresholding.

2.4.2. Watershed Segmentation and Voronoi-Based Approaches

Confluent cells, for instance, are clustered and can barely be divided and segmented by thresholding (Thresholding, § 2.4.1). For such complex structures, watershed segmentation[73,74] or Voronoi-based segmentation[75] has been proven to be very useful. Depending on the staining, cells are typically (i) less intense at the borders in comparison to the average intensity at the perinuclear region or the opposite is true where (ii) cell outlines show a strong contrast and bright intensity. The first case is obtained when staining the cytoplasm, whereas a more inhomogeneous pattern is typically achieved after application of cytoskeletal stains. In the latter case especially ruffles along the outer membrane are highlighted.

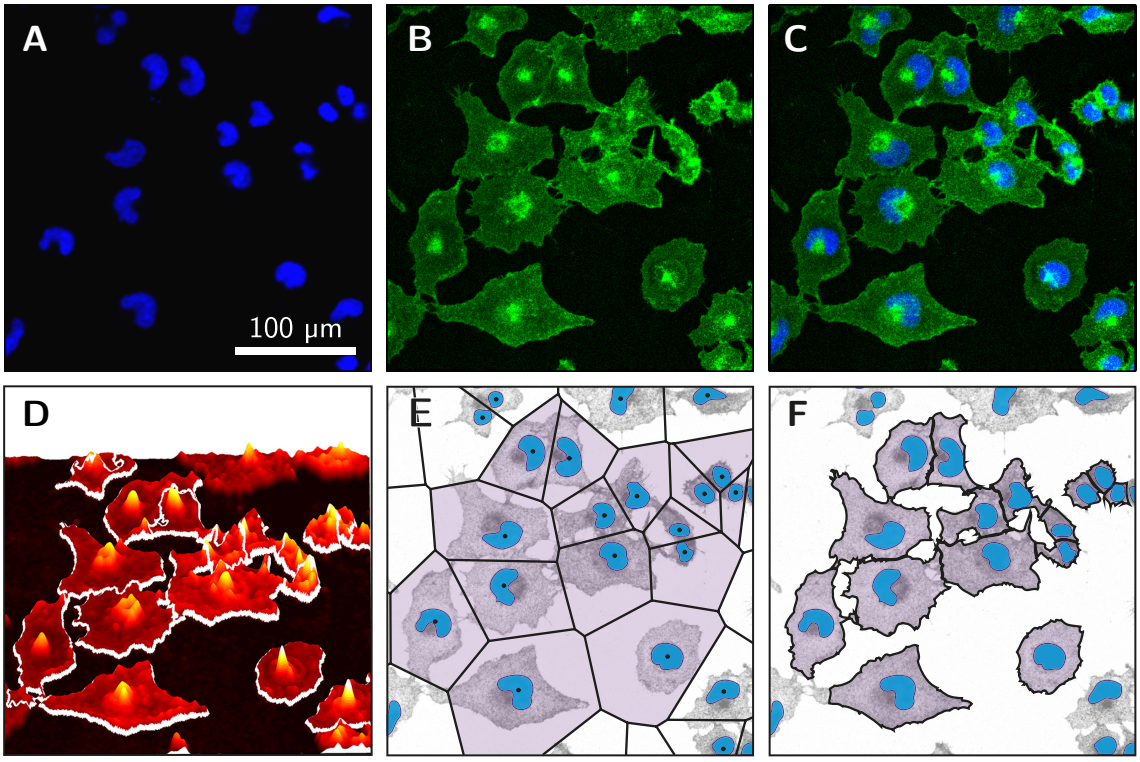

Figure 2.4: Segmentation of cells. A-C: *Two channels of a fluorescence image of fixed HeLa cells stained with Hoechst 33342 (nuclei, blue channel, A), and with fluorescently labeled wheat germ agglutinin (plasma membrane, green channel, B). The overlay of both channels is shown in C.* ***D:*** *The result of seeded (seeds were obtained from the coordinates of the nuclei shown in A) watershed segmentation on a Sobel-filtered (edge enhanced) version of the image shown in B.* ***E:*** *Voronoi diagram[76] based on the positions of the nuclei.* ***F:*** *Voronoi-based segmentation as described by Jones et al.[75]. For comparison, corresponding objects in E and F are shaded and objects touching the border are not outlined. This Figure was created by the author for the purpose of illustration.*

"Watershedding" requires a gradient intensity towards the object borders. Thereby, when image intensity is interpreted as topographic relief, cells can be

thought of as mountains separated by valleys in such an intensity landscape. Watershed segmentation can be imagined as submerging the "image landscape" in water, *i.e.* filling all local minima, and creating boundaries along the lines where different water sources meet in case the water gauge is increased locally and different catchment basins are going to be connected.[73,74] Direct application of the watershed algorithm, as sketched above, leads to oversegmentation (detection of an erroneous high number of separated regions) due to noise and local gradient irregularities.[69] In digital image cytometry this problem is normally solved by providing the algorithm with "seeds" based on the coordinates of unique cellular structures from a parallel image. In case nuclei are stained, they serve as superior markers ("primary objects"), usually being well-separated and easily segmentable by applying a global threshold (Figure 2.4, D).

Voronoi-based segmentation also requires a set of primary objects limiting the number and constraining the position of potential "secondary objects". For each seed a discretized approximation of its Voronoi region[7] (Figure 2.4, E-F) is calculated on a manifold with a metric controlled by local image features.[75]

2.4.3. Shape-Based Segmentation

For segmentation of objects which are either not separated by less intense borders or, when no markers are provided, the inclusion of additional features into the segmentation model is required in order to transform the image structures into other ones, which can be segmented by simple peak-finding algorithms.

The Hough transform is a feature extraction technique which can be used to emphasize structures of any shape.[69,77] In the case of analytically describable shapes, such as lines or circles, a weight is assigned to each pixel of an image, which can be seen as the "probability" of being the origin of an earlier defined parameterized pattern.

For the detection of circular structures (circle Hough transform, CHT) for example, the sum of pixel intensities along a circle of radius r around each pixel px_i is calculated for each pixel, yielding the two-dimensional so-called "accumulator matrix". In this representation, pixels, which are the origins of circular structures of radius r in the original image, appear as bright spots (Figure 2.5). By finding the coordinates of the local maxima in the accumulator matrix, circular structures are registered. In most cases the last task requires additional post-processing and filtering to suppress unwanted side lobs. The CHT is extremely helpful to segment spherical particles in microscopic images which neither show a peak with Gaussian intensity distribution, nor occur in clusters, nor are aggregated (Figure 2.5). By extending the CHT algorithm the identification

[7] Voronoi diagrams describe a distance-controlled partitioning of a plane into regions based on seeds, *cf.* Figure 2.4, E.[76]

of circular objects bearing different sizes is possible (*e.g.* fluorescently labeled polymer capsules, § 4.1), *cf.* Figure 2.6.

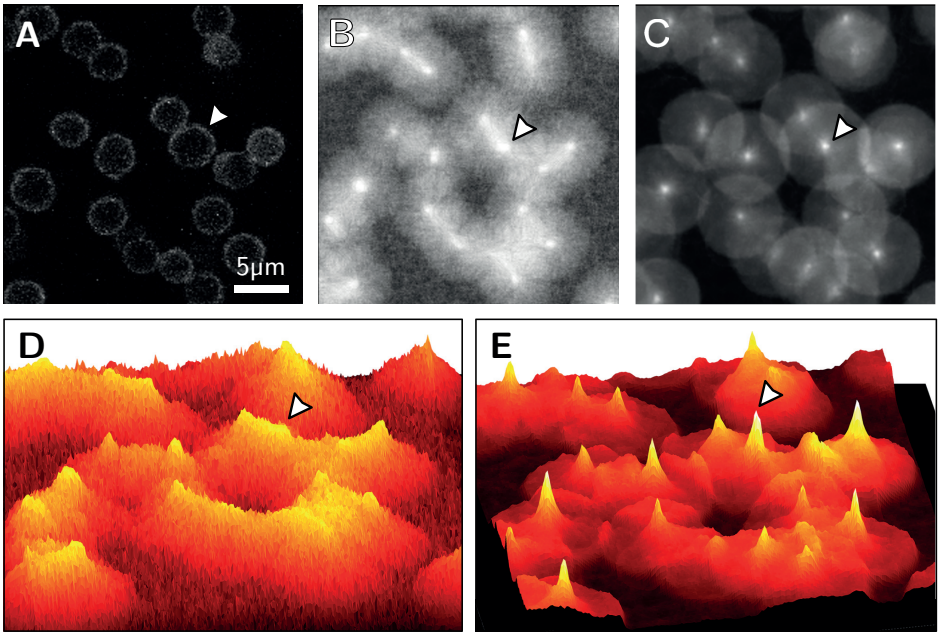

Figure 2.5: Circle Hough transform. ***A:*** *Noisy fluorescence image of hollow and aggregated microcapsules.* ***B, D:*** *Accumulator matrix return from a classical circle Hough transform for circles with $d = 4.2$ µm.* ***C, E:*** *Accumulator matrix obtained from a modified algorithm (Figure 2.6) for identification of center coordinates for capsules with $d < 7$ µm. For registration of the different images one capsule is highlighted with an arrow. This Figure was created by the author for the purpose of illustration.*

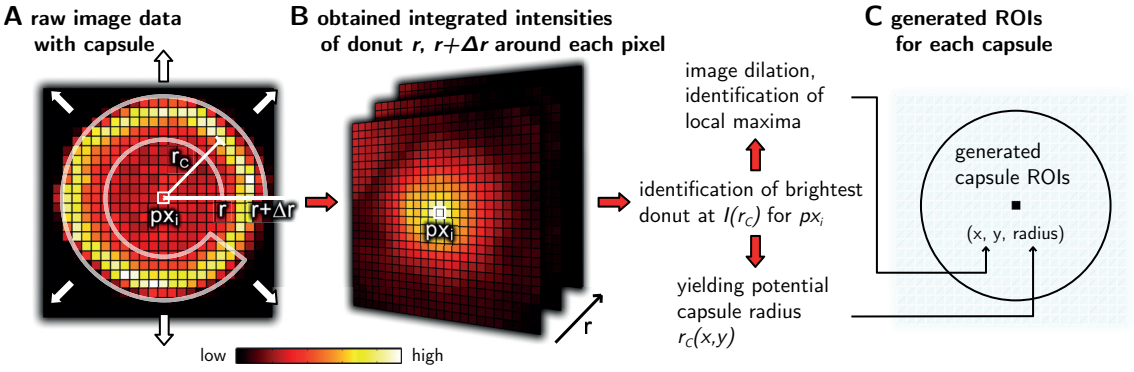

Figure 2.6: Diameter-detecting, modified circular Hough transform. ***A:*** *In fluorescence micrographs, hollow microcapsules appear as circular objects with increased intensity along the shell. By determining the integrated intensity I along a donut or radius r and thickness Δr for each px_i the function $I(r, \Delta r)$ is obtained. When "finding" a shell with origin at px_i and radius r_C, $I(r_C)$ is strongly increased.* ***B:*** *$I(r_C)$ is assigned to the accumulator matrix (Figure 2.5, E).* ***C:*** *Coordinates and radius r_C of the detected structure are obtained. This Figure was created by the author for the purpose of illustration.*

2.5. Feature Extraction and Measurements

Several descriptive features can be extracted from segmented, individual objects in microscopic images. An overview is given by Rodenacker *et al.*[78] Features are either based on the spatial pixel arrangement and describe the shape (morphometric features, *cf.* Table 2.1), give information about the distribution of pixel intensities (densiometric features, *cf.* Figure 2.7), or describe the spatial variations of pixel intensities (textural or structural features, *cf.* Table 2.2). If the microscope images comprise several spectral channels as in the case of fluorescence microscopy, segmented cell-objects based on nuclei and cytoplasm (Watershed Segmentation and Voronoi-Based Approaches, § 2.4.2) can be used to calculate densiometric or textural properties at another spectral region. In other words, the identified objects are used to mask the information in other image channels. By doing so, the spatial intracellular arrangement of tertiary structures can be obtained. Also the level of certain dyes can be observed and related to protein concentrations or expression levels, or the uptake rate of nanomaterials can be quantified. All properties can be related back to the underlying object (*i.e.* cell), and tracked over time (Object Tracking and Digital Video Analysis, § 2.7) in case of live cell imaging.[57,79–81]

Feature	Perimeter d=1µm	0.5µm	0.25µm	0µm
A/µm²	0.78	0.39	0.2	0
P/µm	3.1	2.5	2.2	2
F	1	0.76	0.5	0
Z_0	1	0.5	0.25	0

Table 2.1: Examples for morphometric features. *A = area, P = perimeter, F = form factor = $4\pi A/P^2$, Z_0 = Zernike moment of 0^{th} order. Zernike moments describe the decomposition of an image object onto an orthogonal set of polynomials similar to the way that Fourier coefficients are used to decompose a time series.*[60] *Similar to the form factor F, the 0^{th} moment Z_0 can be used to describe whether a shape is similar to a disk (Z_0 = 1) or more spindle like (Z_0 = 0). d corresponds to the semi-minor axis of the example shapes, if being represented by an ellipse*

Texture					
T_{cont}/a.u.	36	4.2	0.6	0	7.8
T_{corr}/a.u.	-0.5	-0.6	0.3	0	0.7

Table 2.2: Examples for textural features. *Textural features can be used to describe the fine-structure of actin and tubulin staining of cells. T_{cont} = texture contrast, T_{corr} = texture correlation referring to Haralick et al.*[82]

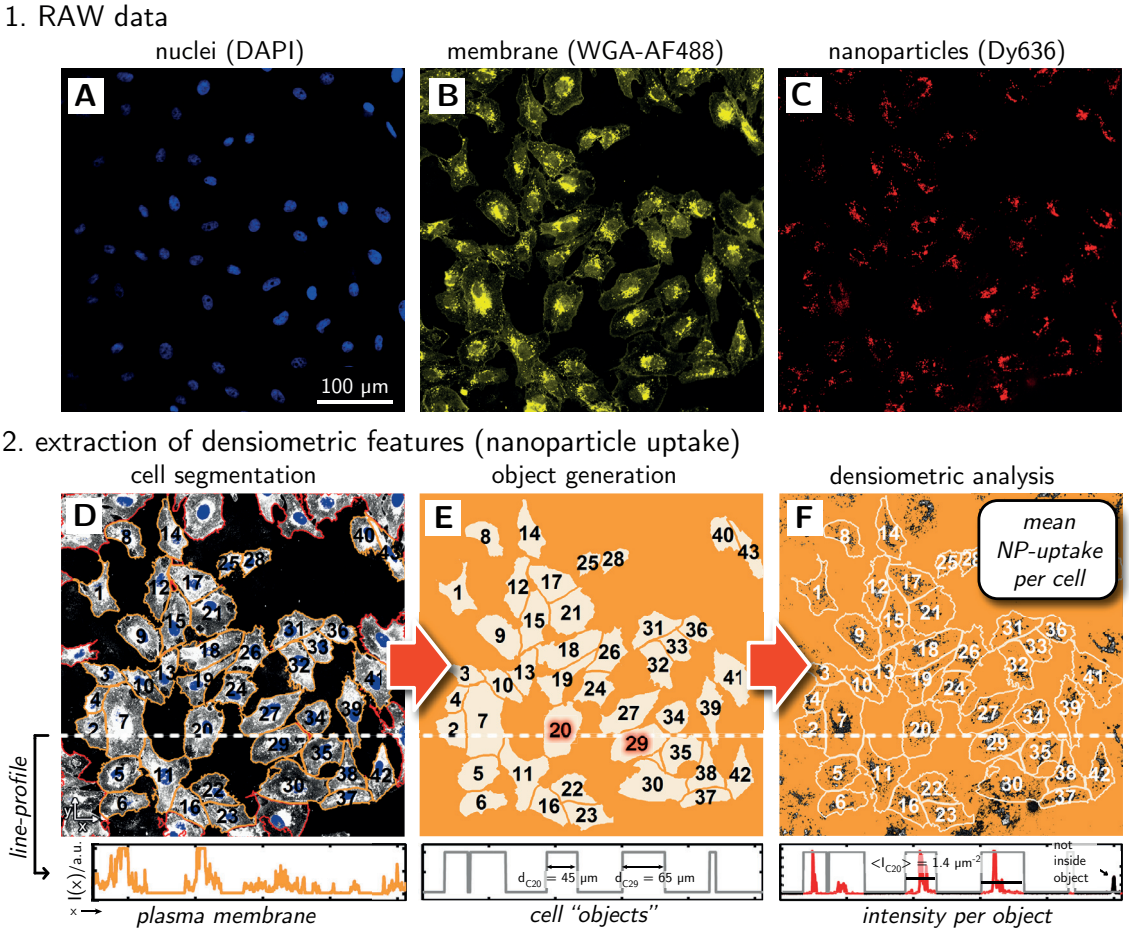

Figure 2.7: Example for densiometric features extraction. *Illustration of the image processing steps to obtain the densiometric feature "integrated intensity" of nanoparticles associated with cells (objects) imaged in an additional fluorescence channel.* ***A-B:*** *For Voronoi-based cell segmentation images of the nuclei (stained with 4',6-diamidino-2-phenylindole, DAPI, blue) and of the outer plasma membrane (stained with AlexaFluor488-labeled wheat germ agglutinin, WGA-AF488, yellow) were used.* ***C:*** *Associated red fluorescence signal of internalized nanoparticles.* ***D:*** *Results of the segmentation procedure. At the bottom, the line intensity profile of the plasma membrane stain along the dashed line is shown.* ***E:*** *Shapes of the obtained cell objects. At the bottom the line intensity profile of the cell objects along the dashed line is shown and cell #20 and #29 are highlighted.* ***F:*** *Overlay of cell object outlines and nanoparticle signal. The integrated nanoparticle intensity I_{Int} is calculated per cell (densiometric feature) and assigned to the corresponding object. In general, the integrated intensity is proportional to the total amount of a fluorescent compound per object. Thus, in this case, the integrated nanoparticle intensity I_{Int} can be related to the total uptake of nanoparticles. For each cell object, I_{Int} is calculated as the mean NP intensity $<I>$ per cell × the area of each object. For clarification in 1D the total uptake I_{Int} along the line profile would be determined as the object length d times the mean NP intensity $<I>$ within the corresponding object (example calculation for cell #20: $I_{Int,C20} = <I_{C20}> \cdot d_{C20} = 47.6$ NP intensity units/µm^{-1}). This Figure was created by the author for the purpose of illustration and can also be found in Pelaz et al.*[83]

2.6. Feature Correlation

Different approaches exist, to investigate the spatial arrangement of intracellular structures from fluorescence microscope images. With the measures introduced below, the degree of co-localization of different patterns being captured in two different fluorescence channels, can be quantified (Table 2.3).[84]

2.6.1. Intensity-Based Correlation

Pearson's correlation coefficient R_r can be used to determine the similarity of two patterns. In the context of digital image cytometry, R_r (Eq. 2.4) can be calculated based on the patterns visible in two distinct fluorescence channels either per image or per underlying cell object (in case statements regarding different cell populations are needed). Pearson's correlation coefficient is defined as the covariance of the intensity values of the two patterns divided by the product of their standard deviations and is widely used in pattern recognition.[69]

$$R_r = \frac{\sum(R_i - \bar{R}) \cdot (G_i - \bar{G})}{\sqrt{\sum(R_i - \bar{R})^2 \cdot \sum(G_i - \bar{G})^2}} \in [-1,1] \qquad \textit{Eq. 2.4}$$

Considering two fluorescent channels R and G, then R_i or G_i, respectively, is the intensity of the ith voxel while $\bar{R}$ and $\bar{G}$ are the mean values of all voxel intensities in the corresponding channel. A positive value for R_r indicates a high degree of co-localization or high pattern similarity, while negative values indicate exclusion. As the average image intensities are included, this coefficient is only slightly biased by different background levels of the two images.[84] If the correction for the average image intensities is not performed (e.g. to compare different labeling efficiencies), then Manders' co-localization coefficient M (Eq. 2.5) is obtained.[85]

$$R_r = \frac{\sum(R_i \cdot G_i)}{\sqrt{\sum R_i^2 \cdot \sum G_i^2}} \in [0,1] \qquad \textit{Eq. 2.5}$$

2.6.2. Object-Based Correlation

In object-based correlation, the spatial arrangement of objects in two distinct channels is analyzed. Therefore, firstly, both images need to be binarized by an appropriate segmentation routine (*e.g.* thresholding) before calculation of either R_r or M. Still, the underlying intensity values of the objects can be used as weightings.

In cases of asymmetrical co-localization (Table 2.3, Example 4) where Pearson's or Manders' coefficients are less meaningful, the use of Manders' distinct

overlap coefficients M_1 and M_2 (Eq. 2.6) might make more sense to quantify the spatial overlap of two patterns.[85] Segmentation is needed to decide whether a voxel is co-localizing or not.

$$M_1 = \frac{\sum R_{i,coloc}}{\sum R_i} \in [0,1] \quad \text{and} \quad M_2 = \frac{\sum G_{i,coloc}}{\sum G_i} \in [0,1] \qquad \textit{Eq. 2.6}$$

Only pixel intensities $R_{i,coloc}$ of pixels co-localizing with an object in the opposite channel are considered. R_i or G_i, respectively, is the intensity of the ith voxel in the corresponding channel.

By dividing the sum of intensities from all co-localizing voxels ($R_{i,coloc}$ or $G_{i,coloc}$, based on Eq. 2.6) by the number N of co-localizing voxels instead of by the sum of all pixel intensities of the corresponding channel, the average fluorescent intensity $\bar{I}$ along all objects O in the opposite channel (O_G or O_R) can be calculated (Eq. 2.7).

$$\bar{I}_R(O_G) = \frac{\sum R_{i,coloc}}{N_{coloc}} \in \mathbb{R}_+ \quad \text{and} \quad \bar{I}_G(O_R) = \frac{\sum G_{i,coloc}}{N_{coloc}} \in \mathbb{R}_+ \qquad \textit{Eq. 2.7}$$

In case of quantifying cell uptake rates of nanomaterials the last equations (Eq. 2.7) are rather useful to assess the density of fluorescent nanomaterials measured for instance in channel R along the certain objects (*e.g.* fluorescence-labeled lysosomes) imaged in channel G, *i.e.* $\bar{I}_R(O_G)$, respectively.

Example	***Type***		R_r	M	M_1	M_2	$\bar{I}_R(O_G)$	$\bar{I}_G(O_R)$
1	*seperated*		-0.34	0	0	0	0	0
2	*partial overlap*		-0.03	0.2	0.42	0.42	35.5	35.5
3	*overlap*		1	1	1	1	85.1	85.1
4	*inclusion*		0.46	0.52	0.42	1	31.1	36.7

Table 2.3: Exemplarily calculated correlation coefficients for representative patterns. ***R_r:*** *Pearson's correlations coefficient,*[69] ***M:*** *Manders' co-localization coefficient,*[85] ***M_1*** *and* ***M_2:*** *Manders' distinct overlap coefficients*[85]*, and* ***$\bar{I}_R(O_G)$*** *and* ***$\bar{I}_G(O_R)$*** *for quantification of the average pixel intensity along objects in channel R or G, respectively.*[36] *The bit-depth of the example images was 8 resulting in a maximum intensity value of 255. All patterns exhibited a linear gradient from I_{max} = 255 to I_{min} = 0. The segmentation method to determine co-localizing pixels in case of the determination of M_1, M_2 and $\bar{I}_R$ and $\bar{I}_G$ was based on thresholding with a threshold of 1.*

2.7. Object Tracking and Digital Video Analysis

Trajectories of individual objects can be extracted from time-lapse fluorescent micrographs by digital video analysis.[86] The time evolution of the distribution of objects (Eq. 2.8) can be used to determine the progression of certain features associated with the objects over time on the level of individual objects (*e.g.* cells or particles).

$$\rho(\vec{r},t) = \sum_{i=1}^{N} \delta(\vec{r} - \vec{r}_i(t)) \qquad \textit{Eq. 2.8}$$

In Eq. 2.8, $\vec{r}_i(t)$ represents the location of the ith object in a field of N particles at time t. In each frame in a sequence of video images, the objects' coordinates and corresponding features (Feature Extraction, § 2.5) are identified by segmentation (Image Segmentation, § 2.4). The trajectories $\rho(\vec{r},t)$ are produced by matching up locations in each image with corresponding locations in latter images. To link objects in two successive frames, the most probable set of N identifications between N locations in two consecutive images is required. Models of the underlying dynamics (*e.g.* Brownian motion for particles) are often considered to increase corrected linking of object coordinates. In addition, unique object features might be included into the probability calculations. Finally, gap closing, merging and splitting steps are needed to correctly handle objects missing in certain video frames (*i.e.* out of focus).[81,86,87]

3. Cellular Responses to Nanoparticles

Besides beneficial aspects of nanoparticle-uptake by cells, such as for the purpose of labeling, diagnosis, or cancer treatment[88,89], the exposure of cells to colloidal nanoparticles can also trigger concentration-dependent responses, including harmful effects which ultimately leads to cell death.[90] For nanometer-sized particles, the specific endocytic uptake mechanism strongly depends on physico-chemical parameters such as size, shape, surface change, elasticity, and surface chemistry.[91,92] In addition to external parameters, such as temperature, time, or the cell type used, the composition of their outermost hydrophilic shell is influencing the attachment of biological molecules in physio-logical environments, forming the so called *nanoparticle protein corona.* Thus, the particles are shielded and specific bare surface functionalities might not come into contact with membrane moieties. Due to this process the initial interaction of nanoparticles with the outer plasma membrane may either be weakened due to charge screening by attached serum proteins or altered by possible ligand-receptor interactions of specific proteins of the nanoparticle corona. Altogether, the corona determines the interaction of nanoparticles with cellular membranes, further uptake, and intracellular trafficking in physiological surroundings.[93,94]

Here, the cellular responses to well-characterized gold nanoparticles (Gold Nanoparticles, § 3.2) were investigated in different studies.[36,40] The application of digital image cytometry is demonstrated exemplary, based on the work *"Colloidal Nanoparticles Induce Changes in Cellular Morphology"* by Ma & Hartmann *et al.*[36] Firstly, the cellular uptake efficiency was examined and secondly, the effect on morphology upon exposure to gold nanoparticles was studied in different types of cells and was related to the nanoparticles' acute cytotoxicity *in vitro*.

In addition *in vitro* uptake studies and investigations of the endocytic pathways of iron oxide and iron platinum nanoparticles were performed during this work.[27,67,83] As they are not directly comparable to gold nanoparticles, which are subject of most of the underlying publications, for detailed results in this regards, the reader should refer to the Appendix.

3.1. Endocytic Pathways

Endocytosis describes the active transport of particles or molecules across the cellular plasma membrane. During this process, invaginations are formed along parts of the outer membrane in contact with the particulate material. By off-pinching, intracellular vesicles (endosomes) are formed containing the internalized molecules (Figure 3.1). Cellular nutrient supply and cellular shape and

volume are mediated *via* endocytosis. In addition this process enables signal transduction and can be utilized for immune responses.[95,96]

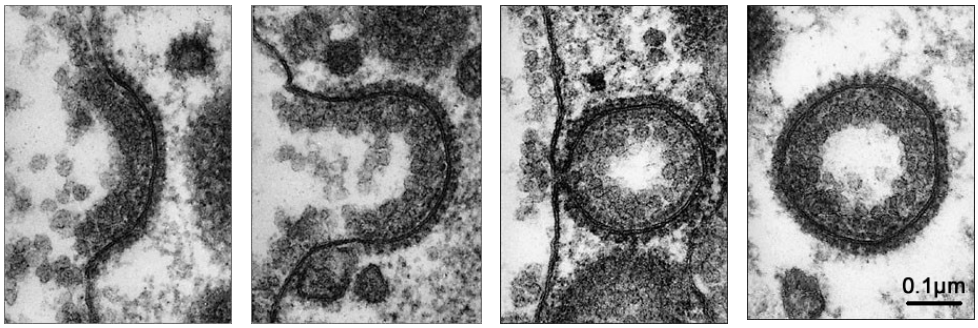

Figure 3.1: Clathrin-mediated endocytosis. *In the transmission electron (TEM) micrographs four succeeding stages of clathrin-mediated endocytosis are visualized. Republished with permission of the Company of Biologists Ltd., from Perry et al.*[97]*; permission conveyed through Copyright Clearance Center, Inc.*

On a closer look, various endocytic pathways can be distinguished by being classified on the base of different mechanisms and endpoints of vesicle migration. Phagocytosis describes the enclosing process of larger membrane segments ($>$ 1 µm) into so-called phagosomes for internalization of particulate material in the magnitude of bacteria or larger (Figure 3.2). The uptake of liquids is seen as pinocytosis, whereas macromolecules and smaller particles are ingested *via* mechanisms that are clathrin- or caveolin-dependent. Both are proteins which are involved in complex interplay with additional factors in vesicle formation and transport. Additional (but less explored) clathrin- and caveolin-independent internalization mechanisms exist which are favored depending on the properties of the extracellular material.[95,98–100] According to the *lipid raft hypothesis*, lipid bilayers, such as the outer cellular plasma membrane, are highly organized by sphingolipids, sterols, and specific proteins whose interplay also influences particle uptake.[101,102]

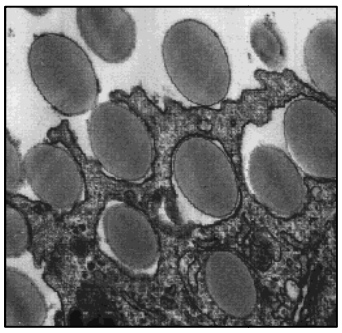

Figure 3.2: Phagocytosis of polystyrene particles. *TEM micrograph of a phagocyte from cavia porcellus internalizing polystyrene particles. This Figure was taken from Doherty et al.*[95]

Ultimately, most of the artificial nanomaterials are enriched in acidic lysosomal compartments which are the endpoint of most internalization pathways.[90,103] On their luminal side these structures are characterized by a high level of lysosomal associated protein 1 (LAMP1). LAMP1 is a glycoprotein often used as a marker for these compartments.[104,105] Off-pinched nanoparticle-

containing vesicles are transported into the perinuclear region while their pH is lowered either by vacuolar H^+-ATPases (V-ATPases), large multi-subunit complexes being able to pump protons into the lumen of organelles or in the extracellular medium,[106] or due to fusion with other vesicles of already much lower pH.[29,107] For functioning of a number of cellular organelles acidic pH is required and thus intracellular pH levels are highly regulated.[108] Acidification is fundamental for endosomal ligand-receptor dissociation, for proper functioning of hydrolases in lysosomes, for antigen-processing in immune cells, for neurosecretion, and for molecule sorting in the trans-Golgi network.[109,110]

3.2. Gold Nanoparticles

The gold nanoparticles (Au NPs) used in this context were obtained by following the Brust method[111] and rendered water-soluble by polymer coating with amphiphilic dodecylamine-modified poly(isobutylene-*alt*-maleic anhydride) (PMA) molecules. The hydrophobic dodecylamine side chains of dodecylamine-modified PMA are intercalating with hydrophobic dodecanethiol ligands attached to the nanoparticle surface. Water-solubility is provided by the hydrophilic PMA backbone (Figure 3.3, A).[25,112–114] To visualize the particles with fluorescence microscopy, their shell was additionally functionalized with fluorescent dyes.

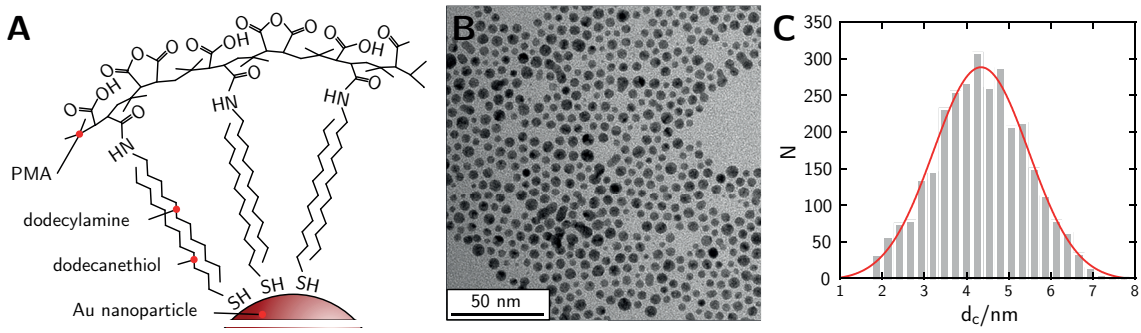

Figure 3.3: Characteristics of PMA-coated Au nanoparticles. A: *Scheme of a polymer-coated NP before phase transfer into aqueous solution. The hydrophobic dodecylamine side chains of dodecylamine-modified PMA are intercalating with hydrophobic dodecanethiol ligands attached to the nanoparticle surface. The thickness of the polymer shell is not sketched in scale. In water the maleic acid anhydride rings of the PMA backbone will open.* ***B:*** *Typical transmission electron micrograph of dried polymer-coated Au NPs.* ***C:*** *Typical core size (d_c) distribution. This Figure was adapted from Figure SI-II.1 taken from Ma et al.*[36]

Gold nanoparticles obtained analogously have been characterized well and are widely used in many laboratories for diverse applications within the last decade. The particles are colloidally stable with a narrow size distribution (4-5 nm core diameter d_c as derived from TEM images, *cf.* Figure 3.3, B-C, and a

hydrodynamic diameter d_h of 10-14 nm determined by dynamic light scattering). Due to the carboxylic groups, which are formed on the PMA backbone upon transfer into aqueous solution, the surface of the nanoparticles is negatively charged. This can be seen in zeta-potentials ζ being typically below -30 mV, as obtained by laser Doppler anemometry.[25,36,40,83,114] The particles are internalized by many types of cells and regarding toxicity, reported IC_{50} concentration values vary from a few hundred nM[53,115] until a few µM or even mM[116,117] depending on the surface coating, the cell types used, and the incubation conditions.

3.3. Cellular Morphology

Eukaryotic cells are complex and highly organized structures containing numerous internal organelles and substructures. Once internalized, nanomaterials can trigger various concentration-dependent responses. Some of them can be observed microscopically, because they induce changes in cellular morphology. Firstly, endocytic compartments are affected, as nanomaterials are typically endocytosed and enriched in lysosomes, leading for instance to lysosome alkalinization. Apart from the visible impacts such as lysosome swelling, the lysosome-based degradative pathway-autophagy is interrupted, which leads to a perturbation of cellular homeostasis.[118] Secondly, alterations in mitochondria morphology are an indicator of increased levels of reactive oxygen species (ROS), which according to several studies is accompanying exposure to Au NPs.[119,120] Thirdly, in the presence of nanoparticles, actin fibers and thereby the cellular cytoskeleton are affected. As the cytoskeleton is responsible for anchoring organelles and general structural integrity, eventually, impacts on global cell morphology-associated parameters such as cell shape, cell spreading, cell adhesion, and cell growth can be observed.[121,122]

In the following, several parameters are introduced (Table 3.1), which can be assessed by digital image cytometry. They are suitable to assay the cellular answer upon exposure to gold nanoparticles, designed as introduced in "Gold Nanoparticles" (§ 3.2). The results obtained by this solely microscopy-based approach are shown in the following, and are related to the performance of classical cyto- and genotoxicological assays in "Colloidal nanoparticles induce changes in cellular morphology" by Ma & Hartmann *et al.*[36] The complete study can be found in the Appendix.

Structure	Parameter	Feature Type	Derived from	Trend	
				HUVEC	***HeLa***
Uptake pattern	Integrated intensity	densiometric	NP fluorescence/ LAMP1 (AB)	+++	+
Viability/ Proliferation rate	Proliferation rate	densiometric	DNA synthesis	--	-
Cell morphology	Area	morphometric	Actin (phalloidin)	--	-
Lysosomes	Fraction of cell area	morphometric	LAMP1 (AB) / Actin (phalloidin)	++	++
Mitochondria	Zernike 0^{th} order	morphometric	CellLight - mitochondria	+++	+
Cytoskeleton	Actin: Texture contrast	textural	Actin (phalloidin)	+	--

Table 3.1: Example parameters obtained by digital image cytometry for quantification of cellular responses upon exposure to Au NPs. *The different feature types are explained in "Feature Extraction" (§ 2.5). The responses of human umbilical vein endothelial cells (HUVEC) and human cervical cancer cells (HeLa) are shown in the trend column. AB = antibody.*

3.3.1. Uptake Pattern

Negatively charged, PMA coated nanoparticles (Gold Nanoparticles, § 3.2) are endocytosed by cells and eventually enriched in lysosomal structures, similarly to polyelectrolyte microcapsules (Internalization Pathways and Intracellular Fate of Microcapsules, § 4.2), which are introduced in the next chapter. Although the final intracellular target is similar, the endocytic routes, the uptake kinetics, and the uptake rates differ strongly.

The uptake of Au NPs and the kinetics of lysosomal enrichment were examined in human umbilical vein endothelial cells (HUVECs) and human cervical cancer cells (HeLa) cells using digital image cytometry and mass spectrometry (Figure 3.4 and Figure 3.5). Obviously Au NPs were endocytosed by cells of both types in a concentration-dependent manner (Figure 3.4), whereas the internalized amount after 24 h was one order of magnitude higher in case of HUVECs. The nanoparticles were enriched in LAMP1-positive lysosomal compartments. In case of HeLa cells a rather linear increase of lysosomal nanoparticle density could be observed (Figure 3.5, B), while for HUVECs a saturation effect became visible for $t > 4$ h, *i.e.* the largest fraction of nanoparticles was transported into the lysosomes within the first four hours (Figure 3.5, C). The saturation was confirmed by mass spectrometry, indicating that intercellular gold levels barely increase from 4 h to 16 h exposure to Au NPs (Figure 3.5, D).

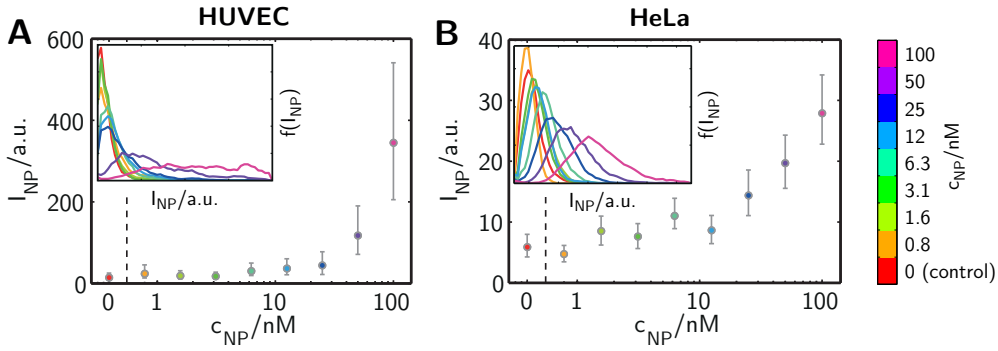

Figure 3.4: Concentration-dependent uptake of Au NPs in HUVECs und HeLa cells. *Displayed are the median integrated fluorescence intensities ± upper/lower quartile of Au NPs inside HUVECs* ***(A)*** *and HeLa cells* ***(B)*** *as measured by digital image cytometry after 24 h of exposure. The insets show the distribution of integrated intensities $f(I_{NP})$ per cell and sample upon exposure to Au NPs at concentration c_{NP}. This Figure was adapted from Figure SI-XI.3 taken from Ma et al.*[36]

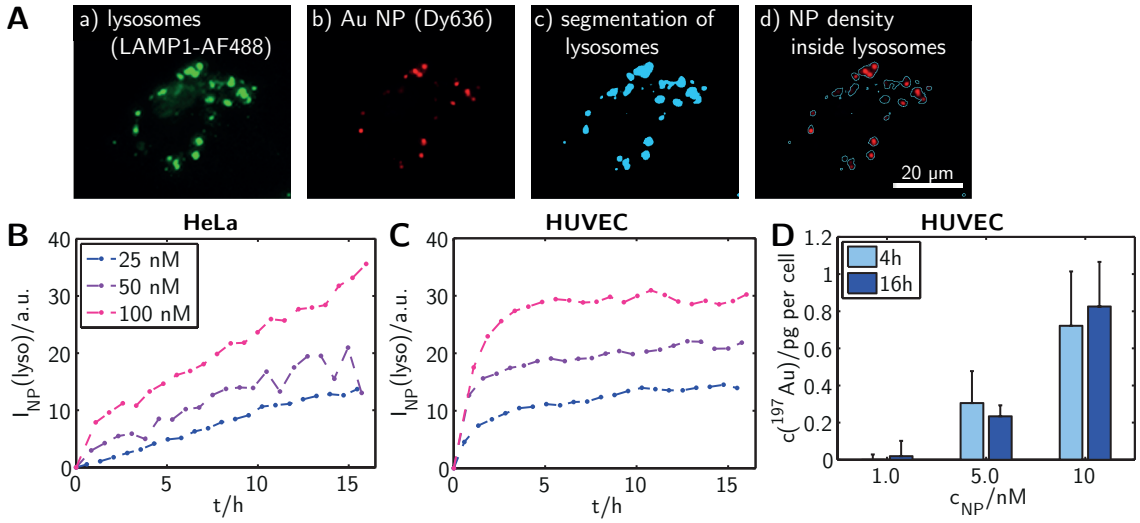

Figure 3.5: Kinetics of lysosomal enrichment of Au NPs inside HeLa and HUVE cells. ***A:*** *Based on fluorescence microscope images the density of Dy636-labeled Au NPs (b) is measured inside lysosomes which are identified from LAMP1-positive organelles (a). This is done by segmentation of the lysosomes (c) and subsequent evaluation of the average fluorescence intensity along the lysosome objects in the channel displaying the signal of the Au NP (d), cf. "Object-Based Correlation" (§ 2.6.2).* ***B:*** *Kinetic of lysosomal Au NP density I_{NP}(lyso) (Eq. 2.7) in HeLa cells.* ***C:*** *Kinetic of lysosomal Au NP density I_{NP}(lyso) in HUVE cells. The absolute intensities are not comparable between HUVECs and HeLa cells as the uptake rate of HeLa cells was much lower and a different detector gain had to be used.* ***D:*** *The observed saturation of intralysosomal Au content for $t > 4$ h in case of HUVECs independent on concentration was confirmed by mass spectrometry for $t = 4$ h and $t = 24$ h. This Figure was adapted from Figure SI-XI.2 taken from Ma et al.*[36] *and Figure 4 taken from Kreyling et al.*[40]

It has to be noted that both types of cells were cultured in different media with unequal amounts of serum added (10 % fetal bovine serum in case of HeLa cells *vs.* 2 % serum content in case of HUVECs). In basal media (*i.e.* without serum) the uptake rates are generally higher. No protein corona is forming around the nano-particles and initial attachment between NPs and the outer cellular plasma membrane is strongly determined by electrostatic interactions.[123] The difference between uptake in serum-containing (10 %) and serum-free medium of 3.5 nm-sized iron-platinum (FePt) nanoparticles by HeLa cells have been observed to be around a factor of ten at 37 °C.[123] However, in the previous example the uptake in serum-containing medium was compared to basal medium without any proteins at all, *i.e.* where nanoparticles completely lacked a protein corona.

The spatial correlation with other endocytotic than LAMP1-positive vesicles was not investigated for the used Au NPs. In previous studies the intracellular pathways of bigger (d_c = 11 nm), but similarly coated iron oxide nanoparticles were examined in human breast adenocarcinoma cells (A549).[27] In the latter case an increase in co-localization with endosomes in the first 10 hours after addition was observed, while the final enrichment in lysosomes occurred later ($>$ 10 h) than for the smaller Au NPs in HUVECs and HeLa cells.

3.3.2. Cellular Proliferation

Cytotoxicity of nanomaterials is typically assessed by measuring the metabolic activity of the exposed cells with Resazurin/Alamar Blue or MTT assays[53,124,125]. Apart from that, cellular proliferation is a sensible viability indicator, because cell growth can be affected at much lower concentrations as cytotoxic effects are detectable with standard cytotoxicity assays. By directly measuring DNA synthesis, cellular proliferation can be examined by digital image cytometry in a very elegant way: DNA synthesis can be monitored by measuring the incorporation of the thymidine-analog EdU (5-ethynyl-2'-deoxyuridine). EdU can be detected by a copper-catalyzed click-reaction between its alkyne group and an azide group-containing fluorescent indicator dye, turning nuclei of proliferated cells fluorescent.[126] After segmentation (Image Segmentation, § 2.4) of all cell nuclei based on a reference staining, the EdU content of each nucleus can be assessed as densiometric feature (Feature Extraction, § 2.5) based on the fluorescence of the indicator dye (Figure 3.6, A-C). As the fluorescence intensity of the indicator dye is correlated with the amount of newly synthesized DNA, the percentages of cells having undergone certain phases of the cell cycle can be estimated.

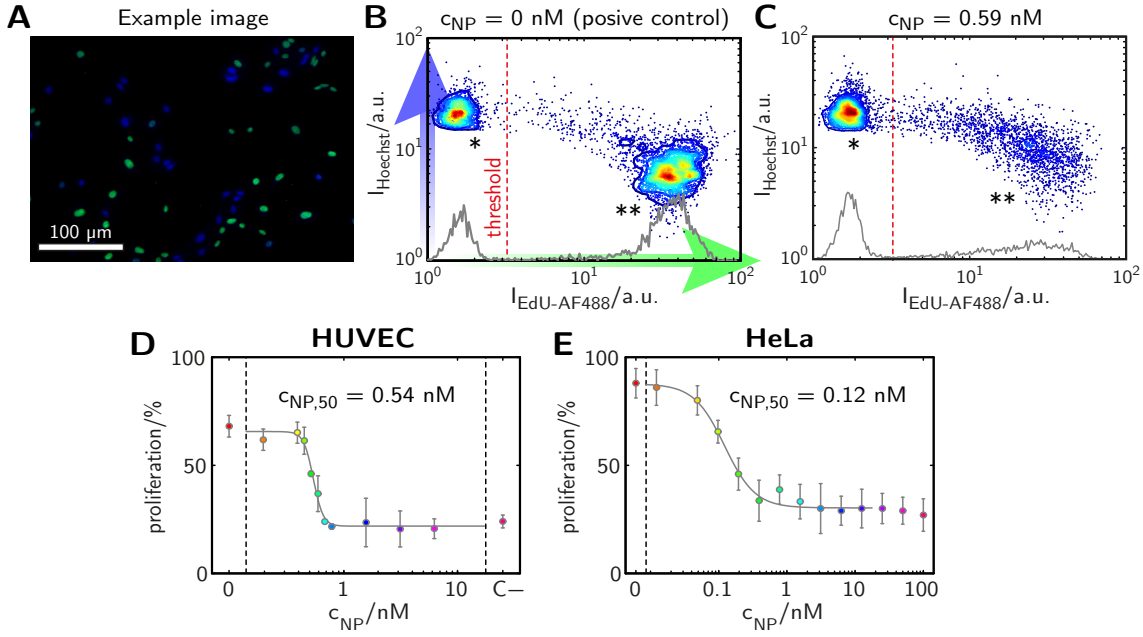

Figure 3.6: Changes in cellular proliferation upon exposure to Au NPs. ***A:*** *Similar fluorescence images, as the one shown, were used to obtain quantitative results. Nuclei of all cells were stained with Hoechst 33342 (blue) for reference. The DNA of nuclei of proliferated cells contains green-fluorescent EdU-AlexaFluor 488 (AF488).* ***B:*** *After segmentation of all reference nuclei, proliferated cells can be detected by analyzing the fluorescence intensity profile of Hoechst 33342 (blue arrow) and EdU-AF488 (green arrow) of all cells. Depending on the nuclei's green fluorescence intensity cells are classified as non-proliferated (*) or proliferated (**), i.e. having undergone at least one S-phase of mitosis. Shown are the data for untreated HUVECs after 24 h.* ***C:*** *Intensity distribution of HUVECs treated with $c_{NP} = 0.59$ nM for 24 h.* ***D:*** *Rate of proliferated cells as obtained for HUVECs upon exposure to Au NPs for 24 h at indicated concentrations.* ***E:*** *Similar results obtained for HeLa cells. Shown are the mean values ± standard deviation for $N = 3$ experiments. The $c_{NP,50}$ values were derived from a sigmoidal fit to the data and represent the point of inflection. This Figure was adapted from Figure SI-IX.7 and Figure SI-IX.8 taken from Ma et al.*[36]

Based on this approach the proliferation rate of HUVECs and HeLa cells upon exposure to Au NPs was examined. As can be seen in Figure 3.6, D-E, cellular proliferation was disrupted at (0.54 ± 0.05) nM (HUVECs), and (0.12 ± 0.08) nM (HeLa cells), respectively, as measured after 24 h of exposure to Au NPs. Even in cell samples exposed to high concentrations of Au NPs, EdU-positive cells could be found after 24 h (always more or less 25 %), indicating, that cells already in the mitotic S-phase in the beginning of the experiment are not interrupted in their cell cycle. Due to the intracellular presence of this type of Au NPs a certain cellular function, required for the initiation of the mitotic S-phase, might be inhibited.

According to Ma *et al.*, viability after 24 h of exposure, as probed by classical cytotoxicity assays, is only reduced at concentrations being more than one order of magnitude higher (> 10 nM for HUVECs and > 100 nM for HeLa

cells).[36,53]

3.3.3. Cell Shape

The cellular shape is described by morphometric features, accessible after segmentation based on a membrane, cytoskeleton or cytoplasm stain. As follows the cell cross-sectional area ("cell area") of HUVECs and HeLa cells upon exposure to Au NPs was examined based on a staining of the actin cytoskeleton with fluorescently labeled phalloidin.

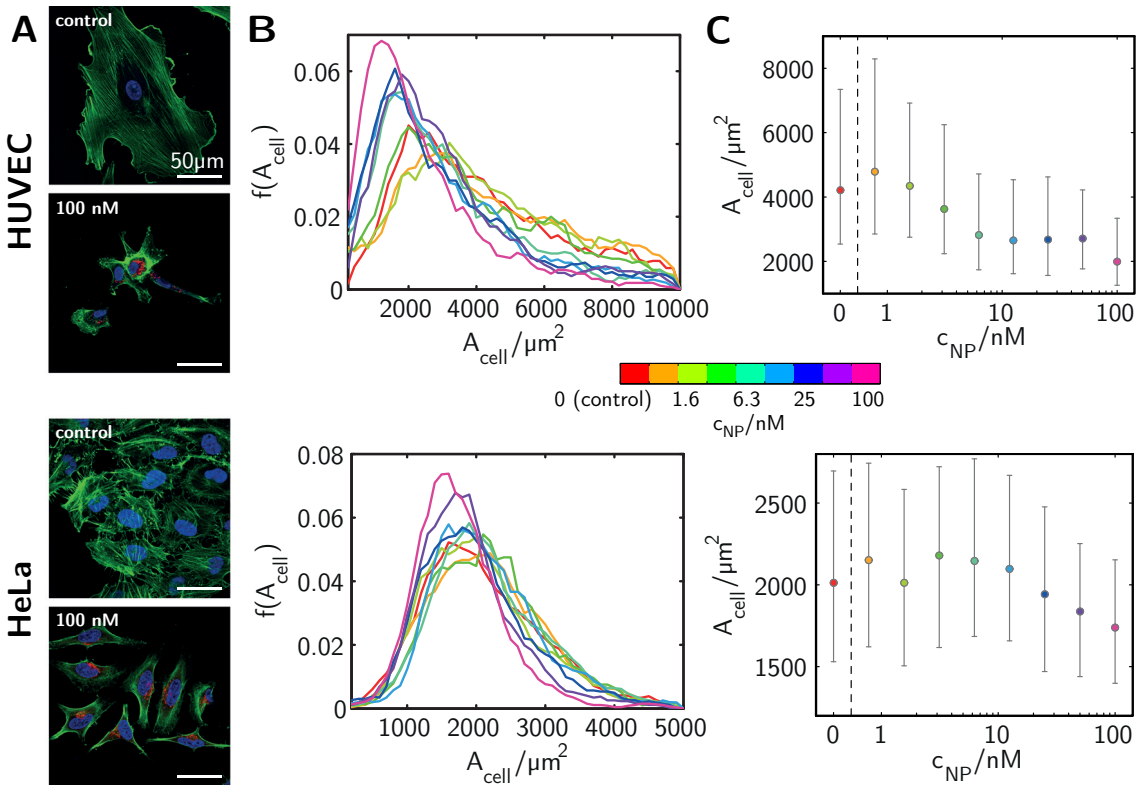

Figure 3.7: Changes in cell cross-sectional area upon exposure to Au NPs. ***A:*** *Fluorescence image tiles showing actin cytoskeleton (green), nuclei (blue), and internalized Au NPs (red) of control cells and cells exposed to Au NPs at* c_{NP} *= 100 nM.* ***B:*** *Distribution of cell areas* $f(A_{cell})$*.* ***C:*** *Derived median values ± upper/lower quartile for the cell areal* A_{cell}*. This Figure was adapted from Figure 1 and Figure SI-IX.4 taken from Ma et al.*[36]

Upon exposure to Au NPs, for $c_{NP} > 2$ nM (HUVECs) and $c_{NP} > 10$ nM the area per cell in a non-confluent cell layer was significantly reduced (Figure 3.7). Interestingly, the average shape, as expressed by the form factor (data shown in Ma *et al.*[36]), did not change in the case of HUVECs and was only slightly altered for $c_{NP} > 10$ nM when HeLa cells were examined. The expression given by the example images in Figure 3.7, A, that cells tended to be more star-like upon exposure to Au NPs at high concentrations, is misleading, because the average shape of the whole cell population only changed in size. Indeed the contrast of

the actin filaments (shown in green in Figure 3.7, A) changed (Actin Filaments, § 3.3.6).

3.3.4. Lysosomal Swelling

As determined by employing correlation analysis (Uptake Pattern, § 3.3.1), Au NPs were enriched in LAMP1-positive lysosomal structures over time. Previous studies have shown that large amounts of aggregated Au NPs inside the lysosome can lead to alkalinization and disturbance of the lysosomal functioning up to alteration in morphology, such as swelling.[118,123,127] In this context lysosome swelling was investigated by comparing the projected area of all lysosomes per cell A_{lyso} with the total area of each cell A_{cell}, as illustrated in Figure 3.8. Lysosomes were immunofluorescently labeled with anti-LAMP1 antibodies.

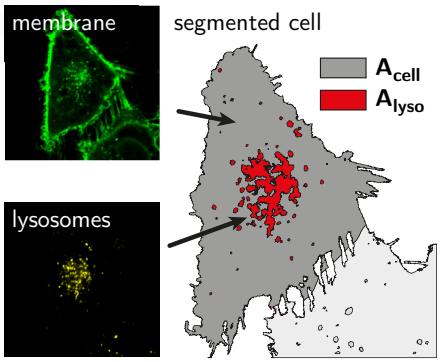

Figure 3.8: Determination of lysosomal area fraction. *For determination of the lysosomal area fraction A_{lyso}/A_{cell} the area occupied by lysosomes A_{lyso}, as obtained from segmentation of an image showing fluorescence staining of lysosomal structures (yellow), is divided the cell cross-sectional area A_{cell}, which can be derived from segmentation of a fluorescence staining reflecting the cell area, e.g. membrane staining (green). This Figure was created by the author for the purpose of illustration.*

As displayed in Figure 3.9, the fraction of cell area occupied by lysosomes increased from 13 % up to 22 % in the case of HUVECs, and from 6 % up to 12 % for HeLa cells, respectively. In both cases the total projected area and, accordingly, the total volume of all LAMP1-positive organelles doubled in size in comparison to the total cell area. Regarding individual lysosomes, swelling was visible especially in HUVECs, whereas in HeLa cells the number of lysosomes seems to increase (Figure 3.9, A).

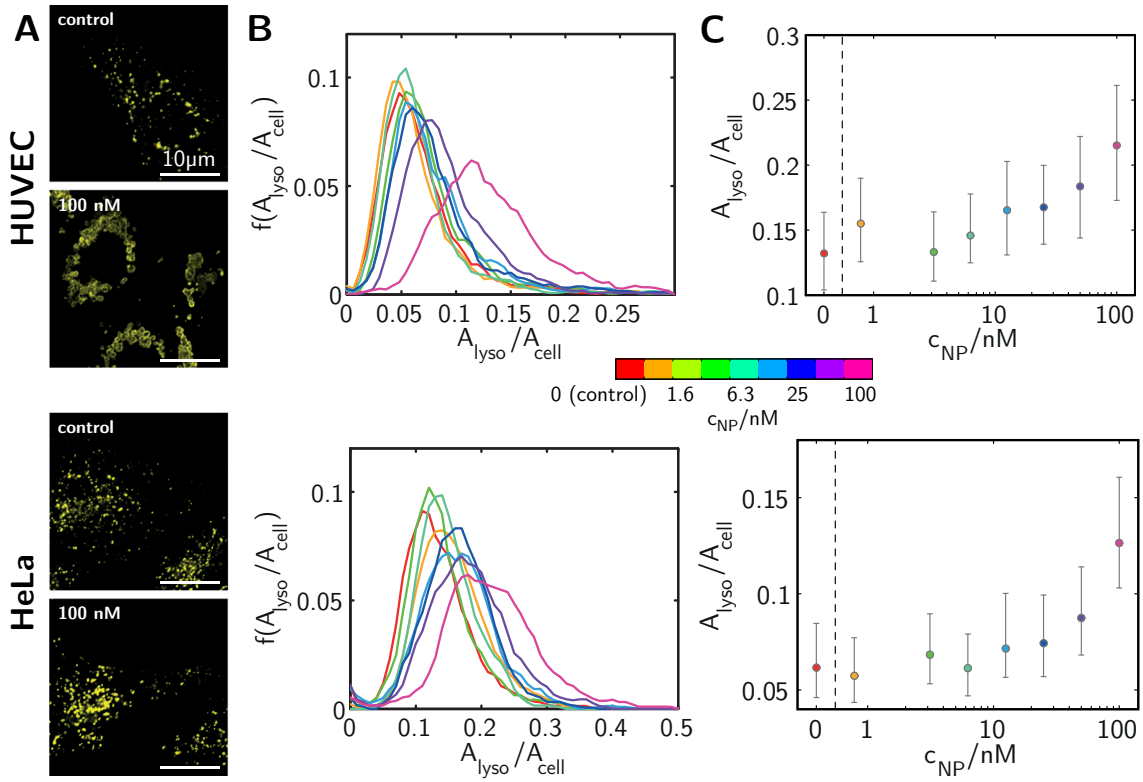

Figure 3.9: Changes in fraction of cell area occupied by lysosomes upon exposure to Au NPs. ***A:*** *Fluorescence image tiles showing lysosomes (yellow) of control cells and cells exposed to Au NPs at* c_{NP} *= 100 nM.* ***B:*** *Distribution of the lysosomal area fraction* $f(A_{lyso}/A_{cell})$*, cf. Figure 3.8 for illustration. C: Derived median values ± upper/lower quartile for the lysosomal area fraction* A_{lyso}/A_{cell}*. This Figure was adapted from Figure 1 and Figure SI-XI.4 taken from Ma et al.*[36]

3.3.5. Mitochondrial Morphology

Mitochondria are important cellular organelles responsible for bioenergetic and redox homeostasis and calcium regulation. They are membrane-bound organelles of highly dynamic nature, constantly undergoing structural transitions. Fusion and fission events are balanced at a steady state. Several studies revealed that cells with a high fusion to fission ratio tend to have long and highly inter-connected mitochondria, whereas cells with a low fusion to fission ratio have a multiplicity of mitochondria that are more sphere-shaped.[128,129]

Several authors claim that exposure of cells to Au NPs has impact on mitochondria. For instance exposure to Au NPs is often accompanied by an increasing intracellular level of ROS, which is typically associated with disturbed mitochondrial functioning.[119,120,130]

The success of measuring the shape distribution of mitochondria by digital image cytometry strongly depends on the success of the segmentation procedure (Image Segmentation, § 2.4). For this study, mitochondria were fluorescently labeled by targeting mitochondrial E1 alpha pyruvate dehydrogenases with a green fluorescent protein (GFP) fusion construct packet in commercially availa-

ble modified baculoviruses.[131] As mitochondria can be quite small (1-10 µm in length), a sufficient resolution is needed for imaging, ideally supported by deconvolution of the data sets to reduce blur. Especially HUVECs have very long and interconnected spindle-like mitochondria, which are difficult to segment properly (Figure 3.11, A). The approach used for segmentation is illustrated in Figure 3.10 and is based on several subsequent segmentation steps with different underlying methods to separate clumpy or interconnected structures. Bad segmentation results (*e.g.* of severely clustered mitochondria) were recognized automatically and excluded from the analysis. Technical details can be found in § VIII.2 of the supplementary information of Ma *et al.*[118]

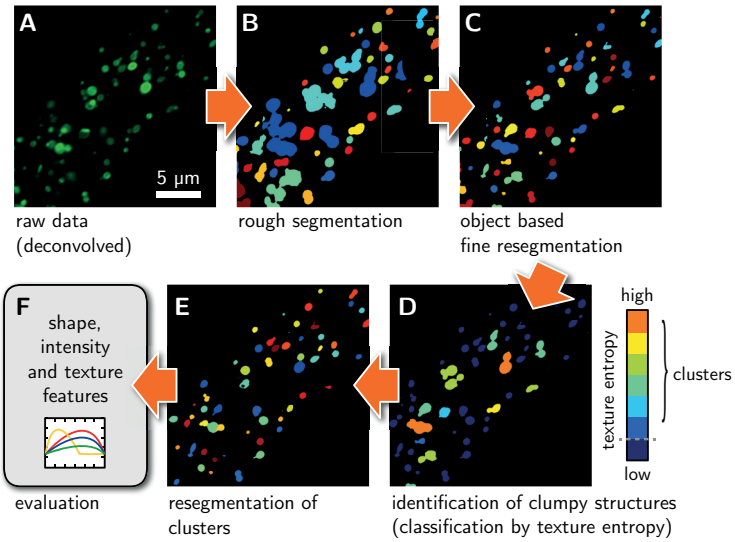

Figure 3.10: Segmentation procedure of mitochondria. A: *Fluorescence image of HUVECs treated with NPs at 12.5 nM showing mitochondria (CellLight Mitochondria-GFP) in the green channel after deconvolution.* ***B-F:*** *Same clipping after subsequent steps of the segmentation procedure. A detailed description including this Figure can be found in the supplementary materials of Ma et al.*[36]

As visible in Figure 3.11, A, the shape of mitochondria changed dramatically after exposure to Au NPs in the selected cell lines. In case of HUVECs the shape changed with increasing concentration of Au NPs from long thread-like structures to polliwog-like forms and finally to small dots with decreasing size. Mitochondria of HeLa cells were already more round shaped in the control group than those of HUVECs under the same conditions. Still, a clear change to smaller and even rounder structures was also observed in the case of HeLa cells. For both types of cells the described transition can be quantified by calculating the "roundness" of the structures in terms of the Zernike coefficient Z_{mito} of 0^{th} order (Table 2.1), as shown in Figure 3.11, B-C. From a sigmoidal fit of the data, the critical concentration $c_{NP,50}$ could be derived which was twice as high for HUVECs (with $c_{NP,50} = 4.4$ nM) than for HeLa cells (with $c_{NP,50} = 2.3$ nM).

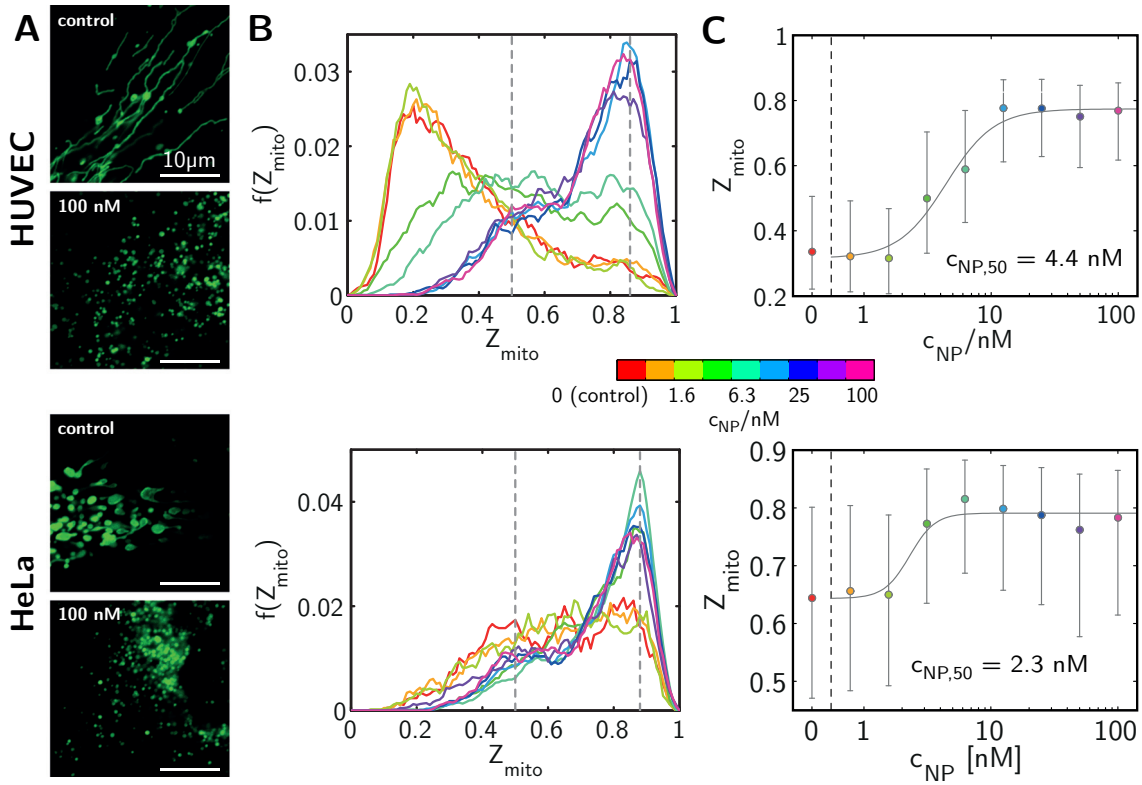

Figure 3.11: Changes in mitochondrial shape upon exposure to Au NPs. ***A:*** *Fluorescence image tiles showing mitochondria (green) of control cells and cells exposed to Au NPs at* c_{NP} *= 100 nM.* ***B:*** *Distribution of the Zernike coefficient of* 0^{th} *order* $f(Z_{mito})$ *describing mitochondrial shape, cf. Table 2.1 for morphometric features.* ***C:*** *Derived median values ± upper/lower quartile for the Zernike coefficient of* 0^{th} *order* Z_{mito}*. The* $c_{NP,50}$ *values were derived from a sigmoidal fit to the data and represent the point of inflection. This Figure was adapted from Figure 1 and Figure SI-XII.3 taken from Ma et al.*[36]

As there is a clear form-function relationship for mitochondria,[132] obviously, the intracellular presence of Au NPs leads to malfunctioning mitochondria above a certain concentration including the disturbance of the cellular apparatus responsible for mitochondrial fusion.[128] The direct role of the Au NPs and also their responsible constituent remain unclear, because mitochondrial fusion and fission activity is influenced by many parameters, such as the level of the mitochondrial membrane potential.[132] Interestingly, the increase in intracellular ROS levels, which is typically accompanying mitochondrial malfunction, was first detectable at a concentration more than twice as high ($c_{NP} > 10$ nM) as such, where shape alterations were observed initially, as demonstrated by Ma *et al.*[36]

3.3.6. Actin Filaments

Actin filaments are dynamically emerging structures which form the cytoskeleton and hence represent the scaffold for many cellular processes. As cell morphology is maintained by actin filaments, if changes in cellular shape occur (as observed in Cell Shape, § 3.3.3), it could be due to a disruption of these structures. In previous studies the following indications were demonstrated: On the one hand diameter, stretching state, and density of actin filaments in human dermal fibroblasts were affected in a concentration-dependent manner upon treatment with Au NPs and on the other hand the intracellular actin fiber distribution was altered.[133,134]

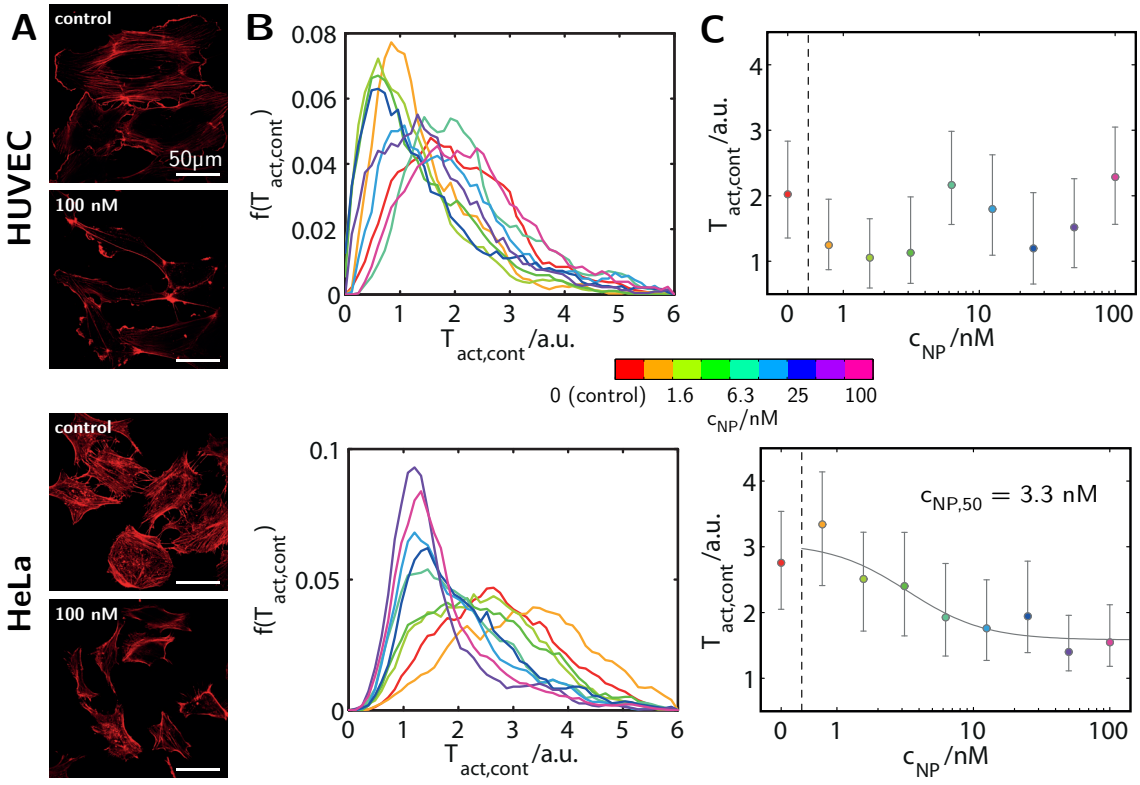

Figure 3.12: Changes in texture of actin filaments upon exposure to Au NPs. ***A:*** *Fluorescence image tiles showing actin filaments (red) of control cells and cells exposed to Au NPs at* c_{NP} *= 100 nM.* ***B:*** *Distribution of the actin filament texture contrast* $f(T_{act,cont})$ *on a length scale of 3 µm, cf. Table 2.2 for textural features.* ***C:*** *Derived median values ± upper/lower quartile for the actin filament texture contrast* $T_{act,cont}$*. The* $c_{NP,50}$ *value was derived from a sigmoidal fit to the data and represent the point of inflection. This Figure was adapted from Figure 1 and Figure SI-XIII.3 taken from Ma et al.*[36]

On this account, the effect of Au NPs on the intensity pattern of fluorescently-labeled actin filaments was examined by determining the actin staining contrast $T_{act,cont}$ for each cell object as an example for a textural feature (Table 2.2). Extensive details can be found in Ma *et al.*[36]

Actin fibers were affected by exposure to the Au NPs as shown in Figure 3.12. The actin texture contrast $T_{act,cont}$, calculated on a length scale of 3 µm, varied strongly for different concentrations of Au NPs in the case of HUVECs, and decreased significantly for $c_{NP} > 3.3$ nM in the case of HeLa cells. A direct effect of Au NPs on actin filament polymerization was observable "in the test tube" for $c_{NP} < 1$ nM in additionally performed control experiments.[36]

4. Investigating the Endocytic Pathways of Micron-Sized Carrier Particles

4.1. Multilayer Microcapsules as Research Tool for Cell Biology

Polymer capsules, e.g. hollow microparticles, as synthesized through use of layer-by-layer (LbL) assembly of oppositely charged polyelectrolytes (Figure 4.1),[135] are internalized by several types of eukaryotic cells including primary cells as well as immortal cell lines. They are seen as a promising delivery system for biomedical applications.[136] In addition, they are a well-suited model system for systematic investigations regarding endocytotic pathways, since their different physico-chemical properties can be tuned independently.[137] Size[138,139] and shape[140–142] can be varied by using different template cores, and the sign of the surface charge is simply determined by the charge of the outermost layer. Stiffness can be tuned by variation of the number of polymer layers or by the polymer materials used.[143–145] *(as published in Hartmann et al.[29])*

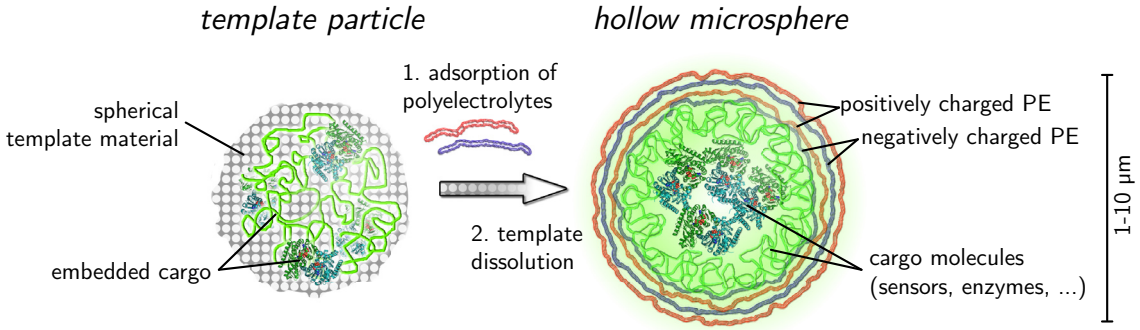

Figure 4.1: Synthesis of polyelectrolyte multilayer capsules. *Layer-by-layer, polyelectrolytes (PE) of alternating charge are adsorbed around template particles of various possible shapes containing embedded cargo molecules. By dissolution of the template material, hollow microspheres are obtained. Depending on the molecular weight, macromolecules are trapped inside the cavity of the capsules, while ions or small molecules can penetrate the shell, which can be utilized for sensing applications. This Figure was created by the author for the purpose of illustration.*

4.2. Internalization Pathways and Intracellular Fate of Microcapsules

Uptake routes and intracellular trafficking of artificial materials on the level of individual cells are typically studied by image cytometry in case the nano/micro material can be labeled fluorescently or be detected by other optical methods. The tagging of target structures with fluorescent molecules of different emission allows for following the materials upon internalization and examining the interplay with certain cellular proteins or other structures. By staining the proteins relevant for certain endocytic processes, the uptake pathways may be reconstructed. In combination with more or less selective inhibition of certain pathways by use of pharmaceutical/chemical inhibitors, more significant conclusions about the observed cellular behavior upon exposure to nanomaterials can be drawn.[96,146,147]

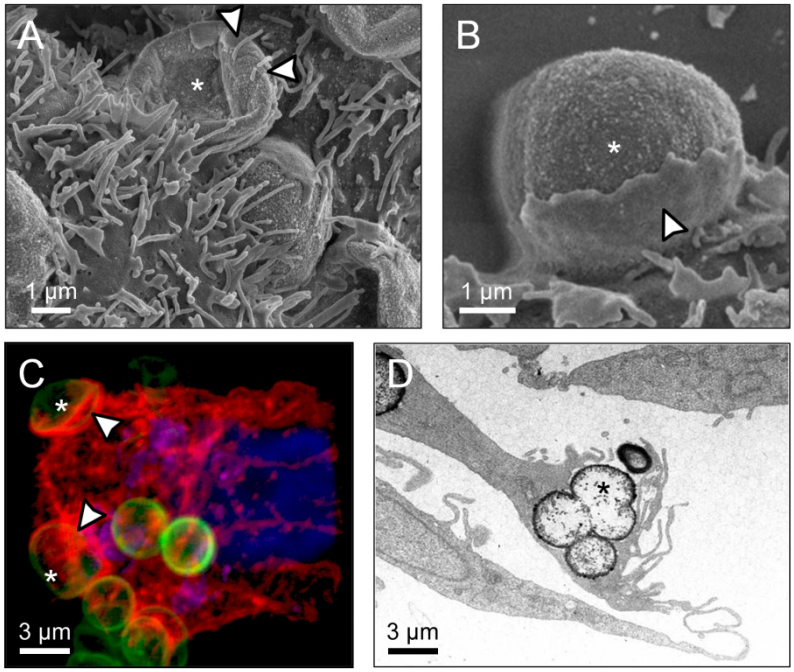

Figure 4.2: Internalization of microcapsules by breast cancer cells. ***A, B:*** *The interaction of hollow particles (indicated with asterisks) with MDA-MB-231 breast cancer cells was visualized by scanning electron microscopy,* ***C:*** *confocal laser scanning microscopy, and* ***D:*** *transmission electron microscopy. In A the formation of filopodia (arrows) can be observed. In B and C the formation of a phagocytic cup is highlighted with arrows. This Figure was adapted from Figure 1 taken from Kastl et al.*[136]

Condition	Concentration	Associated pathway(s)	Inhibition
Cell incubation at 4 °C		All	100 %
Methyl-beta-cyclodextrin	2000 µM	Lipid rafts and lipid-raft-mediated macropinocytosis	93 %
Bafilomycin A1	1 µM	Phagocytosis	84 %
Concanamycin A	0.5 µM	Phagocytosis	63 %
Cytochalasin D	20 µM	Phagocytosis	49 %[8]
Amiloride	500 µM	Macropinocytosis	38 %
Nocodazole	1 µM	Endocytosis	23 %
Heparinases	5 U	Adsorptive mechanisms	17 %
Chlorpromazine	15 µM	Clathrin-mediated endocytosis	16 %
Dynasore	80 µM	Clathrin- and lipid rafts/caveolae-mediated endocytosis	14 %
Potassium depletion		Clathrin-mediated endocytosis	→ 0 %
Nystatin	10 µg/mL	Lipid rafts/caveolae	1 %
Cell incubation in serum-free medium		Determined by the adsorbed proteins	-26 %

Table 4.1: Endocytic pathways of PEM capsules into MDA-MB-231 breast cancer cells. *By interfering with certain cellular uptake mechanisms (i.e. by use of pharmaceutical/chemical inhibitors or by alteration of the cellular environment) the resulting internalization rates were determined by confocal laser scanning microscopy. A detailed description of the used inhibitors and their associated pathways, and the original data can be found in Kastl et al.*[136]*, cf. the Appendix.*

The mechanisms underlying the uptake of polyelectrolyte microcapsules (PEMs) were investigated manually[9] by determining the absolute numbers of internalized capsules per cell upon different exposure conditions, based on 3D image stacks (details can be found in Kastl *et al.*[136], *cf.* the Appendix). The uptake mechanism could be separated into two processes. Firstly, due to sialic acids, which form the terminal groups of many glycoproteins present in the outer cellular plasma membrane, the negative charge on the cell surface (glycocalyx) is increased.[148] PEMs are carrying strongly charged domains on their surface. This results in electrostatically driven interactions between the plasma mem-

[8] cLSM delivered erroneous results regarding the efficiency of inhibition, due to lack of optical resolution. TEM characterization showed a near-complete loss on internalization upon disruption of the actin cytoskeleton with cytochalasin D.[136]

[9] In this early work the uptake of PEMs into MDA-MB-231 and A549 cells was investigated by eye-based manual counting of internalized capsules based on certain criteria. This exhaustive work was a decisive factor to develop and/or implement and finally apply techniques of digital image cytometry for assessing the interaction of nanomaterials and cells with computer-aided approaches.

brane and PEMs, once capsules are in close proximity with a cell. In connection to that, active "grapping" of capsules could be seen in phagocytes such as monocyte-derived dendritic cells.[149] Secondly, once attached, strong action reorganization and filopodia formations occurred, and the formation of phagocytic cups could be observed (Figure 4.2). Eventually, PEMs were transported *via* multiple internalization pathways across the plasma membrane, as shown in Table 4.1. In the beginning of the engulfment process, capsule co-localization with lipid rafts occurred. These structures are fluctuating nano-scale assemblies of sphingolipids, cholesterol, and proteins and are responsible for membrane organization, signaling, and trafficking.[101,136] Possibly due to the large size of PEMs (around 3 µm) clathrin-mediated pathways could be excluded. Upon cytosolic invagination, transport into perinuclear, strongly acidic vesicles was observed. These vesicles are co-localizing with LAMP1 which is a marker for phagolysosome maturation.[105,136,150]

4.3. Elasticity *Versus* Acidification

The impact of certain physico-chemical particle properties, such as: size,[151,152] shape,[24] and charge[25,27] on the internalization behavior of cells is more or less well investigated. Certainly, several other physical properties remain with unclear roles regarding particle uptake. PEMs are excellent for performing systematic investigations, and since many of their properties can be modified without influencing other ones (Polyelectrolyte Multilayer Capsules, § 4.1), their stiffness can be varied exclusively to study possible dependencies between particle uptake and particle elasticity.[29]

Upon internalization by endocytic processes, microcapsules are transferred from the neutral extracellular medium to increasingly acidic intracellular vesicles of different maturity, finally ending up in LAMP1-positive lysosomal structures.[136] Thus, the present stage in the uptake and trafficking cascade can be monitored by the local pH around each capsule (Figure 4.3). For this purpose capsules were loaded with the pH-sensitive fluorophore seminaphtharhodafluor (SNARF) whose emission changes color (from red in neutral to yellow/green in acidic environments) depending on the local pH.[153–155] For evaluation, capsules were segmented by employing a modified Hough transform (Shape-Based Segmentation § 2.4.3) and tracked in successive images frames (Object Tracking and Digital Video Analysis, § 2.7). Each capsule-internalization process was quantified by a set of two parameters, *cf.* Figure 4.3: (i) The processing time $t_{P10\%}$ or $t_{P50\%}$, *respectively,* was introduced as the period of time from the first contact t_C of a capsule with the cell, following its engulfment and finally partial acidification (10 % or 50 %). (ii) The acidification time t_A describes the duration of the acidification process from high to low pH. More detail can be found in Hartmann *et al.*[29], *cf.* the Appendix.

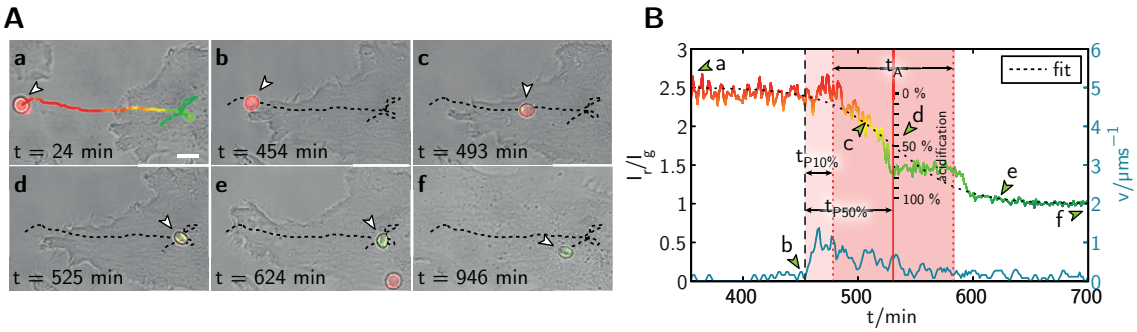

Figure 4.3: Microcapsules with pH-sensing capability. A: *Typical time lapse recording of one pH-sensitive, SNARF-filled microcapsule during its uptake by a HeLa cell. The images (overlay of green and red fluorescence and of bright-field micrograph) recorded at a temporal resolution of 120 s allow the trajectory of the capsule to be determined (scale bar: 5 µm).* ***B:*** *The ratio of red-to-green fluorescence I_r/I_g of the capsule has been determined for each image (Shape-Based Segmentation, § 2.4.3) and is plotted versus the incubation time t. The time points corresponding to the images shown in A are labeled as a - f. A ratio of $I_r/I_g \approx 2.5$ corresponds to a pH value of 7.4, while $I_r/I_g \approx 1$ corresponds to local pH values below 4.5. The acidification time t_A reflects the duration of the acidification process, while the processing time $t_{P10\%}$ is determined as the period from the first contact of the capsule with the cell (b, high velocity v) until the beginning of the acidification process (red area) and $t_{P50\%}$ as the period until the point of inflection of the readout curve (d). This Figure was adapted from Figure 2 taken from Hartmann et al.*[29]

The uptake process was monitored in different types of adherent cells for capsules made of two frequently used polymer systems (non-degradable polymers: poly(sodium 4-styrenesulfonate) (PSS) and poly(allylamine hydrochloride) (PAH), degradable polymers: dextran sulfate sodium salt (DextS) and poly-L-arginine hydrochloride (PLArg)),[136,156] whereas the stiffness was varied in the range from 0.3 until 10 Nm^{-1} by adjusting the capsule shell thickness. For HeLa cells the dependencies are shown in Figure 4.4.

The acidification behavior monitored by non-biodegradable PSS/PAH capsules showed a different trend than those of biodegradable Dext/PLArg capsules. In the first case the acidification time t_A rose linearly with capsule stiffness γ, whereas no such dependency was observed for the degradable capsules. The transition from neutral/slightly alkaline pH to the strongly acidic lysosomal environment is probably faster for degradable capsules. For the non-degradable capsules the duration of this process was longer and additionally slowed down with increasing capsule stiffness. In contrast, the processing time $t_{P10\%}$ rose with the stiffness for both capsules, and for $\gamma < 5$ Nm^{-1} in first approximation even linearly (Figure 4.4, A).

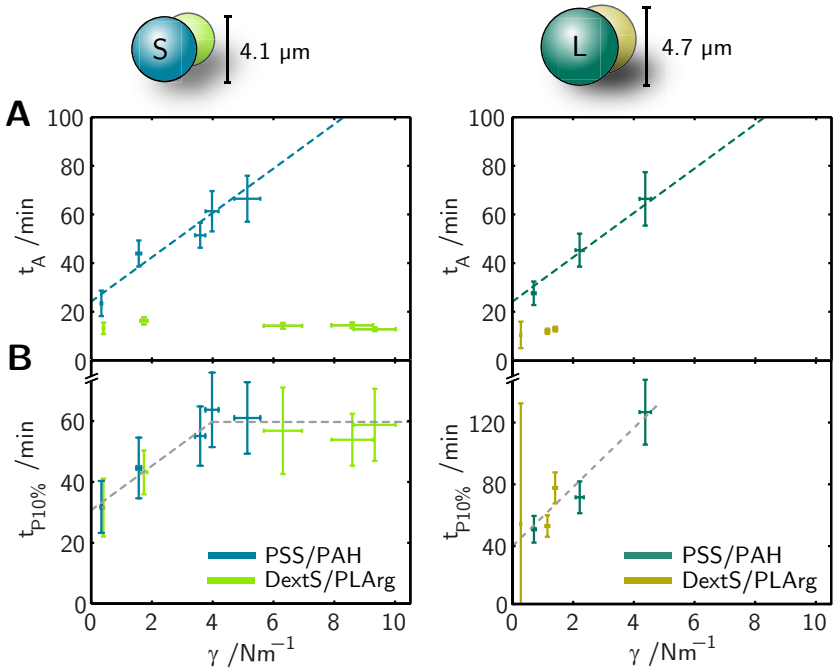

Figure 4.4: Particle stiffness versus intracellular acidification. A, B: *Acidification time t_A and processing time $t_{P10\%}$ of non-biodegradable PSS/PAH and biodegradable DextS/PLArg capsules with variable stiffness γ and of different average diameter (size "S" and "L"), as recorded upon incubation with HeLa cells. Each data point corresponds to the median t_A or $t_{P10\%}$ value including confidence intervals (y-axis) versus the mean stiffness γ value ± standard error (x-axis), as obtained from at least 80 capsules (time values) and 40 capsules (stiffness values). Stiffness values are based on measurements by atomic force microscopy (AFM). The dashed lines are only guides to the eye. Please note that the large error bars for $t_{P10\%}$ and DextS/PLArg capsules (γ < 1 Nm^{-1}, size "L") result from the fact that these capsules are extremely fragile and thus, it is challenging to determine t_C (membrane-attachment). This Figure was adapted from Figure 3 taken from Hartmann et al.*[29]

It can be concluded that the uptake process together with the following endosomal trafficking strongly depends on the particle stiffness. Further processing and acidification in lysosomes are affected mainly by the particle chemistry.[29]

4.4. Investigating Organelle Acidification with Sensor Particles

The sensor particles introduced in "Elasticity *Versus* Acidification" (§ 4.3) can be utilized for several applications, such as: pH measurements inside the cytosol after photothermal release of pH-sensitive molecules upon laser irradiation,[157] analyte sensing,[158] or they can be used to gain a deeper understanding of endocytotic processes on the microscopic level, for example organelle acidification.[159]

For the last case two applications are introduced: (i) By means of image

processing, measurements of the acidification process of microcapsules can be extended by following the spatial arrangement of fluorescently-tagged proteins associated with the uptake process in a parallel image. As microcapsules are identified in each image frame as unique objects during the segmentation process, additional features in another fluorescence channel can be assigned to the capsule object.[29] (ii) Possible impacts of pharmaceutics or changes in cellular functioning on the endosomal acidification cascade can be studied.[155,159]

As outlined in the first example, PEM capsules can be used to correlate the fusion frequency and trafficking of LAMP1-positive structures with the current stage in intracellular processing that is being reported indirectly by pH measurements (Elasticity *Versus* Acidification, § 4.3**)**. Therefore, HeLa cells were transfected to express LAMP1 labeled with GFP to allow live-imaging of lysosomes and the capsule acidification in parallel.[29]

The mean fluorescence intensity of endogenous LAMP1-GFP associated spatially with each sensor capsule was strongly correlated with the reported pH (Figure 4.5**)**. Immediately after engulfment, no fluorescence signal of LAMP1-GFP could be associated with any capsule. With increasing fusion frequency of LAMP1-positive vesicles with the capsule-containing compartment, the local pH around the corresponding capsule was lowered (Figure 4.5, b-d) and the mean fluorescence of LAMP1-GFP ($I_{LAMP1\text{-}GFP}$) increased until both measures (pH and LAMP1-GFP-fluorescence) reached a plateau and kept constant. Certainly, either H^+-pumps directly incorporated inside the membrane of the capsule containing vesicle or fusion with acidic LAMP1-negative vesicles must play an additional role, as likewise decreasing pH values were measured which were not in line with increasing LAMP1-GFP fluorescence (Figure 4.5, B/e).

In the second example to be described in more detail pH sensor capsules were used to measure possible impacts on acidification upon modification of H^+-pumps. In detail, the importance of the V_1G_1-subunit of the V-ATPase was investigated in regulating the activity of the proton pump. This was realized by comparing the acidification patterns of single pH-sensitive PEMs during endocytosis in either overexpressing V_1G_1- or V_1G_1-depleted cells. The subunit is a member of the peripheral stator stalk that connects the peripheral vacuolar V_1-domain with the membrane V_0-domain of the enzyme (Figure 4.6**)**.[160]

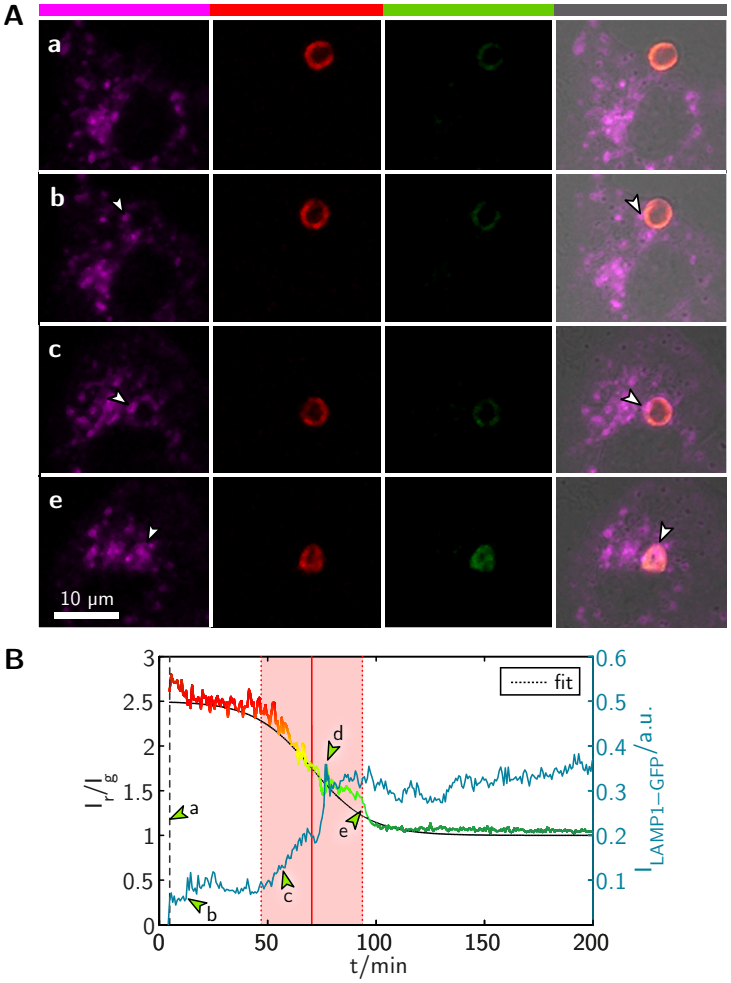

Figure 4.5: Distribution of LAMP-1 during capsule uptake in HeLa cells. ***A:*** *Time lapse recording showing the fluorescence signal of LAMP1-GFP (magenta), the red and green fluorescence channel of the capsule pH-readout and an overlay of all fluorescent channels with the corresponding bright-field image.* ***B:*** *for each image the ratio of red-to-green fluorescence I_r/I_g of the capsule has been determined and is plotted versus the incubation time t. The time points corresponding to the images shown in A are labeled as a - d. The ratio of $I_r/I_g \approx 2.5$ corresponds to a pH value of 7.4, while $I_r/I_g \approx 1$ corresponds to local pH values below 4.5. In addition the mean fluorescence of LAMP1-GFP ($I_{LAMP1\text{-}GFP}$) over the capsule area is plotted in blue. This Figure was adapted from Figure SI-16 taken from Hartmann et al.*[29]

The investigation was performed on HeLa cells. Stable HeLa clones (CTR #2, #1, #3, and #7) with either overexpressing V_1G_1- or V_1G_1-depleted cells were obtained by transfection, *i.e.* by interfering into the cellular gene expression machinery. This is typically achieved by inserting a circular vector of artificial DNA (plasmid) into the cells carrying the genes of interest together with suitable primers to enable transcription and as well, controlling the expression rates. In addition, genes are introduced delivering resistance against a certain antibiotic to allow specific selection of successfully modified cells after transfection.[61] In this specific case in clone #1 and clone #3 additionally to the endogenous expression, tagged V_1G_1 was expressed, whereas in clone #7 the endogenous V_1G_1 level was lowered. The altered expression levels of the V_1G_1-subunit among the different clones were confirmed by sodium dodecyl sulfate polyacrylamide gel electrophoresis (SDS-PAGE) and Western blot analysis (Figure 4.7, A). As a control, cells carrying an empty plasmid were used. Details can be found in Ferraro, de Luca & Hartmann *et al.*[136], *cf.* the Appendix.

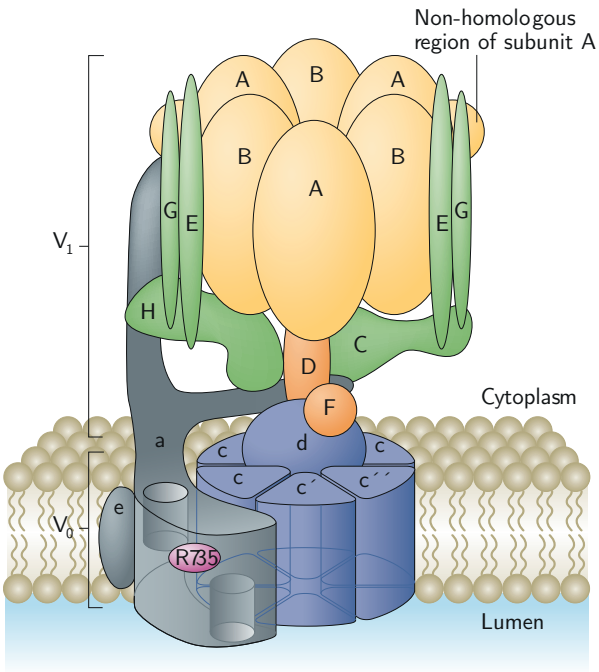

Figure 4.6: Structure of the V-ATPase. *The complex is composed of a peripheral domain V_1 (yellow/orange), which is responsible for ATP hydrolysis, and an integral membrane domain V_0 (blue/grey) which is involved in proton transport across the membrane.*[161] *This Figure was taken from Forgac et al.*[160]*, where a detailed description about the subunits (A-H, a-e, R735) can be found. Reprinted by permission from Macmillan Publishers Ltd: Nature Reviews Molecular Cell Biology, copyright 2007.*

The acidification patterns of PEMs during uptake in these modified cells were quantified as described in "Elasticity *Versus* Acidification" (§ 4.3) by determining the acidification time t_A (Figure 4.3) of each capsule during uptake. The analysis revealed a delay in acidification present in both, in clones expressing additional tagged V_1G_1 (clone #1 and #3) and with V_1G_1 silenced (clone #7), *cf.* Figure 4.7, B-D. Particularly clone #1, which exhibited the highest level of V_1G_1, showed the slowest kinetic of acidification. In addition, the acidification patterns were different among the different clones (data can be found in Ferraro *et al.*[136]).

With the utilized pH sensor capsules it was possible to measure V-ATPase functioning directly. There are indications that correct intracellular protein levels of the V_1G_1-subunit of the proton pump are required for its proper functioning and organelle acidification confirming previous studies.[162–164] Despite these findings, further investigations are needed to resolve questions regarding the exact role of V_1G_1 in regulation of V-ATPase activity.

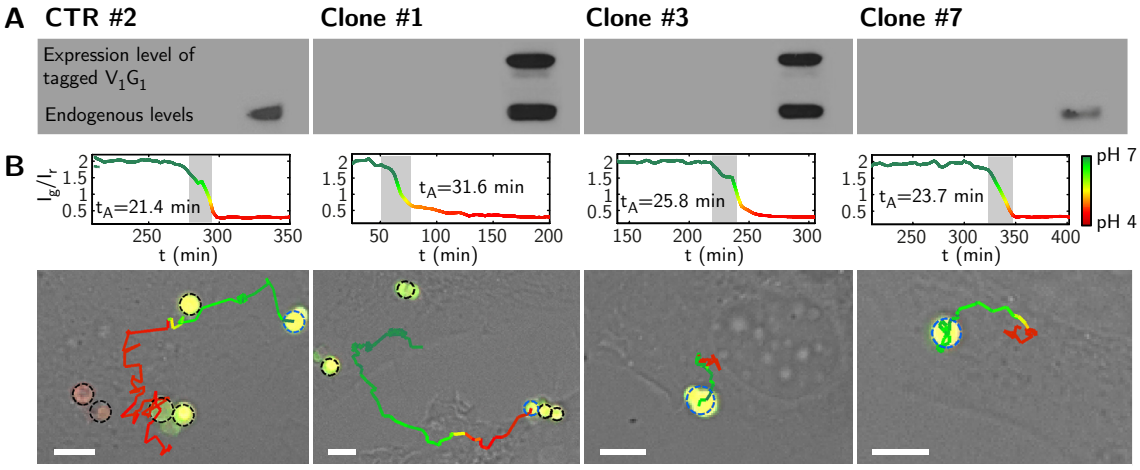

C

Duration of acidification: t_A (min)				
clone	CTR#2	#1	#3	#7
N	299	290	360	378
median	18.77	25.30	19.52	20.40
mean	21.95	30.94	24.12	24.90
Q1	11.07	16.95	11.85	11.75
Q3	27.83	39.57	29.85	30.51

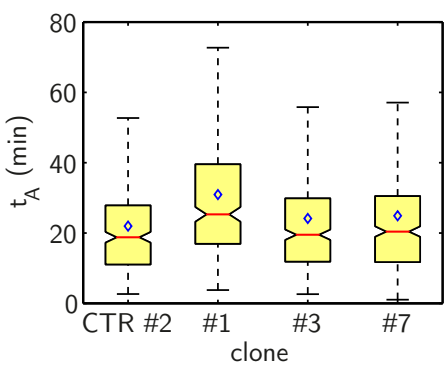

Figure 4.7: Acidification patterns of sensor capsules in either overexpressing V_1G_1- or V_1G_1-depleted HeLa cells. A: *Expression levels of V_1G_1 in the different clones. CTR #2 refers to a control clone. Additionally, tagged V_1G_1 was overexpressed in clones #1 and #3, while the endogenous expression level was lowered in clone #7.* ***B:*** *Examples of use of capsule-based sensors[10] for real-time monitoring of acidification by tracking a single capsule (indicated by blue dashed circles) from the time of initial attachment to the cell until the completion of acidification. In the fluorescence images sensor capsules appear green in neutral local pH and red in an acidic environment. The scale bars correspond to 5 µm.* ***C:*** *Table with number of evaluated trajectories N per clone, mean and median values for the acidification time t_A as well as the corresponding upper and lower quartiles (Q1 and Q3).* ***D:*** *Box plot of acidification times t_A among the different clones. The acidification rate of clone #1 was significantly lower than that of the control cells ($p < 0.0001$, *). P-values were obtained from a two-tailed Wilcoxon–Mann–Whitney test. Additional significance levels: $p < 0.23$ (**), $p < 0.17$ (***). The Figure was adapted from Figure 1 and 4 taken from Ferraro et al.*[159]

[10] In this example capsules were used that were loaded with fluorescein isothiocyanate (FITC) and rhodamine isothiocyanate (RITC). The fluorescence intensity of FITC strongly decreases in acidic environments. RITC (pH-insensitive) was used as a reference dye. Details are described by Ferraro *et al.*[159] The ratio of FITC/RITC-fluorescence was determined over time and is plotted in Figure 4.7, A.

5. Conclusions and Outlook

In the previous chapters the uptake and endocytic pathways of two classes of nano/micromaterials (Au NPs and sensor microcapsules) which are both frequently used in nanobiotechnology, were examined. Hereby, the primary focus was put on the application of digital image cytometry to gather robust and statistically meaningful results.

For measuring the impacts of Au NPs on cellular morphology several assays were presented where the concept was borrowed from high content analysis. The comparison with results obtained by classical viability assays (MTT and resazurin-based) confirming the significance of the observed effects. Abnormalities in morphology occurred at even lower nanoparticle concentrations, as required for the onset of reduced cellular viability. Especially mitochondrial morphology turned out to be a well-accessible and reliable indicator for gold nanoparticle-induced cellular stress.[36] Several studies exist where no cytotoxicity is attributed to Au NPs of similar size.[116,165] This evaluation is outdated,[53,122] and it has to be noted that most of these findings are based on classical viability assays – the same which neither reported acute cytotoxicity below NP concentrations of 100 nM in this case. Regarding PMA-coated Au NPs, the underlying mechanisms causing the cellular cytotoxic responses are not entirely understood. In another study by Kreyling *et al.* it was demonstrated that inside cells the surface coating of such PMA-coated Au NPs comes off *in vivo* and *in vitro*.[40] Hence, cytotoxic potential might be attributed to either the bare Au core which possesses some catalytic activity, the polymer shell, the fluorescent dye, or to potentially released gold ions.[36] The observed inhibition of proliferation at incredibly low concentration of Au NPs was also reported by others,[52,166] but strange to say, was overlooked by Soenen *et al.* who studied gold nanoparticles of similar characteristics in a multiparametric approach.[53] Although Au NPs are probably residing in lysosomes after uptake, they are assumed to block the function of heparin-binding proteins being responsible for cellular proliferation.[167]

Polymer capsules are seen as promising vehicles for intracellular cargo delivery, release and sensing.[168–170] Thus, the cellular parameters which, for instance, determine uptake rates or release kinetics are of great interest. On the one hand large (> 3 µm) polymer capsules are not suitable for *in vivo* applications as they might cause clogging of blood vessels. On the other hand they serve as perfect model systems for systematic studies regarding uptake,[136,171,172] processing,[142,156] and release.[157,173] Due to their large size they are easy to trace with optical microscopy and can carry enormous amounts of cargo molecules. The proteins associated with capsule uptake can be elucidated by correlating their spatial distribution over time with the localization of capsules in a very efficient manner (such as LAMP1, as illustrated in Figure 4.5).

By combining capsule tracking and cell segmentation/identification, release patterns and release kinetics of polymer capsules of different architectures can be monitored with high throughput. An example for the realization of an assay in this regard is described in the following: To study the release profile of polymer capsules with different architecture, dequenching ovalbumin (DQ-OVA) labeled with boron-dipyrromethene (BODIPY) serves as a well-suited model drug when encapsulated.[149,156] Inside the capsule the green fluorescence of the dye BODIPY is almost completely self-quenched due to the close proximity of the dye molecules inside non-fragmented ovalbumin.[174] Inside intact polymer capsules slightly red fluorescent excimers are formed due to the high dye concentration. This red fluorescence signal or the signal of an additionally loaded reference dye would act as a staining to identify and track the capsules during uptake. Upon enzymatic degradation (which would take place after cellular internalization) the green fluorescence intensity of BODIPY would be dramatically increased and potentially released fragments of DQ-OVA would become visible. In combination with single cell identification and tracking, the release per capsule and per cell volume/area could be determined with the aid of a computer, as shown exemplarily in Figure 5.1. Either average release profiles or the processing of single capsules could be monitored quantitatively by digital image cytometry of time lapse image data.

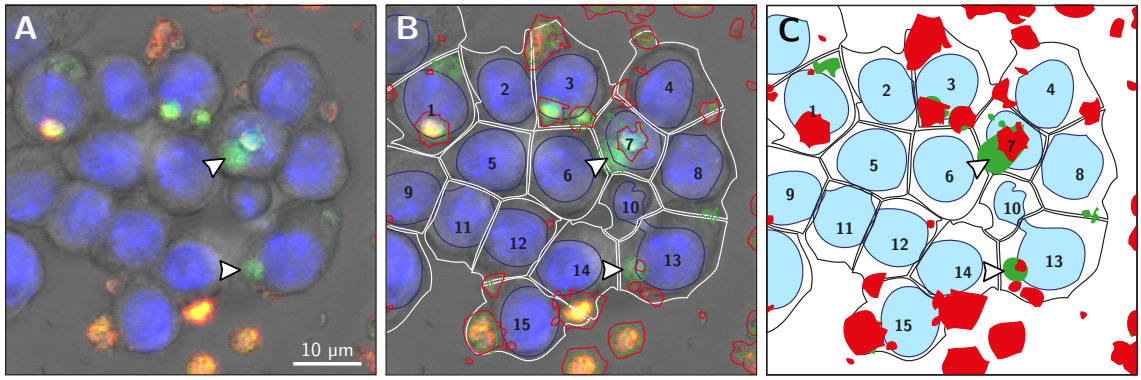

Figure 5.1: Assay for live-monitoring of intracellular release mediated by polymer capsules based on digital image cytometry. *RAW 264.7 macrophages are targeted with biodegradable polyelectrolyte microcapsules loaded with BODIPY-labeled DQ-OVA.* ***A:*** *Example image showing cells in transmission mode. Nuclei are shown in blue (Hoechst 33342) and capsules in red. Intracellularly degraded DQ-OVA is shown in green. Release in cell #7 and cell #13 is marked with arrows.* ***B:*** *Cells can be identified based on their nuclei and the outlines are obtained from the edge-enhanced transmission image (Sobel gradient,[69] image not shown). Released DQ-OVA is detected by green fluorescence not co-localizing with red areas.* ***C:*** *Illustration of the final segmentation result. This Figure was created by the author by applying the proposed algorithm on unpublished image data from Mikhail Zyuzin.*

As demonstrated, digital image cytometry is a powerful tool which simplifies the assessment of processes on the cellular and subcellular level based on high-throughput fluorescence microscopy and image processing. It is closely related to flow cytometry but in comparison to this techniques the list of accessible cell features is increased dramatically.[41,43] The cell segmentation in flow cytometry is "solved" by subsequent passing of individual cells through the exciting laser beam. Accordingly, cell recognition in digital image cytometry is more challenging and requires specific stainings in combination with sophisticated computer vision algorithms. Inappropriate segmentation parameters may lead to inaccurate results including artifacts and/or methodical errors.

In addition the endpoints of the assays have to be selected carefully. The classical mistake which can be made (also in classical flow cytometry) is caused by cytotoxicity-induced cell loss. The profile of the remaining cells does not represent the original population, as the residual cells might behave abnormally in some way making them resistant to the toxic impulse.

The major advantage of digital image cytometry in comparison to flow cytometric approaches is the ability to "look into the cell" in high spatial resolution, to examine cells in their natural state[11], and to measure kinetics. After the measurement, an individual cell is not lost and can be examined again at a later point in time. This can be used either (i) to determine the evolution of global features, *i.e.* similar to measuring several samples representing different points in time with the flow cytometer, or (ii) for tracking of individual cells and evaluation of certain features on the single cell level over time. An example for the first option is shown in Figure 5.2 where the mitochondrial membrane potential (reported by a fluorescence dye) upon treatment with a chemotherapeutic agent is assessed in human promyelocytic leukemia cells (HL-60) time-dependently. From the data the evolution of different cell populations (cells with hyperpolarized and depolarized mitochondrial membranes) can be observed in a high temporal resolution. Every outlier can be traced back to the underlying image, and finally to the underlying cell object.

Still, for all these kinds of measurements the segmentation of cells in every single image frame is required. This implies that on the one hand, the staining techniques have to be optimized carefully to avoid any interference with the cell viability and the actual measurements. On the other hand, large quantities of multidimensional image data whose processing is time consuming and requires computing power are produced for automatic segmentation and feature extraction. Finally, data evaluation and an appropriate representation of the obtained results are a challenge, as the datasets are highly multidimensional.

[11] no detachment and transfer into certain buffers prior to cytometric measurements is required.

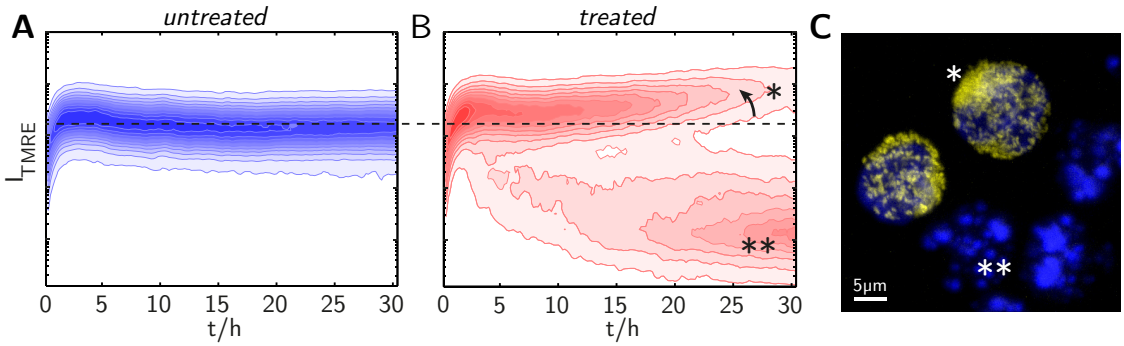

Figure 5.2: Digital image cytometry for time-resolved densiometric measurements. *The mitochondrial membrane potential $\Delta\psi_m$ of human promyelocytic leukemia cells (HL-60) upon treatment with a chemotherapeutic agent cytarabin (AraC) is indicated by the fluorescence of the dye tetramethylrhodamine ethyl (I_{TMRE}). TMRE and AraC were added at $t = 0$ min.* ***A:*** *In untreated control cells the mitochondrial membrane potential is not affected.* ***B:*** *In treated cells hyperpolarization of mitochondrial membranes can be observed before apoptosis occur. The part of the intensity distribution representing cells with hyperpolarized mitochondrial membranes is marked with (*); the part representing apoptotic cells is labeled with (**). The dashed line is drawn to allow comparison of the I_{TMRE} values between treated and untreated cells.* ***C:*** *Fluorescence micrograph showing cells in suspension with high membrane potential (yellow, *) and apoptotic cells with depolarized mitochondrial membranes (**). Nuclei were stained in blue (Hoechst 33342). This Figure was created by the author for the purpose of illustration.*

For segmentation of the image data acquired from living cells, DNA stains (*e.g.* Hoechst 33342), commonly used for identification of primary cell nuclei (Image Segmentation, § 2.4), can cause problems, since they interfere with DNA replication and exhibit phototoxicity.[175] Similar problems can be attributed to membrane stains, as certain receptors might be blocked or undesired cellular responses might be triggered. Consequently, the stain concentrations should always be kept as low as possible even if the quality of the acquired images is reduced by low fluorescence signals. Drawbacks in image quality can usually be solved with appropriate image restoration algorithms or are of no consequence due to the high number of analyzed cells.

A very important point for the successful application of digital image cytometry is the conceptual design of the experiment. Almost all experimental and technical parameters are interrelated. For instance, the fluorescence characteristics of nanomaterials should not interfere with the dyes introduced for later cell segmentation. Image resolution is competing with temporal resolution which in turn is limited by the total cell count and the number of different conditions/samples (*e.g.* wells) to be captured. High cell numbers are desired for high statistical significance. For cell tracking, quite a high temporal resolution is needed for correct cell identification in consecutive time-lapse image frames. On the contrary, a high temporal resolution also limits the total cell count.

Recently, several optical "super-resolution" methods have been developed that are capable of resolving nanostructures down to several tens of nanometers.[176,177] The concept of digital image cytometry presented aims at generating data that represents thousands of individual cells. Yet, super-resolution microscopes are rather slow and hard to automatize. In addition, when covering a comparable growth area with a similar number of cells, the data output would be extreme and slow to process with conventional work stations. Realistically, imaging is limited to subcellular structures or macromolecules in this case. Then, the challenge of image segmentation lies more in recognizing different intracellular compartments than in the detection of whole cells. However, as demonstrated in this work, when assessing the cellular interaction with nanomaterials, it is often not even necessary to resolve individual particles as the cellular response is well-detectable.

High throughput microscopy in combination with digital image cytometry can help to answer the following questions with high statistical relevance:

i) How many nanoparticles are internalized?
ii) Where are they intracellularly transported to?
iii) How do they affect cells?

Within the field of nanobiotechnology particle-cell interactions, intracellular release, sensor particle readout, and particle-induced cellular responses are generally suitable problems for future investigation aided by the introduced methodology. The development of serious nanomedicine is an emerging and fast growing field. Hence, reliable and sensitive assays are needed to probe nanoparticle functioning and cytotoxicity at an early stage, where digital image cytometry does function as a valuable research tool.

6. Publications

The publications providing the basis for this thesis were sorted corresponding to the major topics of this thesis and their publication date. Off-topic scientific contributions are summarized under "Miscellaneous". Review articles and conference proceedings are listed at the end of this section.

For each topic, a short description is given and the author's contribution is highlighted. The full articles can be found in the Appendix.

6.1. Cellular Responses to Nanoparticles

Several types of nanomaterials have already been approved for *in vivo* applications, such as iron oxide NPs for contrast enhancement in MRI. Nonetheless, exposing cells to colloidal nanoparticles can result in concentration-dependent harmful effects. In the articles presented the effects of different nanomaterials on various eukaryotic cell types were elucidated by performing several quantitative approaches based on digital image cytometry.

In the first work *"Quantification of the Internalization Patterns of Superparamagnetic Iron Oxide Nanoparticles with Opposite Charge"*[27] the uptake patterns of oppositely charged iron oxide nanoparticles were analyzed by performing a quantitative correlation analysis of the intracellular locations of the nanomaterials and different cellular organelles (*i.e.*, endosomes, lysosomes) using images obtained by confocal fluorescence laser scanning microscopy. Strong differences in cellular uptake of anionic versus cationic particles were observed. In the book chapter *"Investigating Nanoparticle Internalization Patterns by Quantitative Correlation Analysis of Microscopy Imaging Data"*[67] the focus is placed on the applied methodology firstly introduced in [27].

The composition of the outermost hydrophilic shell of a nanoparticle influences the attachment of biological molecules in physiological environments forming the so called *nanoparticle protein corona* which in turn governs the initial interaction of nanoparticles with cellular membranes and further uptake and intracellular trafficking. In "*Effect of Surface Functionalization with Polyethylene Glycol (PEG) of Polymer-Coated Nanoparticles on Human Serum Albumin Adsorption and Cell Uptake*"[83] the implications of enshrouding polymer-coated iron platinum NPs with polyethylene glycol on the adsorption of proteins and cellular uptake was assessed.

Before any acute cytotoxicity becomes visible cellular gene expression levels and morphological changes in subcellular structures can be observed. Especially the last issue was addressed in *"Colloidal Nanoparticles Induce Changes in Cellular Morphology"*[36]. Computer vision was applied to probe shape alterations in

cellular organelles, such as lysosomes or mitochondria, and to monitor changes of more macroscopic parameters, such as cell shape and cytoskeletal texture based on fluorescence microscope images. Upon exposure to small-sized (5 nm) polymer coated Au NPs, the morphology of several cellular structures was already significantly changed at concentrations one order of magnitude lower than those at which cellular viability is decreased.

In collaboration with Philipp Nold and Prof. Dr. Cornelia Brendel from the Division of Hematology at the University Medical Center in Marburg/Giessen the potential of Au NPs for labeling of mesenchymal stem cells (MSCs) during bioreactor-aided expansion was investigated in *"Gold Nanoparticle-Labeling of Bioreactor-Expanded Human Mesenchymal Stem Cells"*. The experimental parameters were optimized to detect a low number of Au labeled MSCs inside tissue by mass spectroscopy, ultimately aiming to trace MSC migration *in vivo* after intravenous re-introduction. The amount of Au NPs required for sufficient labeling has already affected cellular migration and proliferation significantly, which might exclude nano-sized Au particles as a labeling reagent for this purpose.

In *"In Vivo Integrity of Polymer-Coated Inorganic Colloidal Nanoparticles"*[40] the integrity of polymer coated Au NPs with excellent colloidal stability was addressed. For the observation of bio-distribution and retention times polymer and core material were radioactively labeled. The data indicate that upon intravenous administration into rats a partial separation of polymer shell and inorganic NP core occurred. Considering additional *in vitro* experiments, the degradation might be caused by proteolytic enzymes.

1) C. Schweiger*, R. Hartmann*, *et al.*, "Quantification of the Internalization Patterns of Superparamagnetic Iron Oxide Nanoparticles with Opposite Charge", *J. Nanobiotechnology* **2012**, *10*, 28.[27]

2) R. Hartmann, *et al.*, "Investigating Nanoparticle Internalization Patterns by Quantitative Correlation Analysis of Microscopy Imaging Data", in *Inorg. Nanoparticles vs Org. Nanoparticles*, **2012**, p. 181.[67] (book chapter)

   Experimental: Cell culture and *in vitro* uptake experiments, immunofluorescence
   Data analysis: revealing uptake pathways using quantitative correlation analysis
   Manuscript: Preparation of the corresponding section of the supplementary materials and preparation of book chapter[67]

3) B. Pelaz, P. d. Pino, P. Maffre, R. Hartmann, *et al.*, "Effect of Surface Functionalization with Polyethylene Glycol (PEG) of Polymer-Coated Nanoparticles on Human Serum Albumin Adsorption and Cell Uptake".[83]

(submitted to ACS Nano)

Data analysis: Quantification of nanoparticle uptake rates by 3T3 cells
Manuscript: Preparation of corresponding parts of the supplementary materials

4) X. Ma*, R. Hartmann*, *et al.*, „Colloidal Nanoparticles Induce Changes in Cellular Morphology".[36] *(accepted for publication in Nano Today after revision)*

Experimental: Development of assays probing changes in morphology, cytotoxicity assays, helium ion microscopy
Data analysis: Digital image processing, segmentation, feature extraction, result compilation
Manuscript: Major contribution to the preparation of the manuscript and the supporting information

5) P. Nold*, R. Hartmann*, *et al.*, "Gold Nanoparticle-Labeling of Bioreactor-Expanded Human Mesenchymal Stem Cells". *(working title, in preparation)*

Experimental: Cell culture und *in vitro* uptake, proliferation and migrations assays
Data analysis: Assay readout
Manuscript: Major contribution to the preparation of the manuscript and the supporting information

6) W. Kreyling, [...], R. Hartmann, *et al.*, "*In Vivo* Integrity of Polymer-Coated Inorganic Colloidal Nanoparticles", *DOI: 10.1038/NNANO.2015.111.*[40]

Experimental: Cell culture und *in vitro* NP uptake and degradation experiments
Manuscript: Preparation of corresponding parts of the supplementary materials

* equally contributing authors

6.2. Investigating the Endocytic Pathways of Micron-Sized Carrier Particles

Polyelectrolyte multilayer capsules (PEMs) are seen as carrier vehicles with high potential for biomedical applications. Understanding the internalization pathway of these systems is mandatory for their future design of biocompatible and effective therapeutic delivery systems (*e.g.* for cancer).

In the first article *"Multiple Internalization Pathways of Polyelectrolyte Multilayer Capsules into Mammalian Cells"*[136] the endocytic uptake mechanisms of PEM capsules were investigated thoroughly by image cytometry. By switching off certain endocytic pathways with specific chemical inhibitors and by correlation of the intracellular localization of PEMs upon internalization with endocytic markers, an uptake mechanism could be identified "strongly dependent on cholesterol-rich domains and organelle acidification" but "independent of clathrin and caveolae".[136] The impact of mechanical parameters of the used particles on the uptake efficiency still remained uninvestigated. In addition, the question arose whether a correlation between the current progression in the uptake process and the local pH around a capsule was possible.

Both issues were further investigated in the second publication *"Stiffness-Dependent In Vitro Uptake and Lysosomal Acidification of Colloidal Particles"*[29]. Here, pH-sensitive fluorescent dye molecules where embedded into PEMs and a quantitative method was developed which allowed these systems to be tracked with sufficient temporal resolution during cellular uptake, thus allowing a sophisticated quantitative analysis of their endocytic processing. The particle systems used were characterized particularly with respect to their mechanical properties, as the applied assembly method allowed for reproducible tuning of particle stiffness without changing other parameters, such as size, surface charge, or surface chemistry. Hence, a correlation between uptake/acidification patterns and particle elasticity was possible. Based on the statistical analysis of hundreds of single particle trajectories, the authors found a significant impact of particle stiffness on particle internalization and acidification.

Finally, this approach was used to unravel the role of the V_1G_1-subunit of the V-ATPase, a multi subunits large H^+-pump, for its interplay in lysosomal acidification in *"Capsule-Based Fluorescent Sensors for Measuring Acidification of Endocytic Compartments in Living Cells with Altered Expression of V-ATPase Subunit V_1G_1"*[159]. By comparing the acidification patterns of single pH-sensitive PEMs during endocytosis in either overexpressing V_1G_1- or V_1G_1-depleted cells the importance of the V_1G_1-subunit on organelle acidification was demonstrated.

7) L. Kastl, D. Sasse, V. Wulf, R. Hartmann, *et al.*, "Multiple Internalization Pathways of Polyelectrolyte Multilayer Capsules into Mammalian Cells", *ACS Nano* **2013**, 7, 6605–6618.[136]

   Experimental: Monitoring of pH during capsule uptake
   Data analysis: Aggregation of results
   Supervision of Christiane Ranke's (co-author) bachelor thesis

8) R. Hartmann, *et al.*, "Stiffness-Dependent In Vitro Uptake and Lysosomal Acidification of Colloidal Particles", *Angew. Chemie Int. Ed.* **2015**, *54*, 1365–1368.[29]

   Conceptual design
   Experimental: Synthesis and characterization of pH-sensitive polyelectrolyte microcapsules (except elasticity measurements); cell culture (isolation of primary cells, maintenance of cell lines) & *in vitro* uptake experiments
   Data analysis: Development of a Matlab-based toolbox ("ParticleAnalyzer") for digital image cytometry, particle tracking and automated trajectory analysis
   Manuscript: Preparation of manuscript and supporting information

9) M. M. Ferraro*, M. d. Luca*, R. Hartmann*, *et al.*, "Capsule-Based Fluorescent Sensors for Measuring Acidification of Endocytic Compartments in Living Cells with Altered Expression of V-ATPase Subunit V_1G_1".[159] *(submitted to BMC Biol.)*

   Experimental: Cell culture and *in vitro* uptake experiments of pH-sensitive particles
   Data analysis: Particle tracking and quantitative analysis
   Manuscript: Preparation of corresponding parts of the supporting information, data visualization and illustrations

* equally contributing authors

6.3. Miscellaneous

Additional projects which are thematically not related to the scope of this thesis are mentioned in the following.

10) K. Baum, R. Hartmann, *et al.*, "Three-Dimensional Surface Reconstruction within Noncontact Diffuse Optical Tomography Using Structured Light", *J. Biomed. Opt.* **2012**, *17*, 126009.[178]

    Experimental: Software development for acquisition and analysis of diffuse optical tomography data
    Manuscript: Major contribution

    This work was not performed under the supervision of Prof. Dr W. J. Parak

11) M. Mahmoudi, [...], R. Hartmann, *et al.*, "Cell-Imprinted Substrates Direct the Fate of Stem Cells", *ACS Nano* **2013**, *7*, 8379–84.[179]

    Experimental: Cell culture and differentiation experiments, imaging

12) M. Mahmoudi, [...], R. Hartmann, *et al.*, "Temperature: the 'Ignored' Factor at the NanoBio Interface", *ACS Nano* **2013**, *7*, 6555–6562.[123]

    Data analysis: Development of a Matlab-based toolbox for cell segmentation and quantification of nanoparticle uptake ("High Content Screening" assay)
    Manuscript: Preparation of corresponding parts of the supplementary materials

13) X. Yu, D. Y. Lei, F. Amin, R. Hartmann, *et al.*, "Distance Control In-Between Plasmonic Nanoparticles *via* Biological and Polymeric Spacers", *Nano Today* **2013**, *8*, 480–493.[180]

    Data analysis: Image segmentation and processing for determination of radial distribution functions

14) S. Carregal-Romero, P. Guardia, X. Yu, R. Hartmann, *et al.*, „Magnetically Triggered Release of Molecular Cargo from Iron Oxide Nanoparticle Loaded Microcapsules", *Nanoscale* **2014**, 7, 570-576.[181]

    Data analysis: Image segmentation and processing for the quantification of remaining cargo material in polyelectrolyte multilayer capsules after photo-thermal release

15) P. K. Harimech*, R. Hartmann*, *et al.*, „Encapsulated Enzymes with Integrated Fluorescence-Control of Enzymatic Activity". *J. Mater. Chem. B* **2015**, *00*, 1–7.[158]

Experimental: Synthesis of enzyme containing polyelectrolyte multilayer capsules and imaging
Data analysis: Video segmentation and processing of time-lapse confocal fluorescent microscopy data to determine enzyme reaction kinetics inside micron-sized bioreactors
Manuscript: Major contribution to the preparation of the manuscript

16) A. Ott, X. Yu, R. Hartmann, *et al.*, "Light-Addressable and Degradable Silica capsules for Delivery of Molecular Cargo to the Cytosol of Cells", *Chem. Mater.* **2015**, 27, 1929-1942.[127]

Data analysis: Contribution of algorithms for data analysis
Manuscript: Preparation of corresponding parts of the supplementary materials

17) D. Kuhn*, R. Hartmann*, *et al.*, „Cellular Uptake and Cell-to-Cell Transfer of Polyelectrolyte Microcapsules within a Triple Bi-Culture System Representing Parts of the Respiratory Tract".[149] *(accepted for publication at S.T.A.M.)*

Experimental: Cell culture and imaging
Data analysis: Quantification of uptake rates of polyelectrolyte multilayer capsules by primary cells within a 3D cell model
Manuscript: Major contribution to the preparation of the manuscript and the supporting information

18) W.-C. Liao, C.-H. Lu, R. Hartmann, *et al.*, "ATP-Triggered Release of Macromolecular and Nanoparticle Loads from Aptamer/DNA-Crosslinked Microcapsules".[182] *(submitted to Adv. Func. Mat.)*

Experimental: Conceptual design, capsule template synthesis

* equally contributing authors

6.4. Review Articles

The current knowledge regarding the interaction of colloidal nanoparticles with cellular membranes was summarized in *"Interaction of stable colloidal nanoparticles with cellular membranes."*[183] (as of 2013). In *"Fluorescence-based ion-sensing with colloidal particles"*[184] problems accompanying fluorescence-based ion-sensing with colloidal particles were addressed.

19) M. Mahmoudi, [...], R. Hartmann, *et al.*, "Interaction of Stable Colloidal Nanoparticles with Cellular Membranes", *Biotechnol. Adv.* **2014**, *32*, 679–92.[183]

    Manuscript: Minor contribution

20) S. Ashraf, [...], R. Hartmann, *et al.*, „Fluorescence-Based Ion-Sensing with Colloidal Particles", *Curr. Opin. Pharmacol.* **2014**, *18C*, 98–103.[184]

    Manuscript: Minor contribution

6.5. Conference Proceedings

The contributions to the following scientific conferences were published inside conference proceedings:

21) K. Baum, R. Hartmann, T, *et al.*, in *Eur. Conf. Biomed. Opt.*, **2011**, p. 80881V–80881V.[185]

22) R. Hartmann, *et al.*, in *Eur. Biophys. J. WITH Biophys. Lett.*, **2011**, p. 227.[186]

23) R. Hartmann, *et al.*, in *Eur. Biophys. J. WITH Biophys. Lett.*, **2013**, pp. S112–S112.[187]

7. Abbreviations

3T3	-	murine fibroblast cell line
A549	-	human breast adenocarcinoma cell line
AB	-	antibody
AF	-	AlexaFluor
AFM	-	atomic force microscopy
AraC	-	cytarabin
ATP	-	adenosine triphosphate
BODIPY	-	boron-dipyrromethene
CCD	-	charge coupled device
CdTe	-	cadmium telluride
CHT	-	circular Hough transform
cLSM	-	confocal laser scanning microscopy
CTR	-	control
DAPI	-	4',6-diamidino-2-phenylindole
DextS	-	dextran sulfate sodium salt
DNA	-	deoxyribonucleic acid
DQ-OVA	-	dequenching ovalbumin
EdU	-	5-ethynyl-2'-deoxyuridine
FePt	-	iron-platinum
GFP	-	green fluorescent protein
HCA	-	high content analysis
HCS	-	high content screening
HeLa	-	human cervical cancer cell line
HL-60	-	human promyelocytic leukemia cell line
HUVEC	-	human umbilical vein endothelial cell line
LAMP1	-	lysosomal associated protein 1
LbL	-	layer-by-layer
MDA-MB-231	-	breast cancer cell line
MRI	-	magnetic resonance imaging
MSC	-	mesenchymal stem cell
MTT	-	3-(4,5-dimethylthiazol-2-yl)-2,5-diphenyltetrazolium bromide
NA	-	numerical aperture
NP	-	nanoparticle
PAH	-	poly(allylamine hydrochloride)
PE	-	polyelectrolytes
PEG	-	polyethylene glycol
PEMs	-	polyelectrolyte microcapsules
PLArg	-	poly-L-arginine hydrochloride
PMA	-	poly(isobutylene-*alt*-maleic anhydride)
PSF	-	point spread function
PSS	-	poly(sodium 4-styrenesulfonate)
QD	-	quantum dot
ROS	-	reactive oxygen species
SDS-PAGE	-	sodium dodecyl sulphate polyacrylamide gel electro-

		phoresis
TEM	-	transmission electron microscopy
TMRE	-	tetramethylrhodamine ethyl
V-ATPases	-	vacuolar H^+-ATPases
WGA	-	wheat germ agglutinin

8. Bibliography

[1] H. Goesmann, C. Feldmann, *Angew. Chemie Int. Ed.* **2010**, *49*, 1362–1395.

[2] P. K. Jain, X. Huang, I. H. El-Sayed, M. A. El-Sayed, *Acc. Chem. Res.* **2008**, *41*, 1578–1586.

[3] J. a. Barreto, W. O'Malley, M. Kubeil, B. Graham, H. Stephan, L. Spiccia, *Adv. Mater.* **2011**, *23*, H18–H40.

[4] D. Guo, G. Xie, J. Luo, *J. Phys. D. Appl. Phys.* **2014**, *47*, 013001.

[5] M. C. Daniel, D. Astruc, *Chem. Rev.* **2004**, *104*, 293–346.

[6] L. Brannon-Peppas, J. O. Blanchette, *Adv. Drug Deliv. Rev.* **2012**, *64*, 206–212.

[7] J. R. McCarthy, K. A. Kelly, E. Y. Sun, R. Weissleder, *Nanomedicine (Lond).* **2007**, *2*, 153–67.

[8] M. Liong, J. Lu, M. Kovochich, T. Xia, S. G. Ruehm, A. E. Nel, F. Tamanoi, J. I. Zink, *ACS Nano* **2008**, *2*, 889–896.

[9] Y. W. Jun, J. H. Lee, J. Cheon, *Angew. Chemie - Int. Ed.* **2008**, *47*, 5122–5135.

[10] M. F. Casula, P. Floris, C. Innocenti, A. Lascialfari, M. Marinone, M. Corti, R. a. Sperling, W. J. Parak, C. Sangregorio, *Chem. Mater.* **2010**, *22*, 1739–1748.

[11] S. Dutz, W. Andrä, R. Hergt, I. Hilger, R. Müller, J. Töpfer, M. Zeisberger, M. E. Bellemann, in *World Congr. Med. Phys. Biomed. Eng. 2006 SE - 76* (Ed.: R. Magjarevic), Springer Berlin Heidelberg, **2007**, pp. 271–274.

[12] R. A. Sperling, P. Rivera Gil, F. Zhang, M. Zanella, W. J. Parak, *Chem. Soc. Rev.* **2008**, *37*, 1896–1908.

[13] Y. Xia, *Nat. Mater.* **2008**, *7*, 758–760.

[14] R. C. Somers, M. G. Bawendi, D. G. Nocera, *Chem. Soc. Rev.* **2007**, *36*, 579–591.

[15] J. M. Klostranec, W. C. W. Chan, *Adv. Mater.* **2006**, *18*, 1953–1964.

[16] C. J. Murphy, A. M. Gole, J. W. Stone, P. N. Sisco, A. M. Alkilany, E. C. Goldsmith, S. C. Baxter, *Acc. Chem. Res.* **2008**, *41*, 1721–1730.

[17] K. Saha, S. S. Agasti, C. Kim, X. Li, V. M. Rotello, *Chem. Rev.* **2012**, *112*, 2739–2779.

[18] R. Lévy, U. Shaheen, Y. Cesbron, V. Sée, *Nano Rev.* **2010**, *1*, DOI 10.3402/nano.v1i0.4889.

[19] B. Thiesen, A. Jordan, *Int. J. Hyperthermia* **2008**, *24*, 467–474.

[20] P. K. Jain, I. H. ElSayed, M. A. El-Sayed, *Nano Today* **2007**, *2*, 18–29.

[21] A. Neely, C. Perry, B. Varisli, A. K. Singh, T. Arbneshi, D. Senapati, J. R. Kalluri, P. C. Ray, *ACS Nano* **2009**, *3*, 2834–2840.

[22] J. Fan, H. Li, J. Jiang, L. K. Y. So, Y. W. Lam, P. K. Chu, *Small* **2008**, *4*, 1058–1062.

[23] S. Zhang, J. Li, G. Lykotrafitis, G. Bao, S. Suresh, *Adv. Mater.* **2009**, *21*, 419–424.

[24] L. C. Stoehr, E. Gonzalez, A. Stampfl, E. Casals, A. Duschl, V. Puntes, G. J. Oostingh, *Part. Fibre Toxicol.* **2011**, *8*, 36.

[25] D. Hühn, K. Kantner, C. Geidel, S. Brandholt, I. De Cock, S. J. H. Soenen, P. Riveragil, J. M. Montenegro, K. Braeckmans, K. Müllen, et al., *ACS Nano* **2013**, *7*, 3253–3263.

[26] O. Harush-Frenkel, E. Rozentur, S. Benita, Y. Altschuler, *Biomacromolecules* **2008**, *9*, 435–443.

[27] C. Schweiger, R. Hartmann, F. Zhang, W. J. Parak, T. H. Kissel, P. Rivera_Gil, *J. Nanobiotechnology* **2012**, *10*, 28.

[28] S. Anguissola, D. Garry, A. Salvati, P. J. O'Brien, K. a. Dawson, *PLoS One* **2014**, *9*, e108025.

[29] R. Hartmann, M. Weidenbach, M. Neubauer, A. Fery, W. J. Parak, *Angew. Chemie Int. Ed.* **2015**, *54*, 1365–1368.

[30] X. Banquy, F. Suarez, A. Argaw, J.-M. Rabanel, P. Grutter, J.-F. Bouchard, P. Hildgen, S. Giasson, *Soft Matter* **2009**, *5*, 3984.

[31] W. Liu, X. Zhou, Z. Mao, D. Yu, B. Wang, C. Gao, *Soft Matter* **2012**, *8*, 9235.

[32] T. Cedervall, I. Lynch, S. Lindman, T. Berggård, E. Thulin, H. Nilsson, K. a Dawson, S. Linse, *Proc. Natl. Acad. Sci. U. S. A.* **2007**, *104*, 2050–2055.

[33] A. E. Nel, L. Mädler, D. Velegol, T. Xia, E. M. V Hoek, P. Somasundaran, F. Klaessig, V. Castranova, M. Thompson, *Nat. Mater.* **2009**, *8*, 543–557.

[34] M. P. Monopoli, C. Aberg, A. Salvati, K. a Dawson, *Nat. Nanotechnol.* **2012**, *7*, 779–786.

[35] X. Jiang, C. Röcker, M. Hafner, S. Brandholt, R. M. Dörlich, G. U. Nienhaus, *ACS Nano* **2010**, *4*, 6787–6797.

[36] X. Ma, R. Hartmann, D. Jimenez de Aberasturi, F. Yang, S. J. Soenen, B. Manshian, J. Franz, D. Valdeperez, B. Pelaz, N. Hampp, et al., *Nano Today* **n.d.**, in revision.

[37] J. A. Kim, C. Åberg, A. Salvati, K. A. Dawson, *Nat. Nanotechnol.* **2011**, *7*, 62–68.

[38] W. H. De Jong, W. I. Hagens, P. Krystek, M. C. Burger, A. J. A. M. Sips, R. E. Geertsma, *Biomaterials* **2008**, *29*, 1912–1919.

[39] M. Van Der Zande, R. J. Vandebriel, E. Van Doren, E. Kramer, Z. Herrera Rivera, C. S. Serrano-Rojero, E. R. Gremmer, J. Mast, R. J. B. Peters, P. C. H. Hollman, et al., *ACS Nano* **2012**, *6*, 7427–7442.

[40] W. Kreyling, A. M. Abdelmonem, Z. Ali, A. Wenk, F. Alves, M. Geiser, S. Hirn, R. Hartmann, K. Kantner, N. Haberl, et al., *Nat. Nanotechnol.* **2015**, DOI 10.1038/NNANO.2015.111.

[41] S. a. Haney, *High Content Screen. Sci. Tech. Appl.* **2007**, 1–391.

[42] F. Gasparri, *Expert Opin. Drug Discov.* **2009**, *4*, 643–657.

[43] D. L. Taylor, J. R. Haskins, K. A. Giuliano, *High Content Screening : A Powerful Approach to Systems Cell Biology and Drug Discovery*, **2007**.

[44] G. R. Richards, A. J. Smith, F. Parry, A. Platts, G. K. Y. Chan, M. Leveridge, J. E. Kerby, P. B. Simpson, *Assay Drug Dev. Technol.* **2006**, *4*, 143–152.

[45] M. Fennell, H. Chan, A. Wood, *J. Biomol. Screen. Off. J. Soc. Biomol. Screen.* **2006**, *11*, 296–302.
[46] J. R. Inglefield, C. J. Larson, S. J. Gibson, H. Lebrec, R. L. Miller, *J. Biomol. Screen. Off. J. Soc. Biomol. Screen.* **2006**, *11*, 575–585.
[47] H. Lövborg, J. Gullbo, R. Larsson, *Anticancer. Drugs* **2005**, *16*, 593–599.
[48] M. Bertelsen, A. Sanfridson, *Assay Drug Dev. Technol.* **2005**, *3*, 261–271.
[49] P. Lang, K. Yeow, A. Nichols, A. Scheer, *Nat. Rev. Drug Discov.* **2006**, *5*, 343–356.
[50] J. Moffat, D. A. Grueneberg, X. Yang, S. Y. Kim, A. M. Kloepfer, G. Hinkle, B. Piqani, T. M. Eisenhaure, B. Luo, J. K. Grenier, et al., *Cell* **2006**, *124*, 1283–1298.
[51] M. Bjorklund, M. Taipale, M. Varjosalo, J. Saharinen, J. Lahdenpera, J. Taipale, *Nature* **2006**, *439*, 1009–1013.
[52] E. Jan, S. J. Byrne, M. Cuddihy, A. M. Davies, Y. Volkov, Y. K. Gun'ko, N. A. Kotov, *ACS Nano* **2008**, *2*, 928–38.
[53] S. J. Soenen, B. Manshian, J. M. Montenegro, F. Amin, B. Meermann, T. Thiron, M. Cornelissen, F. Vanhaecke, S. Doak, W. J. Parak, et al., *ACS Nano* **2012**, *6*, 5767–5783.
[54] L. J. Solmesky, M. Shuman, M. Goldsmith, M. Weil, D. Peer, *Nanotechnology* **2011**, *22*, 494016.
[55] A. Verma, F. Stellacci, *Small* **2010**, *6*, 12–21.
[56] J. Lindblad, Development of Algorithms for Digital Image Cytometry, **2002**.
[57] A. E. Carpenter, T. R. Jones, M. R. Lamprecht, C. Clarke, I. H. Kang, O. Friman, D. a Guertin, J. H. Chang, R. a Lindquist, J. Moffat, et al., *Genome Biol.* **2006**, *7*, R100.
[58] D. a. Basiji, W. E. Ortyn, L. Liang, V. Venkatachalam, P. Morrissey, *Clin. Lab. Med.* **2007**, *27*, 653–670.
[59] K. E. Dreinhöfer, B. Baldetorp, M. Åkerman, M. Fernö, A. Rydholm, P. Gustafson, *Clin. Cytom.* **2002**, *50*, 19–24.
[60] M. V. Boland, M. K. Markey, R. F. Murphy, *Cytometry* **1998**, *33*, 366–375.
[61] T. K. Kim, J. H. Eberwine, *Anal. Bioanal. Chem.* **2010**, *397*, 3173–3178.
[62] J. G. Donaldson, *Curr. Protoc. Immunol.* **2002**, *Chapter 21*, Unit 21.3.
[63] T. Suzuki, T. Matsuzaki, H. Hagiwara, T. Aoki, K. Takata, *Acta Histochem. Cytochem.* **2007**, *40*, 131–137.
[64] I. Nanoparticles, O. Nanoparticles, *Nanoparticles for Therapy*, Elsevier, **2012**.
[65] C. Zeiss, *Zeiss* **1998**.
[66] R. W. Cole, T. Jinadasa, C. M. Brown, *Nat. Protoc.* **2011**, *6*, 1929–41.
[67] R. Hartmann, S. Carregal-Romero, W. J. Parak, P. Rivera_Gil, in *Inorg. Nanoparticles vs Org. Nanoparticles* (Eds.: J.M. de la Fuente, V. Grazu), Elsevier Ltd, **2012**, p. 181.
[68] J. B. Pawley, B. R. Masters, *J. Biomed. Opt.* **2008**, *13*, 029902.
[69] R. C. Gonzalez, R. E. Woods, **2007**, 976.
[70] J. Lindblad, E. Bengtsson, *Proc. 12th Scand. Conf. Image Anal.* **2001**, 264–271.

[71] L. Landmann, *Imaging* **2002**, *208*, 134 –147.
[72] S. Chen, H. Leung, *J. Electron. Imaging* **2004**, *13*, 220.
[73] L. Vincent, *IEEE Trans. Image Process.* **1993**, *2*, 176–201.
[74] F. Meyer, S. Beucher, *J. Vis. Commun. Image Represent.* **1990**, *1*, 21–46.
[75] T. Jones, A. Carpenter, P. Golland, *Comput. Vis. Biomed. Image ...* **2005**, pp 535–543.
[76] F. Aurenhammer, *ACM Comput. Surv.* **1991**, *23*, 345–405.
[77] D. H. Ballard, *Pattern Recognit.* **1981**, *13*, 111–122.
[78] K. Rodenacker, E. Bengtsson, *Anal. Cell. Pathol.* **2003**, *25*, 1–36.
[79] Z. E. Perlman, M. D. Slack, Y. Feng, T. J. Mitchison, L. F. Wu, S. J. Altschuler, *Science* **2004**, *306*, 1194–1198.
[80] T. J. Mitchison, *ChemBioChem* **2005**, *6*, 33–39.
[81] K. Jaqaman, D. Loerke, M. Mettlen, H. Kuwata, S. Grinstein, S. L. Schmid, G. Danuser, *Nat. Methods* **2008**, *5*, 695–702.
[82] R. M. Haralick, *Proc IEEE* **1979**, *67*, 786–804.
[83] B. Pelaz, P. del Pino, P. Maffre, R. Hartmann, M. Gallego, S. Rivera, J. M. de la Fuente, G. U. Nienhaus, W. J. Parak, *ACS Nano* **n.d.**, submitted.
[84] R. Hartmann, S. Carregal-Romero, W. J. Parak, P. Rivera-Gil, *Front. Nanosci.* **2012**, *4*, 181–196.
[85] E. M. M. Manders, F. J. Verbeek, J. a Aten, *J. Microsc.* **1993**, *169*, 375–382.
[86] J. Crocker, J. Crocker, D. Grier, *J. Colloid Interface Sci.* **1996**, *179*, 298–310.
[87] K. Jaqaman, G. Danuser, *Cold Spring Harb. Protoc.* **2009**, *4*, DOI 10.1101/pdb.top65.
[88] T. L. Doane, C. Burda, *Chem. Soc. Rev.* **2012**, *41*, 2885–2911.
[89] E. C. Dreaden, M. A. Mackey, X. Huang, B. Kang, M. A. El-Sayed, *Chem. Soc. Rev.* **2011**, *40*, 3391–3404.
[90] S. J. Soenen, W. J. Parak, J. Rejman, B. Manshian, *Chem. Rev.* **2015**, *115*, 2109–2135.
[91] N. Lewinski, V. Colvin, R. Drezek, *Small* **2008**, *4*, 26–49.
[92] A. Verma, F. Stellacci, *Small* **2010**, 12–21.
[93] M. Lundqvist, J. Stigler, G. Elia, I. Lynch, T. Cedervall, K. a Dawson, *Proc. Natl. Acad. Sci. U. S. A.* **2008**, *105*, 14265–14270.
[94] M. Mahmoudi, A. M. Abdelmonem, S. Behzadi, J. H. Clement, S. Dutz, M. R. Ejtehadi, R. Hartmann, K. Kantner, U. Linne, P. Maffre, et al., *ACS Nano* **2013**, *7*, 6555–6562.
[95] G. J. Doherty, H. T. McMahon, *Annu. Rev. Biochem.* **2009**, *78*, 857–902.
[96] A. I. Ivanov, *Methods Mol. Biol.* **2008**, *440*, 15–33.
[97] M. M. Perry, a B. Gilbert, *J. Cell Sci.* **1979**, *39*, 257–272.
[98] S. Mayor, R. E. Pagano, *Nat. Rev. Mol. Cell Biol.* **2007**, *8*, 603–612.
[99] T. R. Graham, M. M. Kozlov, *Curr. Opin. Cell Biol.* **2010**, *22*, 430–436.
[100] G. Sahay, D. Y. Alakhova, A. V Kabanov, *J. Control. Release* **2010**, *145*, 182–195.
[101] D. Lingwood, K. Simons, *Science* **2010**, *327*, 46–50.
[102] L. J. Pike, *J. Lipid Res.* **2009**, *50 Suppl*, S323–S328.

[103] T. G. Iversen, T. Skotland, K. Sandvig, *Nano Today* **2011**, *6*, 176–185.
[104] J. B. Chem, S. R. Carlssons, *J. Biol. Chem.* **1990**, *265*, 20488–20495.
[105] E. L. Eskelinen, Y. Tanaka, P. Saftig, *Trends Cell Biol.* **2003**, *13*, 137–145.
[106] V. Marshansky, M. Futai, *Curr. Opin. Cell Biol.* **2008**, *20*, 415–426.
[107] C. Brandenberger, C. Mühlfeld, Z. Ali, A. G. Lenz, O. Schmid, W. J. Parak, P. Gehr, B. Rothen-Rutishauser, *Small* **2010**, *6*, 1669–1678.
[108] J. R. Casey, S. Grinstein, J. Orlowski, *Nat. Rev. Mol. Cell Biol.* **2010**, *11*, 50–61.
[109] S. Mukherjee, R. Ghosh, F. Maxfield, *Physiol. Rev.* **1997**, *77*, 759–803.
[110] O. a Weisz, *Traffic* **2003**, *4*, 57–64.
[111] M. Brust, M. Walker, D. Bethell, D. J. Schiffrin, R. Whyman, *J. Chem. Soc., Chem. ...* **1994**, 801–802.
[112] C. A. J. Lin, R. a. Sperling, J. K. Li, T. Y. Yang, P. Y. Li, M. Zanella, W. H. Chang, W. J. Parak, *Small* **2008**, *4*, 334–341.
[113] F. Zhang, E. Lees, F. Amin, P. Rivera-Gil, F. Yang, P. Mulvaney, W. J. Parak, *Small* **2011**, *7*, 3113–3127.
[114] G. Charron, D. Hühn, A. Perrier, L. Cordier, C. J. Pickett, T. Nann, W. J. Parak, *Langmuir* **2012**, *28*, 15141–15149.
[115] S. J. Soenen, B. B. Manshian, A. M. Abdelmonem, J. M. Montenegro, S. Tan, L. Balcaen, F. Vanhaecke, A. R. Brisson, W. J. Parak, S. C. De Smedt, et al., *Part. Part. Syst. Charact.* **2014**, *31*, 794–800.
[116] R. Shukla, V. Bansal, M. Chaudhary, A. Basu, R. R. Bhonde, M. Sastry, *Langmuir* **2005**, *21*, 10644–10654.
[117] Y. Pan, S. Neuss, A. Leifert, M. Fischler, F. Wen, U. Simon, G. Schmid, W. Brandau, W. Jahnen-Dechent, *Small* **2007**, *3*, 1941–1949.
[118] X. Ma, Y. Wu, S. Jin, Y. Tian, X. Zhang, Y. Zhao, L. Yu, X. J. Liang, *ACS Nano* **2011**, *5*, 8629–8639.
[119] Y. Pan, A. Leifert, D. Ruau, S. Neuss, W. Brandau, U. Simon, W. Jahnen-dechent, *Small* **2009**, *5*, 2067–2076.
[120] A. Chompoosor, K. Saha, P. S. Ghosh, D. J. Macarthy, O. R. Miranda, Z.-J. Zhu, K. F. Arcaro, V. M. Rotello, *Small* **2010**, *6*, 2246–2249.
[121] N. Pernodet, X. Fang, Y. Sun, A. Bakhtina, A. Ramakrishnan, J. Sokolov, A. Ulman, M. Rafailovich, *Small* **2006**, *2*, 766–773.
[122] T. Mironava, M. Hadjiargyrou, M. Simon, V. Jurukovski, M. H. Rafailovich, *Nanotoxicology* **2010**, *4*, 120–137.
[123] M. Mahmoudi, A. M. Abdelmonem, S. Behzadi, J. H. Clement, S. Dutz, M. R. Ejtehadi, R. Hartmann, K. Kantner, U. Linne, P. Maffre, et al., *ACS Nano* **2013**, *7*, 6555–6562.
[124] J. O'Brien, I. Wilson, T. Orton, F. Pognan, *Eur. J. Biochem.* **2000**, *267*, 5421–5426.
[125] T. R. Mosmann, R. L. Coffman, *Immunol. Today* **1987**, *8*, 223–7.
[126] A. Salic, T. J. Mitchison, *Proc. Natl. Acad. Sci. U. S. A.* **2008**, *105*, 2415–2420.
[127] A. Ott, X. Yu, R. Hartmann, J. Rejman, A. Schütz, M. Ochs, W. J. Parak, S. Carregal-Romero, *Chem. Mater.* **2015**, *27*, 1929–1942.
[128] S. a Detmer, D. C. Chan, *Nat. Rev. Mol. Cell Biol.* **2007**, *8*, 870–879.

[129] H. Sesaki, R. E. Jensen, *J. Cell Biol.* **1999**, *147*, 699–706.
[130] L. Wang, Y. Liu, W. Li, X. Jiang, Y. Ji, X. Wu, L. Xu, Y. Qiu, K. Zhao, T. Wei, et al., *Nano Lett.* **2011**, *11*, 772–780.
[131] T. a Kost, J. P. Condreay, D. L. Jarvis, *Nat. Biotechnol.* **2005**, *23*, 567–575.
[132] C. a. Galloway, Y. Yoon, *J. Gen. Physiol.* **2012**, *139*, 455–463.
[133] J. A. Yang, S. E. Lohse, C. J. Murphy, *Small* **2014**, *10*, 1642–1651.
[134] Y.-L. Wu, N. Putcha, K. W. Ng, D. T. Leong, C. T. Lim, S. C. J. Loo, X. Chen, *Acc. Chem. Res.* **2013**, *46*, 782–791.
[135] J. Borges, J. F. Mano, *Chem. Rev.* **2014**, *114*, 8883–8942.
[136] L. Kastl, D. Sasse, V. Wulf, R. Hartmann, J. Mircheski, C. Ranke, S. Carregal-Romero, J. A. Martínez-López, R. Fernández-Chacón, W. J. Parak, et al., *ACS Nano* **2013**, *7*, 6605–6618.
[137] E. Donath, G. B. Sukhorukov, F. Caruso, S. a Davis, H. Möhwald, *Angew. Chemie Int. Ed.* **1998**, *37*, 2201–2205.
[138] H. Zhu, E. W. Stein, Z. Lu, Y. M. Lvov, M. J. McShane, *Chem. Mater.* **2005**, *17*, 2323–2328.
[139] C. S. Peyratout, L. Dähne, *Angew. Chemie Int. Ed.* **2004**, *43*, 3762–3783.
[140] O. Shchepelina, V. Kozlovskaya, E. Kharlampieva, W. Mao, A. Alexeev, V. V. Tsukruk, *Macromol. Rapid Commun.* **2010**, *31*, 2041–2046.
[141] A. Yashchenok, B. Parakhonskiy, S. Donatan, D. Kohler, A. Skirtach, H. Möhwald, *J. Mater. Chem. B* **2013**, *1*, 1223.
[142] O. Shimoni, Y. Yan, Y. Wang, F. Caruso, *ACS Nano* **2013**, *7*, 522–530.
[143] C. Gao, E. Donath, S. Moya, V. Dudnik, H. Möhwald, *Eur. Phys. J. E* **2001**, *5*, 21–27.
[144] F. Dubreuil, N. Elsner, a. Fery, *Eur. Phys. J. E* **2003**, *12*, 215–221.
[145] A. Fery, R. Weinkamer, *Polymer (Guildf).* **2007**, *48*, 7221–7235.
[146] S. De Koker, B. G. De Geest, S. K. Singh, R. De Rycke, T. Naessens, Y. Van Kooyk, J. Demeester, S. C. De Smedt, J. Grooten, *Angew. Chemie - Int. Ed.* **2009**, *48*, 8485–8489.
[147] U. Reibetanz, D. Haložan, M. Brumen, E. Donath, *Biomacromolecules* **2007**, *8*, 1927–1933.
[148] S. Kelm, R. Schauer, in *Int. Rev. Cytol.*, Academic Press Inc, San Diego, **1997**, pp. 137–240.
[149] D. A. Kuhn, R. Hartmann, K. Fytianos, A. Petri-Fink, B. Rothen-Rutishauser, W. J. Parak, *Sci. Technol. Adv. Mater.* **2015**, accepted.
[150] M. Desjardins, G. Griffiths, *Curr. Opin. Cell Biol.* **2003**, *15*, 498–503.
[151] W. Jiang, B. Y. S. Kim, J. T. Rutka, W. C. W. Chan, *Nat. Nanotechnol.* **2008**, *3*, 145–150.
[152] S. Zhang, J. Li, G. Lykotrafitis, G. Bao, S. Suresh, *Adv. Mater.* **2009**, *21*, 419–424.
[153] L. L. Del Mercato, A. Z. Abbasi, M. Ochs, W. J. Parak, *ACS Nano* **2011**, *5*, 9668–9674.
[154] O. Kreft, A. M. Javier, G. B. Sukhorukov, W. J. Parak, *J. Mater. Chem.* **2007**, *17*, 4471.
[155] P. Rivera-Gil, M. Nazarenus, S. Ashraf, W. J. Parak, *Small* **2012**, *8*, 943–948.

[156] P. Rivera-Gil, S. De Koker, B. G. De Geest, W. J. Parak, *Nano Lett.* **2009**, *9*, 4398–4402.
[157] S. Carregal-Romero, M. Ochs, P. Rivera-Gil, C. Ganas, A. M. Pavlov, G. B. Sukhorukov, W. J. Parak, *J. Control. Release* **2012**, *159*, 120–127.
[158] P. K. Harimech, R. Hartmann, J. Rejman, P. del Pino, P. Rivera-Gil, W. J. Parak, *J. Mater. Chem. B* **2015**, *00*, 1–7.
[159] M. M. Ferraro, M. De Luca, R. Hartmann, P. Rivera-Gil, A. Klingl, M. Nazarenus, A. Ramirez, W. J. Parak, C. Bucci, R. Rinaldi, et al., *BMC Biol.* **2015**, submitted.
[160] M. Forgac, *Nat. Rev. Mol. Cell Biol.* **2007**, *8*, 917–29.
[161] T. Nishi, M. Forgac, *Nat. Rev. Mol. Cell Biol.* **2002**, *3*, 94–103.
[162] M. Ohira, A. M. Smardon, C. M. H. Charsky, J. Liu, M. Tarsio, P. M. Kane, *J. Biol. Chem.* **2006**, *281*, 22752–22760.
[163] J. J. Tomashek, L. a. Graham, M. U. Hutchins, T. H. Stevens, D. J. Klionsky, *J. Biol. Chem.* **1997**, *272*, 26787–26793.
[164] M. De Luca, L. Cogli, C. Progida, V. Nisi, R. Pascolutti, S. Sigismund, P. P. Di Fiore, C. Bucci, *J. Cell Sci.* **2014**, *127*, 2697–2708.
[165] E. E. Connor, J. Mwamuka, A. Gole, C. J. Murphy, M. D. Wyatt, *Small* **2005**, *1*, 325–327.
[166] R. Bhattacharya, C. R. Patra, R. Verma, S. Kumar, P. R. Greipp, P. Mukherjee, *Adv. Mater.* **2007**, *19*, 711–716.
[167] P. Mukherjee, R. Bhattacharya, P. Wang, L. Wang, S. Basu, J. a Nagy, A. Atala, D. Mukhopadhyay, S. Soker, *Clin. Cancer Res.* **2005**, *11*, 3530–3534.
[168] A. P. R. Johnston, C. Cortez, A. S. Angelatos, F. Caruso, *Curr. Opin. Colloid Interface Sci.* **2006**, *11*, 203–209.
[169] B. G. De Geest, S. De Koker, G. B. Sukhorukov, O. Kreft, W. J. Parak, A. G. Skirtach, J. Demeester, S. C. De Smedt, W. E. Hennink, *Soft Matter* **2009**, *5*, 282–291.
[170] B. G. De Geest, G. B. Sukhorukov, H. Möhwald, *Expert Opin. Drug Deliv.* **2009**, *6*, 613–24.
[171] S. De Koker, B. G. De Geest, C. Cuvelier, L. Ferdinande, W. Deckers, W. E. Hennink, S. De Smedt, N. Mertens, *Adv. Funct. Mater.* **2007**, *17*, 3754–3763.
[172] A. M. Javier, O. Kreft, M. Semmling, S. Kempter, A. G. Skirtach, O. T. Bruns, P. Del Pino, M. F. Bedard, J. Rädler, J. Käs, et al., *Adv. Mater.* **2008**, *20*, 4281–4287.
[173] B. G. De Geest, N. N. Sanders, G. B. Sukhorukov, J. Demeester, S. C. De Smedt, *Chem. Soc. Rev.* **2007**, *36*, 636–649.
[174] M. K. Mansour, E. Latz, S. M. Levitz, *J. Immunol.* **2006**, *176*, 3053–3061.
[175] M. Purschke, N. Rubio, K. D. Held, R. W. Redmond, *Photochem. Photobiol. Sci.* **2010**, *9*, 1634–1639.
[176] S. a Jones, S.-H. Shim, J. He, X. Zhuang, *Nat. Methods* **2011**, *8*, 499–508.
[177] B. Huang, M. Bates, X. Zhuang, *Annu. Rev. Biochem.* **2009**, *78*, 993–1016.
[178] K. Baum, R. Hartmann, T. Bischoff, J. O. Oelerich, S. Finkensieper, J. T. Heverhagen, *J. Biomed. Opt.* **2012**, *17*, 126009.

[179] M. Mahmoudi, S. Bonakdar, M. a. Shokrgozar, H. Aghaverdi, R. Hartmann, A. Pick, G. Witte, W. J. Parak, *ACS Nano* **2013**, *7*, 8379–8384.

[180] X. Yu, D. Y. Lei, F. Amin, R. Hartmann, G. P. Acuna, A. Guerrero-Martínez, S. a. Maier, P. Tinnefeld, S. Carregal-Romero, W. J. Parak, *Nano Today* **2013**, *8*, 480–493.

[181] S. Carregal-Romero, P. Guardia, X. Yu, R. Hartmann, T. Pellegrino, W. J. Parak, *Nanoscale* **2015**, *7*, 570–576.

[182] W.-C. Liao, C.-H. Lu, R. Hartmann, F. Wang, S. Y. Sung, W. Parak, I. Willner, *Adv. Funct. Mater.* **n.d.**, submitted.

[183] M. Mahmoudi, J. Meng, X. Xue, X. J. Liang, M. Rahman, C. Pfeiffer, R. Hartmann, P. R. Gil, B. Pelaz, W. J. Parak, et al., *Biotechnol. Adv.* **2014**, *32*, 679–692.

[184] S. Ashraf, C. Carrillo-Carrion, Q. Zhang, M. G. Soliman, R. Hartmann, B. Pelaz, P. Del Pino, W. J. Parak, *Curr. Opin. Pharmacol.* **2014**, *18C*, 98–103.

[185] K. Baum, R. Hartmann, T. Bischoff, F. Himmelreich, J. T. Heverhagen, in *Eur. Conf. Biomed. Opt.*, **2011**, p. 80881V–80881V–6.

[186] R. Hartmann, C. Schweiger, F. Zhang, W. J. Parak, T. Kissel, P. R. Pdf, in *Nanax 5*, **2012**, p. 227.

[187] R. Hartmann, P. R. Gil, W. J. Parak, in *Eur. Biophys. J. With Biophys. Lett.*, **2013**, pp. S112–S112.

9. Appendix

9.1. Publication List

A selection of full articles of the research work summarized in § 9 can be found on the following pages. Supplementary material is only attached in case the provided information is inevitable for understanding and cross referenced in the text, or the corresponding main article is not published, yet.

X. Yu, D. Y. Lei, F. Amin, R. Hartmann, *et al.*, "Distance Control In-Between Plasmonic Nanoparticles *via* Biological and Polymeric Spacers", *Nano Today* 2013, *8,* 480–493.[180]	-
S. Carregal-Romero, P. Guardia, X. Yu, R. Hartmann, *et al.*, „Magnetically Triggered Release of Molecular Cargo from Iron Oxide Nanoparticle Loaded Microcapsules", *Nanoscale* 2014, 7, 570-576.[181]	-
P. K. Harimech*, R. Hartmann*, *et al.*, „Encapsulated Enzymes with Integrated Fluorescence-Control of Enzymatic Activity". *J. Mater. Chem. B* 2015, *00,* 1–7.[158]	A-I.111-117
A. Ott, X. Yu, R. Hartmann, *et al.*, "Light-Addressable and Degradable Silica capsules for Delivery of Molecular Cargo to the Cytosol of Cells", *Chem. Mater.* 2015, 27, 1929-1942.[127]	-
D. Kuhn*, R. Hartmann*, *et al.*, „Cellular Uptake and Cell-to-Cell Transfer of Polyelectrolyte Microcapsules within a Triple Bi-Culture System Representing Parts of the Respiratory Tract".[149] *(accepted for publication at S.T.A.M.)*	A-I.119-127
└ Supplementary Material	A-I.119-127
W.-C. Liao, C.-H. Lu, R. Hartmann, *et al.*, "ATP-Triggered Release of Macromolecular and Nanoparticle Loads from Aptamer/DNA-Crosslinked Microcapsules".[182] *(submitted to Adv. Func. Mat.)*	-
M. Mahmoudi, [...], R. Hartmann, *et al.*, "Interaction of Stable Colloidal Nanoparticles with Cellular Membranes", *Biotechnol. Adv.* 2014, *32,* 679–92.[183]	-
S. Ashraf, [...], R. Hartmann, *et al.*, „Fluorescence-Based Ion-Sensing with Colloidal Particles", *Curr. Opin. Pharmacol.* 2014, *18C,* 98–103.[184]	-

* equally contributing authors

ARTICLE

Multiple Internalization Pathways of Polyelectrolyte Multilayer Capsules into Mammalian Cells

Lena Kastl,[†,#] Daniel Sasse,[†,#] Verena Wulf,[†] Raimo Hartmann,[†] Josif Mircheski,[‡] Christiane Ranke,[†] Susana Carregal-Romero,[†,§] José Antonio Martínez-López,[‡] Rafael Fernández-Chacón,[‡] Wolfgang J. Parak,[†] Hans-Peter Elsasser,[⊥] and Pilar Rivera Gil[†,∥,*]

[†]Fachbereich Physik, Philipps-Universität Marburg, Renthof 7, 35037 Marburg, Germany, [‡]Instituto de Biomedicina de Sevilla (IBiS) Hospital Universitario Virgen del Rocío/CSIC/Universidad de Sevilla, Departamento de Fisiologia Medica y Biofísica, and CIBERNED, Avenida Manuel Siurot s/n, 41013, Sevilla, Spain, [§]Andalusian Center for Nanomedicine and Biotechnology (BIONAND), Andalusian Technological Park, C/Severo Ochoa, 35, 29590 Campanillas, Málaga, Spain, and [⊥]Institute of Cytology and Cytopathology, Philipps-Universität Marburg, Robert-Koch Straße 6, 35033 Marburg, Germany. [#]L. Kastl and D. Sasse contributed equally. [∥]Present address: Pilar Rivera Gil, ICMAB-CSIC, UAB Campus, 08193 Bellaterra (Barcelona), Spain. E-mail: privera@icmab.es.

ABSTRACT Polyelectrolyte multilayer (PEM) capsules are carrier vehicles with great potential for biomedical applications. With the future aim of designing biocompatible, effective therapeutic delivery systems (*e.g.*, for cancer), the pathway of internalization (uptake and fate) of PEM capsules was investigated. In particular the following experiments were performed: (i) the study of capsule co-localization with established endocytic markers, (ii) switching-off endocytotic pathways with pharmaceutical/chemical inhibitors, and (iii) characterization and quantification of capsule uptake with confocal and electron microscopy. As result, capsules co-localized with lipid rafts and with phagolysosomes, but not with other endocytic vesicles. Chemical interference of endocytosis with chemical blockers indicated that PEM capsules enter the investigated cell lines through a mechanism slightly sensitive to electrostatic interactions, independent of clathrin and caveolae, and strongly dependent on cholesterol-rich domains and organelle acidification. Microscopic characterization of cells during capsule uptake showed the formation of phagocytic cups (vesicles) to engulf the capsules, an increased number of mitochondria, and a final localization in the perinuclear cytoplasma. Combining all these indicators we conclude that PEM capsule internalization in general occurs as a combination of different sequential mechanisms. Initially, an adsorptive mechanism due to strong electrostatic interactions governs the stabilization of the capsules at the cell surface. Membrane ruffling and filopodia extensions are responsible for capsule engulfing through the formation of a phagocytic cup. Co-localization with lipid raft domains activates the cell to initiate a lipid-raft-mediated macropinocytosis. Internalization vesicles are very acidic and co-localize only with phagolysosome markers, excluding caveolin-mediated pathways and indicating that upon phagocytosis the capsules are sorted to heterophagolysosomes.

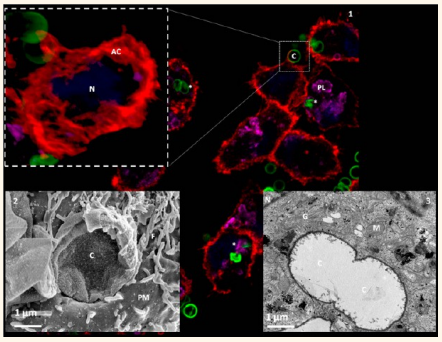

KEYWORDS: polyelectrolyte multilayer capsules · mechanisms of internalization · cancer cells · pharmacological inhibitors · phagocytosis · macropinocytosis · clathrin mediated uptake · lipid rafts · caveolin mediated uptake · intracellular localization · lysosomes · endosomes · actin cytoskeleton · colloids · layer by layer assembly

Polyelectrolyte multilayer (PEM) capsules constitute a promising delivery system[1] for biomedical applications. The capsules are formed by sequential addition of oppositely charged polyelectrolytes onto a spherical template in a process called layer-by-layer assembly.[2−4] The whole system is stabilized predominantly by electrostatic interaction of the components. However, other types of stabilization processes have been used to create more sophisticated capsule systems.[5,6] After addition of a defined number of layers to the template, the template is chemically dissolved to obtain hollow capsules. The great advantage of these carrier systems is that PEM capsules can be modified with different functionalities.[7,8] For example, cargo molecules (*e.g.*, analyte-sensitive fluorophores, drugs, oligonucleotides, proteins) have been encapsulated within the cavity of PEM capsules.[9,10] Analyte-sensitive fluorophores in the cavity provide information about the environment in which the capsules are

* Address correspondence to pilar.riveragil@physik.uni marburg.de.

Received for review December 30, 2012 and accepted July 4, 2013.

Published online July 04, 2013
10.1021/nn306032k

dispersed.[11,12] Biodegradable capsules promote the release of cargo from the cavity over time independently from an external trigger.[13−15] Other functional groups (*e.g.*, polyethylene glycol (PEG), colloidal nanoparticles, and proteins) can be integrated in the polyelectrolyte layer or attached to the surface of the PEM capsules. Surface modification of these capsules with PEG molecules increases the colloidal stability of the system due to the low fouling properties of these molecules, but their uptake by cells is reduced.[16,17] By embedding magnetic nanoparticles[18,19] or by linking molecules with molecular recognition properties (*e.g.*, DNA, antibodies, proteins),[20] PEM capsules can be either locally accumulated or targeted to specific cell populations,[21,22] respectively. Modifying the capsule wall with plasmonic nanoparticles[23−25] allows for controlled opening of single capsules and release of cargo inside the cells with light as an external trigger.[26,27] The materials selected to synthesize as well as to functionalize the capsules (*i.e.*, the polyelectrolytes for the shell and the type of core template) determine the physicochemical properties of the PEM capsules (*e.g.*, biodegradability, size, charge density, colloidal stability, molecular recognition, stimuli sensitivity, responsiveness).[28−31]

Despite the great biomedical potential of these carrier systems and the multiple biological potential applications already described in the literature, pathways for the internalization of PEM capsules and a correlation of their physicochemical properties and their intracellular fate still require further investigation. Reports in the literature indicate that incorporation of the capsules occurs spontaneously. For a more specific uptake, an improvement of the molecular recognition properties of the capsules would be required. Internalization has been demonstrated to be non-cell specific for a variety of cell lines.[32] Several groups have suggested macropinocytosis or lipid rafts as main entry pathways into eukaryotic cells, based on the use of one or two pharmacological inhibitors.[14,33,34] However, it is well known that no chemical inhibitor is absolutely specific for exclusively one pathway,[35] and thus additional studies are required. In general, the internalization of capsules by cells appears to be a highly energy-consuming, actin-mediated process, which depends on microcapsules' intrinsic factors, such as their physicochemical properties, rather than on the cell type. Although the exact mechanism of cellular uptake is still not fully unraveled, some important parameters that regulate this process have been recently elucidated. For instance, the overall charge of capsules has been demonstrated to play a role in capsule uptake. In analogy to smaller colloidal nanoparticles, charged capsules are ingested faster than uncharged ones,[16] and positively charged capsules are found to be engulfed more than negatively charged ones.[36] Anyhow, adsorption of cell medium proteins to the capsule surface tends to reduce differences in surface chemistry in the case of long incubation times. Softness also plays a role, as hydrogel-based capsules tend to accumulate in late endosomes,[10,37] in comparison to more rigid capsules, which end up in the phagolysosome.

In order to understand the uptake of PEM capsules by cells, it is helpful to understand the available body of literature on particle incorporation by cells in general. The plasma membrane of eukaryotic cells is a crucial interface that delimits the intracellular from the extracellular space. Since the 1970s, the plasma membrane is described according to the fluid mosaic model, which gives fluidity, dynamics, and asymmetry to this interface.[38] It is formed by a lipid bilayer made out of amphipathic lipids (phospholipids, glycolipids, and cholesterol) as well as of several kinds of associated proteins (integral and peripheral proteins, as well as glycoproteins). Cholesterol hinders solidification at low (room) temperature and prevents the membranes from becoming too fluid at high temperatures. By forming plasma membrane vesicles, cells can incorporate solids and liquids ranging from the nanometer up to the micrometer scale by numerous endocytic processes.[39,40] Roughly, endocytosis can be divided into phagocytosis (engulfment of large objects) and pinocytosis (macropinocytosis, lipid rafts, clathrin-dependent, caveolin-dependent, and clathrin- and caveolin-independent pathways).[41,42] Despite the common thought that only phagocytes are able to perform phagocytosis, most eukaryotic cells preserve this function.[43] The entry of solutes and liquids into the cell *via* endocytic pathways involves multiple stages. First, objects are taken up in plasma membrane invaginations toward the cytosol. Inward invaginations include lipid rafts, clathrin- or caveolin-mediated pathways, as well as clathrin- and lipid-rafts-independent pathways, whereas an outward engulfment of objects is more characteristic for phagocytosis and macropinocytosis. These invaginations are then pinched-off to form plasma-membrane-containing vesicles. Second, these vesicles mature into different specialized structures, *i.e.*, phagosomes, endosomes, caveosomes, and macropynosomes, depending on the endocytic machinery being activated, thus enabling sorting of the cargo. Finally, the cargo is delivered into intracellular compartments (*e.g.*, lysosomes, phagolysosomes), recycled back to the plasma membrane, or transported across the cells (*i.e.*, transcytosis). The morphological or biochemical distinction between the different endocytic pathways (clathrin- and caveolin-(in)dependent mechanisms, macropinocytosis, and phagocytosis) is quite difficult. During vesicle maturation there is a sequential fusion and fission of different endocytic vesicles and molecular markers where vesicular contents are bidirectionally exchanged. Thus, constituents from the plasma membrane, endosomes, and lysosomes appear in all of these endocytic vesicles.[43] Nevertheless, each

internalization mechanism exhibits several characteristic patterns, which are not entirely selective. As pointed out before, phagocytosis and macropinocytosis imply the formation of membrane protrusions to incorporate cargo, whereas all other pathways involve inward invaginations. Furthermore, phagocytosis can be distinguished from macropinocytosis by the type of exvagination formed. In the case of the macropinocytosis, the plasma membrane forms a kind of "arm" to surround the loose cargo (mostly liquids and small solutes). However, in the case of phagocytosis there is a formation of a sort of "cup" that tightly wraps around the cargo (mostly big solids). In both cases, the kinds of vesicles formed are on the micrometer scale, which fits the size of the capsules as investigated in this study. Other types of endocytic pathways (*i.e.*, clathrin- and caveolin-dependent and -independent mechanisms as well as lipid rafts) involve rather small membrane-bound vesicles (usually below 300 nm), and the scission from the plasma membrane is mostly dependent on the presence of dynamin.[40] Clathrin-dependent internalization processes are characterized by the presence of several adaptor proteins and by a clathrin coating. These routes are mostly associated with receptor-mediated endocytosis.[41] Lipid rafts are stationary vesicles on the plasma membrane. Like caveolin vesicles, they are cellular domains rich in cholesterol and sphingolipids, which lead to regions of enhanced packing and reduced fluidity. The presence of caveolae in the vesicles distinguishes lipid rafts from caveolin-dependent uptake processes. Cholesterol appears to be a key player in the formation of lipid rafts. The pH also plays a role in distinguishing the different internalizing vesicles. Most of the sorting vesicles reduce their pH upon maturation, thus reaching the lowest value when meeting the lysosomes or phagolysosomes, with the exception of the caveosomes, which are characterized by a neutral/slightly alkaline pH.[44]

In this study, the internalization mechanism of PEM capsules by mammalian cells was elucidated. The contribution of this article is the systematic study of the role of different endocytic processes on the internalization of PEM capsules by cells.

RESULTS

Microscopic Characterization of Capsule Uptake. The internalization of PEM capsules of different sizes by living cells is a well-established process, independently shown by several groups.[32,45] Despite their relatively "large" size (normally a few μm) (Figure SI-1), PEM capsules are easily incorporated not only by specialized phagocytic cells (*e.g.*, macrophages, dendritic cells) but also by a great variety of different cells (*e.g.*, embryonic fibroblasts, neuro- and glioblastoma cells, epithelial cancer cells) including primary cells in culture (Figures 1, 2, and SI-3) (*e.g.*, monocyte-derived dendritic cells, bone marrow mouse cells, and astrocytes)[14,46] (Figure SI-3.2.A H). However, primary hippocampal neurons in culture took up capsules very inefficiently (Figure SI-3.1.D F). In our study PEM capsules composed of PSS/PAH (polystyrene sulfonate/poly(allylamine hydrochloride)) as a prototype of synthetic nondegradable capsules and of pARG/DEXS (poly-L-arginine/dextrane sulfate) as a prototype of biodegradable capsules were used. Experiments were mainly performed on the example of the breast cancer cell line MDA-MB-231, but for comparison of the results obtained, A549 lung cancer cells were also used (Figure SI-7). Electron microscopy images clearly show that the uptake of the capsules by the cells does not interfere with their viability. Infoldings of the inner membrane of the mitochondria were perfectly defined and did not collapse. The number and the size of some mitochondria were, however, increased. This would be consistent with the assumptions that (i) the uptake is an energy-consuming process and that (ii) lipid recovery to the plasma membrane is being performed. Furthermore, the nuclear membranes were also found to be intact and the chromatin to be perfectly distributed over the nucleus. All these signs indicate that cell viability was not impaired by uptake of the capsules. The idea that the internalization of PEM capsules is an active process was confirmed upon the sensitivity of uptake to a decrease in the incubation temperature (Figure 3.A).

A closer look at the interaction of PEM capsules with MDA-MB-231 breast cancer cells shows that the filopodia of the cells surround the capsules to stabilize them at the cell membrane (Figure 1.A). Extension of the plasma membrane (membrane ruffling and redistribution of the actin cytoskeleton) to engulf the capsules occurs (*cf.* Figure 1), rather than the formation of invaginations, which would have to be pinched off. This suggests the exclusion of pathways like clathrin- and caveolin/lipid rafts-(in)dependent mechanisms. The formation of a phagocytic cup can be clearly seen in Figure 1.B and 1.C, thus pointing out phagocytosis rather than macropinocytosis as the internalization pathway (for more images concerning the internalization of PEM capsules by different kinds of cells *via* CLSM, TEM, and SEM see Figure SI-3).

Intracellular Localization of PEM Capsules. The study of intracellular trafficking was performed by observing the co-localization of PEM capsules with endocytic markers (see Table 2). There are two common ways to perform co-localization. One method uses the labeling of constituents (*e.g.*, lysosomal-associated membrane protein 1 (LAMP1), caveolin, early endosome antigen 1 (EEA1), clathrin) of specific organelles involved in internalization pathways (*i.e.*, phagolysosomes, caveolae vesicles, early endosomes, clathrin pits, respectively) with fluorescent molecules. In the other method, the so-called "pulse-chase" analysis,[47,48] the cells are exposed to markers with known uptake pathways (*e.g.*, cholera toxin B1 (CTXB) as a marker for lipid rafts). In both cases the location of the fluorescent PEM capsules within these organelles can be confirmed by the

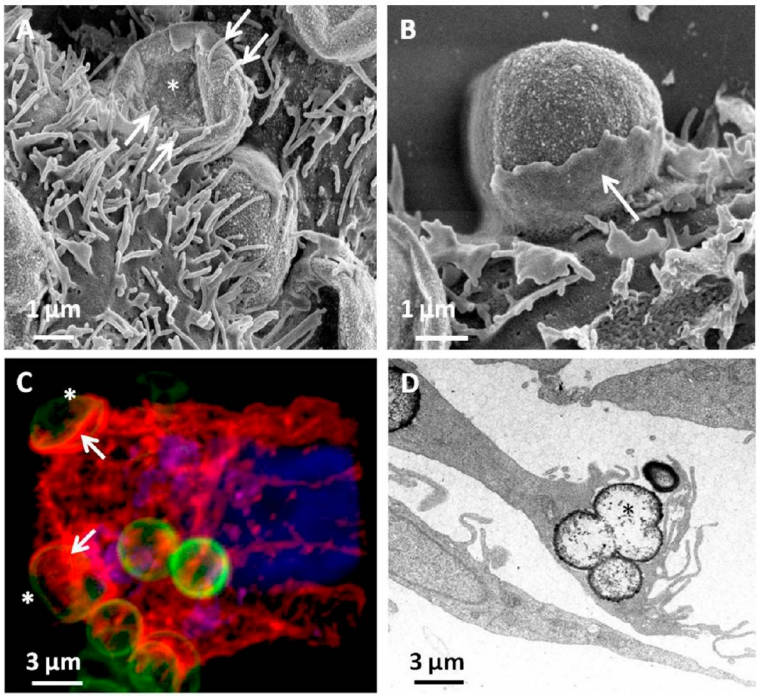

Figure 1. Microscopic characterization of capsule cell interactions. Cultured MDA MB 231 breast cancer cells were incubated with fluorescently labeled PSS/PAH capsules whose walls were modified with electron dense gold nanoparticles (highlighted with a star). (A, B) Scanning electrom microscopy (SEM) images of the cells' plasma membranes. (A) The formation of filopodia (highlighted with arrows) to stabilize the capsules as well as (B) the formation of a phagocytic cup (highlighted with arrows) to engulf the PEM capsules can be clearly seen in these pictures. (C) Confocal laser scanning microscope (CLSM) images showing the reorganization of actin cytoskeleton (red) to internalized PEM capsules (green, highlighted with a star) in the same kind of phagocytic cup. The cell nucleus is shown in blue. (D) Transmission electron microscope (TEM) image of a cell elongating its body to engulf several capsules.[13]

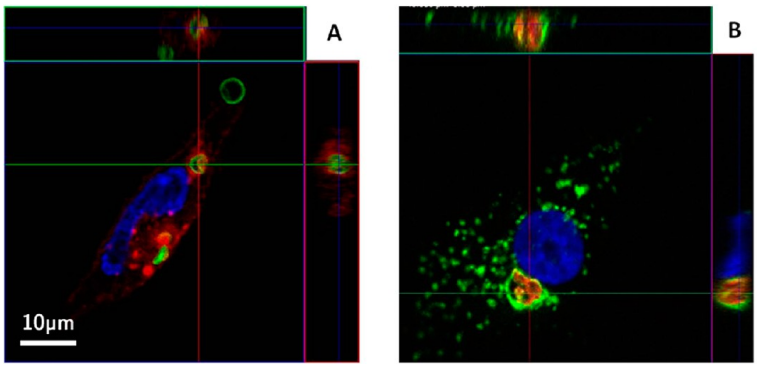

Figure 2. Co localization of fluorescently labeled PSS/PAH capsules (green in A or red in B) with a marker for lipid rafts (cholera toxin B1 (red) in A) and with LAMP1 (green), a protein highly expressed in phagolysosomes' membrane with CLSM (B). The MDA MB 231 cell's nucleus is shown in blue. An orthogonal view from different planes (*x*/*y*, *x*/*z*, or *y*/*z*) of the confocal microscope image shows the co localization of the capsules with the different cellular structures.

co-localization between the fluorescent marker and the capsule. We observed that after an initial engulfment of capsules in types of phagocytic cups (Figure 1), there is a co-localization of the capsules with lipid rafts (marked with CTXB) (Figure 2.A). Lipid rafts are functional membrane microdomains enriched in cholesterol, specific proteins, and glycosphingolipids.[49] The observed co-localization of PEM capsules with structures containing LAMP1, which is a marker for phagolysosomes at a very early and later stage of phagocytosis[48,50] (Figure 2.B), demonstrates that phagosomes are the final localization of the capsules. Few signs of co-localization with other endocytic vesicles such as endoplasmic reticulum (ER), caveolin, endosomes,[10] and clathrin were observed (Figure SI-4.1).

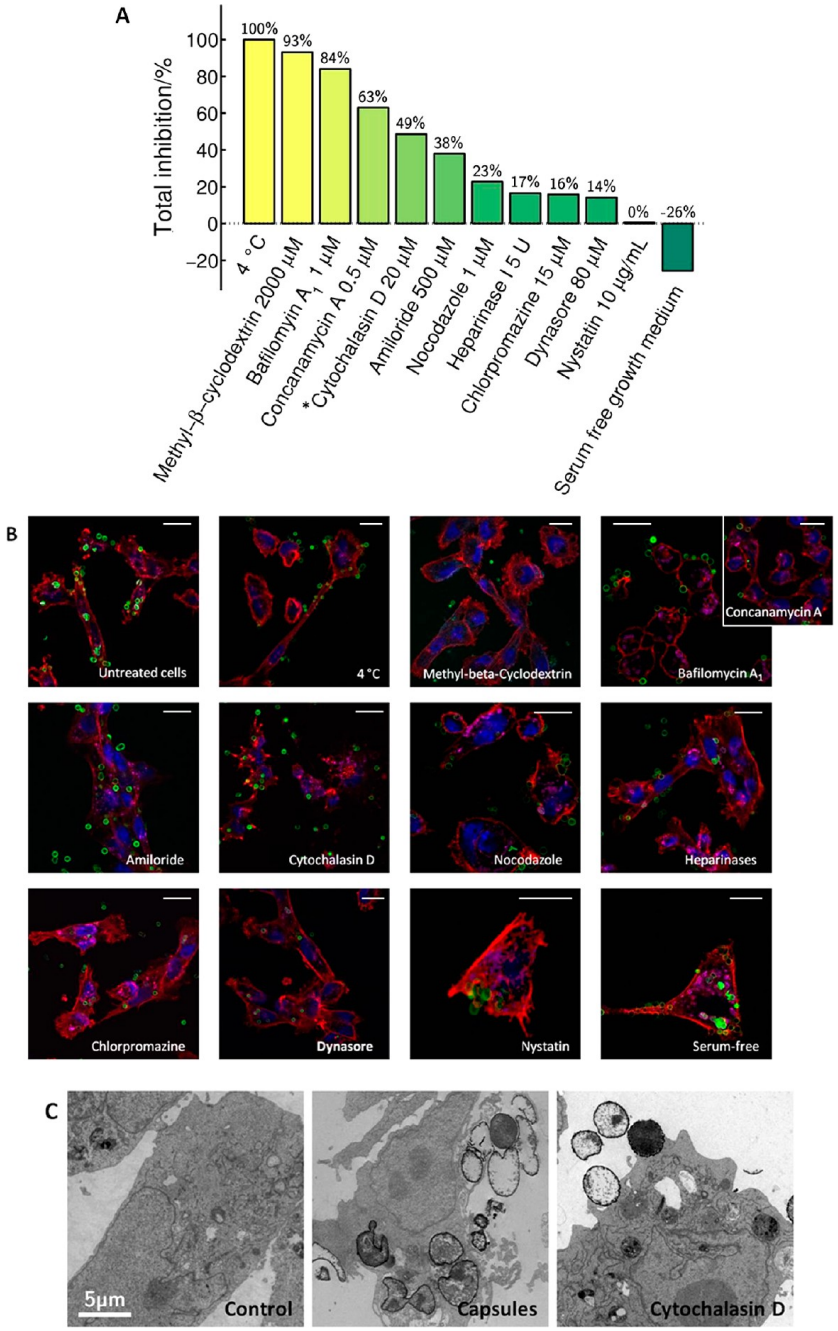

Figure 3. Pharmacological/chemical inhibition of all known internalization pathways. (A) Quantification of capsule uptake inhibition as described in the Methods section. *See comments in Table 1. (B) CLSM images of MDA MB 231 breast cancer cells in the presence or absence (control cells) of the different inhibitors. The cytoskeleton (red), phagolysosomes (pink), and the nucleus (blue) of the cells were stained to assess internalization of FITC modified PSS/PAH capsules (green). The length of the scale bar is 20 μm. (C) Positive effect of cytochalasin D on the inhibition of gold nanoparticle modified PSS/PAH capsule internalization assessed in more detail. TEM images of MDA MB 231 breast cancer cells in the absence of capsules and inhibitor (control), absence of inhibitor but incubated with capsules (capsules), and treated with cytochalasin D previous to capsule incubation (cytochalasin D).

The results obtained by the co-localization of capsules with different endocytic markers (Figure 2 and Figure SI-4.1 and SI-4.2) together with the results obtained by the microscopic analysis of internalization (Figure 1) suggest an exclusion of pathways such as clathrin- or caveolin-mediated endocytosis. On the contrary, they indicate that other processes, lipid rafts, macropinocytosis, or phagocytosis, are involved in the uptake of PEM capsules.

TABLE 1. Summary of the Results (in descending order) Obtained by Quantification of PSS/PAH Capsule Internalization by MDA MB 231 Breast Cancer Cells upon Interfering with All Known Pathways

pharmacological/chemical inhibitor or alteration of the cellular environment	concentration	associated pathway	quantification of inhibition	references
cell incubation at 4 °C		all	100%	
methyl beta cyclodextrin	2000 μM	lipid rafts and lipid raft mediated macropinocytosis	93%	35, 59
bafilomycin A_1	1 μM	phagocytosis	84%	64, 65, 67, 68
concanamycin A	0.5 μM	phagocytosis	63%	64, 65, 67, 68
cytochalasin D	20 μM	phagocytosis	49%[a]	43
amiloride	500 μM	macropinocytosis	38%	35, 52, 59
nocodazole	1 μM	endocytosis	23%	69 72, 43, 53
heparinases	5 U	adsortive mechanisms	17%	73
chlorpromazine	15 μM	clathrin mediated endocytosis	16%	35, 52
dynasore	80 μM	clathrin and lipid rafts/caveolae mediated endocytosis	14%	74
potassium depletion		clathrin mediated endocytosis	→0%	35
nystatin	10 μg/mL	lipid rafts/caveolae	1%	35
cell incubation in serum free medium		determined by the adsorbed proteins	26%	

[a] CLSM delivered erroneous results regarding the efficiency of inhibition, due to lack of optical resolution. TEM characterization showed a near complete loss on internalization upon disruption of the actin cytoskeleton with cytochalasin D (Figures 3.C, 4, and SI 8). However we were unable to do quantification due to the limitation of this technique to process a significant amount of images over time.

Pharmacological/Chemical Inhibition of Endocytic Pathways and Quantification of PEM Capsule Uptake. To date, the most efficient, reliable, and affordable tool for testing endocytosis is chemical inhibition of internalization.[35] Therefore, the endocytic pathways used by PEM capsules were characterized on the basis of their differential sensitivity to pharmacological/chemical inhibitors (Figure 3 and Figure SI-6). However, nonspecific effects of such inhibitors have been reported and thus need to be considered upon data analysis.[35] MDA-MB-231 breast cancer cells were treated with different inhibitors of known internalization pathways (see Table 1 and SI §2 for a precise description of all inhibitors used), and the number of internalized capsules per cell was calculated (Figure 3). Concentrations were chosen in a way that the inhibitors are active, but still not harmful to cells, as determined *via* viability assays (Figure SI-5). From the statistical analysis of capsule uptake (cumulative distribution functions, CDFs), which is available in the Supporting Information, we derived a mean blocking efficiency of each inhibitor. The results of inibition of capsule uptake for PSS/PAH-based capsules and MDA-MB-231 breast cancer cells are summarized in Table 1. Similar results were obtained for pARG/DEXS-based capsules and MDA-MB-231 breast cancer cells and PSS/PAH-based capsules and A549 human lung cancer cells (*cf.* the Supporting Information).

(i) Cell surface heparan sulfate proteoglycan-mediated internalization is ruled by electrostatic interaction between the negatively charged glycocalix and the charged particles.[51] Atomic force microscopy measurements of adhesive forces between capsules and cell membranes showed that the uptake of PEM capsules correlates with the adhesion of capsules to the outer cell membrane.[36] Indeed, treatment with heparinases that hydrolyze proteoglycans[52] showed a 17% decrease in the uptake of PEM capsules (Figures 3. A, 3.B, and SI-6.1). Thus, electrostatic interactions are indeed responsible for an effective cell capsule interaction by improving capsule attachment to the negatively charged cell surface.

(ii) Cytoskeleton assembly: The intracellular localization and motility of endocytic organelles is linked to microtubules and to actin filaments, which provide molecular motors to sort, transport, and mature the different endocytic/phagocytic vesicles. Mostly all uptake processes, except macropinocytosis and phagocytosis, appear to be enhanced by, but are not strictly dependent on, a functional cytoskeleton. Intact microtubules are required for vesicle maturation.[43,53] Actin and microtubule polymerization around the nascent vesicles (*i.e.*, macropinosomes and phagosomes) is responsible for the formation of large F-actin-coated vesicles. This constitutes a feature of all types of phagocytosis[54] and macropinocytosis. Use of F-actin and microtubule depolymerizing drugs such as cytochalasins and nocodazole, respectively, completely blocks these processes.[55] Nevertheless, F-actin has been lately described to be involved in the plasma membrane rearrangement during processes such as ruffling, migration, and phagocytosis.[43] Furthermore, actin polymerization around the emerging phagosome is a feature of all types of phagocytosis.[54]

Incubation of MDA-MB-231 breast cancer cells with cytochalasin D clearly disturbed the internalization of PEM capsules. Unexpectedly, a reduction of "only" 49% of capsule uptake could be stated by CLSM (Figures 3.A and 3.B, and SI-6.2). However, a closer look at the cell membrane with TEM confirmed a complete abolishment of capsule uptake when actin polymerization was blocked (Figures 3.C, 4, and SI-8). It seems that although attachment to the plasma membrane and an attempt at internalization were visible with the CLSM, the actin

cytoskeleton was not able to reorganize properly and invagination of the vesicles into the cytosolic side of the cells was not completed (Figures 3.C, 4, and SI-8). On the other hand, the cellular uptake of capsules was slightly sensitive (23% reduction of uptake) to microtubule polymerization, as demonstrated upon incubation with nocodazole (Figures 3.A, 3.B, and SI-6.2). The higher sensitivity to cytochalasin compared to nocodazole and the fact that to internalize these kind of capsules, the endocytic vesicles have to be around 2 4 μm in diameter (which is considered large) confirmed the assumption that the phagosome size governs the type of motor system used.[56] Whereas small endocytic vesicles (<1 μm) are transported along the microtubules, bigger endocytic vesicles (*e.g.*, phagosomes) travel along the actin cytoskeleton. These results highlight the utilization of the actin microfilaments to propel the capsule-containing endocytic vesicle and give additional evidence for phagocytosis as a final uptake modus.

(iii) Clathrin- and caveolin/lipid-raft-mediated endocytosis: Certain cellular internalization proteins involved in the clathrin- and caveolin-mediated endocytosis, such as clathrin or EEA1 and caveolin, respectively, did not colocalize with the PEM capsules (Figure SI-4.1). However, capsules did co-localize with lipid rafts and phagocytosis markers such as CTXB and LAMP1 (Figures 2 and SI-4). CTXB binding does not necessarily correlate with caveolae vesicles,[49] thus establishing a difference between caveolin-dependent pathways and lipid rafts. These results suggested an exclusion of clathrin- and caveolin-mediated endocytosis. However, they do not exclude lipid rafts, macropinocytosis, or phagocytosis as uptake pathways. Indeed, PEM capsules were not internalized through clathrin-mediated endocytosis, as chlorpromazine (Figures 3.A and SI-6.4) or potassium depletion (Figure 4), which are specific blockers of this pathway,[35] did not influence their uptake. The caveolin-mediated pathway can be excluded because the pH of the endocytic vesicles was not alkaline[44] (Figure 5). The pH of these vesicles during capsule uptake was measured by tracking pH-sensitive capsules in confocal images.[57] The results indicated that the capsules were in an acidic environment, thus being in accordance with the co-localization studies (Figure SI-4) showing no signs of localization of the capsules with caveolin. Furthermore, treatment of breast cancer cells with dynasore (Figures 3.A, 3.B, and SI-6.4), which inhibits the scission of dynamin-dependent vesicles from the plasma membrane[58] and the induction of clathrin- and lipid raft-dependent and -independent endocytosis had no effect on the uptake of PEM capsules. Taking these results together, it can be concluded that neither clathrin- nor caveolin-mediated endocytosis is participating in the internalization of PEM capsules. However, the results do not provide a profound statement about the involvement of lipid rafts and do not exclude macropinocytosis or phagocytosis.

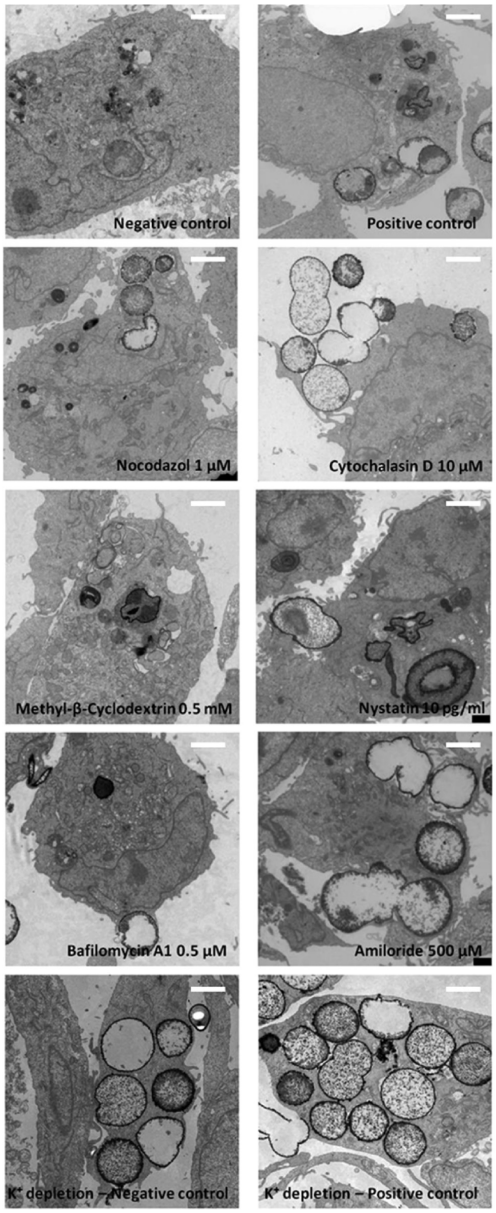

Figure 4. TEM characterization of the internalization of gold nanoparticle modified PSS/PAH capsules by MDA MB 231 breast cancer cells in the presence and absence (control) of the different pharmacological/chemical inhibitors of different cellular processes that have been associated with specific pathways. Negative and positive controls are cells treated without and with capsules, respectively. The length of the scale bar is 3 μm.

Lipid-raft-mediated endocytosis (which may be dependent or independent of caveolae) as well as macropinocytosis, which has been described as a sort of lipid raft-dependent and receptor-independent form of endocytosis,[59] are sensitive to drugs that alter the structure of cholesterol-rich plasma membrane domains.[60] These drugs include methyl-beta-cyclodextrin (MβCD) and nystatin, which respectively deplete and sequestrate

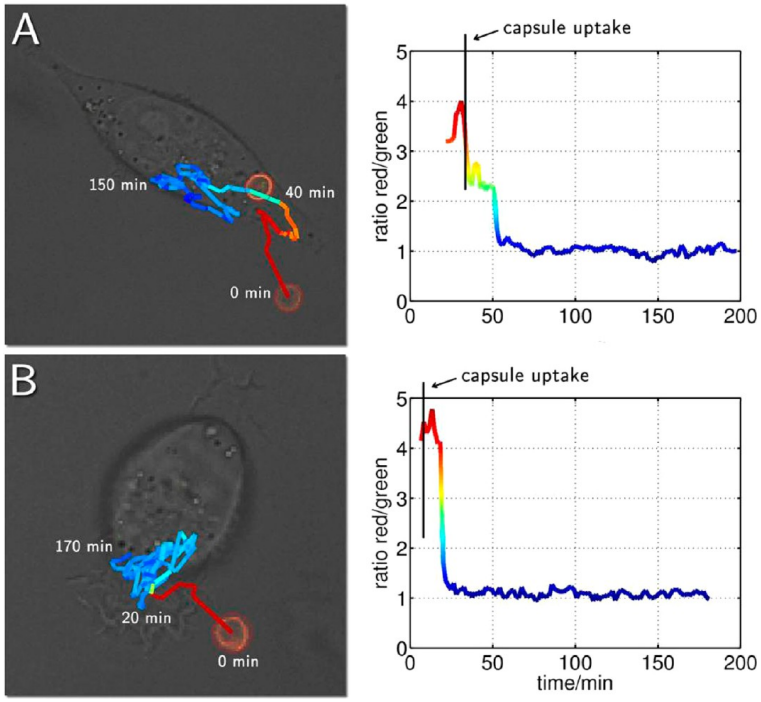

Figure 5. The acidification of endocytic vesicles of MDA MB 231 breast cancer cells was measured by tracking pH sensitive, SNARF filled PSS/PAH capsules in confocal images. The intensity ratio of the two emissions of each capsule can be used to estimate the local pH around the capsule (depicted in red ≈ pH 7 to blue ≈ pH 5 in the graphs).

cholesterol from the plasma membrane of the cells. Surprisingly, only cholesterol depletion by treatment with MβCD induces an almost complete (93%) loss of capsule internalization (Figures 3.A, 3.B, 4, and SI-6.3), whereas cholesterol sequestration evoked by nystatin had no effect on the internalization of the capsules (Figures 3.A, 3.B, 4, and SI-6.3). These results demonstrate a crucial role of cholesterol in the packing of the plasma membrane to engulf the capsules. However, they do not distinguish between lipid rafts and the related macropinocytosis. In summary we have observed that PEM capsules co-localize with lipid rafts (marked with CTXB), and the uptake is strongly sensitive to MβCD, which sequestrates cholesterol from the plasma membrane and has a significant effect on the cytoskeleton, especially on the dispersion of a cortical F-actin.[61] However, it is not sensitive to dynasore or potassium depletion. Furthermore, the size of the lipid rafts is normally significantly smaller than the size of the capsule. Gathering up the data concerning the role of lipid rafts and macropinocytosis in the uptake of capsules, it can be concluded that lipid-raft-mediated macropinocytosis, but not lipid rafts, plays an important role in the uptake of PEM capsules at the level of capsule invagination to the cytosolic side.

(iv) Phagocytosis *vs* macropinocytosis: These forms of cellular entry lack distinctive pharmacological tools to be distinguished. As already introduced, they can be differentiated from other forms of endocytosis due to the formation of large, outward vesicles (phagosomes and macropinosomes). The formed vacuoles are plasma membrane derivates and lack specific proteins/lipids or coatings. These vesicles undergo a series of fusion events with other intracellular vesicles, thus changing their composition upon maturation. Due to the lack of pharmacological targets, it is very difficult to selectively distinguish one from another. Alteration of the intracellular/intravacuolar acidification with selective drugs is the best choice to study macropinocytosis and phagocytosis because these drugs have the fewest collateral effects on other pathways.[35] Amiloride inhibits the sodium proton (Na^+/H^+) exchange and causes strong cytosolic acidification. As a result, amiloride is commonly used to inhibit (macro)pinocytosis.[52,62] However, its specificity is limited, as amiloride derivatives have been reported to also induce actin reorganization.[35] Bafilomycin A_1 is a strong inhibitor of the vacuolar type H^+-ATPase (V-ATPase), which is responsible for the acidity of lysososomes, the biogenesis of phagolysosomes and for the degradation of endocytosed material.[63] During phagosome biogenesis a proper lysosomal acidification is required, thus making phagocytosis sensitive to this antibiotic.[55,64,65]

As seen in Figures 3.A, 3.B, and SI-6.5, treatment of breast cancer cells with bafilomycin A_1 exhibited a significantly strong reduction (84%) of PEM capsule uptake, whereas incubation with amiloride moderately (38%) decreased their uptake. Treatment with concanamycin A, an analogue of bafilomycin A_1, showed the

same effect on diminishing the capsule uptake. These results were confirmed qualitatively with TEM (Figures 4 and SI-8).

The reduction of internalization mediated by amiloride together with the results obtained previously (lipid raft co-localization and MβCD sensitivity) confirms the role of lipid-raft-mediated macropinocytosis as stated before. However, the almost complete reduction of capsule uptake obtained by disrupting the acidification and biogenesis of the phagolysosome after bafilomycin A_1 treatment strongly involves phagocytosis at the internalization stage of capsule sorting. This is also supported by the co-localization of capsules with LAMP1, the strong sensitivity of uptake to cytochalasin D, and the formation of large phagocytic cups observed before.

(v) Disruption of plasma membrane fluidity: When MDA-MB-231 breast cancer cells were cooled from 37 °C to 4 °C, there was a complete inhibition (100%) of the internalization of the capsules (Figures 3.A, 3.B, and SI-6.6). At low temperatures the plasma membrane loses fluidity and increases rigidity; that is, the rapid lateral and slow axial movement of proteins and lipids is impaired. These movements are essential, for example, for receptor-mediated endocytosis. However, an increase in the plasma membrane rigidity also has a negative effect on the formation of protrusions that engulf the capsules. This kind of treatment served additionally as a control for achieving a complete uptake inhibition.

(vi) Inhibition of the opsonization of the capsules by pretreating the MDA-MB-231 breast cancer cells without nutrients (preincubation in serum-free medium) previous to and during the cell treatment with capsules significantly increased the internalization of the capsules compared to control cells (Figures 3.A, 3.B, and SI-6.7). These results give evidence that the mechanism of internalization of the capsules might not be determined by the serum proteins (mostly receptor-mediated[66]) that could adhere to the surface of bare capsules. These results help to relate the internalization patterns of the capsules with their physicochemical properties. Thus, providing the capsules with a surface chemistry that blocks protein coating might help to predict the behavior of these capsules. Additionally, by avoiding capsule serum protein interaction, the charge density of the capsules is maintained and the electrostatic interaction with the negatively charged glycocalix of the cells is preserved. Thus, the important role of an adsorptive mechanism of internalization to stabilize the capsules at the cell membrane previous to internalization is confirmed.

DISCUSSION

The results presented provide a more detailed analysis compared to other publications that aim only at a single pathway.[10,14,33,66] Previous reports focused on collateral studies concerning either the co-localization of PEM capsules with one or a few markers of endocytic vesicles, or inhibited only one pathway. In the frame of this work, several markers and inhibitors of mostly all uptake pathways were studied *via* optical and electron microscopy. The internalization of PEM capsules was quantified with several approaches.

Within the frame of this systematic study it can be concluded that different internalization modes are activated to incorporate PSS/PAH-based PEM capsules by MDA-MB-231 breast cancer cells. Our results show (i) an adsorptive mechanism responsible for the primary cell capsule contact due to electrostatic interactions between the capsules and the negatively charged glycocalix; (ii) the formation of filopodia and a strong actin reorganization to form large protrusions (in the form of a cup) to engulf the capsules similar to phagocytic processes; (iii) a co-localization with lipid rafts and phagolysosomes, but not with caveolin, clathrin, or ER; (iv) dynamin-independent internalization; (v) the absence of inhibition by nystatin, chlorpromazin, and potassium depletion; and (vi) the inhibition of uptake by cytochalasin D, MβCD, bafilomycin A_1 and its analogue, concanamycin A, and to a lesser extent amiloride and nocodazole.

On one hand, we have presented evidence, in accordance with other publications,[14] that discards clathrin-mediated endocytosis and assesses the involvement of lipid rafts in the uptake of PEM capsules. However, our results indicate that the involvement of lipid rafts contributes to a more complex pathway rather than becoming solely responsible for it. Due to the large size of the capsules and the small size of clathrin or caveolin/lipid raft vesicles,[40−42] it was expected that these processes were not involved in the direct uptake of capsules. We could easily exclude associated internalization routes. Nevertheless, since previous works showed that 300 nm to 1 μm, soft, hydrogel, silica capsules were internalized *via* clathrin-mediated endocytosis,[37] we wanted to test if this mechanism was involved in the uptake of bigger, more rigid capsules.

According to the results, there was a lack of co-localization of the capsules with characteristic markers for clathrin-mediated endocytosis (EEA1, clathrin), and the uptake was insensitive to all pharmacological/chemical inhibitors used for this pathway (chlorpromazin, dynasore, and potassium depletion).

Interestingly, regarding lipid rafts, our results excluded caveolin-mediated endocytosis but not caveolin-independent lipid rafts. First, there was not a co-localization of the capsules with the caveosomes (stained by caveolin). Second, caveosomes are transported within the cell along microtubules, and inhibition of microtubule formation with nocodazole had little effect on the internalization of the capsules. Finally, caveosomes have a different pH (neutral) and a different content compared to endosomes (acid) and do not end up fusing with lysosomes.[75] In contrast,

the vesicles involved in the internalization of the capsules are clearly acidic[11,57] and possess lysosomal markers (LAMP1).[48] As seen in Figure 5, the pH of the internalized vesicles is acidic from almost the beginning of the uptake process. Lipid rafts are commonly stabilized with caveolin. If caveolin-mediated pathways were involved, the internalizing vesicles should show, at least initially, a more neutral pH proper for the caveosomes. The steady decline in the luminal pH of the vesicles transporting the capsules is associated with phagosome maturation, and therefore this result represents a sign of phagocytosis.[50] Additionally, it is well known that the surface area of phagosomes can be increased by replenishing the plasma membrane with endosomal, ER, and post-Golgi membranes.[76−78] In Figure 2.B, a large phagolysosome (stained by LAMP1) containing approximately four capsules is clearly visible, thus confirming the ability of these cells to increase the surface area of phagolysosomes to engulf large objects. Proteomics and biochemical analysis have demonstrated that several proteins from the ER (*e.g.*, calnexin) are present in the membrane of phagolysosomes or phagosomes during their biogenesis.[65,79,80] Furthermore, Desjardins *et al*. proposed an ER-mediated phagocytosis where ER is recruited to the plasma membrane to supply membrane for the formation of the phagocytic cup.[65] This would explain the drastic increase in the size of phagolysosomes upon capsule uptake observed in Figure 2.B, where a vesicle containing several capsules can be clearly seen. Although our results showed few signs of co-localization of the ER (labeled by calnexin) with the capsules after 4 h (Figure SI-4.1.F), we observed a co-localization with the plasma membrane (stained with wheat germ agglutinin) (Figure SI-4.1.F). This gives an indication of a possible recruitment of the ER to the plasma membrane. The lack of co-localization with the ER can be explained either because the ER is not involved in this kind of internalization pathway (ER-independent phagocytosis)[48] or because of the (late) time frame selected for microscopic visualization (*i.e.*, 4 h). Calnexin is a protein present in early forming phagosomes at early stages of phagocytosis, such as the phagocytic cup, and suffers fast (after 1 h) degradation upon phagosome maturation.[65] During the biogenesis of phagocytic structures, the decrease in calnexin correlates with LAMP1 accumulation,[65] which indeed confirmed our results.

Concerning the caveolin-independent lipid rafts, macropinocytosis-mediated lipid rafts play an important role at an early stage of the capsule internalization process after the formation of the phagocytic cup, *i.e.*, at the level of invagination of endocytic vesicles containing the capsules to the cytosolic side of the cell. This is supported by the co-localization of the capsules with lipid rafts (CTXB) and the sensitivity of uptake to amiloride (a Na^+/H^+ pump blocker related to macropinocytosis[59]) but not to dynasore (an inhibitor influencing the lipid rafts), but also by the size of lipid rafts compared to the capsules and to the initial formation of a phagocytic cup, which strongly depends on the actin cytoskeleton. Furthermore, the uptake of the capsules after 4 h was completely inhibited by MβCD, which removes cholesterol from cultured cells, thus inhibiting membrane packing at a first stage but also uptake-associated processes such as macropinocytosis and lipid rafts.

Cellular incubation with bafilomycin A_1 and its analogue concanamycin A disturbed the capsule uptake in a concentration-dependent manner. Both are specific inhibitors of the vacuolar-type H^+-ATPase, which prevents reacidification of the lysosome,[11] which is required for the maturation of the phagosomes. Treatment with amiloride (which also affects acidification) had a less significant effect on the uptake of PEM capsules compared to MβCD or bafilomycin A_1.

These results, together with the co-localization studies that demonstrate a primary localization in plasma membrane invaginations (enriched in cholesterol and glycosphingolipids) and a final localization in phagolysosomes located in the perinuclear region, suggest a multistep mechanism of PEM capsule internalization. This mechanism combines lipid-raft-mediated macropinocytosis and phagocytosis. Such a synergism has already been described for the entry of the bacterium *Mycobacterium tuberculosis* and the HIV virus.[81] Furthermore, a possible role of lipid rafts in the phagolysosome maturation[80] cannot be excluded, as co-localization of CTXB with LAMP1 was observed in the presence of the capsules (Figure SI-4.2).

Obviously, the generality of results raises the question of whether the results are limited to one type of capsules (PSS/PAH-based) and one type of cell line (MDA-MB-231) as used here. The polyelectrolytes PSS/PAH have been chosen as a prototype, as these materials are synthetic and thus nondegradable, and most capsule-based studies in the literature are related to this system. There is no special feature based on which MDA-MB-231 have been chosen, besides the fact that several of our previous studies were based on these cells. We repeated some of the inhibition experiments for two other configurations. In the first set we used the same cell type (*i.e.*, MDA-MB-231) but incubated them with capsules produced with different polyelectrolytes (pARG/DEXS) and, thus, different surface chemistries. The pARG/DEXS system is also known to be a prototype of biodegradable capsules. In the second set of experiments, we took a different cell line (A549 human lung cancer cells) and incubated them with the same capsules (*i.e.*, PSS/PAH). As can be seen in the data presented in the Supporting Information (§7), the results are highly similar, which suggests that the results obtained in this work are not limited to the special capsule cell configuration but rather are valid in a broader context. It has to

be pointed out that for the work presented here no functionalization of the capsule surface with active (*e.g.*, targeting) molecules such as antibodies, PEG, and peptides was performed, and thus capsule uptake has to be considered nonspecific. Therefore, we cannot exclude that the internalization pathway might be altered in the case where an active modification of the surface of the capsules is performed.

Summarizing, PEM capsule entry begins with the formation of a phagocytic cup, followed by a lipid-raft-mediated macropinocytosis and a final activation of the phagocytic machinery to sort PEM capsules in the heterophagolysosomes.

CONCLUSIONS

The aim of this research article was to elucidate and to fully describe the role of all endocytic pathways in the uptake patterns of PEM capsules. The comprehensiveness of this work is based on using different methods, *i.e.*, morphological characterization and pharmacological/chemical inhibition of capsule internalization and capsule organelle co-localization. Data suggest that multiple internalization pathways are involved at different stages of PEM capsule uptake. First of all, adsorptive mechanisms due to the electrostatic interactions induce a nonspecific, initial interaction of the capsules with the cells. Second, strong actin reorganization and filopodia formation occur to form a phagocytic cup (proper for phagocytosis[65]) to stabilize the capsules at the plasma membrane. At the early stage of engulfment, the capsules co-localize with the lipid rafts and require cholesterol-rich lipid domains, which are responsible for a proper cytosolic invagination. Due to the capsule size being larger than lipid rafts, the independence on an active dynamin, and the acidity of the internalizing vesicles (which exclude caveolin-mediated endocytosis), lipid-raft-mediated macropinocytosis plays a decisive role at this early stage of internalization. Clathrin-mediated endocytosis can be excluded due to the insensitivity of capsule uptake to chlorpromazine as well as to K^+-depletion and to dynasore. The absence of co-localization with calnexin, a marker for early, new-forming phagosomes, suggests that phagocytosis is not involved at this early stage of endocytosis. Upon cytosolic invagination, the PEM capsules are transported to the perinuclear cytoplasma of the cells within acidic vesicles. The transmembrane signaling cascade that might be activated remains unclear. However, a local membrane-induced polymerization of actin on the cell surface, as well as the requirement of vesicle acidification and the strong co-localization with LAMP1 is typical at all stages of phagolysosome maturation.[79,82] Consequently, in the last step of capsule uptake the phagocytic machinery is activated to transport PEM capsules until they reach their final location, the heterophagolysosomes.

METHODS

For more details regarding the experimental section and additional results, the reader is referred to the Supporting Information.

Synthesis of Fluorescent Gold Nanoparticle Functionalized PEM capsules. The synthesis (SI §1) of poly(sodium 4 styrenesulfonate) and poly(allylamine hydrochloride) (PSS/PAH) and of poly L arginine and dextran sulfate (pARG/DEXS)[13] capsules functionalized with gold nanoparticles and fluorescein isothiocyanate (FITC) was carried out following our previous protocols.[83] Gold nanoparticles and FITC were used for visualization with the electron microscope and with the optical microscope, respectively.

Cell Culture and Treatment. MDA MB 231 human breast adenocarcinoma cells and A549 human lung cancer cells (see SI §2) were seeded and grown overnight in growth medium (DMEM supplemented with 10% fetal bovine serum, insulin, and 1% penicillin/streptomycin). PEM capsules were added at a concentration of 20 capsules per cell and incubated for 4 h, at 37 °C and 5% CO_2. In the case of incubation with the different pharmacological/chemical inhibitors (see SI §2), the inhibitors were diluted in medium at concentrations (given in Table 1) that were determined to be nontoxic to the cells by cytotoxicity assays (see §5 and Figure SI 5 of the Supporting Information). Control cells were treated with medium only, instead of inhibitor solution. The inhibitors were added 1 h previous to capsule incubation and were maintained for 4 h.

In the case of potassium depletion, the cells were first incubated with a hypotonic medium (EMEM/H_2O, 1:1) for 5 min at 37 °C, then with isotonic medium A (100 mM NaCl in 50 mM HEPES pH 7.4) for 10 min at 37 °C, and finally with isotonic medium B (100 mM NaCl, 1 mM $CaCl_2$, 2.5% w/v BSA in 50 mM HEPES pH 7.4) for 30 min at 37 °C. Control cells were incubated with both isotonic media (A and B), supplemented with 10 mM KCl in order to avoid K^+ ion exchange.

Immunofluorescence. MDA MB 231 cells were fixed and permeabilized previous to incubation with the primary and the secondary antibodies (see Table 1 in the SI, §2) and to the staining of the cytoskeleton with phalloidin/tetramethylrhodamine and of the cells' nuclei with DAPI (4′,6 diamidino 2 phenylindole). If required, staining of the cell membrane with wheat germ agglutinin/tetramethylrhodamine was performed just before permeabilization. Finally, the cells were mounted on slides using Flouromount G.

Confocal Laser Scanning Microscopy. To visualize the capsules and different stained cellular structures, a CLSM 510 Meta (Zeiss) microscope was used. It was equipped with a laser diode emitting at 405 nm, an argon laser with a line at 488 nm, and a helium neon laser for excitation at 543 and 633 nm, respectively. Images were taken with a Plan Apochromat 63×/1.40 oil DIC M27 objective, and the pinhole was set to 0.86 1.32 airy units.

Tracking the pH of the Medium Surrounding Capsules to Establish the Acidification of Endocytic Vesicles Involved in the Uptake of PEM Capsules. The acidification of endocytic vesicles of MDA MB 231 cells was measured by tracking pH sensitive, SNARF filled PEM capsules in confocal images. The emission of SNARF (excitation: 488 and 543 nm) was recorded at 550 615 and 615 700 nm. The ratio of both emission intensities was plotted against the time.

Ultrastuctural Analysis *via* TEM. For transmission electron microscopy, MDA MB 231 cells were treated according to Ito and Karnovsky.[84] Postfixation was performed in 1% osmium tetroxide for 1 h at room temperature followed by an overnight incubation with 0.3% uranyl acetate dissolved in 50 mM maleate buffer (pH 5.0). Samples were embedded in Epon according to standard procedures. Thin sections were contrasted with lead citrate and examined with a Zeiss EM 109S electron microscope equipped with a TRS wide angle dual speed CCD camera.

TABLE 2. Illustration of the Different Cellular Structures Used to Study Their Co localization with the PSS/PAH Capsules[a]

cellular structure	target/*dye*	co localization	endocytic pathway
endosomes	EEA1	no	clathrin and caveolin (in)dependent endocytosis
clathrin coated vesicles	clathrin	no	clathrin mediated endocytosis
caveolin coated lipid rafts	caveolin 1	no	caveolin mediated lipid rafts
lipid rafts	CTXB	yes	lipid rafts
endoplasmic reticulum (ER)	calnexin	no	ER mediated phagocytosis
phagolysosomes	LAMP1[b]	yes	phagocytosis
cell membrane	*WGA*	*n/a*	*n/a*
actin cytoskeleton	*phalloidin*	*n/a*	*n/a*
nucleus	*DAPI*	*n/a*	*n/a*

[a] Their associated pathways of entry and the degree of co localization with the capsules observed *via* CLSM after 4 h incubation with MDA MB 231 cells are also presented. The staining of structures (italicized text), such as the cell membrane or the actin cytoskeleton and the nucleus, were done to help quantify the number of internalized capsules and to facilitate imaging, respectively. AF: Alexa fluor. EEA1: early endosome antigen 1. CTXB: cholera toxin B1. LAMP1: lysosomal associated membrane protein 1. WGA: wheat germ agglutinin. [b] The hybridoma antibody LAMP1 developed by J. Thomas August and James E. K. Hildreth was obtained from the Developmental Studies Hybridoma Bank developed under the auspices of the NICHD and maintained by The University of Iowa, Department of Biology, Iowa City, IA 52242, USA.

Quantification of the Inhibition of Capsule Uptake. The cellular uptake of capsules was quantified by manual CLSM image analysis. All images were acquired and evaluated as *z* stacks. Capsules surrounded by lysosomal associated membrane pro tein 1 were always classified as intracellular. Capsules clearly surrounded by actin were classified as intracellular, but were distinguished from capsules that were only located between densely grown cells. Also, visible deformation of capsules, which can be frequently observed after capsule uptake (once they are already located in the phagolysosome), was considered as an indication of intracellular localization. Dividing and not fully depicted cells were not taken into account. Please note that we purposely decided against flow cytometry, although this would have allowed for a higher number of investigated cells. With flow cytometry it is not straightforward to distinguish between capsules just adherent to the outer cell membrane and actually internalized capsules,[85] whereas this was easily possible with CLSM with the above described criteria.

Following the scheme for CLSM detection of capsules, the number of intracellular capsules was individually determined for each cell. For every inhibitor concentration, two or three inde pendent experiments with at least 100 cells analyzed per experi ment were conducted. To check for classification bias, parts of the image analysis were performed as single blinded analyses.

Instead of plotting the number of internalized capsules per cell in the format of a histogram, data are presented as cumulative distribution functions (see SI §6). The CDF $0 \leq p(N_{in}) \leq 100\%$ represents the probability of a cell having 0 to N_{in} capsules internalized. As an example, $p(2) = 0.87$ signifies that 87% of the analyzed cells do not have more than two capsules internalized (*i.e.*, either 0, 1, or 2 capsules per cell). CDF plots for at least three independent experiments were arithme tically averaged directly without weighting and merged into one diagram. The standard deviation was calculated from the deviation of the independent CDFs of the three different experiments per each data set.

For the sake of clarity and for a better comparison of the results obtained for all inhibitors, the total efficiency of inhibition was presented. To address the total efficiency E_T of inhibition with one single value, the area A_I lined by the CDF $I(N)$ for inhibited cells and the line $p = 1$ was determined and divided by the area A_C enclosed by the graph of the control $C(N)$ and $p = 1$. Finally, the effectiveness of one inhibitor was calculated as $E_T = 1 \quad A_I/A_C$.

Conflict of Interest: The authors declare no competing financial interest.

Supporting Information Available: A detailed description of the methods followed in this work and additional results are available free of charge *via* the Internet at http://pubs.acs.org.

Acknowledgment. Parts of this project were funded by NANOSYN ERA NET Neuron Program (BMBF Germany to W.J.P. and Spanish Ministry of Economy and Competitivity to R.F.C., EUI2009 04084), DFG Germany (SPP 1313, project PA794/4 2 to W.J.P. and P.R.G.), and BFU2010 15713 and Junta de Andalucía (P07 CVI 02854) to R.F.C. We are grateful to Alejandro Arroyo and M. Carmen Rivero for excellent technical assistance and to Loretta L. del Mercato, Azhar Z. Abassi, and Xiang Yu for their contribution to the synthesis of the capsules. Part of this work was performed at CITIUS (University of Seville, Spain). The authors are thankful to Christian Allebach for proofreading the manuscript.

REFERENCES AND NOTES

1. Rivera Gil, P.; Parak, W. J. Composite Nanoparticles Take Aim at Cancer. *ACS Nano* **2008**, *2*, 2200 2205.
2. Decher, G.; Lehr, B.; Lowack, K.; Lvov, Y.; Schmitt, J. New Nanocomposite Films for Biosensors Layer by Layer Adsorbed Films of Polyelectrolytes, Proteins or DNA. *Biosens. Bioelectron.* **1994**, *9*, 677 684.
3. Donath, E.; Sukhorukov, G. B.; Caruso, F.; Davis, S. A.; Möhwald, H. Novel Hollow Polymer Shells by Colloid Templated Assembly of Polyelectrolytes. *Angew. Chem., Int. Ed.* **1998**, *37*, 2202 2205.
4. Sukhorukov, G. B.; Donath, E.; Lichtenfeld, H.; Knippel, E.; Knippel, M.; Budde, A.; Mohwald, H. Layer by Layer Self Assembly of Polyelectrolytes on Colloidal Particles. *Col loids Surf., A* **1998**, *137*, 253 266.
5. De Geest, B. G.; Van Camp, W.; Du Prez, F. E.; De Smedt, S. C.; Demeester, J.; Hennink, W. E. Biodegradable Micro capsules Designed Via 'Click' Chemistry. *Chem. Commun.* **2008**, 190 192.
6. Caruso, F.; Caruso, R. A.; Möhwald, H. Production of Hollow Microspheres from Nanostructured Composite Particles. *Chem. Mater.* **1999**, *11*, 3309 3314.
7. Rivera Gil, P.; del Mercato, L. L.; del Pino, P.; Munoz Javier, A.; Parak, W. J. Nanoparticle Modified Polyelectrolyte Cap sules. *Nano Today* **2008**, *3*, 12 21.
8. Sukhorukov, G. B.; Mohwald, H. Multifunctional Cargo Sys tems for Biotechnology. *Trends Biotechnol.* **2007**, *25*, 93 98.
9. De Geest, B. G.; Sanders, N. N.; Sukhorukov, G. B.; Demeester, J.; De Smedt, S. C. Release Mechanisms for Polyelectrolyte Capsules. *Chem. Soc. Rev.* **2007**, *36*, 636 649.
10. Yan, Y.; Johnston, A. P. R.; Dodds, S. J.; Kamphuis, M. M. J.; Ferguson, C.; Parton, R. G.; Nice, E. C.; Heath, J. K.; Caruso, F. Uptake and Intracellular Fate of Disulfide Bonded Polymer Hydrogel Capsules for Doxorubicin Delivery to Colorectal Cancer Cells. *ACS Nano* **2010**, *4*, 2928 2936.
11. Rivera Gil, P.; Nazarenus, M.; Ashraf, S.; Parak, W. J. pH Sensitive Capsules as Intracellular Optical Reporters for Monitoring Lysosomal pH Changes Upon Stimulation. *Small* **2012**, *8*, 943 948.
12. del Mercato, L. L.; Abbasi, A. Z.; Ochs, M.; Parak, W. J. Multiplexed Sensing of Ions with Barcoded Polyelectrolyte Capsules. *ACS Nano* **2011**, *5*, 9668 9674.

13. Rivera Gil, P.; Koker, S. D.; De Geest, B. G.; Parak, W. J. Intracellular Processing of Proteins Mediated by Biodegradable Polyelectrolyte Capsules. *Nano Lett.* **2009**, *9*, 4398 4402.
14. De Koker, S.; De Geest, B. G.; Singh, S. K.; De Rycke, R.; Naessens, T.; Van Kooyk, Y.; Demeester, J.; De Smedt, S. C.; Grooten, J. Polyelectrolyte Microcapsules as Antigen Delivery Vehicles to Dendritic Cells: Uptake, Processing, and Cross Presentation of Encapsulated Antigens. *Angew. Chem., Int. Ed.* **2009**, *48*, 8485 8489.
15. De Geest, B. G.; Vandenbroucke, R. E.; Guenther, A. M.; Sukhorukov, G. B.; Hennink, W. E.; Sanders, N. N.; Demeester, J.; Smedt, S. C. d. Intracellularly Degradable Polyelectrolyte Microcapsules. *Adv. Mater.* **2006**, *18*, 1005 1009.
16. Wattendorf, U.; Kreft, O.; Textor, M.; Sukhorukov, G. B.; Merkle, H. P. Stable Stealth Function for Hollow Poly electrolyte Microcapsules through a Poly(Ethylene Glycol) Grafted Polyelectrolyte Adlayer. *Biomacromolecules* **2008**, *9*, 100 108.
17. Heuberger, R.; Sukhorukov, G.; Vörös, J.; Textor, M.; Möhwald, H. Biofunctional Polyelectrolyte Multilayers and Microcapsules: Control of Non Specific and Bio Specific Protein Adsorption. *Adv. Funct. Mater.* **2005**, *15*, 357 366.
18. Hu, S. H.; Tsai, C. H.; Liao, C. F.; Liu, D. M.; Chen, S. Y. Controlled Rupture of Magnetic Polyelectrolyte Microcap sules for Drug Delivery. *Langmuir* **2008**, *24*, 11811 11818.
19. del Pino, P.; Munoz Javier, A.; Vlaskou, D.; Rivera Gil, P.; Plank, C.; Parak, W. J. Gene Silencing Mediated by Magnetic Lipospheres Tagged with Small Interfering RNA. *Nano Lett.* **2010**, *10*, 3914 3921.
20. Johnston, A. P. R.; Kamphuis, M. M. J.; Such, G. K.; Scott, A. M.; Nice, E. C.; Heath, J. K.; Caruso, F. Targeting Cancer Cells: Controlling the Binding and Internalization of Anti body Functionalized Capsules. *ACS Nano* **2012**, *6*, 6667 6674.
21. Kamphuis, M. M. J.; Johnston, A. P. R.; Such, G. K.; Dam, H. H.; Evans, R. A.; Scott, A. M.; Nice, E. C.; Heath, J. K.; Caruso, F. Targeting of Cancer Cells Using Click Functionalized Poly mer Capsules. *J. Am. Chem. Soc.* **2010**, *132*, 15881 15883.
22. Cortez, C.; Tomaskovic Crook, E.; Johnston, A. P. R.; Scott, A. M.; Nice, E. C.; Heath, J. K.; Caruso, F. Influence of Size, Surface, Cell Line, and Kinetic Properties on the Specific Binding of A33 Antigen Targeted Multilayered Particles and Capsules to Colorectal Cancer Cells. *ACS Nano* **2007**, *1*, 93 102.
23. Skirtach, A. G.; Dejugnat, C.; Braun, D.; Susha, A. S.; Parak, W. J.; Möhwald, H.; Sukhorukov, G. B. The Role of Metal Nanoparticles in Remote Release of Encapsulated Materi als. *Nano Lett.* **2005**, *5*, 1371 1377.
24. Hühn, D.; Govorov, A.; Rivera Gil, P.; Parak, W. J. Photo stimulated Au Nanoheaters in Polymer and Biological Media: Characterization of Mechanical Destruction and Boiling. *Adv. Funct. Mater.* **2012**, *22*, 294 303.
25. Bedard, M. F.; Braun, D.; Sukhorukov, G. B.; Skirtach, A. G. Toward Self Assembly of Nanoparticles on Polymeric Microshells: Near IR Release and Permeability. *ACS Nano* **2008**, *2*, 1807 1816.
26. Carregal Romero, S.; Ochs, M.; Rivera Gil, P.; Gana, C.; Pavlov, A. M.; Sukhorukov, G. B.; Parak, W. J. NIR Light Triggered Delivery of Macromolecules into the Cytosol. *J. Controlled Release* **2012**, *159*, 120 127.
27. Skirtach, A. G.; Javier, A. M.; Kreft, O.; Köhler, K.; Alberola, A. P.; Möhwald, H.; Parak, W. J.; Sukhorukov, G. B. Laser Induced Release of Encapsulated Materials inside Living Cells. *Angew. Chem., Int. Ed.* **2006**, *45*, 4612 4617.
28. Ochs, C. J.; Such, G. K.; Stadler, B.; Caruso, F. Low Fouling, Biofunctionalized, and Biodegradable Click Capsules. *Bio macromolecules* **2008**, *9*, 3389 3396.
29. del Mercato, L. L.; Rivera Gil, P.; Abbasi, A. Z.; Ochs, M.; Ganas, C.; Zins, I.; Sönnichsen, C.; Parak, W. J. Lbl Multilayer Capsules: Recent Progress and Future Outlook for Their Use in Life Sciences. *Nanoscale* **2010**, *2*, 458 467.
30. Shchukin, D. G.; Shutava, T.; Shchukina, E.; Sukhorukov, G. B.; Lvov, Y. M. Modified Polyelectrolyte Microcapsules as Smart Defense Systems. *Chem. Mater.* **2004**, *16*, 3446 3451.
31. Wang, Y. J.; Bansal, V.; Zelikin, A. N.; Caruso, F. Templated Synthesis of Single Component Polymer Capsules and Their Application in Drug Delivery. *Nano Lett.* **2008**, *8*, 1741 1745.
32. Muñoz Javier, A.; Kreft, O.; Semmling, M.; Kempter, S.; Skirtach, A. G.; Bruns, O.; Pino, P. d.; Bedard, M. F.; Rädler, J.; Käs, J.; *et al*. Uptake of Colloidal Polyelectrolyte Coated Particles and Polyelectrolyte Multilayer Capsules by Living Cells. *Adv. Mater.* **2008**, *20*, 4281 4287.
33. Becker, A. L.; Johnston, A. P. R.; Caruso, F. Layer by Layer Assembled Capsules and Films for Therapeutic Delivery. *Small* **2010**, *6*, 1836 1852.
34. Reibetanz, U.; Halozan, D.; Brumen, M.; Donath, E. Flow Cytometry of Hek 293t Cells Interacting with Polyelectro lyte Multilayer Capsules Containing Fluorescein Labeled Poly(Acrylic Acid) as a pH Sensor. *Biomacromolecules* **2007**, *8*, 1928 1933.
35. Ivanov, A. I. Pharmacological Inhibition of Endocytic Path ways: Is It Specific Enough to Be Useful? *Methods Mol. Biol.* **2008**, *440*, 15 33.
36. Muñoz Javier, A.; Kreft, O.; Piera Alberola, A.; Kirchner, C.; Zebli, B.; Susha, A. S.; Horn, E.; Kempter, S.; Skirtach, A. G.; Rogach, A. L.; *et al*. Combined Atomic Force Microscopy and Optical Microscopy Measurements as a Method to Investigate Particle Uptake by Cells. *Small* **2006**, *2*, 394 400.
37. Zelikin, A. N.; Breheney, K.; Robert, R.; Tjipto, E.; Wark, K. Cytotoxicity and Internalization of Polymer Hydrogel Cap sules by Mammalian Cells. *Biomacromolecules* **2010**, *11*, 2123 2129.
38. Jacobson, K.; Sheets, E. D.; Simson, R. Revisiting the Fluid Mosaic Model of Membranes. *Science* **1995**, *268*, 1441 1442.
39. Wieffer, M.; Maritzen, T.; Haucke, V. Snapshot: Endocytic Trafficking. *Cell* **2009**, *137*, 382e1 382.e3.
40. Doherty, G. J.; McMahon, H. T. Mechanisms of Endocytosis. *Annu. Rev. Biochem.* **2009**, *78*, 857 902.
41. Mayor, S.; Pagano, R. E. Pathways of Clathrin Independent Endocytosis. *Nat. Rev. Mol. Cell Biol.* **2007**, *8*, 603 612.
42. Conner, S. D.; L.Schmid, S. Regulated Portals of Entry into the Cell. *Nature* **2003**, *422*, 37 41.
43. Vieira, O. V.; Botelho, R. J.; Grinstein, S. Phagosome Matura tion: Aging Gracefully. *Biochem. J.* **2002**, *366*, 689 704.
44. Pfeffer, S. R. Caveolae on the Move. *Nat. Cell Biol.* **2001**, *3*, E108 E110.
45. De Geest, B. G.; De Koker, S.; Sukhorukov, G. B.; Kreft, O.; Parak, W. J.; Skirtach, A. G.; Demeester, J.; De Smedt, S. C.; Hennink, W. E. Polyelectrolyte Microcapsules for Biomedi cal Applications. *Soft Matter* **2009**, *5*, 282 291.
46. De Koker, S.; De Geest, B. G.; Cuvelier, C.; Ferdinande, L.; Deckers, W.; Hennink, W. E.; De Smedt, S.; Mertens, N. *In Vivo* Cellular Uptake, Degradation, and Biocompatibility of Polyelectrolyte Microcapsules. *Adv. Funct. Mater.* **2007**, *17*, 3754 3763.
47. Sahay, G.; Alakhova, D. Y.; Kabanov, A. V. Endocytosis of Nanomedicines. *J. Controlled Release* **2010**, *145*, 182 195.
48. Luzio, J. P.; Pryor, P. R.; Bright, N. A. Lysosomes: Fusion and Function. *Nat. Rev. Mol. Cell Biol.* **2007**, *8*, 622 632.
49. Kenworthy, A. K.; Petranova, N.; Edidin, M. High Resolution Fret Microscopy of Cholera Toxin B Subunit and Gpi Anchored Proteins in Cell Plasma Membranes. *Mol. Biol. Cell* **2000**, *11*, 1645 1655.
50. Rogers, L. D.; Foster, L. J. The Dynamic Phagosomal Pro teome and the Contribution of the Endoplasmic Reticulum. *Proc. Natl. Acad. Sci. U.S.A.* **2007**, *104*, 18520 18525.
51. Bishop, J. R.; Schuksz, M.; Esko, J. D. Heparan Sulphate Proteoglycans Fine Tune Mammalian Physiology. *Nature* **2007**, *446*, 1030 1037.
52. Mano, M.; Teodosio, C.; Paiva, A.; Simoes, S.; de Lima, M. C. P. On the Mechanisms of the Internalization of S4(13) Pv Cell Penetrating Peptide. *Biochem. J.* **2005**, *390*, 603 612.
53. Blocker, A.; Griffiths, G.; Olivo, J. C.; Hyman, A. A.; Severin, F. F. A Role for Microtubule Dynamics in Phagosome Movement. *J. Cell Sci.* **1998**, *111*, 303 312.

54. Aderem, A.; Underhill, D. M. Mechanisms of Phagocytosis in Macrophages. *Annu. Rev. Immunol.* **1999**, *17*, 593 623.
55. McNally, A. K.; Anderson, J. M. Multinucleated Giant Cell Formation Exhibits Features of Phagocytosis with Partici pation of the Endoplasmic Reticulum. *Exp. Mol. Pathol.* **2005**, *79*, 126 135.
56. Toyohara, A.; Inaba, K. Transport of Phagosomes in Mouse Peritoneal Macrophages. *J. Cell Sci.* **1989**, *94*, 143 153.
57. Kreft, O.; Javier, A. M.; Sukhorukov, G. B.; Parak, W. J. Polymer Microcapsules as Mobile Local pH Sensors. *J. Mater. Chem.* **2007**, *17*, 4471 4476.
58. Van Hamme, E.; Dewerchin, H. L.; Cornelissen, E.; Verhasselt, B.; Nauwynck, H. J. Clathrin and Caveolae Independent Entry of Feline Infectious Peritonitis Virus in Monocytes Depends on Dynamin. *J. Gen. Virol.* **2008**, *89*, 2147 2156.
59. Wadia, J. S.; Stan, R. V.; Dowdy, S. F. Transducible Tat Ha Fusogenic Peptide Enhances Escape of Tat Fusion Pro teins after Lipid Raft Macropinocytosis. *Nat. Med.* **2004**, *10*, 310 315.
60. Smart, E. J.; Anderson, R. G. W.; Chandan, K.; Sen, L. P. Alterations in Membrane Cholesterol That Affect Structure and Function of Caveolae. *Methods Enzymol.* **2002**, *353*, 131 139.
61. Kanzaki, M.; Pessin, J. E. Caveolin Associated Filamentous Actin (Cav Actin) Defines a Novel F Actin Structure in Adipocytes. *J. Biol. Chem.* **2002**, *277*, 25867 25869.
62. West, M. A.; Bretscher, M. S.; Watts, C. Distinct Endocytotic Pathways in Epidermal Growth Factor Stimulated Human Carcinoma A431 Cells. *J. Cell Biol.* **1989**, *109*, 2731 2739.
63. Yoshimori, T.; Yamamoto, A.; Moriyama, Y.; Futai, M.; Tashiro, Y. Bafilomycin A1, a Specific Inhibitor of Vacuolar Type H+ Atpase, Inhibits Acidification and Protein Degra dation in Lysosomes of Cultured Cells. *J. Biol. Chem.* **1991**, *266*, 17707 17712.
64. Bidani, A.; Heming, T. A. Effects of Bafilomycin a(1) on Functional Capabilities of Lps Activated Alveolar Macro phages. *J. Leukoc. Biol.* **1995**, *57*, 275 281.
65. Gagnon, E.; Duclos, S.; Rondeau, C.; Chevet, E.; Cameron, P. H.; Steele Mortimer, O.; Paiement, J.; Bergeron, J. J. M.; Desjardins, M. Endoplasmic Reticulum Mediated Phago cytosis Is a Mechanism of Entry into Macrophages. *Cell* **2002**, *110*, 119 131.
66. Reibetanz, U.; Claus, C.; Typlt, E.; Donath, J. H. Defoliation and Plasmid Delivery with Layer by Layer Coated Colloids. *Macromol. Biosci.* **2006**, *6*, 153 160.
67. Werner, G.; Hagenmaier, H.; Drautz, H.; Baumgartner, A.; Zahner, H. Metabolic Products of Microorganisms. 224. Bafilomycins, a New Group of Macrolide Antibiotics Production, Isolation, Chemical Structure and Biological Activity. *J. Antibiot.* **1984**, *37*, 110 117.
68. Bowman, E. J.; Siebers, A.; Altendorf, K. Bafilomycins a Class of Inhibitors of Membrane Atpases from Microor ganisms, Animal Cells, and Plant Cells. *Proc. Natl. Acad. Sci. U.S.A.* **1988**, *85*, 7972 7976.
69. Marx, K. A.; Zhou, T.; Montrone, A.; McIntosh, D.; Braunhut, S. J. A Comparative Study of the Cytoskeleton Binding Drugs Nocodazole and Taxol with a Mammalian Cell Quartz Crystal Microbalance Biosensor: Different Dynamic Responses and Energy Dissipation Effects. *Anal. Biochem.* **2007**, *361*, 77 92.
70. Lu, S. W.; Tager, L. A.; Chitale, S.; Riley, L. W. A Cell Penetrating Peptide Derived from Mammalian Cell Uptake Protein of Mycobacterium Tuberculosis. *Anal. Biochem.* **2006**, *353*, 7 14.
71. Parsons, A. B.; Lopez, A.; Givoni, I. E.; Williams, D. E.; Gray, C. A.; Porter, J.; Chua, G.; Sopko, R.; Brost, R. L.; Ho, C. H.; *et al.* Exploring the Mode of Action of Bioactive Compounds by Chemical Genetic Profiling in Yeast. *Cell* **2006**, *126*, 611 625.
72. Kuhn, M. The Microtubule Depolymerizing Drugs Noco dazole and Colchicine Inhibit the Uptake of Listeria Mono cytogenes by P388d1 Macrophages. *FEMS Microbiol. Lett.* **1998**, *160*, 87 90.
73. Zhang, H.; Xia, T.; Meng, H.; Xue, M.; George, S.; Ji, Z.; Wang, X.; Liu, R.; Wang, M.; France, B.; *et al.* Differential Expression of Syndecan 1 Mediates Cationic Nanoparticle Toxicity in Undifferentiated *versus* Differentiated Normal Human Bronchial Epithelial Cells. *ACS Nano* **2011**, *5*, 2756 2769.
74. Macia, E.; Ehrlich, M.; Massol, R.; Boucrot, E.; Brunner, C.; Kirchhausen, T. Dynasore, a Cell Permeable Inhibitor of Dynamin. *Dev. Cell* **2006**, *10*, 839 850.
75. Pelkmans, L.; Puntener, D.; Helenius, A. Local Actin Polym erization and Dynamin Recruitment in Sv40 Induced Internalization of Caveolae. *Science* **2002**, *296*, 535 539.
76. Desjardins, M.; Huber, L. A.; Parton, R. G.; Griffiths, G. Biogenesis of Phagolysosomes Proceeds through a Se quential Series of Interactions with the Endocytic Appara tus. *J. Cell Biol.* **1994**, *124*, 677 688.
77. Jahraus, A.; Tjelle, T. E.; Berg, T.; Habermann, A.; Storrie, B.; Ullrich, O.; Griffiths, G. *In Vitro* Fusion of Phagosomes with Different Endocytic Organelles from J774 Macrophages. *J. Biol. Chem.* **1998**, *273*, 30379 30390.
78. Becker, T.; Volchuk, A.; Rothman, J. E. Differential Use of Endoplasmic Reticulum Membrane for Phagocytosis in J774 Macrophages. *Proc. Natl. Acad. Sci. U.S.A.* **2005**, *102*, 4022 4026.
79. Desjardins, M.; Griffiths, G. Phagocytosis: Latex Leads the Way. *Curr. Opin. Cell Biol.* **2003**, *15*, 498 503.
80. Garin, J.; Diez, R.; Kieffer, S.; Dermine, J. F.; Duclos, S.; Gagnon, E.; Sadoul, R.; Rondeau, C.; Desjardins, M. The Phagosome Proteome: Insight into Phagosome Functions. *J. Cell Biol.* **2001**, *152*, 165 180.
81. Vergne, I.; Chua, J.; Singh, S. B.; Deretic, V. Cell Biology of Mycobacterium Tuberculosis Phagosome. *Annu. Rev. Cell Dev. Biol.* **2004**, *20*, 367 394.
82. Greenberg, S.; Grinstein, S. Phagocytosis and Innate Immunity. *Curr. Opin. Immunol.* **2002**, *14*, 136 145.
83. del Mercato, L. L.; Gonzalez, E.; Abbasi, A. Z.; Parak, W. J.; Puntes, V. Synthesis and Evaluation of Gold Nanoparticle Modified Polyelectrolyte Capsules under Microwave Irradiation for Remotely Controlled Release for Cargo. *J. Mater. Chem.* **2011**, *21*, 11468 11471.
84. Ito, S.; Karnovsky, M. J. Formaldehyde Glutaraldehyde Fixatives Containing Trinitro Compounds. *J. Cell Biol.* **1968**, *39*, 168a 169a.
85. Semmling, M.; Kreft, O.; Muñoz Javier, A.; Sukhorukov, G. B.; Käs, J.; Parak, W. J. A Novel Flow Cytometry Based Assay for Cellular Uptake Studies of Polyelectrolyte Microcap sules. *Small* **2008**, *4*, 1763 1768.

Angewandte International Edition Chemie

DOI: 10.1002/anie.201409693

Endocytosis

Stiffness-Dependent In Vitro Uptake and Lysosomal Acidification of Colloidal Particles**

*Raimo Hartmann, Marcel Weidenbach, Martin Neubauer, Andreas Fery, and Wolfgang J. Parak**

Abstract: *The physico chemical properties of colloidal particles determine their uptake into cells. For a series of microparticles only one parameter, the mechanical stiffness, was varied, whereas other parameters such as size, shape, and charge were kept constant. The uptake was monitored in situ by analyzing individual particle trajectories including the progress of endocytosis, derived from local pH measurements around each particle. Evidence is presented that soft particles with low stiffness are transported faster to lysosomes than stiffer ones.*

The number of applications based on the interaction of colloids with cells has been increasing steadily over the past few years, mostly for sensing or delivery based applications. As most of the approaches require particle internalization, cellular uptake mechanisms have been heavily studied.[1] Unfortunately, the ultimate goal, to entirely correlate the uptake process with the physico chemical particle properties, is not trivial, in particular as many of these properties are interrelated.[2] Thus, it is extremely challenging to obtain consistent studies, in which only one particular parameter of the particles is varied, while all other properties are held constant. Properties that have been studied systematically comprise particle size,[3] shape,[4] and charge.[5] While size, shape, and charge are the "standard" well investigated parameters influencing in vitro particle incorporation by cells, there are many additional well defined physical properties, for instance particle stiffness, which might also play an important role. Dependent on their stiffness, hollow microparticles are compressed and deformed upon cellular internalization.[6,7] Based on theoretical considerations Yi et al. claimed that cellular processing of deformable particles might be different to that of stiffer counterparts, because these particles are less prone to membrane wrapping.[8] Hydrogel based nanoparticles with a Young's modulus between 30 and 140 kPa were found to be internalized more efficiently by RAW 264.7 macrophages than softer (< 30 kPa) or stiffer (> 140 kPa) nanoparticles.[9] Liu et al. reported that the uptake rate of flexible micron sized hydrogel particles (15 35 kPa) was higher than that of less elastic ones (75 160 kPa) by HepG2 cells.[10]

Polymer capsules, for example, hollow microparticles synthesized by layer by layer (LbL) assembly of oppositely charged polyelectrolytes,[11] are a well suited model system for systematic investigations, since their various physico chemical properties can be tuned independently.[12] Size[13] and shape[14] can be varied by using different template cores, and the sign of the surface charge is simply determined by the charge of the outermost layer. Stiffness can be tuned by variation of the number of polymer layers or by the polymer materials used.[15,16] Thus, polyelectrolyte capsules are a convenient particle system to investigate stiffness dependent in vitro uptake by cells, in a way such that particle size, shape, charge, and surface chemistry remain constant, while stiffness is varied. Most important, with this system it is possible to change exclusively one parameter, whereby the outer surface remains the same, and physicochemical parameters other than stiffness are fully maintained.

Upon internalization, capsules (i.e. particles) are taken up via endocytic processes and are transferred from the neutral extracellular medium to increasingly acidic intracellular vesicles of different maturity, and finally end up in the lysosome.[17] The local pH around each particle can be used as readout that describes its present stage of uptake. For this purpose particles can be loaded with pH sensitive fluorophores such as fluorescein based dyes[18,19] and seminaphtharhodafluor (SNARF),[19,20] which allow for the time resolved detection of the local pH around the capsules in extra and intracellular environments.[6,20,21]

Based on LbL assembly[11] around sacrificial $CaCO_3$ template cores we synthesized pH sensitive capsules with a different number of layers to vary capsule stiffness with two frequently used polymer systems (nondegradable polymers: poly(sodium 4 styrenesulfonate) (PSS) and poly(allylamine hydrochloride) (PAH); degradable polymers: dextran sulfate sodium salt (DextS) and poly L arginine hydrochloride (PLArg);[17,22] cf. Figure 1a). Two batches of template cores with resulting diameters of 4.1 μm (size "S") and 4.7 μm (size "L") were used. The pH sensitivity was achieved by embedding SNARF 1[19,20] labeled dextran into the cavity of the capsules. Response curves relating the ratio of red (I_r; 615 700 nm) to yellow (I_g; 560 615 nm, shown in green) fluorescence I_r/I_g(pH) were obtained for each type of capsule (Figure 1b). With this setup changes in pH could be monitored down to values around 4.5. However, SNARF 1

[*] R. Hartmann, M. Weidenbach, Prof. W. J. Parak
Fachbereich Physik, Philipps Universität Marburg
35037 Marburg (Germany)
E mail: wolfgang.parak@physik.uni marburg.de
Prof. W. J. Parak
CIC BiomaGUNE, 20009 San Sebastian (Spain)
M. Neubauer, Prof. A. Fery
Fakultät für Chemie, Universität Bayreuth (Germany)

[**] This work was supported by LOEWE (project Synchembio to W.J.P.). We thank Dr. Andreas Schaper for his kind introduction into ultrasectioning and Dr. Pilar Rivera Gil for stimulating technical discussions at the initial stages of this work.

Supporting information for this article is available on the WWW under http://dx.doi.org/10.1002/anie.201409693.

Angewandte
Communications

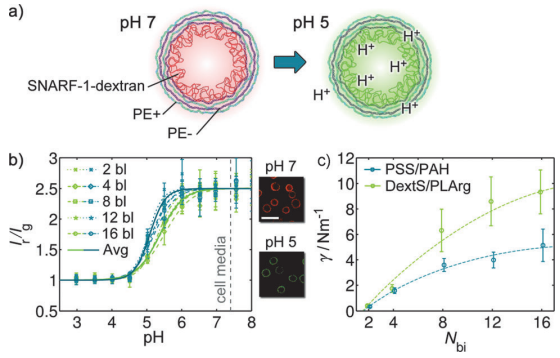

Figure 1. a) Sketch of one polyelectrolyte capsule, which comprises N_{bi} 2 bilayers, each composed out of one negatively charged (PE− (purple), PSS, or DextS) and one positively charged (PE+ (light blue), PAH, or PLArg) polyelectrolyte layer. Due to the positively charged outermost layer the whole particle is positively charged (cf. Figure SI 7). pH sensitive fluorophores SNARF 1 conjugated to dextran are located inside the cavity. b) The red to green ratio (false colors) of the fluorescence signal I_r/I_g from the capsule cavity depends on the local pH around each capsule. Response curves are shown for capsules of 2 16 bilayers (bl) of size "S" (green: DextS/PLArg, blue: PSS/PAH) and are normalized to pH 7.4 (cell media). The solid lines (labeled "Avg") show the average response curves for both types. The insets (scale bar: 2 μm) show fluorescence microscopy images of capsules at neutral (red fluorescence) and acidic pH (green fluorescence). c) The dependence of the mechanical stiffness γ for the different capsules ($d \approx 4.1$ μm, size "S") as determined by AFM is plotted versus on the number of bilayers N_{bi} making up the capsule shell. The dashed lines are guides to the eye only.

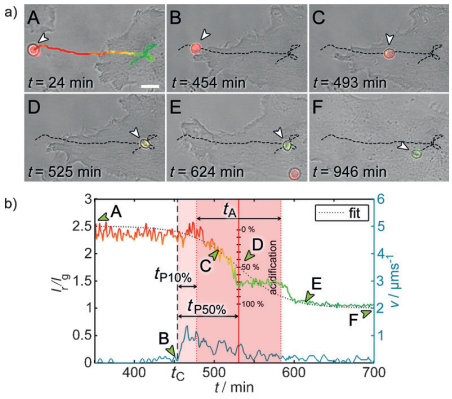

Figure 2. a) Typical timelapse recording of one PSS/PAH capsule (N_{bi} 8, size "L") during its uptake by a HeLa cell. The images (overlay of green and red fluorescence and the brightfield micrograph) recorded at a temporal resolution of 120 s are used to determine the trajectory of the capsule (scale bar: 5 μm). b) The ratio of red to green fluorescence I_r/I_g of the capsule has been determined for each image and is plotted versus the incubation time t. The time points corresponding to the images in (a) are labeled A F. A ratio of $I_r/I_g \approx 2.5$ corresponds to a pH 7.4, while $I_r/I_g \approx 1$ corresponds to local pH < 4.5 (Figure 1b). The acidification time t_A reflects the duration of the acidification process while the processing time $t_{P10\%}$ is determined as the period from the first contact of the capsule with the cell (B, high velocity) until the beginning of the acidification process (red area) and $t_{P50\%}$ as the period until the point of inflection of the readout curve (D).

embedded in biodegradable DextS/PLArg capsules was slightly less sensitive at lower pH values.

The stiffness of the capsules in solution was determined by atomic force microscopy (AFM) for each type of capsule[16] (Figure 1c). As expected, the stiffness of the capsules increased with the number of polyelectrolyte layers. Presum ably this is a direct consequence of the shell thickness, which increases with the number of polyelectrolyte layers. In particular, in case of the DextS/PLArg capsules there were batch to batch variations of the absolute stiffness values (cf. the Supporting Information (SI), Figure SI 5).

The uptake process was monitored in different adherent cells (cell lines as well as primary cells). Upon internalization, the local environment of the capsules changed from neutral (cell medium) to strongly acidic (lysosome), which can be seen by the ratiometric readout of the pH sensitive fluoro phores embedded in the capsules[20,21] (Figure 2a). First (image A), each capsule is located in neutral/slightly alkaline cell medium, thus leading to high, constant I_r/I_g values. At one point in time, here defined as t_C, the particle touches the cell surface (image B) and then it moves along the outer plasma membrane, as visible by the red emission which demonstrates extracellular location. It is then engulfed by the cell, as visualized by the change in fluorescence, and subsequently passed to more and more acidic compartments (images C and D), until at one point the pH seems to remain constant. At this point (image E) the capsule reaches its final destination, the lysosome.[17] If the pH decreases below 4.5 changes to an even more acidic environment are no longer observable due to the limited sensitivity of the pH indicator used (Figure 1b). Figure 2b shows that the pathway of uptake is not necessarily continuous, as can be seen by the jump of the pH values along the trace in image D at $t = 525$ min. We speculate that at this point in time the capsule containing vesicular compartment may have fused with a vesicle of potentially much lower pH. (A correlation of fusion events of acidic vesicles with the pH values of the capsule containing compartment can be found in Figure SI 16.) In order to derive quantitative data from the $I_r/I_g(t)$ traces we define t_A as the acidification time and $t_{P10\%}/t_{P50\%}$ as the processing time. The processing time is the duration from the first contact t_C (membrane attachment) of the capsule with the cell, following its incorporation and finally partial acidification (10% or 50%). The acidification time describes the duration of acidification from high to low pH following the sigmoidally shaped time dependent $(I_r/I_g)(t)$ curve (Figure 2b, for more details see Figure SI 9).

The uptake of microcapsules can differ significantly between different cell types and capsule materials.[6,17] In most previous studies research focused on quantifying the amount of incorporated capsules versus time, while in this work the acidification and processing time of individual capsules was quantified during uptake. Whereas PSS/PAH and DextS/PLArg capsules are differently processed by cells (nondegradable versus degradable),[22] both are internalized in a similar way and are ultimately located in the lysosomes.[17] It has to be noted that the acidification time and processing time, t_A and $t_{P50\%}$, respectively, depend on the cell line used

(see Figure SI 14). There is also a significant difference between the capsule types (PSS/PAH versus DextS/PLArg, and batch "S" versus "L") regarding t_A, while the values for $t_{P50\%}$ are comparable for both materials. The differences are more distinct for HeLa cells than for phagocytes such as monocyte derived macrophages (MDM) and monocyte derived dendritic cells (MDDC), which are known for rapid phagocytosis of micron sized particles.

In the following we focused on HeLa cells, in order to probe for the dependence of uptake on the stiffness of the capsules (as calibrated in Figure 1c). The data shown in Figure 3a demonstrate that independent of the particle size of the nondegradable PSS/PAH capsules the acidification time t_A

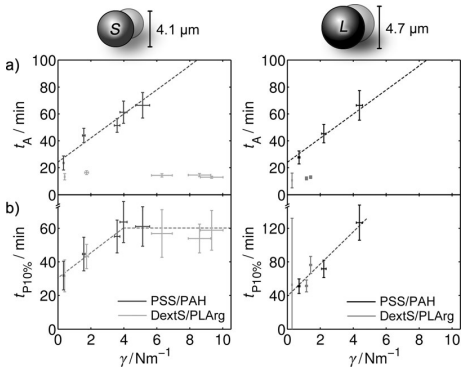

Figure 3. a) Acidification time t_A and b) processing time $t_{P10\%}$ of PSS/PAH and DextS/PLArg capsules with variable number of bilayers N_{bi} and different average diameters as recorded upon incubation with HeLa cells. For each number of bilayers N_{bi} the stiffness γ was taken from Figure 1c and then t_A and $t_{P10\%}$ were plotted against γ. Each data point corresponds to the median t_A or $t_{P10\%}$ value including confidence intervals (y axis) versus the mean stiffness γ value ± standard error (x axis), as obtained from at least 80 capsules (time values) and 40 capsules (stiffness values). The dashed lines are guides to the eye only. Please note that the large error bars in (b) for $t_{P10\%}$ and DextS/PLArg capsules (N_{bi} 1, size "L") result from the fact that these capsules are extremely fragile and thus the determination of t_C (membrane attachment) is challenging.

increases linearly with capsule stiffness γ, whereas for degradable DextS/PLArg capsules there is no such depend ency. In other words, for the degradable capsules the transition from neutral/slightly alkaline extracellular pH to the highly acidic pH of lysosomes is faster. In comparison, for the nondegradable capsules the duration of this process is longer and in addition becomes even slower with increasing capsule stiffness. The dwelling time for the capsules in the cascade of intracellular vesicles during internalization thus may be different for the two types of capsules. In contrast, the processing time $t_{P10\%}$ increases with the stiffness for both capsules, for $\gamma < 5\ N\,m^{-1}$ in a first approximation even linearly (Figure 3b). Hence, $t_{P10\%}$ is universally determined by γ. The acidification time only reflects the duration of the event where the local pH of the particle containing vesicle is lowered, whereas the processing time also comprises the full uptake process. This involves the duration of engulfment by the cellular plasma membrane, pinching off into an endocytic vesicle, and subsequent processing to more acidic environ ments. While t_A is fully derived from a sigmoidal fit to the response function $I_r/I_g(t)$, it is not biased. In contrast, the processing time requires the determination of the time of first contact t_C with the cellular plasma membrane for each capsule. Hence, this parameter is less robust, as t_C is difficult to determine accurately especially if the substrate is very crowded and particles are passed between cells before they are fully endocytosed. From our results we conclude that the uptake itself and the subsequent endosomal trafficking is strongly dependent on the stiffness of the particle, while further processing and acidification is governed mainly by the particle chemistry.

After contact with cells up to their internalization, particles undergo a cascade in which the particle containing intracellular vesicles grow steadily in size, for example by fusion with other (smaller) vesicles.[23] From a mechanistic point of view one can regard this cascade as an intracellular sorting mechanism. Particles are passed from one vesicle to a subsequently larger one by fusion. Upon each fusion step the pH is lowered, which has been observed by fluorescence staining of acidic vesicles while the pH value around the capsule is recorded (see Figure SI 16). In a simplified view one can imagine that upon such sorting the stiffness plays a decisive role. The more flexible the particle, the better it can adopt its shape and allow evolution of vesicular containers. Thus, less deformable, that is, stiffer particles that can follow shape fluctuations to a lesser degree are more prone to delay their processing within this cascade. The same has been observed for particles that are agglomerated and therefore less "flexible" towards well dispersed particles.[23] Our data clearly demonstrate that the transport of particles from the outer cellular membrane to the lysosome is determined by the mechanical properties of the particles, that is, by the stiffness of the particles.

One might speculate that these findings could be recip rocal. This would lead to a situation in which cells with higher deformability would be more efficient at incorporating a given type of particle. For such an analysis the data shown in Figure 3b would need to be related with the stiffness of cells. It is clearly known from the literature that cell stiffness can differ significantly for different cells types. For instance, cancerous cells are softer than their noncancerous counter parts (MCF7 versus MCF10).[24] While measurements of cell stiffness as obtained with optical tweezers indicate the global stiffness of cells in suspension,[24] measurements with AFM indicate the local stiffness of adherent cells.[25,26] The softest part of a cell is the nuclear region and the cell becomes stiffer towards its exterior regions.[26] Concerning the cells as investigated in this study, the following elastic moduli are known from the literature: HeLa: (105 ± 17) kPa[27] and (13 ± 7) kPa,[28] A549: (12 ± 5) kPa,[29] MDM: (44 ± 9) kPa (podo some containing regions) versus (8 ± 2) kPa (podosome free regions)[30] and HUVEC: (6 ± 5) kPa.[26] If we compare these values with our data shown in Figure SI 15 no direct correlation of processing times t_P with the elastic moduli E of cells can be concluded, which is likely because these values cannot be compared directly to those from other studies. For

such data future AFM experiments would be required, in which the elastic moduli are recorded under controlled conditions.

Our study demonstrates how the cellular uptake of particles indeed is controlled by basic physico chemical parameters such as low stiffness. A comprehensive picture about such dependencies will make it possible to synthesize particles with defined cellular interaction patterns. In addition the introduced system might improve our understanding of specific endocytic mechanisms related to lysosomal acidifica tion.

Experimental Section

Polyelectrolyte capsules composed out of different polymers (biode gradable/non biodegradable) and having different stiffnesses (adjusted by varying the number of adsorbed layers) loaded with SNARF 1 were synthesized according to procedures described in the literature.[17,21,22] Force spectroscopy measurements in aqueous solu tion were performed with a Nanowizard I device from JPK Instru ments. The capsule uptake by cells (HeLa, A549, MDM, MDDC, SH SY5Y, and HUVEC) was monitored by confocal laser scanning microscopy (LSM Meta 510, Zeiss) with a temporal resolution of $\Delta t <$ 2 min. Image processing and capsule tracking was performed with Matlab (MathWorks). A detailed description can be found in the Supporting Information.

Received: October 2, 2014
Published online: December 5, 2014

Keywords: biosensors · mechanical properties · nanoparticles · polymeric capsules

[1] S. Parveen, R. Misra, S. K. Sahoo, *Nanomed. Nanotechnol.* **2012**, *8*, 147.
[2] P. Rivera Gil, D. Jimenez de Aberasturi, V. Wulf, B. Pelaz, P. del Pino, Y. Zhao, J. de La Fuente, I. Ruiz de Larramendi, T. Rojo, X. J. Liang, et al., *Acc. Chem. Res.* **2013**, *46*, 743.
[3] a) W. Jiang, B. Y. S. Kim, J. T. Rutka, W. C. W. Chan, *Nat. Nanotechnol.* **2008**, *3*, 145; b) S. L. Zhang, J. Li, G. Lykotrafitis, G. Bao, S. Suresh, *Adv. Mater.* **2009**, *21*, 419.
[4] L. C. Stoehr, E. Gonzalez, A. Stampfl, E. Casals, A. Duschl, V. Puntes, G. J. Oostingh, *Part. Fibre Toxicol.* **2011**, *8*, 3.
[5] a) A. Muñoz Javier, O. Kreft, A. Piera Alberola, C. Kirchner, B. Zebli, A. S. Susha, E. Horn, S. Kempter, A. G. Skirtach, A. L. Rogach, et al., *Small* **2006**, *2*, 394; b) D. Hühn, K. Kantner, C. Geidel, S. Brandholt, I. De Cock, S. J. H. Soenen, P. Rivera Gil, J. M. Montenegro, K. Braeckmans, K. Müllen, et al., *ACS Nano* **2013**, *7*, 3253.
[6] A. Muñoz Javier, O. Kreft, M. Semmling, S. Kempter, A. G. Skirtach, O. Bruns, P. d. Pino, M. F. Bedard, J. Rädler, J. Käs, et al., *Adv. Mater.* **2008**, *20*, 4281.
[7] R. Palankar, B. E. Pinchasik, S. Schmidt, B. G. De Geest, A. Fery, H. Möhwald, A. Skirtach, M. Delcea, *J. Mater. Chem. B* **2013**, *1*, 1175.
[8] X. Yi, X. H. Shi, H. J. Gao, *Phys. Rev. Lett.* **2011**, *107*, 098101.
[9] X. Banquy, F. Suarez, A. Argaw, J. M. Rabanel, P. Grutter, J. F. Bouchard, P. Hildgen, S. Giasson, *Soft Matter* **2009**, *5*, 3984.
[10] W. Liu, X. Zhou, Z. Mao, D. Yu, B. Wang, C. Gao, *Soft Matter* **2012**, *8*, 9235.
[11] J. Borges, J. F. Mano, *Chem. Rev.* **2014**, *114*, 8883.
[12] E. Donath, G. B. Sukhorukov, F. Caruso, S. A. Davis, H. Möhwald, *Angew. Chem. Int. Ed.* **1998**, *37*, 2201; *Angew. Chem.* **1998**, *110*, 2323.
[13] a) H. G. Zhu, E. W. Stein, Z. H. Lu, Y. M. Lvov, M. J. McShane, *Chem. Mater.* **2005**, *17*, 2323; b) C. S. Peyratout, L. Dähne, *Angew. Chem. Int. Ed.* **2004**, *43*, 3762; *Angew. Chem.* **2004**, *116*, 3850.
[14] a) O. Shchepelina, V. Kozlovskaya, E. Kharlampieva, W. Mao, A. Alexeev, V. V. Tsukruk, *Macromol. Rapid Commun.* **2010**, *31*, 2041; b) A. Yashchenok, B. Parakhonskiy, S. Donatan, D. Kohler, A. Skirtach, H. Mohwald, *J. Mater. Chem. B* **2013**, *1*, 1223; c) O. Shimoni, Y. Yan, Y. Wang, F. Caruso, *ACS Nano* **2013**, *7*, 522.
[15] C. Gao, E. Donath, S. Moya, V. Dudnik, H. Mohwald, *Eur. Phys. J. E* **2001**, *5*, 21.
[16] a) F. Dubreuil, N. Elsner, A. Fery, *Eur. Phys. J. E* **2003**, *12*, 215; b) A. Fery, R. Weinkamer, *Polymer* **2007**, *48*, 7221.
[17] L. Kastl, D. Sasse, V. Wulf, R. Hartmann, J. Mircheski, C. Ranke, S. Carregal Romero, J. A. Martínez López, R. Fernández Chacón, W. J. Parak, et al., *ACS Nano* **2013**, *7*, 6605.
[18] U. Reibetanz, M. H. A. Chen, S. Mutukumaraswamy, Z. Y. Liaw, B. H. L. Oh, S. Venkatraman, E. Donath, B. Neu, *Biomacro molecules* **2010**, *11*, 1779.
[19] L. L. del Mercato, A. Z. Abbasi, W. J. Parak, *Small* **2011**, *7*, 351.
[20] O. Kreft, A. Muñoz Javier, G. B. Sukhorukov, W. J. Parak, *J. Mater. Chem.* **2007**, *17*, 4471.
[21] P. Rivera Gil, M. Nazarenus, S. Ashraf, W. J. Parak, *Small* **2012**, *8*, 943.
[22] P. Rivera Gil, S. D. Koker, B. G. De Geest, W. J. Parak, *Nano Lett.* **2009**, *9*, 4398.
[23] C. Brandenberger, C. Mühlfeld, Z. Ali, A. G. Lenz, O. Schmid, W. J. Parak, P. Gehr, B. Rothen Rutishauser, *Small* **2010**, *6*, 1669.
[24] B. Lincoln, H. M. Erickson, S. Schinkinger, F. Wottawah, D. Mitchell, S. Ulvick, C. Bilby, J. Guck, *Cytometry Part A* **2004**, *59A*, 203.
[25] J. Domke, S. Dannöhl, W. J. Parak, O. Müller, W. K. Aicher, M. Radmacher, *Colloids Surf. B* **2000**, *19*, 367.
[26] T. G. Kuznetsova, M. N. Starodubtseva, N. I. Yegorenkov, S. A. Chizhik, R. I. Zhdanov, *Micron* **2007**, *38*, 824.
[27] A. Berquand, A. Holloschi, M. Trendelenburg, P. Kioschis, *Microsc. Today* **2010**, *19*, 34.
[28] J. Ren, S. Yu, N. Gao, Q. Zou, *Phys. Rev. E* **2013**, *88*, 052711.
[29] L. Xiao, M. Tang, Q. Li, A. Zhou, *Anal. Methods* **2013**, *5*, 874.
[30] A. Labernadie, C. Thibault, C. Vieu, I. Maridonneau Parini, G. M. Charrière, *Proc. Natl. Acad. Sci. USA* **2010**, *107*, 21016.

Stiffness-Dependent In Vitro Uptake and Lysosomal Acidification of Colloidal Particles

SUPPORTING INFORMATION

1. Cell Culture

Adenocarcinomic human alveolar basal epithelial (A549) cells and Human cervical cancer (HeLa) cells were maintained in Dulbecco's Modified Eagles Medium (DMEM, Sigma-Aldrich, Germany, #D6546) with 4.5 g L^{-1} glucose supplemented with 10 % fetal bovine serum (FBS, Biochrom, Germany, #S0615), 1 % penicillin/streptomycin (P/S, Sigma-Aldrich, #P4333) and 2 mM L-glutamine (Sigma-Aldrich, #G7513) at 5 % CO_2 and 37 °C.

Neurons (SH-SY5Y cells) were maintained in Dulbecco's Modified Eagles Medium/Ham's Nutrient Mixture F12 (DMEM/F-12, Sigma-Aldrich, #D6421) supplemented with 15 % FBS, 1 % P/S, and 2 mM L-glutamine at 5 % CO_2 and 37 °C.

Human umbilical vein endothelial cells (HUVECs) were cultured in Endothelial Cell Growth Medium (ECGM, PromoCell, Germany, #C-22010) at 5 % CO_2 and 37 °C.

Monocyte derived macrophages (MDMs) and monocyte derived dendritic cells (MDDCs) were obtained from peripheral blood monocytes following the protocol from Sallusto et al.[1]. Briefly, monocytes were isolated from buffy coats (blood donation service Universitätsklinikum Giessen Marburg, Giessen, Germany) by using density gradient centrifugation in Ficoll-Paque (GE Healthcare, Germany, #17-1440-02) and matured in RPMI 1640 (Sigma-Aldrich, #R0883) supplemented with 5% heat-inactivated, pooled) human serum (blood donation service, Zentrum für Klinische Transfusionsmedizin, Tübingen, Germany), 1 % P/S and 2 mM L-glutamine at 5 % CO_2 and 37 °C. Monocytes were matured in the presence of 34 ng mL^{-1} human IL-4 (New England Biolabs, Germany, #8919SC) and 50 ng mL^{-1} human GM-CSF (New England Biolabs, #8922SF) for 7-9 days to obtain MDDCs, whereas for the generation of MDMs no additional supplements were used.

2. Polyelectrolyte multilayer capsules

2.1. Synthesis

pH-sensitive capsules with a different number of layers to vary capsule elasticity (1, 2, 4, 6, 8, 12 and 16 bilayers, N_{bi}) were synthesized with 2 frequently

used polymer systems (non-degradable polymers: poly(sodium 4-styrenesulfonate), $M_w \approx 70$ kDa, PSS and poly(allylamine hydrochloride), $M_w \approx 56$ kDa, PAH, degradable polymers: dextran sulfate, $M_w \approx 40$ kDa, DextS and poly-L-arginine, $M_w \approx 15$-70 kDa, PLArg). Based on layer-by-layer assembly polyelectrolytes of alternating charge were adsorbed around sacrificial template cores according to published protocols.[2, 3] The pH-sensitivity was achieved by embedding SNARF-1[4]-labeled dextran into the cavity of the capsules following the co-precipitation method.[5] For all capsules of the same class of polyelectrolytes but diffe ent wall thickness core templates from the same batch (having all the same size distribution) were used to minimize artifacts due to different sizes. For each class of polyelectrolytes two different batches "S" & "L" with different size ("S": smaller, "L": larger) and unequal mechanical properties were prepared to cover a broad range of elasticity values, cf. Figure SI-5).

3.1.1. Chemicals

PSS ($M_w \approx 70$ kDa, #243051), PAH ($M_w \approx 56$ kDa, #283223), DextS ($M_w \approx 40$ kDa #42867), PLArg ($M_w \approx 15$-70 kDa, #P7762), calcium chloride dehydrate ($CaCl_2$, #223506), sodium carbonate (Na_2CO_3, #S7795) and ethylenediaminetetraacetic acid disodium salt dihydrate (EDTA disodium salt, #E5134) were purchased fr n Sigma-Aldrich (Germany), SNARF-1 dextran ($M_w \approx 70$ kDa, #D3304) from life technologies (USA) and sodium chloride (NaCl, #HN00.2) was tained from Roth (Karlsruhe, Germany). Deioniz l water (ddH_2O, MilliQ® Academic, Millipore, Billerica, USA) with a resistance greater than 18.2 MΩ c $^{-1}$ was used for all experiments.

3.1.2. Procedure

$CaCO_3$ microparticles were prepared at room temperature (RT) from solutions of $CaCl_2$ and Na_2CO_3 under vigorous stirring in the pr ence of SNARF-1 dextran. 1 mL of aqueous solutio of $CaCl_2$ (0.33 M), 1.4 mL SNARF-1 dextran 70 kDa (0.5 mg mL^{-1}) were mixed in a glass vial. During magnetic stirring (1000 rpm) 1 mL of aqueous solution of Na_2CO_3 (0.33 M) solution was added qu kly. After 30 s the stirrer was turned off and particle growth was stopped after additional 2 min by centrifugation. The particles were washed three times with ddH_2O and then directly used for the layer-by-layer assembly of polyelectrolytes.

Biodegradable capsules w re obtained by depositing alternating layers of negatively charged DextS (2 mg mL^{-1} in 0.5 M NaCl) and positively charged PLArg (2 mg mL^{-1} in 0.5 M NaCl onto the charged microparticles as described previously.[2, 6] For coating with each layer the microparticles were suspended in 1 mL of polyelectrolyte solution. The dissolution of the cores was carried out by Ca^{2+} ion complexion with EDTA (1 mL, 0.2 M, pH 6.5).

Non-biodegradable capsules were obtained by using PSS as negatively and PAH as positively charged polymers.

Samples carrying 1, 2, 4, 6 and 8 bilayers were synthesized in both cases.

2.2. Characterization

The size distributions of the polyelectrolyte multilayer (PEM) capsules were derived from confocal laser scanning fluorescence (cLSM) micrographs (cf. Figure SI-1). The shell-thickness and structure were examined by transmission- and scanning electron microscopy (TEM and SEM), while the mechanical properties were investigated by atomic force microscopy (AFM) mea rements.

3.1.3. Size distribution

Size distributions (cf. Figure SI-2) were derived from fluorescent micrographs of PEM capsules (cf. Figure SI-1) taken at pH 7 in DMEM. For details regarding the image acquisition we refer to § 3.1. Capsules being in focus were automatically segmented and quantified with respect to size (we refer to § 3.2 for details). More than 200 capsules were analyzed in each case.

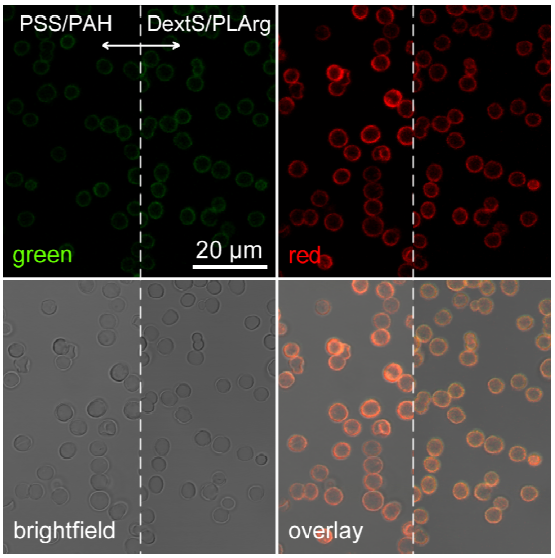

Figure SI-1 – Fluorescent micrographs of pH-sensitive microcapsules. *The fluorescence images of PSS/PAH (left) and DextS/PLArg (right) capsules (N_{bi} = 4, size "L") as recorded between 560 and 615 nm ("green" cannel - in false colors) and > 615 nm ("red" channel), brightfield*

images, and the corresponding overlays are shown. Images were taken at pH 7 in DMEM. It can be seen that most of the SNARF-dextran is attached to the inner membrane of the capsules instead of being homogeneously distributed in the capsule cavity.[7]

3.1.4. Shell thickness

The shell thickness was determined from TEM images of 70 nm thin capsule cross-sections (cf. Figure SI-3) and derived fr n AFM height-measurements of dried (collapsed) capsules (cf. Figure SI-4).

I) obtained from ultrathin cross-sections

PEM capsules were embedded in resin as described by Pretzl et al.[8]. The sectioning was performed with an ultramicrotome (EM UC7, Leica, Germany) and the sections were imaged using a JEM-3010 (Jeol, Japan). The shell thick ess was derived by extracting cross-sectional intensity profiles that were analyzed with Matlab (MathWorks, USA).

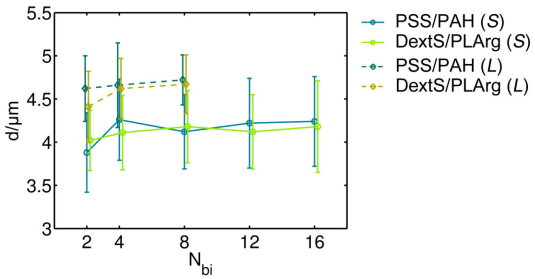

"S" (small) *"L"* (large)

	d/µm	
N_{bi}	PSS/ PAH	DextS/ PLArg
2	3.88 ± 0.46	4.02 ± 0.35
4	4.26 ± 0.47	4.11 ± 0.43
8	4.12 ± 0.43	4.18 ± 0.42
12	4.22 ± 0.52	4.12 ± 0.43
16	4.24 ± 0.52	4.18 ± 0.53

	d/µm	
N_{bi}	PSS/ ᵎAH	DextS/ PLArg
2	4.62 ± 0.38	4.41 ± 0.41
4	4.66 ± 0.49	4.62 ± 0.35
8	4.72 ± 0.29	4.67 ± 0.34

Figure SI-2 – Size distribution of m rocapsules. *The size distributions of the capsule diameters d were obtained from fluorescent micrographs of capsules with N_{bi} = 2-16 bilayers at pH 7 in DMEM.*

The capsule wall can be segmented into two distinct structures (Figure SI-3): The outer membrane (d_1) is most likely the polyelectro ᵎte shell, while the porous structure (d_2) is SNARF- ɔxtran adhering to the inner surface of the polyelectrolyte shell. The thickness of d_2 increases with increasing thickness of d_1. We assume that during dissolution of the $CaCO_3$-templates with EDTA in the case of thinner capsules with less bilayers the leakage of SNARF-dextran out of the capsules is higher due to higher porosity of the shell. Shell-attached dextran might influence the capsule stiffness. As the fluorescence which is attributed to SNARF-labeled extran is also higher in the capsule shell in fluorescence micrographs in aqueous solution (cf. Figure SI-1) the observed phenomenon is not an artifact caused by the ethanol-drying of the capsules during sample preparation for embedding into epoxy resin.

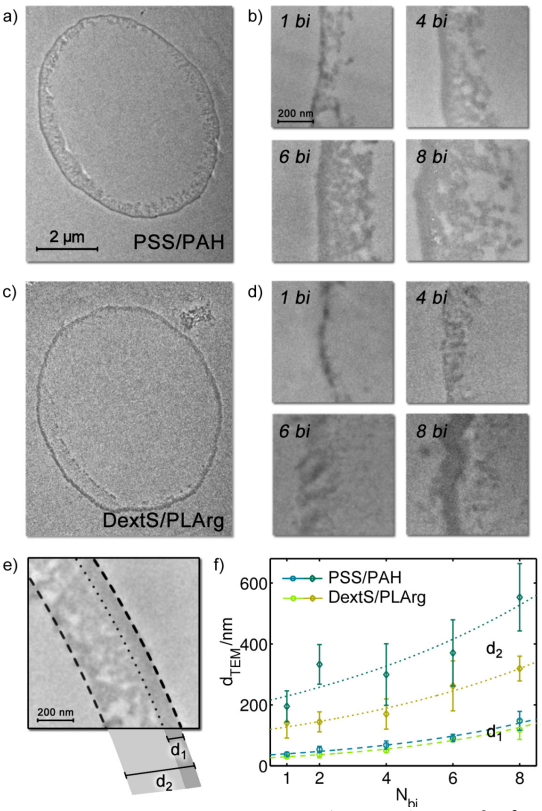

Figure SI-3 – Shell thickness (TEM). *a) TEM micrograph of a 70 nm thick cross-section of a PSS/PAH capsule composed of 4 bilayers (N_{bi} = 4, size "L") embedded in epoxy resin. b) Cross-section of PSS/PAH-capsule membranes for N_{bi} = 1, 4, 6, and 8 bilayers in higher magnification. c) TEM micrograph of DextS/PLArg capsules with 4 bilayers. d) Cross-section of DextS/PLArg-capsule membranes for N_{bi} = 1, 4, 6, and 8 bilayers in higher magnification. e) The thickness of only the outer layer d_1 which is supposed to be composed of polyelectrolytes measured from TEM images and d_2 included also a porous structure which is probably SNARF adhering to the inner surface of the polyelectrolyte shell. f) Thickness values for d_1 and d_2 for non-biodegradable PSS/PAH and biodegradable DextS/PLArg capsules measured for N_{bi} = 1-8 ize "L").*

II) derived from collapsed capsules by atomic force microscopy (AFM)

AFM imaging of collapsed capsules was carried out in intermittent contact mode at the MFP-3D

(Asylum Research, Santa Barbar CA, USA) which was combined with the optical microscope Axiovert 200 (Zeiss, Jena, Germany). Silic nitride cantilevers (NSC 36, no Al coating, MikroMasch, Tallinn, Estonia) with a nominal spring constant of 0.6 Nm^{-1} were used. Measurements were performed in the MFP liquid cell filled with deionized water (MilliQ® Academic, Millipore, Billerica, USA). To ensure adhesion of the capsules the glass substrate was coated with one bilayer of polyethylenimine (PEI) and PSS. Collapse of the capsules was achieved through drying the capsules directly on the substrate. More rigid capsules (4 to 8 bilayers) were treated with ultrasound for 1 min in an ultrasonic bath prio to drying.

The thickness of the capsules measured by AFM (d_{AFM}) (cf. Figure SI-4), is between d_1 and d_2 (cf. Figure SI-3). SNARF-dextran present in d_2 might be compressed during the drying process of the capsules.

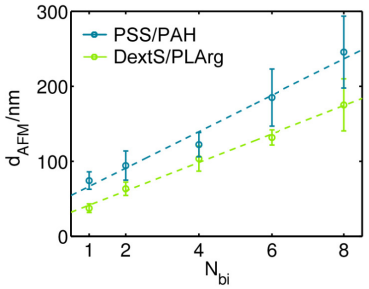

Figure SI-4 – Shell thickness (AFM). *Shell thickness of PSS/PAH and DextS/PLArg capsules, respectively, composed of 1-8 bilayers (size "L") obtained from AFM measurements.*

3.1.5. Mechanical properties

Force spectroscopy measurements were carried out at the Nanowizard I® (JPK nstruments, Berlin, Germany) which was combined with the inverted optical microscope Axiovert 200 (Zeiss, Jena, Germany). As a probe we used tip-less silicon nitride cantilevers (NSC 12, no Al coating, MikroMasch, Tallinn, Estonia) with nominal spring constants of 0.65 and 14 Nm^{-1}. These cantilevers were modified by gluing a glass sphere of colloidal dimensions (diameter 30-40 µm, Polysciences Europe GmbH, Eppelheim, Germany) with two component epoxy glue (UHU Endfest 300, UHU GmbH & Co. KG, Bühl, Germany) under their very front (colloidal probe). The exact spring consta of the employed cantilevers was determined prior to any modification from their thermal vibration spect um (thermal noise method[9]). Before probing the microcapsules, the cantilever's optical lever sensitivity was determined by pressing the cantilever against the non-deformable glass substrate. All measurements were performed in home-built Petri dishes (diameter 2 cm, height 0.5 cm) filled with ddH_2O. To promote capsule adhesion the glass bottom of the dishes were coated with one layer of each PEI and PSS. The stiffness of the capsules' shell was obtained as the slope of the linear part of the recorded force vs. deformation curves for small deformations in the order o the shell thickness. A representative force-deformation characteristic is displayed in Figure SI-6. Obtained results are shown in Figure SI-5.

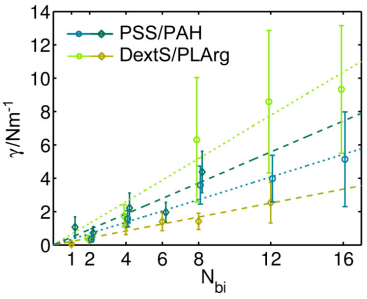

Figure SI-5 – Stiffness γ of PSS/PAH and DextS/PLArg capsules, respectively *(size "S": dashed line, size "L": dotted line).*

The leakage of SNARF-dextran out of the capsules during dissolution of the sacrificial core-templates[10] strongly depended on t ɜ thickness of the polyelectrolyte shell and decreased with increasing numbers of polymer layers. As the encapsulated SNARF-dextran was attached rather to the inner membrane of the capsules instead of being homogeneously distributed ɜide the cavities[7] (cf. Figure SI-1 and Figure SI-3) it might have also influenced the stiffness of the capsules.

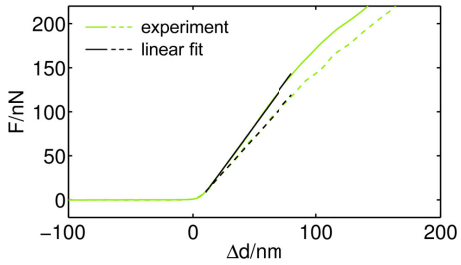

Figure SI-6 – Representative force-deformation characteristics *of 4-bilayer DextS/PLArg microcapsules and linear fits in the small deformation regime (deformation: Δd) yielding the capsule's stiffness (size "S": solid line, size "L": dashed line).*

3.1.6. pH-response

The fluorescence response of the SNARF-capsules to changes in pH was measured by adding a drop containing capsules to cell culture medium samples with differently adjusted pH-values (cf. Figure 1b, main manuscript). The fluorescent readout was

measured using confocal laser scanning microscopy as described in § 3.1 with the difference that the capsules in pH-adjusted cell media were imaged on top of a conventional glass slide. For each pH-value approximately 200 capsules were imaged to obtain the average red/green ratio at a specific ionic concentration. We note again that in the images the fluorescence is displayed in false colors.

3.1.7. Zeta-potential

The Zeta potential (ζ) was measured in ddH_2O by dynamic light scattering (DLS) using a Zetasizer Nano ZS (Malvern Instruments, UK). Biodegradable DextS/PLArg PEM capsules turned out to carry a higher positive potential than their non-biodegradable counterparts made from PSS/PAH (cf. Figure SI-7).

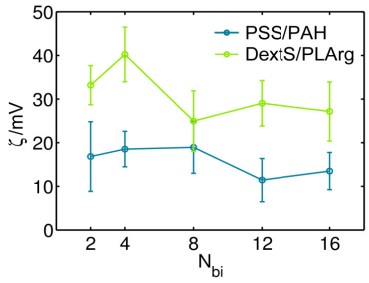

***Figure SI-7 – Zeta-potential (ζ) of PSS/PAH and DextS/PLArg capsules**, respectively, composed of 2-16 bilayers (size "S") derived from DLS measurements.*

3. Uptake studies

For tracking the internalization of the different PEM capsule systems 15.000 cells/well were seeded into each well of an 8-well µ-slide (Ibidi, Germany, #80826), whereby the growth area of each well was 1 cm^2, filled with 300 µL medium. Imaging was performed on the next day.

3.1. Live confocal fluorescence microscopy

The capsule uptake was studied using a confocal laser-scanning fluorescence microscope (CLSM 510 Meta, Zeiss) equipped with a portable incubator (Pecon, Germany) to maintain the µ-slides at 37 °C with 5% CO_2. Prior to image acquisition approximately 7 capsules/cell were added and time lapse image series were acquired using a Plan-Apochromat 63x/1.40 Oil DIC M27 objective. SNARF-1 was excited at 543 nm (with a HeNe-laser) and its fluorescence was recorded between 560 and 615 nm ("green" channel, false color) and > 560 nm ("red" channel). To minimize bleaching the acquisition parameters were tuned to detect fluorescence at very low excitation power. The lateral sampling frequency was set to 1.32 µm while the temporal resolution was set to 45-150 s, depending on the acidification rate during uptake of each cell type. The absolute axial position of the boundary layer µ-dish substrate/medium was determined by detecting the z-position of the increased level of scattered photons in this boundary layer. Two images of the same lateral position were acquired: To catch internalized capsules, one slice was imaged 2.2 µm above the substrate which was typically located in the cell interior. Another slice was obtained 3 µm higher to resolve capsules located on top of cells. The pinhole of the confocal system was adjusted to image 2 µm thick sections in both cases. This alignment was recovered before each time point by a software-based autofocus routine. After acquisition the dimension was reduced by calculating the projection along the z-axis of both slices for further analysis.

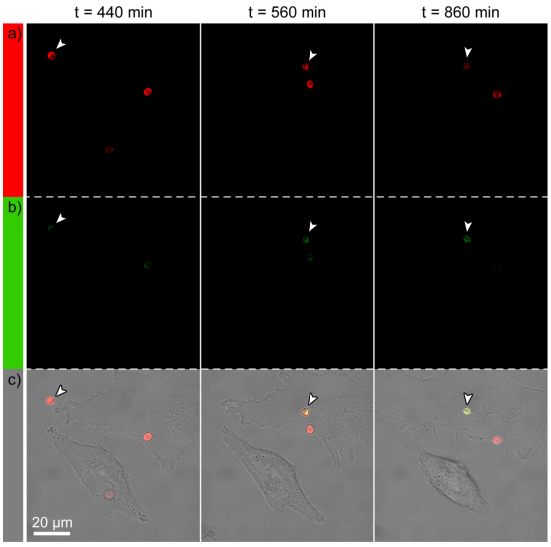

***Figure SI-8 – Time lapse image series of capsule uptake.** Three representative time points of a typical image series tracing PSS/PAH capsules (N_{bi} = 8, size "L") during their uptake by HeLa cells are displayed. a) shows the fluorescence of the SNARF-filled capsules in the red channel (> 615 nm), b) shows their fluorescence in the green channel (560-615 nm), and c) shows the overlay of both channels with the corresponding brightfield image. The white arrows highlight a capsule which shows a transition from red to green, indicating its transfer into an acidic lysosomal compartment.*

3.2. Image processing

For automated image processing, capsule segmentation, tracking and visualization a toolbox was developed using Matlab (MathWorks, USA). In the following the workflow (Figure SI-9) is described briefly. First, photon shot noise in the red and green channel was reduced by median-filtering and the background was completely removed by defining a threshold (Figure SI-9b.1). As a microcapsule

typically appears as a slightly filled circle in a confocal fluorescence image a modified Hough transformation[11] was computed to identify all capsules positions and their corresponding radii automatically to create masks for further intensity value readout (Figure SI-9). It turned out that in the case of several clustered capsules or image regions with high capsule density this segmentation method performed better than object identification by thresholding strategies. Each pixel was considered as the origin of a parameterization of a circle with similar radius as the structure to be found. The sum of all pixel intensities which were hit by the circle was calculated and assigned to the rigin pixel of the circle. Basically each pixel was tested if its position was likely to be the origin of a ci le of given radius. By doing so the center positions of all circles were identified. A classical Hough transform does not yield the radius of the round features it is finding. To identify the position and the dimension of each capsule a parameterization of a do ut-shaped structure with a shell thickness of 0.64 µm vas used. For each pixel the radius r of this structure was varied within given boundaries (derived from th size distribution of the capsules), and the underlying pixel intensities were summed up as a function of r. The position of the first maximum of this function was identified as the capsule radius, and the corresponding maximum was assigned to the initial pixel. For each pixel in the original image a number represe ing the probability to be the center of a capsule with radius r was obtained. The local maxima in this probability depiction were identified as the centers of all capsules being present in the current frame. To reduce computational time the transformation was only calculated for image regions in w ich capsules were present. These regions were obtained by a morphological area opening to remove structures smaller than the capsules, morphological closing with a disk-shaped structuring element to fill dark gaps in the capsule walls, and finished by filling all holes in the image (i.e. filling "empty" capsules). The local maxima (i.e. capsule center posit ons) generated by the modified Hough transform w re emphasized by image dilation and stored. Final the segmentation performance was evaluated for each detected capsule to reduce artifacts. The coordinates and the radius (x position y position, radius) were used to create a mask for each capsule (ROI) in the red and green channel, respectively. Within this mask the average pixel intensity ratio red/green (I_r/I_g) wa :alculated from the noise-corrected raw data (Figure SI-9b.1) indicating the local pH. To obtain the progression of I_r/I_g versus time for each capsule during uptake and cellular trafficking (further referred to as "trajectory") a capsule-tracking routine was applied, which was inspired by the particle tracking algorithms developed by John Crocker et al.[12], and provided for Matlab by Danial Blair and Eric Dufresne. The described procedure resulted in almost gap-less two-dimensional capsule trajectories. Finally each trajectory was checked manually and errone us lateral displacements where corrected by adjusting the capsules ROIs if needed.

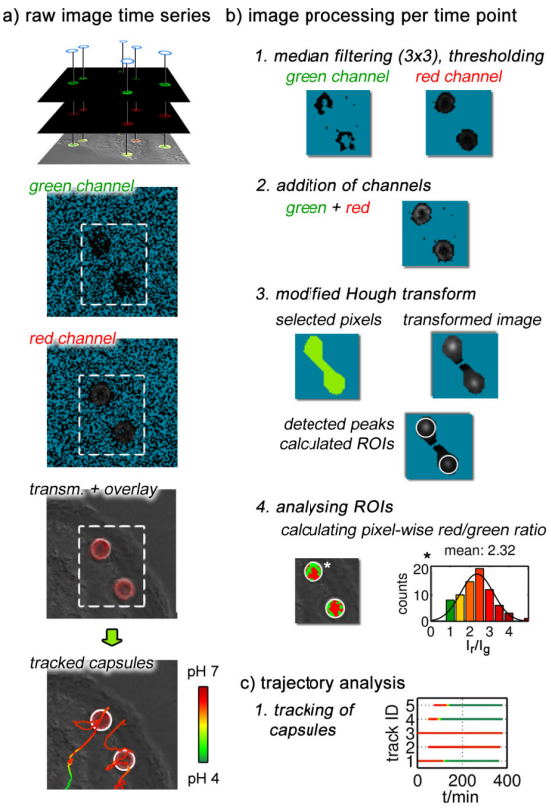

Figure SI-9 – Overview over the image processing workflow. *Time lapse image series of cellular capsule uptake were acquired with an automated confocal fluorescence microscope. To derive capsule-trajectories the indicated image processing routines were applied. Pixels with zero intensity are colored in blue. For calculating the per-pixel red/green ratio only pixels with intensity values above a certain threshold in both channels were considered (colored in green in b.4).*

3.3. Trajectory processing

For illustration a typical trajectory is shown in Figure 2 (main manuscript). From each trajectory the processing times $t_{P10\%}$ i.e. $t_{P50\%}$, respectively, and the acidification time t_A were derived. The processing time is the time from the first contact t_C (membrane-attachment, as visible from the brightfield images) of the capsule with the cell, which is taking up the microcapsule until its acidification. The acidification

time describes the duration of aci fication from high to low pH following the sigmoidal curve. Consequently, the experimental data were fitted with the following curve: $(I_r/I_g)(t) = (R_a-R_b)/(1+\exp((t-t_{50\%})/\Delta t))+R_b$.

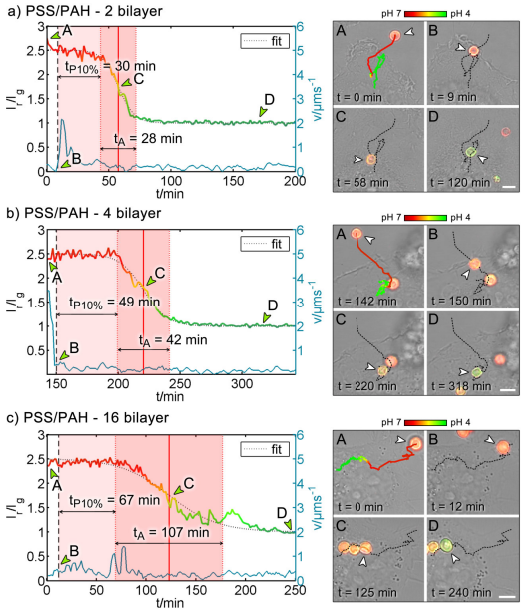

Figure SI-10 – Example trajectories of PSS/PAH capsules of different thickness in HeLa cells. *On the left side typical SNARF-response curves of 2, 4 and 16 bilayer thick (cf. a, b and c) non-biodegradable PSS/PAH capsules (type "S") are shown during uptake by HeLa cells. $I_r/I_g \approx 2.5$ corresponds to neutral pH while capsules with $I_r/I_g \approx 1$ are located inside acidic vesicles. On the right side corresponding microscopic images are shown for the time points A-D marked with a green arrow inside the graph. The respective tracked capsule is highlighted with a white arrow. The scale bar length is 5 µm.*

Hereby, the acidification time is defined as $\Delta t_A = t_{90\%}-t_{10\%} = 2\Delta t \cdot \ln(9)$. The time points $t_{90\%}$ and $t_{10\%}$ are derived from the equations $(I_r/I_g)(t_{10\%}) = 0.9\cdot(R_a-R_b)+R_b$ and $(I_r/I_g)(t_{90\%}) = 0.1\cdot(R_a-R_b)+R_b$. In other words: Δt_A is the duration of the acidification process of a single particle, cf. Figure 2b (main manuscript). The processing times for different endpoints $t_{P10\%}$ and $t_{P50\%}$ are derived from these data as $t_{P10\%} = t_{10\%}-t_C$ and $t_{P50\%} = t_{50\%}-t_C$. In this way each uptake trajectory is defined by two quantitative parameters: t_A and $t_{P10\%}$ or $t_{P50\%}$, respectively.

4. Elasticity dependent intracellular processing

In this section additional fi ıres are presented which show the influence of the capsule shell thickness and the used polyelectrolytes (non-biodegradable PSS/PAH vs. biodegradable DextS/PLArg) on the endocytic processing during uptake by HeLa cells. In Figure SI-10 and Figure SI-11 typical trajectories from capsules of different shell thickness (N_{bi} = 2, 4 and 16, size "S") were selected and the pH-response during nternalization is plotted. For each trajectory the duration of acidification is displayed (acdidification tim t_A) and the processing time is shown ($t_{P10\%}$). Typical events are marked in the pH-response curve (A: first appearance of capsule, B: first contact with cell which internalizes the capsules later, C: partial acidification, D: capsule is fully acidified) and the corresponding microscopic images are given showing the particular point in time. In Figure SI-12, Figure SI-13 and Figure SI-14 the acidification times t_A and the processing times $t_{P10\%}$ and $t_{P50\%}$ are shown and correlated with the particle stiffness γ.

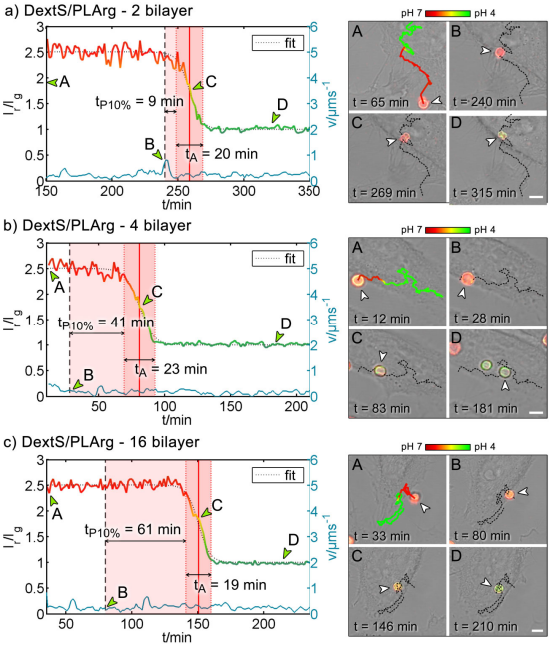

Figure SI-11 – Example trajectories of DextS/PLArg capsules of different thickness in HeLa cells. *On the left side typical SNARF-response curves of 2, 4 and 16 bilayer thick (cf. a, b and c) biodegradable DextS/PLArg capsules (type "S") are shown during uptake by HeLa cells. $I_r/I_g \approx 2.5$ corresponds to neutral pH while capsules with $I_r/I_g \approx 1$ are located inside acidic vesicles. On the right side corresponding microscopic images are shown for the time points A-D marked with a green arrow inside the graph. The respective tracked capsule is highlighted with a white arrow. The scale bar length is 5 µm.*

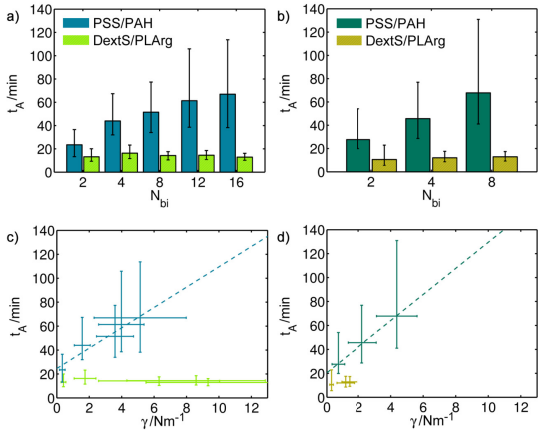

Figure SI-12 – Acidification time t_A for capsules af different stiffness in HeLa cells. *The time period t_A is reflecting the duration of acidification during endocytosis for non-biodegradable PSS/PAH and biodegradable DextS/PLArg capsules of batch "S" (a) and batch "L" (b). In c)-d) the obtained t_A-values are displayed versus the average stiffness γ of the respective capsule type. Each data point corresponds to the median processing time t_A value ± upper and lower quartile (y-axis) versus the mean stiffness γ value ± standard deviation (x-axis), as obtained from at least 80 capsules (time values) and 40 capsules (stiffness values).*

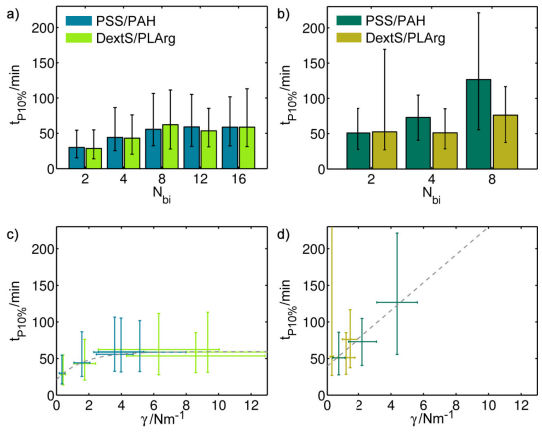

Figure SI-13 – Processing time $t_{P10\%}$ for capsules af different stiffness in HeLa cells. *The time period $t_{P10\%}$ is measured between first contact and the beginning of the acidification process upon internalization of non-biodegradable PSS/PAH and biodegradable DextS/PLArg capsules of batch "S" (a) and batch "L" (b). In c)-d) the obtained $t_{P10\%}$-values are displayed versus the average stiffness γ of the respective capsule type. Each data point corresponds to the median processing time $t_{P10\%}$ value ± upper and lower quartile (y-axis) versus the mean stiffness γ value ± standard deviation (x-axis), as obtained from at least 80 capsules (time values) and 40 capsules (stiffness values).*

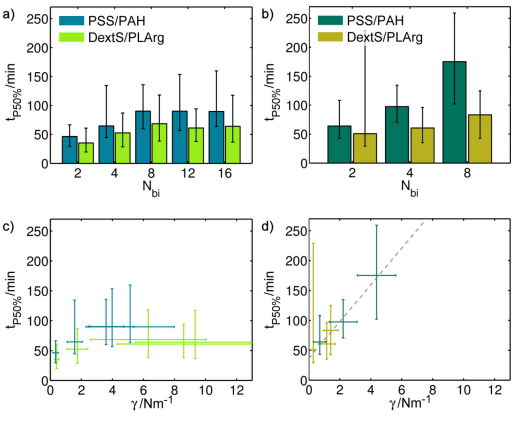

Figure SI-14 – Processing time $t_{P50\%}$ for capsules af different stiffness in HeLa cells. *The time period $t_{P50\%}$ is measured between first contact and 50%-acidification during internalization of non-biodegradable PSS/PAH and biodegradable DextS/PLArg capsules of batch "S" (a) and batch "L" (b). In c)-d) the obtained $t_{P50\%}$-values are displayed versus the average stiffness γ of the respective capsule type. Each data point corresponds to the median processing time $t_{P50\%}$ value ± upper and lower quartile (y-axis) versus the mean stiffness γ value ± standard deviation (x-axis), as obtained from at lea 80 capsules (time values) and 40 capsules (stiffness values).*

4.1. Acidification and processing in different types of cells

Capsule acidification and processing was investigated in various types of cells including cell lines and primary cells such as HeLa cells, A549 cells, MDMs, MDDCs, SH-SY5Y neurons and HUVECs. Biodegradable and non-biodegradable capsules with 4 bilayers of type "L" were used. The corresponding data is s own in Figure SI-15.

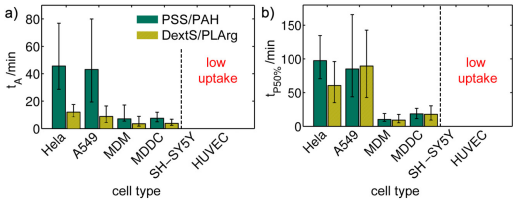

Figure SI-15 – Acidification and processing in different types of cells. *The acidification time t_A (a), and processing time $t_{P50\%}$ (b) of PSS/PAH and DextS/PLArg capsules (N_{bi} = 4, size "L") as recorded upon incubation with different types of cells. For neurons (SH-SY5Y) and human umbilical vein endothelial cells (HUVECs) under the present conditions only few uptake events were observed. Each data point corresponds to the median value ± upper and lower quartile.*

5. Distribution of LAMP1 during processing and acidification

Lysosomal associated protein 1 (LAMP1) is a glycoprotein, mostly situated at the luminar membrane of late endosomes and lysoso ıes and commonly used

as a marker for acidic vesicles.[9, 13] To correlate the trafficking of acidic vesicles during capsule uptake HeLa were transfected to express LAMP1 labeled with green fluorescent protein (GFP) to allow live-imaging of lysosomes and the capsule acidification in parallel.

For the experiment approximately 5,000 cells per well were seeded into an 8-well Ibidi µ-slide. After 12 hours 2 µL of CellLight Lysos nes-GFP BacMam 2.0 (life technologies, #C10596) were added corresponding to 20 virus particles per cell. After 24 h capsule uptake experiments were performed as described in § 3. In addition to the capsule fluorescence GFP was excited at 488 nm using an Argon-laser and emitted photons were recorded between 505 and 550 nm. For each time point the intensity of LAMP1-GFP was measured along the capsule area to detect the amount of LAMP1 being incorporated into the endocytic vesicle containing the internalized capsule. In addition the fusion frequency of LAMP1-positive vesicles was monitored. Fluorescent micrographs and a corresponding trajectory are shown in Figure SI-16.

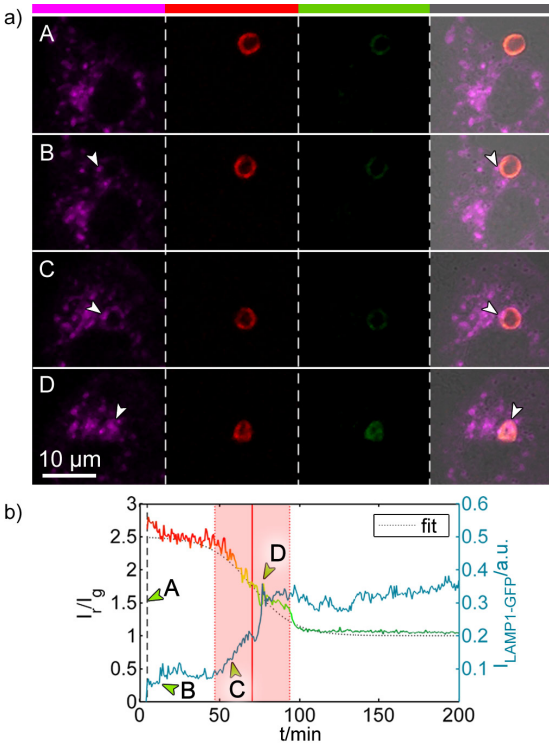

Figure SI-16 – Distribution of LAMP-1 during capsule uptake in HeLa cells. *In a) a time lapse recording is displayed showing the fluorescent signal of LAMP1-GFP (magenta), the red and green fluorescence channel of the capsule (N_{bi} = 4, size "L") pH-readout and an overlay of all fluorescent channels with a brightfield image. In b) for each image the ratio of red-to-green fluorescence I_r/I_g of the capsule has been determined and is plotted versus the incubation time t. The time points corresponding to the images shown in a) are labeled as A - D. A ratio of $I_r/I_g \approx 2.5$ corresponds to a pH value of 7.4, while $I_r/I_g \approx 1$ corresponds to local pH values below 4.5, cf. Figure 1b (main manuscript). In addition the mean fluorescence of LAMP1-GFP ($I_{LAMP1-GFP}$) over the capsule area is plotted in blue.*

Immediately after capsule uptake no fluorescent signal of LAMP1-GFP could be associated with the capsules (cf. Figure SI-16a). After several minutes of incubation the first fusion of AMP1-positive vesicles with the capsule-containing vesicles could be observed (cf. Figure SI-16b). With increasing fusion frequency the local pH around the capsules dropped (cf. Figure SI-16c) and th mean fluorescence of LAMP1-GFP ($I_{LAMP1-GFP}$) associated with the endocytic vesicles in which capsules were contained continued to rise until both measures (pH and LAMP1-GFP-fluorescence) reached a plateau and kept constant.

We speculate that the fusion of LAMP1-positive vesicles which should be acidic mediate the decrease in pH of the larger capsule-containing vesicles.

6. Integrity-investigations of capsules

To investigate possible reasons for the fast elasticity-independent acidification of bio-degradable DextS/PLArg capsules the tegrity within the first 46 h upon contact with cells was examined. To be able to spot capsule fragmentation or release of cargo the conjugate DQ-ovalbumin (DQ-OVA) was encapsulated into 2-16 bilayer thick capsules being either composed out of PS /PAH or DextS/PLArg following the protocol described by Rivera Gil et al.[2] DQ-OVA is composed out of BODIPY dye-saturated protein ovalbumin. Due to the close proximity of the dye molecules the green fluorescence of the BODIPY dye is almost completely self-quenched[14] and forming dye excimers are showing a light red fluorescence signal. Upon enzymatic degradation inside cells the fluorescence is dramatically increased independent on pH. Due to these properties internalized capsules filled ith DQ-OVA can be easily recognized (bright green fluorescence) and potential released fragments of DQ-OVA or capsule disruption becomes visible.[2]

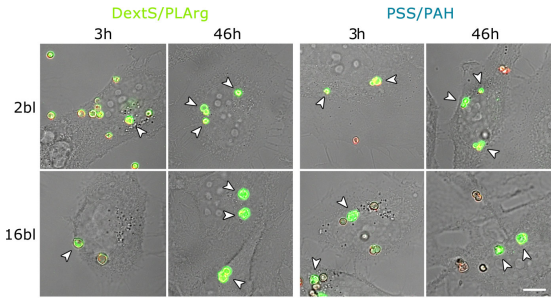

Figure SI-17 – Probing proteolytic degradation of microcapsules. *DQ-OVA-filled microcapsules show an increase in green fluorescence after internalization by HeLa cells (indicated by white arrows) independent on the number of bilayers (N_{bi} = 2 and 16). Even after 46 h no fragmentation occurs. The scale bar corresponds to 10 µm.*

For the experiment DQ-OVA loaded capsules with 2-16 bilayers were prepared as described in § 3.1.2 replacing SNARF-1 by DQ-OVA (1.25 mg mL^{-1}, life technologies, #D12053). Approximately 5,000 cells per well were seeded into an 8-well Ibidi µ-slide. After attachment 7.5 capsules/cell were added and CLSM images were taken after 3 h, 24 h and 46 h. DQ-OVA was exited at 488 nm (emission: 520/30 nm, "green channel") and 543 nm (emission: LP 650, "red channel"). Fluorescent micrographs are shown in Figure SI-17.

In agreement with already published data[2] the cargo of non-biodegradable PSS/PAH capsules is not completely protected by proteolytic degradation, visible as increased green fluorescence inside the cavity of internalized capsules, even for N_{bi} = 16. For bio-degradable DextS/PLArg capsules the increase is much stronger, though. Within the first 46 h no visible evidence was found that either high amount of DQ-OVA was released or capsules became fragmented neither for PSS/PAH capsules nor for DextS/PLArg ones. This is in agreement with the study of Rivera Gil et al.[2] who observed a spreading into the cytoplasm of the cells after 3-5 days.

7. References

[1] F. Sallusto, A. Lanzavecchia, *J. Exp. Med.* **1994**, *179*, 1109.
[2] P. Rivera Gil, S. D. Koker, B. G. De Geest, W. J. Parak, *Nano Lett.* **2009**, *9*, 43[illegible]3.
[3] S. De Koker, R. Hoogenboom, B. G. De Geest, *Chem. Soc. Rev.* **2012**, *41*, 2867.
[4] J. E. Whitaker, R. P. Haugland, F. G. Prendergast, *Anal. Biochem.* **1991**, *194*, 330.
[5] A. P. Petrov, D. V. Volodkin, G. B. Sukhorukov, *Biotechnol. Prog.* **2005**, *21*, 918.
[6] a) B. G. De Geest, R. E. Vandenbroucke, A. M. Guenther, G. B. Sukhorukov, W. E. Hennink, N. N. Sanders, J. Demeester, S. C. d. Smedt, *Adv. Mater.* **2006**, *18*, 1005; b) S. De Koker, B. G. De Geest, C. Cuvelier, L. Ferdinande, V. Deckers, W. E. Hennink, S. De Smedt, N. Mertens, *Adv. Funct. Mater.* **2007**, *17*, 3754; c) S. Carregal-Romero, M. Ochs, P. Rivera Gil, C. Ganas, A. M. Pavlov, G. B. Sukhorukov, W. J. Parak, *J. Control. Release* **2012**, *159*, 120.
[7] L. L. del Mercato, A. Z. Abbasi, W. J. Parak, *Small* **2011**, *7*, 351.
[8] M. Pretzl, M. Neubauer, N. Tekaat, C. Kunert, C. Kuttner, G. Leon, D. Berthier, P. Erni, L. Ouali, A. Fery, *ACS Appl. Mater. Interfaces* **2012**, *4*, 2940.
[9] J. L. Hutter, J. Bechhoefer, *Rev. Sci. Instrum.* **1993**, *64*, 1868.
[10] O. Kreft, A. Muñoz Javier, G. B. Sukhorukov, W. J. Parak, *J. Mater. Chem.* **2007**, *17*, 4471.
[11] R. C. W. R. E. Gonzalez, *Digital image processing*, Pearson Prentice Hall, New Jersey, **2008**.
[12] J. C. Crocker, D. G. Grier, *J. Colloid Interface Sci.* **1996**, *179*, 298.
[13] S. R. Carlsson, M. Fukuda, *J. Biol. Chem.* **1990**, *265*, 20488; E. L. Eskelinen, Y. Tanaka, P. Saftig, *Trends Cell Biol.* **2003**, *13*, 137.
[14] M. K. Mansour, [illegible]. Latz, S. M. Levitz, *J. Immunology* **2006**, *176*, 305

Submitted to BMC Biology, DRAFT ONLY

RESEARCH ARTICLE Open Access

Advances in use of capsule-based fluorescent sensors for measuring acidification of endocytic compartments in cells with altered expression of V-ATPase subunit V_1G_1

Marzia M. Ferraro[1†], Maria De Luca[2†], Raimo Hartmann[3†], Pilar Rivera-Gil[3], Andreas Klingl[4], Moritz Nazarenus[3], Agnese Ramirez[3], Wolfgang J. Parak[3,5], Cecilia Bucci[2,*], Rosaria Rinaldi[1,6], and Loretta L. del Mercato[1*]

*Correspondence: cecilia.bucci@unisalento.it; loretta.delmercato@nano.cnr.it
†Contributed equally
[1]NNL-Istituto Nanoscienze, CNR, Via per Arnesano, Km 5, 73100, Lecce, Italy. [2]Dipartimento di Scienze e Tecnologie B ologiche ed Ambientali (DiSTeBA), Università del Salento, Campus Univers tar o Ecotekne, Via Lecce-Monteroni, 73047, Monteroni di Lecce, Italy. Full list of author information is available at the end of the article.

Received 5 May 2015

Abstract

Background: Acidification of eukaryotic cell compartments is accomplished by vacuolar H+-ATPases (V-ATPases), large multi-subunit complexes which are able to pump protons into the lumen of organelles or in the extracellular medium. Here, the role of the V_1G_1 subunit of V-ATPases in regulating the activity of the proton pump is investigated.

Results: Firstly, stable cell lines overexpressing V_1G_1 or V_1G_1-depleted were constructed. Secondly, fluorescent capsule-based pH sensors were used to monitor acidification before and during internalization by modified and control living cells. The intracellular pH measurements indicate a delay in acidification in either overexpressing V_1G_1 or V_1G_1-depleted cells compared to controls. Finally, transmission electron microscopy and confocal microscopy further demonstrate uptake of the capsule-based sensors and subsequent engulfment in acidic vesicles in both modified cell lines.

Conclusions: Capsule-based fluorescence sensors represent practical biosensors for real-time and non-invasive ratiometric read-out of cellular proton concentrations inside endocytic compartments. The use of capsule-based pH sensors allowed for demonstrating the importance of the V_1G_1 subunit in V-ATPase activity concerning intravesicular acidification.

Background

In order to process multiple reactions efficiently and timely, eukaryotic cells are compartmentalized into distinct membrane-bound organelles. Intracellular pH plays a pivotal role in cellular processes and is highly regulated in every organelle [1]. Indeed, proper function of a number of organelles requires acidic pH. Acidification has multiple roles: for instance, it is fundamental for ligand-receptor dissociation in endosomes, for activation of hydrolases in lysosomes, for antigen processing in immune cells, for sorting of molecules in the Trans Golgi Network, and for neurosecretion [2, 3]. Acidification of compartments is accomplished by vacuolar H^+-ATPases (V-ATPases), large multi-subunit complexes that are able to pump protons into the lumen of the organelles or in the extracellular medium [4, 5]. Also, the structural stability and function of proteins are tightly associated with pH [6]. For example, it has been shown that mutations in the V-ATPase, responsible for acidification of the Golgi compartment, result in impaired glycosylation of proteins [7]. Alteration of acidification is a hallmark of a number of diseases including cancer [8, 9]. In fact, in several important human diseases, such as renal tubular acidosis, osteopetrosis, diabetes and defects in sperm maturation, acidification defects are detected [1, 5]. In cancer cells, acidification is of great importance as it affects invasion properties being required for activation of secreted lysosomal hydrolases in order to degrade the extracellular matrix [8, 9]. Indeed, V-ATPases are considered as promising pharmaceu-

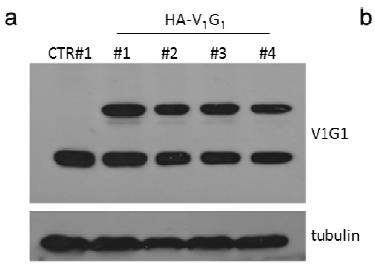

Figure 1 Expression of V_1G_1 in stable cell lines over-expressing V_1G_1 and depleted in V_1G_1. Stable cell lines were lysed and processed for Western blot analysis using an antibody against V_1G_1 to show (a) V_1G_1 over-expression or (b) V_1G_1 silencing. The numbers over the blots represent the different isolated clones. Antibodies against tubulin were used as loading control.

ticals targets against development and dissemination of metastasis [8, 9]. Therefore, tools to sense and monitor pH, in particular inside cellular organelles, are fundamental in order to establish how pH is regulated and, possibly, to find ways to regulate it.

Polyelectrolyte capsule-based sensors are an intriguing tool for monitoring changes of the pH inside cells and, in particular, inside endocytic organelles and lysosomes. They possess ping-pong ball-like geometry. A very thin semipermeable wall surrounds a big cavity, in which pH-sensitive fluorophores can be encapsulated [10-12]. After spontaneous uptake by cells, these capsules are mainly transported to lysosomes [13-20], hence, they are an appropriate pH-meter for studying the regulation of pH by the proton pump V-ATPase. Recently, the suitability of such mobile, capsule-based sensors was demonstrated to detect changes in the local pH around individual capsules during the ingestion process [12, 20-25]. In addition, real time monitoring of changes in the lysosomal pH of living cells has recently been demonstrated [26].

In the present work, we investigated the importance of the V_1G_1 subunit of the V-ATPase for acidification of endocytic vesicles. This subunit is part of the peripheral stator stalk that links the peripheral cytoplasmic V_1 domain with the membrane V_0 domain of the V-ATPase [8], and has been proposed to be important for V-ATPase assembly and functioning [27-30]. For the investigation, we constructed stable cell lines which either overexpressed V_1G_1 or were V_1G_1-depleted. Then, we tracked individual capsule-based pH sensors along their pathway from the extracellular to the intracellular environment of these cells and monitored the pH step by step. By comparing the acidification patterns among the different cell lines, the importance of the V_1G_1 subunit in V-ATPase activity could be demonstrated.

Results and Discussion

Generation of stable cell lines overexpressing V_1G_1 or with V_1G_1-depleted

In order to study the role of the subunit of the V-ATPase in vesicle acidification, we generated stable cell lines overexpressing HA-tagged V_1G_1 (abbreviated as HA-V_1G_1) and silencing V_1G_1 (abbreviated as sh-V_1G_1) (see Methods Section). After selection with the G418 antibiotic, HA-tagged and V_1G_1 over-expressing clones were isolated. As control we used a clone of HeLa cells stably transfected with an empty plasmid. Lysates of control and HA-V_1G_1 expressing independent clones were subjected to sodium dodecyl sulfate polyacrylamide gel electrophoresis (SDS-PAGE) and Western blot analysis using an anti-V_1G_1 antibody. The analysis revealed the presence of two bands in the HA-V_1G_1 transfected clones corresponding to the endogenous and exogenous V_1G_1, thus demonstrating V_1G_1 over-expression (Figure 1a). The HA-tagged V_1G_1 expression level was highest in clone #1. For all clones the expression of exogenous HA-tagged V_1G_1 was comparable to endogenous level of V_1G_1. Indeed, expression of HA-tagged V_1G_1 was similar to the endogenous V_1G_1 in clone #1, while it was about 60-80% in the other clones. In contrast, as expected, both V_1G_1-depleted cell clones showed a strong decrease of about 80% of V_1G_1 protein levels compared to control cells transfected with sh-control plasmid (Figure 1b).

Assembly and *in vitro* calibration of the capsule-based pH sensors

First, we fabricated capsule-based pH sensors with encapsulated fluorescent pH indicators and reference dyes for ratiometric measurements using polyelectrolyte multilayer (PEM) capsules as carrier platform [31, 32]. PEM capsules, fabricated *via* layer-by-layer (LbL) assembly of oppositely charged polyelectrolytes [33], have a porous multilayered wall that surrounds a cavity [34]. The pH-sensitive dye, fluorescein isothiocyanate (FITC), and the reference dye, rhodamine B isothiocyanate (RITC), were covalently linked to dextran molecules and subsequently co-loaded into the cavities of the capsules. The attachment of the fluorophores to dextran increased their molecular weight, in order to prevent dyes from leaching out of the capsules through their semipermeable shells. The polyelectrolyte multilayer wall protects the sensor elements from interferences in the cell while allowing small molecules,

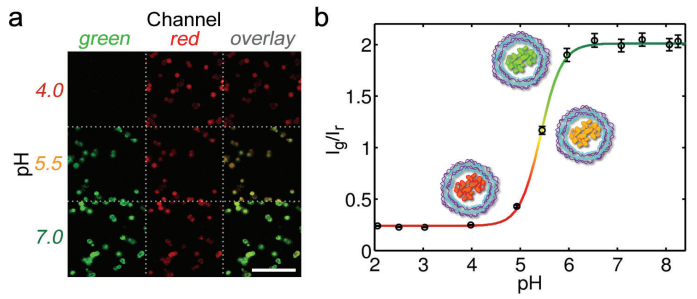

Figure 2 Calibration of capsule-based pH sensors. a) CLSM micrographs showing the pH-dependence of capsule fluorescence in pH-adjusted cell medium (FITC was excited at 488 nm and RITC at 543 nm). Green channel (505-530 nm), red channel (> 560 nm), and overlay of the fluorescence channels are reported. The size of the scale bar corresponds to 20 µm. b) Ratiometric calibration curve of capsule-based sensors on fluorescence intensity ratio of green and red channels derived from fluorescence micrographs.

in particular H^+, to diffuse into the cavity for detection [35-37]. As a result, upon ingestion of the capsule-based pH sensors, the fluorescence emission of the capsules changes depending on the local concentration of H^+ around individual capsules. Recently, the upper limit of the time response of capsule-based pH sensors was found to be around 500 ms, indicating that PEM capsules are suitable for time-resolved ratiometric pH sensing in living cells [26, 35].

Secondly, we tested the pH sensitivity of the capsule-based sensors under different proton concentrations (*i.e.* pH-values). For this purpose, capsules were diluted in cell media of which the pH was adjusted between pH 2.0 and pH 8.0 (see Methods Section for more details). In a subsequent step the fluorescence response was monitored *via* both spectrofluorimetric analysis and confocal laser scanning microscopy (CLSM) (see Additional File 1: Figures S1 and S2). FITC was excited at 488 nm and RITC was excited at 543 nm, and the emission signals were collected between 505 nm and 530 nm for the green channel and >560 nm for the red channel, respectively. By increasing the pH of the medium the overall color of the capsules shifts from 'red' to 'yellow' to 'green' as result of the strong pH dependence of FITC (indicator dye) and the insensitivity of RITC (reference dye). The response of the capsule-based sensors can be observed in Figure 2a where the fluorescence micrographs of capsules at pH 4.0, 5.5 and 7.0 are reported. At pH 4.0 the FITC fluorescence (green channel) is very low and the overlay of the green and red channels shows red colored capsules. At pH 5.5 the FITC fluorescence increases. Accordingly, the overlay of the green and red channels shows yellow-green colored capsules. At pH 7.0 the emission of FITC increases further and in the overlay of the green and red channels capsules appear in bright green color. The intensity ratios of green and red channels were calculated for each pixel positions allocated by capsules and averaged for approximately 500 capsules/pH-value. The fluorescence intensity ratio of the green and red channels derived from fluorescence micrographs were ultimately plotted as a function of pH (Figure 2b). According to literature data for ratiometric pH sensors based on FITC/RITC fluorophores [22, 23, 31, 38], our capsule-based pH sensors show a sigmoidal-like dependence of fluorescence, as a function of pH. Importantly, the sensors are able to measure pH changes down to 4, and thus, cover the pH range of endocytic organelles and lysosomes [39].

Intracellular pH sensing in cells with modified V-ATPase

We subsequently used the above described capsule-based pH sensors for comparing the pH along the internalization pathway in the different generated cell lines (see Figure 1). The capsule-based sensors were added to the cell culture medium of control cells, HA-V_1G_1 expressing cells and V_1G_1-depleted cells in a ratio 15:1. Capsule uptake was followed *via* CLSM time lapse microscopy up to 24 h. We used different clones (the ones indicated in Figure 1) in order to be sure that any reported effect was actually due to the expression or silencing of the V_1G_1 protein and to improve the statistics. In particular, we used clones #1, #2, #3 and #4 for HA-V_1G_1 cells, and clones #7 and #8 for sh-V_1G_1 cells. As controls, we used stably trasfected HeLa cells with pCDNA3 empty plasmid (CTR #1) and stably transfected HeLa cells with sh-control plasmids (CTR #2). Capsules are internalised by a huge variety of cells [13-19], involving the concomitant activation of phagocytosis and lipid rafts-mediated macropinocytosis [20]. Cholesterol enriched domaines of the plasma membrane are crucial for the initial uptake and the final localisation of the capsules inside phagolysosomes [20]. Furthermore, the capsules are deformed upon incorporation by cells, likely due to the mechanical pressure within the intracellular vescicles that leads to squeezing of the capsules [19, 40, 41]. Namely, this deformation does not impair the sensing properties of the capsules that retain both, the pH-sensitive and the reference fluorophores within their cavities. Figure 3a shows three

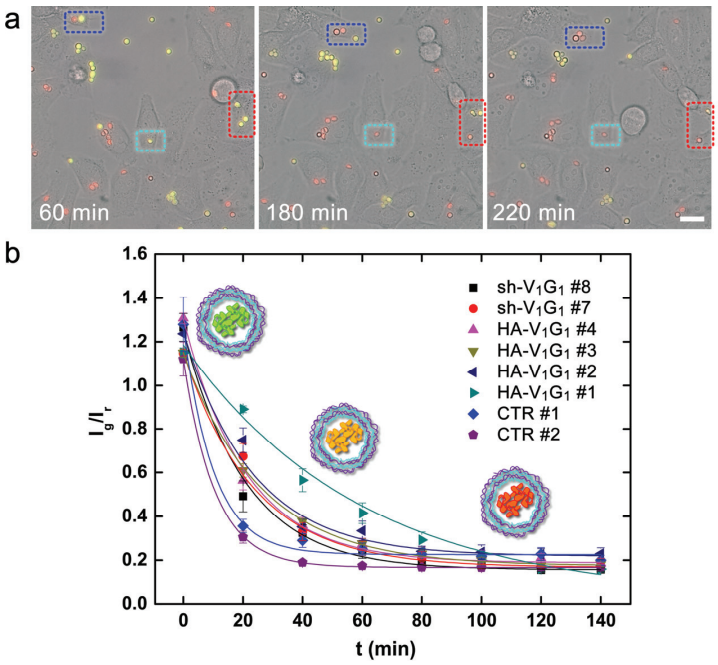

Figure 3 *In vitro* pH-response of capsule-based sensors following cellular uptake. a) Time-lapse fluorescence micrographs showing the color changes of capsule-based pH sensors added to control cells (CTR #2), as recorded after 60 min, 180 min, and 220 min. Before internalization, capsules display a strong green fluorescence due to the neutral pH of the cell medium. After internalization, the capsules display a strong red fluorescence due to their confinement in acidic endosomal/lysosomal compartments inside cells. Dashed rectangles highlight the color shift from green to red of capsules being internalized by cells over several hours of incubation. Images were taken in green and red fluorescence and transmission channels. The overlay of the three channels is presented in the Figure. Scale bar: 25 µm. b) Fluorescence intensity ratios (I_g/I_r) of capsule-based sensors added to controls (CTR #1 and #2), sh-V_1G_1 and HA-V_1G_1 clones. The fluorescence of capsules was measured at different time points by time-lapse microscopy and then plotted versus time. The continuous lines are fits to the data using the function $I_g/I_r\,(t) = I_g/I_r(t=0)\cdot\exp(-t/\tau) + I_g/I_r(t\to\infty)$, with the 3 fit parameters τ, $I_g/I_r(t=0)$, and $I_g/I_r(t\to\infty)$. The bigger τ, the faster acidification occurs. The error bars represent the standard deviation calculated over 45 capsules analyzed at the indicated time points.

representative time lapse micrographs of control cells (CTR #2) at different time points (60 min, 180 min, and 220 min). The overlay of the bright, 'green' and 'red' channels show capsules with different colors because of their localization in enviroments with different local pH values. Precisely, the capsules in 'green' color are outside the cells or attached to the cell membrane, whereas the capsules in 'red' color are entering the cells or have already been confined into acidic intracellular vesicles. Thus, the color changes displayed by the internalized capsule-based pH sensors can be correlated to intracellular local pH changes. From the fluorescence intensity of the indicator (I_g) and reference (I_r) dyes, the I_g/I_r ratio displayed by capsules in each cell line was calculated and plotted against the time (Figure 3b). At each time point, several images were taken and over 45 capsules/sample were analyzed. Because the ingestion of capsules may occur at different time points within the same cell culture (the uptake is a statistical process over the time period), we fixed, for each individual capsule-based sensor, t0 as the time-point in which the capsule is still located in the extracellular environment (overall green color) just before being engulfed by the cell and passed to the acidic compartments (overall yellow and red colors). As shown in Figure 3b, the two control cells (HeLa cells transfected with pCDNA3 empty vector and HeLa cells transfected with control sh-plasmid) showed similar $I_g/I_r(t)$ behaviors. In contrast, the cell lines in which the HA-tagged V_1G_1 was expressed (HA-V_1G_1, clones #1, #2, #3, and #4) showed a slower kinetic of acidification, as compared to the control cells. Notably, the clone HA-V_1G_1 #1, that showed the strongest expression of HA-V_1G_1 (see Figure 1), displayed the strongest effect (although the trend is the same). Furthermore, also in the cell lines in which V_1G_1 was silenced (sh-V_1G_1, clones #7 and #8), the kinetics of acidification was slower compared to control cells. These data indicate that expression of the right amount of the V_1G_1 subunit is crucial as overexpression or reduced expression of this subunit results in slower kinetics of acidification, suggesting that the V_1G_1 subunit is fundamental for the correct functioning of the

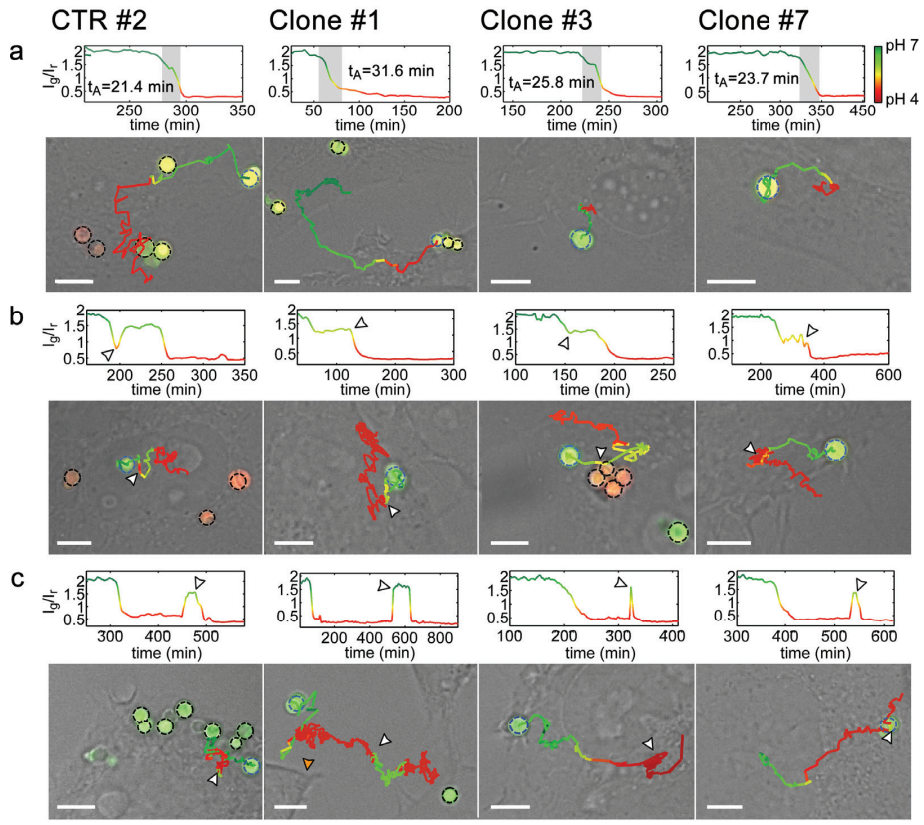

d

Trajectories without plateaus: t_A (min)				
clone	**CTR#2**	**#1**	**#3**	**#7**
N	299	290	360	378
median	18.77	25.30	19.52	20.40
mean	21.95	30.94	24.12	24.90
Q1	11.07	16.95	11.85	11.75
Q3	27.83	39.57	29.85	30.51

e

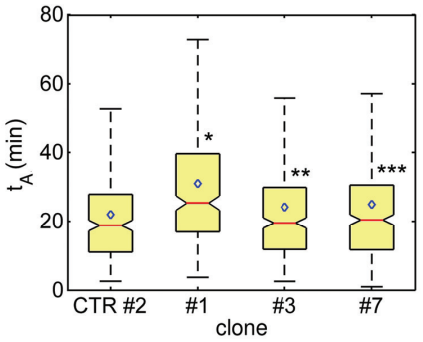

Figure 4 Real-time measurements of cell acidification by capsule-based sensors. a) Examples of use of capsule-based sensors for real-time monitoring of acidification by tracking the fluorescence intensity of a single capsule (indicated by blue dashed regions of interest (ROIs)) from the time of initial attachment to the cell through the completion of acidification (red color). The acidification times t_A are derived from a sigmoidal fit to each individual trajectory and are representing the time period between high pH (green plateau) and low pH (red plateau) locally around each capsule. b)-c) In some cases, the acidification is not a continuous process and nodes (duration t_l), indicated by white arrows in the fluorescence images, at intermediate pH levels occur (around pH 5.6) (see Additional File 3). The size of the scale bar corresponds to 5 µm. d) Table with number of evaluated trajectories N per clone, mean and median values for the acidification time t_A as well as the corresponding upper and lower quartiles (Q1 and Q3). e) In the box plot t_A is plotted for all different clones ignoring trajectories with nodes. The blue diamonds correspond to the mean values of the distribution. The acidification rate of clone #1 was significantly lower than that of the control cells ($p < 0.0001$, *). P-values were obtained from a two-tailed Wilcoxon–Mann–Whitney test. Additional significance levels: $p < 0.23$ (**), $p < 0.17$ (***).

pump. In order to gain deeper insight into the acidification mechanisms, we have focused our attention on the overexpressing clones #1 (HA-V_1G_1 #1), #3 (HA-V_1G_1 #3), and on the silenced clone #7 (sh-V_1G_1 #7). We have followed the uptake of single capsule-based sensors by tracking their movement from the extracellular medium to the intracellular compartments. As the two control cells showed analogous $I_g/I_r(t)$ behaviors, we have selected CTR #2 cells for the tracking

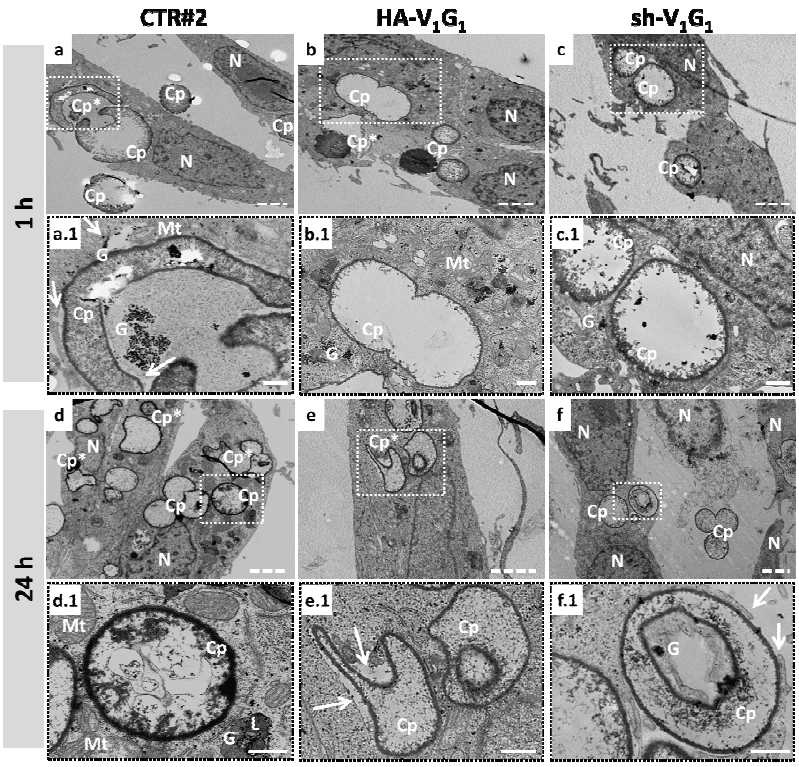

Figure 5 Internalization of PEM capsules by V_1G_1 overexpressing or silenced cells. The images show the uptake of the capsules that have been added to control cells (CTR #2) and cells overexpressing (HA-V_1G_1,) or lacking (sh-V_1G_1) the V_1G_1 subunit. Upon internalization, the capsules are squeezed and consequently they suffer from deformations. Images were taken after 1 h (a-c) and 24 h (d-f) of cell-capsule interaction. Cp, Capsules; N, Nucleus; Mt, Mitochondria; G, Glycogen; L, Lysosome. Stars, examples of deformed capsules. Dashed box, zoomed areas of representative capsules. Solid arrow, plasma membrane surrounding the capsules. Scale bars: dashed line: 2 µm; straight line: 500 nm.

analysis. We calculated the acidification time in control cells, in cells overexpressing V_1G_1, and in V_1G_1 depleted cells (Figure 4) (see Additional File 2 for details about tracking measurements). This analysis confirmed that a delay in acidification is present both, in clones expressing HA-V_1G_1 or with V_1G_1 silenced. Furthermore, the overexpressing clone #1 showed again the slowest kinetic of acidification (Figure 4d and 4e). In addition, this tracking analysis allowed us for following the capsules step by step together with their acidification state. In most cells (79 %), acidification was a continuous process, as shown in Figure 4a. The pH decrease started immediately after the engulfment of the capsules, and the FITC/RITC ratio remained fairly constant at a pH below 5.0. However, in some cells acidification was not a continuous process and showed stops at intermediate pH levels (Figure 4b and Additional File 3). This trend was present in 21 % of the observed capsule trajectories and could possibly be due to a slower kinetics of movement towards the cell centre or to slower and/or less fusion events with already more acidic vesicles. Furthermore, although most capsules showed a regular acidification trend while moving toward the cell centre (Figure 4a), in some cases (6 % of all trajectories), we could observe a sudden increase in pH followed by a rapid or slow re-acidification (Figure 4c). In this case, capsules might be present in compartments that fuse with less acidic organelles, thus, increasing the local pH.

Localization of capsule-based pH sensors in cells with modified V-ATPase

We further assessed the internalization of the capsules *via* transmission electron microscopy (TEM) analysis (Figure 5 and Additional File 5) and CLSM analysis (Figure 6). For both methods we selected two time points, 1 h and 24 h, as at this stage of our investigation we specially focused on comparing the initial and final localization of the capsules in all analyzed cells. The membranes and cristae within the mitochondria are visible and do not seem to be distorted or broken. The cytoplasm is homogenous, showing free ribosomes, rough endoplasmic reticulum with attached ribosomes and vesicles. Within the cytoplasm, vesicular structures, most likely lysosomes and endosomes are found. A double membrane surrounds the nucleus with regular interruptions

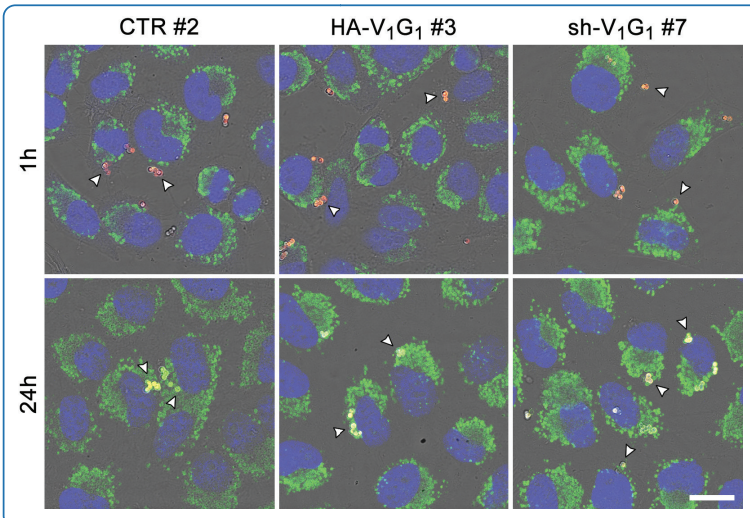

Figure 6 Co-localization of capsules internalized by V_1G_1 overexpressing or silenced cells. CLSM images of control cells (CTR #2), HA-V_1G_1 cells (clone #3), and sh-V_1G_1 cells (clone #7) following 1 h (top row) and 24 h (bottom row) incubation with fluorescently labeled $(PSS/PAH)_5$ capsules (white arrows). Dex-RITC-loaded capsules (red); LAMP1 (green); DAPI staining (blue). Overlay images of red, green, blue and transmission channels. Scale bar: 20 µm.

consisting of nuclear pore complexes. Furthermore, hetero- as well as euchromatin can be distinguished. As shown in Figure 5, several capsules can be seen inside the different cell clones at 1 h and, as expected, the number of internalized capsules increased with time. Internalization is a statistical process and therefore, over time, the capsules are continuously in contact with the cell membrane or within the cytoplasm, corresponding to the progress of being phagocytozed. Those capsules exhibited an electron dense outer layer due to the presence of gold nanoparticles which had been added to the capsule walls (Figure 5a.1 and d.1) (see also Additional File 5: Figure S10a.1 and S11a), and were surrounded by a lipid monolayer after internalization, indicated by the solid arrows in Figures 5a.1, 5e.1 and 5f.1 (see also Additional File 5: Figures S8a.1, S8b, S9b.1, S10a.1, S10b, S11a, S11c, 5f.1). The already mentioned deformation of capsules at some later point after phagocytosis was also observed in all images. The capsules were sorted to the lysosomes [20]. Examples of co-localization and merging of the lysosomes with the phagosomes can be seen in Figures S8c, S9b.1, S10b, S10c, S11a, and S11d. Furthermore, in some cases, capsule-based sensors can be observed being partly degraded or broken. Particularly, in Figure S10c a highly degraded capsule is shown.

Co-localization of the capsules with lysosomes was also confirmed by CSLM (Figure 6). Fluorescently labeled $(PSS/PAH)_5$ capsules were incubated with control cells (CTR #2), with cells overexpressing V_1G_1, and with V_1G_1-silenced cells, for 1 h and 24 h. The intracellular localization of the capsules was studied using confocal immunofluorescence analysis with antibodies against LAMP1 (lysosomal-associated membrane protein 1), a protein that resides in membranes of late endosomes and lysosomes [42, 43]. At 1 h incubation time point, no co-localization of capsules (red) with LAMP1-positive organelles (green) was observed (Figure 6, top row). In all cells, the capsules were located in the cell periphery or close to the cell membrane, as being internalized by the cells. In contrast, at 24 h incubation time point, the capsules were predominantly distributed around the nuclei, where lysosomes were mostly grouped. In all cells, the overall color of internalized capsules shifted from red to yellow (Figure 6, bottom row), indicative of co-localization with LAMP1-positive acidic organelles, such as late phagosomes and phagolysosomes.

Conclusion

Altogether, these data indicate the utility of capsule-based pH sensors to measure the pH inside endocytic compartments, such as phagosomes and phagolysosomes. In contrast to other methods available for measuring pH (*e.g.,* injection of fluorescent pH indicators), the main advantage of capsule-based pH sensors lies in the fixed intracellular terminal distribution. Indeed, capsules end up in the lysosomes/phagolysosomes, where they stay for long time. Therefore, they represent a valuable tool to follow acidification in living cells over time and to study the acidification process during the endocytic pathway. Furthermore, the data obtained on V_1G_1-silenced or V_1G_1-overexpressing clones demonstrate that the V_1G_1 subunit is important for V-ATPase activity confirming previous works [27-30], and indicate that these sensors can be used to investigate V-ATPase functioning. Clearly, further work will be necessary to resolve questions about the exact role of V_1G_1 in regulation of the V-ATPase activity.

Methods

Materials

Poly(sodium 4-styrenesulfonate) (PSS, M_w ~70.000 kDa, #243051), poly(allylamine hydrochloride) (PAH, M_w ~56.000 Da, #283223), calcium chloride dehydrate ($CaCl_2$, M_w = 147.01 Da, #223506), sodium carbonate (Na_2CO_3, M_w = 105.99 Da, #S7795), dextran (M_w ~ 2000.000 Da, #95771), fluorescein 5(6)-isothiocyanate (FITC, M_w = 389.38 Da, #46950), rhodamine B isothiocyanate (RITC, M_w = 536.08 Da, #R1755), ethylenediaminetetraacetic acid disodium salt dihydrate (EDTA, #E5134) were purchased from Sigma-Aldrich. Amino dextran (AM-dextran, M_w ~500.000 Da, #D-7144) was obtained from Invitrogen. Gold colloids 5 nm were obtained from (#EM.GC15) BBI International and bis(p-sulfonatophenyl)phenylphosphine dihydrate dipotassium salt (#15-0463) from Stream Chemicals. All chemicals were used as received. Ultrapure water with a resistance greater than 18.2 MΩ/cm was used for all experiments.

Cell cultures

All cells were cultured in phenol-red free Dulbecco's Modified Eagles Medium (DMEM, Sigma-Aldrich, Germany, #D6546) supplemented with 10% fetal bovine serum (FBS, Biochrom, Germany, #S0615), 1 % penicillin/streptomycin (P/S, Sigma-Aldrich, Germany, #P4333) and 2 mM L-glutamine (Sigma-Aldrich, Germany, #G7513) at 5 % CO_2 and 37 °C.

Generation of stable cell lines

Stable cell lines over-expressing and/or silencing V_1G_1 were generated using pCDNA3_2xHA-V_1G_1 or sh-RNA V_1G_1 plasmids (sc-36797-SH, Santa Cruz Biotechnology), respectively. Stable cell lines were selected by adding G-418 (1 mg/mL, Calbiochem) to cells transfected with HA-V_1G_1 or Puromycin (3 µg/mL, Sigma-Aldrich) to V_1G_1-silenced cells. Cells were kept in selective media for about two weeks or until clones were visible. About 10 independent clones were picked for each sample and propagated. Lysates of some of the clones were processed for Western blot analysis to verify V_1G_1 overexpression or silencing. HA control cells were transfected with an empty vector and selected with G-418, while sh-control cells were transfected with a control sh-plasmid and selected with puromycin. After the selection the clones over-expressing HA-V_1G_1 were cultured in medium supplemented with 0.25 mg/mL G418, whereas V_1G_1-silenced clones and control cells were maintained in medium supplemented with 0.75 µg/mL puromycin.

Western Blotting (WB)

HeLa cells were lysed in RIPA buffer (Sigma-Aldrich) plus proteinase inhibitors cocktail (Roche). Lysates were loaded on SDS-PAGE and separated proteins were transferred onto PVDF membranes from Millipore. The filter was blocked in 5 % milk in phosphate buffered saline (PBS) for 30 minutes at room temperature, incubated with the appropriate primary antibody mouse monoclonal anti-V_1G_1 (1:100, sc-25333, Santa Cruz Biotechnology) and mouse monoclonal anti-tubulin (1:3000, clone B512, Sigma-Aldrich), and then with a secondary antibody conjugated with HRP (1:5000, G21040 Invitrogen). Bands were visualized using Western blot Luminol Reagent (Santa Cruz).

Synthesis of capsule-based pH sensors

The preparation of capsule-based pH sensors was carried out following our previous protocol [31]. Briefly, 0.615 mL 0.33 M $CaCl_2$, 0.615 mL 0.33 M Na_2CO_3, 0.4 mL FITC-dextran solution (30 µM), and 0.37 mL RITC-dextran solution (30 µM) were rapidly mixed and thoroughly agitated on a magnetic stirrer for 30 s at room temperature. After the agitation, the precipitate was separated from the supernatant by centrifugation (4500 rpm, 5 s) and washed three times with water. Then, the resulting $CaCO_3$ particles, containing FITC-dextran and RITC-dextran, were subjected to the LbL deposition of PSS (2 mg/mL, 0.5 M NaCl, pH = 6.5) and PAH (2 mg/mL, 0.5 M NaCl, pH = 6.5) polyelectrolytes (15 minutes under agitation) to give the following multilayer wall architecture: $(PSS/PAH)_5$. Short ultrasound pulses were applied to the sample prior to the addition of each polyelectrolyte in order to prevent particle aggregation. The decomposition of the $CaCO_3$ core, resulting in hollow microcapsules, was achieved by treatment with 1 mL EDTA (0.2 M, pH 7.0) followed by triple washing with water. The microcapsules were stored as suspension in water at 4 °C.

Synthesis of gold nanoparticle-functionalized capsules

To visualize the capsules with the transmission electron microscope, we added electron-dense gold nanoparticles (Au-NPs) into the walls. The synthesis was carried out as follows. In a vial equal volumes (1.2 mL) of aqueous $CaCl_2$ and Na_2CO_3 solutions (0.33 M) were mixed in the presence of 1.54 mL of dextran (13 mg/mL). The solution was thoroughly mixed on a magnetic stirrer for 30 s and afterwards, the mixture was left without stirring for 3 minutes. After three washing steps with Milli-Q water, the resulting particles were coated with one bilayer of polyelectrolytes ($CaCO_3$@(PSS/PAH)). Then, the coated cores were functionalized with phosphine-stabilized Au-NPs following our previous protocols [44]. Afterwards, 4 more bilayers of (PSS/PAH) were added. The dissolution of the cores was carried out as described above. The final architecture of the capsules was therefore (PSS/PAH)Au-

$NPs(PSS/PAH)_4$. We incorporated dextran (2000 kDa) into the $CaCO_3$ cores, as dissolution of cores including dextran by addition of EDTA is faster than that of cores without dextran. Naturally, in this way traces of dextran remain in the capsule cavities after core dissolution [44].

Characterizations of capsules

Capsule size was determined from fluorescence micrographs. The diameter of the microcapsules produced was 2.6 $\pm$ 0.3 µm (N = 4130).

The Zeta potential (ζ) of the capsules was measured in Milli-Q water by dynamic light scattering (DLS) using a Zetasizer Nano ZS (Malvern Instruments, UK). The results were averaged from 3 parallel measurements. All microcapsules used in this work had a zeta potential value of 11.9 $\pm$ 0.2 mV.

The capsule number per volume was determined with a haemocytometer under an optical microscope. A drop of a diluted solution of capsules was added onto the chamber and the number of capsules in the volume defined by the haemocytometer was counted by using a 20X objective in phase contrast mode. The capsules concentration was estimated to be around $1.5 \cdot 10^8$ capsules mL^{-1}.

Spectrofluorometer and confocal intensity titrations

For *in vitro* spectrofluorometric titrations, first, the pH of the cell medium was adjusted to various pH values ranging from 2.0 to 8.0 (by 1 M NaOH or 1 M HCl). The pH of the final solutions was checked with a pH meter (Professional-Meter PP-50, Sartorius). Then, 10 µL of capsules ($1.5 \cdot 10^8$ capsules mL^{-1}) were mixed with an excess of cell medium to buffer ratio of about 1:10 and measured with a Fluorolog (FL3–122) fluorescence spectrometer equipped with a 450 W Xenon short arc lamp (Ushio-UXL-450S-O) as the source of excitation. Emission spectra were collected at 500–550 nm ($\lambda_{exc\,tat\,on}$ = 488 nm) for FITC and 565–625 nm ($\lambda_{excitat\,on}$ = 543 nm) for RITC. For *in situ* confocal microscopy titrations, 10 µl capsules suspension aliquots (with the same buffers used for each pH point) were pipetted on coverslips. Confocal scans were normally performed with a Leica TCS SP5 (Leica Microsystems, Germany) or, where indicated, with a CLSM 510 Meta (Zeiss, Germany). Laser power, acquisition parameters and excitation light exposure times were adjusted to optimize signal-to-noise ratios and minimize photobleaching and were kept constant throughout each pH titration series. FITC was excited at 488 nm with an argon laser and its fluorescence was collected between 505 and 530 nm ('green' channel). RITC was exited at 543 nm using a helium neon laser; the fluorescence was detected with a long-pass filter >560 nm ('red' channel).

Live confocal fluorescence microscopy

For internalization of the capsule-based pH sensors, approximately 10,000 cells per cm^2 were seeded in a sterile microscopy chambers (8-well µ-slide, Ibidi) in complete DMEM. Before analysis, cells were incubated with 15 capsules/cell in L-15 medium (without phenol red, Leibowitz medium, GIBCO).

For capsule tracking experiments, Clone #1 and #3 (overexpressing V_1G_1), clone #4 (silencing V_1G_1) and stably transfected HeLa cells with sh-control plasmids (CTR #2) were selected. 15,000 cells/well were seeded into each well of an 8-well µ-slide (Ibidi, Germany, #80826). The µ-slides were transferred to a CLSM (CLSM 510 Meta, Zeiss, Germany) equipped with a portable incubator (Pecon, Germany) and maintained at 37 °C with 5 % CO_2. Immediately before image acquisition, approximately 15 capsules/cell were added and a time-lapse image series was acquired using a Plan-Apochromat 63x/1.40 Oil DIC M27 objective. To minimize the effect of photobleaching, the acquisition parameters were tuned to detect FITC/RITC-fluorescence at very low excitation power. Images were acquired with a lateral sampling frequency of 0.2 µm and a temporal resolution of 150 s. To image capsules being already internalized (a) and those still adhering to the outer plasma membrane on top of the cells (b), two images at the same lateral position but different axial positions were acquired. For (a) one slice was imaged 2.2 µm above the substrate, which was typically located in the cell interior. For (b) another image was obtained at a position 3 µm higher to resolve capsules located on top of cells. The pinhole of the confocal system was adjusted to capture 2 µm thick sections in both cases. This alignment was recovered before each time point by a software-based autofocus routine which was searching for the boundary layer µ-dish substrate/medium characterized by an increased level of scattered photons. After acquisition, the projection along the z-axis of both slices was calculated and used for further analysis. The described procedure resulted in almost gapless two-dimensional capsule trajectories.

Ultrastuctural analysis via Transmission Electron Microscopy (TEM)

For TEM analysis, samples were chemically fixed with glutaraldehyde. For the chemical fixation protocol, the different clones were seeded in a Petri dish (Ø 100 mm) until 80 % confluence and then were treated with the sensor capsules (20 capsules/cell) for 1 h and 24 h. Cells were placed in the fixative solution (2.5 % glutaraldehyde) for 45 min at room temperature (RT). Afterwards the cells were collected with a scraper and concentrated *via* centrifugation, discarding the supernatant. Postfixation was performed in 1 % osmium tetroxide for 1.5 h at 4 °C. Then, cells were dehy-

drated in grading series of acetone, infiltrated with an EPON:acetone mixture, and finally embedded in pure EPON resin. Resins were polymerized at 60 °C for 48 h. Ultra-fine sections were contrasted with 2 % aqueous uranyl acetate for 30 min at RT first and followed by exposure to Reynolds´s lead citrate for 10 min at RT. Sections were imaged with a JEOL JEM 1010 (100 kV) transmission electron microscope equipped with a Bioscan Gatan wide angle slow scan CCD camera.

Confocal immunofluorescence microscopy

HeLa cells stably transfected with sh-control plasmids (CTR #2), clones HA-V_1G_1 #3, and sh-V_1G_1 #7 were selected for co-localization studies. $(PSS/PAH)_5$ capsules, carrying only dextran-RITC into the cavities, were produced by following the procedure described above. Cells were grown on 11-mm round glass coverslips; 1 h and 24 h before the fixation, the cells were incubated with 15 capsules/cell in complete DMEM. Then, the cells were fixed in 3 % paraformaldehyde (PFA, Sigma-Aldrich), permeabilized with piperazine-N,N′-bis(2 ethanesulfonic acid) (PIPES)-Saponin 0.1 %, and incubated with primary antibodies for 1 h. After 3 washes with PBS-Saponin 0.1 %, the cells were incubated for 30 min with the secondary antibodies and then with DAPI dye (1 µg/mL). The following antibodies were used: mouse anti-Lamp1 at a 1:250 dilution (H4A3, Developmental Hybridoma Bank University of Iowa), goat anti-mouse AlexaFluor488 at a 1:500 dilution (A11001, Invitrogen). Subsequently, cells were viewed with a CLSM microscope (TCS-SP5; Leica, Germany) equipped with a laser diode emitting at 405 nm, an argon-ion laser with a line at 488 nm, and a helium-neon laser for excitation at 543 nm. The fluorescence signal of DAPI was detected after filtering with a band pass filter within the range 415-500 nm, the fluorescence signal of AlexaFluor488 was detected with a band pass filter 510-550 nm, and the fluorescence signal of RITC was detected with a 560 nm long pass filter. Images were taken with a HCX PL APO lambda blue 63.0 x 1.40 oil-immersion objective and a pinhole aperture of 1 Airy unit.

Additional material

Additional File 1: Calibration of capsule-based pH sensors. Figure S1 shows the pH-dependence of capsule fluorescence in pH-adjusted cell medium, as measured with a fluorescence spectrometer. Figure S2 shows the CLSM micrographs of capsule-based pH sensors in pH-adjusted cell medium between pH 2.0 and pH 8.0 (FITC was excited at 488 nm and RITC at 543 nm).

Additional File 2: Capsule tracking measurements. This file includes the complete and detailed description of the tracking measurements and data analysis.

Additional File 3: Data from tracking experiments. In this file additional trajectory patterns are discussed which are observed in 21 % of all analyzed trajectories.

Additional File 4: Mean velocity profile of capsule-based pH sensors during acidification. Figure S7 shows the mean velocity profile of capsule-based pH sensors during acidification. To obtain the data all single trajectories where shifted by that point in time where the I_g/I_r-value has dropped to 50 % of its initial value ($t_{50\%}$, *cf.* Figure S4). Finally, the corresponding velocity values $v(t\text{-}t_{50\%})$ were averaged over all trajectories per sample to obtain $\langle v \rangle (t\text{-}t_{50\%})$. It can be seen that on average the beginning of the acidification process is correlated to a significantly higher capsule velocity. Notably, the velocity of capsule-based pH sensors being internalized by clone #1 (HA-V_1G_1 cells) is slightly higher.

Additional File 5: Ultrastuctural Analysis via transmission electron microscopy. This file includes the detailed description of the method used for TEM analyses and provides additional ultrastructural images (Figures S8-S11) of HA-V_1G_1, sh-V_1G_1 and control cells (CTR #1 and CTR #2) showing the interaction of the capsules with different cellular structures at different time lapses (1 h, 24 h).

Acknowledgements

This work was partially supported by AIRC (Grant IG2013 N. 14709 to C.B.), by MIUR (PRIN2010-2011 to C.B.), and by LOEWE (SynChemBio to W.J.P.). M.M.F., R.R and L.L.d.M acknowledge the financial support from PON02_00563_3448479-F 'RINOVATIS' and PONa3_00134 'Omics and nanotechnology for early diagnosis of human diseases – ONEV'. P.R-G acknowledges the MICINN (RYC-2012-10059) for the financial support. A.K. received financial support from the LOEWE Research Centre for Synthetic Microbiology (Synmikro). Prof. Dr. Uwe-G. Maier is acknowledged for allocation of the EM facility and high-pressure freezer and Marion Debus for technical assistance.

Author details

[1]NNL-Istituto Nanoscienze, CNR, Via per Arnesano, Km 5, 73100, Lecce, Italy. [2]Dipartimento di Scienze e Tecnologie Biologiche ed Ambientali (DiSTeBA), Università del Salento, Campus Universitario Ecotekne, Via Lecce-Monteroni, 73047, Monteroni di Lecce, Italy. [3]Fachbereich Physik, Philipps-Universität Marburg, 35037, Marburg, Germany. [4]LOEWE Centre for synthetic Microbiology (Synmikro) and Department of Cell Biology, Philipps-Universität Marburg, Karl-von-Frisch-Str. 8, 35043, Marburg, Germany; Plant Development, Department of Biology I, Biocenter LMU Munich, Grosshaderner Str. 2-4, 82152 Planegg-

Martinsried, Germany. [5]CIC biomaGUNE, Parque tecnológico de San Sebastián, Ed. Pº Miramón 182, 20009, San Sebastian, Spain. [6]Dipartimento di Matematica e Fisica "Ennio De Giorgi", Università del Salento, Campus Universitario Ecotekne, Via Lecce-Monteroni, 73047, Monteroni di Lecce, Italy. Current address of P.R-G: Department of Physical and Inorganic Chemistry, Rovira i Virgili University and the Chemistry Technology Center of Catalonia (CTQC), 43007 Tarragona, Spain.

Authors' contributions

MDL and CB generated stable cell lines over-expressing and/or silencing V_1G_1 subunit of V-ATPase and performed western blot analyses. MMF, RH and LLdM produced capsule-based pH sensors, performed sensing measurements in the cell lines over-expressing and/or silencing V_1G_1 and analyzed the data. RH carried out the tracking experiments and developed the method for data processing and analysis. MN, AR, PRG, and AK performed the TEM analyses. MMF, MDL and LLdM performed the co-localization studies via CLSM analysis. CB, LLdM, WJP and RR conceived the study, participated in its design and coordination. CB and LLdM drafted the manuscript. MDL, RH, PRG, AK, WJP and RR contribute to writing and revising of the manuscript. All authors read and approved the final manuscript.

References

1. Casey J, Grinstein S, Orlowski J: **Sensors and regulators of intracellular pH**. *Nat Rev Mol Cell Biol* 2010, **11**:50-61.
2. Weisz OA: **Organelle acidification and disease**. *Traffic* 2003, **4**(2):57-64.
3. Mukherjee S, Ghosh RN, Maxfield FR: **Endocytosis**. *Physiol Rev* 1997, **77**(3):759-803.
4. Sun-Wada GH, Wada Y, Futai M: Diverse and essential roles of mammalian vacuolar-type proton pump ATPase: toward the physiological understanding of inside acidic compartments. *Biochim Biophys Acta* 2004, 1658(1-2):106-114.
5. Marshansky V, Futai M: The V-type H+-ATPase in ves cular trafficking: targeting, regulation and function. *Curr Opin Cell Biol* 2008, 20:415-426.
6. Wh tten ST, García-Moreno EB, Hilser VJ: Local conformational fluctuat ons can modulate the coupling between proton binding and global structural transitions in proteins. *Proc Natl Acad Sci U S A* 2005, 102:4282-4287.
7. Kornak U, Reynders E, Dimopoulou A, van Reeuwijk J, Fischer B, Rajab A, Budde B, Nürnberg P, Foulquier F, Group AD-tS *et al*: **Impaired glycosylation and cutis laxa caused by mutations in the vesicular H+-ATPase subunit ATP6V0A2**. *Nat Genet* 2008, **40**(1):32-34.
8. Forgac M: Vacuolar ATPases: rotary proton pumps in physiology and pathophysiology. *Nat Rev Mol Cell Biol* 2007, 8(11):917-929.
9. Hinton A, Bond S, Forgac M: **V-ATPase functions in normal and disease processes**. *Pflugers Arch* 2009, **457**:589-598.
10. del Mercato LL, Ferraro MM, Baldassarre F, Mancarella S, Greco V, Rinaldi R, Leporatti S: **Biological applications of LbL multilayer capsules: From drug delivery to sensing**. *Adv Colloid Interface Sci* 2014, **207**:139-154.
11. Kazakova L, Shabarchina L, Anastasova S, Pavlov A, Vadgama P, Skirtach A, Sukhorukov G: **Chemosensors and biosensors based on polyelectrolyte microcapsules containing fluorescent dyes and enzymes**. *Anal Bioanal Chem* 2013, **405**(5):1559-1568.
12. Kreft O, Javier AM, Sukhorukov GB, Parak WJ: **Polymer microcapsules as mobile local pH-sensors**. *J Mat Chem* 2007, **17**:4471-4476.
13. Munoz Javier A, Kreft O, Piera Alberola A, Kirchner C, Zebli B, Susha AS, Horn E, Kempter S, Skirtach A, Rogach AL *et al*: **Combined atomic force microscopy and optical microscopy measurements as a method to investigate particle uptake by cells**. *Small* 2006, **2**:394-400.
14. Ai H, Pink JJ, Shuai XT, Boothman DA, Gao JM: **Interactions between self-assembled polyelectrolyte shells and tumor cells**. *J Biomed Mater Res A* 2005, **73A**(3):303-312.
15. Reibetanz U, Halozan D, Brumen M, Donath E: Flow cytometry of HEK 293T cells interacting with polyelectrolyte multilayer capsules containing fluorescein-labeled poly(acryl c acid) as a pH sensor. *Biomacromol* 2007, 8:1927-1933.
16. Cortez C, Tomaskov c-Crook E, Johnston APR, Radt B, Cody SH, Scott AM, N ce EC, Heath JK, Caruso F: **Targeting and uptake of multilayered particles to colorectal cancer cells**. *Adv Mater* 2006, **18**:1998-2003.
17. Zelikin AN, Breheney K, Robert R, Tjipto E, Wark K: **Cytotoxicity and Internalization of Polymer Hydrogel Capsules by Mammalian Cells**. *Biomacromol* 2010, **11**:2123-2129.
18. Yan Y, Johnston APR, Dodds SJ, Kamphuis MMJ, Ferguson C, Parton RG, Nice EC, Heath JK, Caruso F: Uptake and Intracellular Fate of Disulfide-Bonded Polymer Hydrogel Capsules for Doxorubicin Delivery to Colorectal Cancer Cells. *ACS Nano* 2010, 4:2928-2936.
19. Muñoz Javier A, Kreft O, Semmling M, Kempter S, Skirtach AG, Bruns OT, del Pino P, Bedard MF, Rädler J, Käs J *et al*: **Uptake of Colloidal Polyelectrolyte-Coated Particles and Polyelectrolyte Multilayer Capsules by Living Cells**. *Adv Mater* 2008, **20**:4281-4287.
20. Kastl L, Sasse D, Wulf V, Hartmann R, Mircheski J, Ranke C, Carregal-Romero S, Martinez-Lopez JA, Fernandez-Chacon R, Parak WJ *et al*: **Multiple Internalization Pathways of Polyelectrolyte Multilayer Capsules into Mammalian Cells**. *ACS Nano* 2013, **7**:6605-6618.
21. Reibetanz U, Chen MH, Mutukumaraswamy S, Liaw ZY, Oh BH, Venkatraman S, Donath E, Neu B: **Colloidal DNA carriers for direct localization in cell compartments by pH sensoring**. *Biomacromol* 2010, **11**(7):1779-1784.
22. Song X, Li H, Tong W, Gao C: Fabr cation of triple-labeled polyelectrolyte microcapsules for localized rat ometric pH sensing. *J Colloid Interface Sci* 2014, 416:252-257.
23. Zhang P, Song X, Tong W, Gao C: Nanoparticle/Polymer Assembled M crocapsules with pH Sensing Property. *Macromol Biosci* 2014, in press.
24. Hartmann R, Weidenbach M, Neubauer M, Fery A, Parak WJ: **Stiffness-dependent in vitro uptake and lysosomal acidification of colloidal particles**. *Angew Chem Int Ed Engl* 2015, **54**(4), 1365-1368.
25. Liang K, Gunawan ST, Richardson JJ, Such GK, Cui JW, Caruso F: **Endocytic Capsule Sensors for Probing Cellular Internalization**. *Adv Healthc Mater* 2014, **3**(10):1551-1554.
26. Rivera-Gil P, Nazarenus M, Ashraf S, Parak WJ: pH-Sens tive Capsules as Intracellular Optical Reporters for Monitoring Lysosomal pH Changes Upon Stimulation. *Small* 2012, 8(6):943-948.
27. Ohira M, Smardon AM, Charsky CM, Liu J, Tarsio M, Kane PM: The E and G subunits of the yeast V-ATPase interact tightly and are both present at more than one copy per V1 complex. *J Biol Chem* 2006, 281:22752-22760.
28. Tomashek JJ, Graham LA, Hutchins MU, Stevens TH, Kl onsky DJ: **V1-situated Stalk Subunits of the Yeast Vacuolar Proton-translocating ATPase**. *J Biol Chem* 1997, **272**(42):26787-26793.
29. De Luca M, Bucci C: A new V-ATPase regulatory mechanism mediated by the Rab interacting lysosomal protein (RILP). *Commun Integr Biol* 2014, 7(5):1-4.
30. De Luca M, Cogli L, Progida C, Nisi V, Pascolutti R, Sigismund S, Di Fiore PP, Bucci C: **The Rab-interacting lysosomal protein (RILP) regulates vacuolar ATPase acting on the V1G1 subunit**. *J Cell Sci* 2014, **127**:2697-2708.
31. del Mercato LL, Abbasi AZ, Parak WJ: Synthesis and Characterizat on of Ratiometric Ion-Sensitive Polyelectrolyte Capsules. *Small* 2011, 7(3):351-363.

32. del Mercato LL, Abbasi AZ, Ochs M, Parak WJ: **Multiplexed sensing of ions with barcoded polyelectrolyte capsules**. *ACS Nano* 2011, **5**:9668-9674.
33. Decher G: Fuzzy nanoassemblies: Toward layered polymeric multicomposites. *Science* 1997, 277:1232-1237.
34. Sukhorukov GB, Donath E, L chtenfeld H, Knippel E, Knippel M, Budde A, Mohwald H: **Layer-by-layer self assembly of polyelectrolytes on colloidal particles**. *Colloids Surf A Physicochem Eng Asp* 1998, **137**:253-266.
35. Carregal-Romero S, Rinklin P, Schulze S, Schafer M, Ott A, Huhn D, Yu X, Wolfrum B, Weitzel KM, Parak WJ: **Ion Transport Through Polyelectrolyte Multilayers**. *Macromol Rapid Commun* 2013, **34**:1820-1826.
36. Antipov AA, Sukhorukov GB, Mohwald H: Influence of the ionic strength on the polyelectrolyte multilayers' permeability. *Langmuir* 2003, 19:2444-2448.
37. Sukhorukov GB, Brumen M, Donath E, Mohwald H: **Hollow polyelectrolyte shells: Exclusion of polymers and donnan equilibrium**. *J Phys Chem B* 1999, **103**:6434-6440.
38. Murphy RF, Powers S, Cantor CR: Endosome pH measured in single cells by dual fluorescence flow cytometry: rapid acidification of insulin to pH 6. *J Cell Biol* 1984, 98:1757-1762.
39. Haas A: The phagosome: Compartment with a license to kill. *Traffic* 2007, 8:311-330.
40. Sukhorukov GB, Rogach AL, Zebli B, Liedl T, Skirtach AG, Kohler K, Antipov AA, Gaponik N, Susha AS, Winterhalter M *et al*: **Nanoengineered polymer capsules: Tools for detection, controlled delivery, and site-specific manipulation**. *Small* 2005, **1**:194-200.
41. Palankar R, Pinchasik BE, Schm dt S, De Geest BG, Fery A, Mohwald H, Skirtach AG, Delcea M: Mechanical strength and intracellular uptake of CaCO3-templated LbL capsules composed of biodegradable polyelectrolytes: the influence of the number of layers. *J Mat Chem B* 2013, 1:1175-1181.
42. Pols MS, van Meel E, Oorschot V, ten Brink C, Fukuda M, Swetha MG, Mayor S, Klumperman J: **hVps41 and VAMP7 function in direct TGN to late endosome transport of lysosomal membrane proteins**. *Nat Commun* 2013, **4**:1361.
43. Luzio JP, Pryor PR, Bright NA: **Lysosomes: fusion and function**. *Nat Rev Mol Cell Biol* 2007, **8**:622-632.
44. del Mercato LL, Gonzalez E, Abbasi AZ, Parak WJ, Puntes V: Synthesis and Evaluation of Gold Nanoparticle-Modified Polyelectrolyte Capsules under M crowave Irradiation for Remotely Controlled Release for Cargo. *J Mater Chem* 2011, 21:11468-11471.
45. Rachel R, Meyer C, Klingl A, Gürster S, Heimerl T, Wasserburger N, Burghardt T, Küper U, Bellack A, Schopf S *et al*: **Analysis of the Ultrastructure of Archaea by Electron Microscopy**. *Methods Cell Biol* 2010, **96**:47-69.
46. Hempel F, Bozarth AS, Lindenkamp N, Klingl A, Zauner S, Linne U, Steinbüchel A, Maier UG: **Microalgae as bioreactors for bioplastic production**. *Microb Cell Fact* 2011, **10**:81.
47. Peschke M, Mood D, Klingl A, Maier UG, Hempel F: **Evidence for glycoprotein transport into complex plastids**. *Proc Natl Acad Sci U S A* 2013, **110**(26):10860-10865.

Additional Information

Additional File 1:

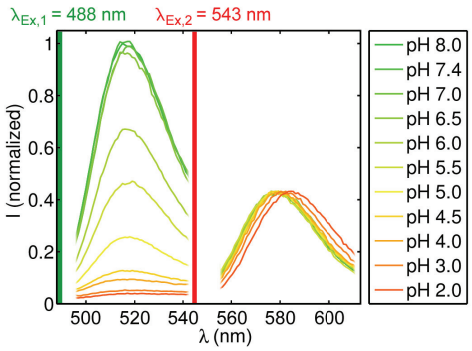

Figure S1 Fluorescent spectra of capsule-based sensors in pH-adjusted cell medium. While the wavelength of maximum emission of FITC at 518 nm is strongly reduced in acidic medium, the emission intensity of RITC at 580 nm is relatively stable.

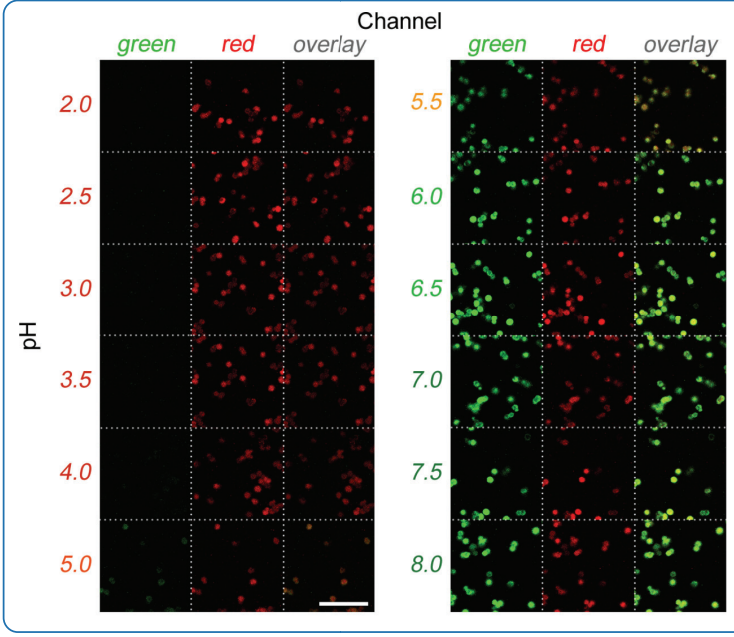

Figure S2 CLSM micrographs of capsule-based pH sensors in pH-adjusted cell medium. Scale bar: 20 µm.

Additional File 2:

Image processing

Image processing, capsule segmentation, tracking and visualization were performed as described in the literature using Matlab (Mathworks) [1]. In the following the workflow (Figure S3) is described briefly: First, shot noise was reduced by median-filtering and thresholding. Second, capsule regions of interest (ROIs, comprising x position, y position, radius around the x, y position) were derived from a modified Hough-transform [2]. Third, per pixel ratios (I_g/I_r values) of green and red channel intensities were calculated based on the unfiltered raw-data and averaged over the area of each capsule. The identified capsules were tracked during uptake and cellular trafficking to obtain $I_g/I_r(t)$ per capsule (further referred to as 'trajectory').

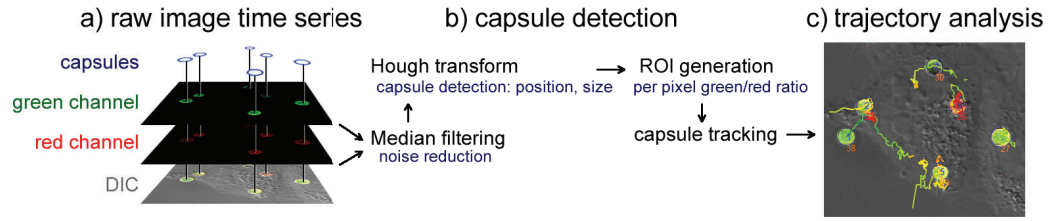

Figure S3 Workflow. Time-lapse image series of cellular capsule uptake were acquired with an automated confocal fluorescence microscope. To derive capsule-trajectories the indicated image processing routines were applied.

For all capsules whose trajectories showed an acidification of the local environment the duration of this process was measured by calculating the acidification time t_A which was derived from a sigmoidal fit $(I_g/I_r)(t) = (I_a-I_b)/(1+\exp((t-t_{50\%})/\Delta t))+I_b$ to the I_g/I_r-values (*cf.* Figure S4). According to Hartmann *et al*. [1] the acidification time was defined as $t_A = t_{90\%}-t_{10\%} = 2\Delta t\cdot\ln(9)$. Hereby, the time points $t_{90\%}$ and $t_{10\%}$ are derived from the equations $(I_r/I_g)(t_{10\%}) = 0.9\cdot(I_a-I_b)+I_b$ and $(I_r/I_g)(t_{90\%}) = 0.1\cdot(I_a-I_b)+I_b$.

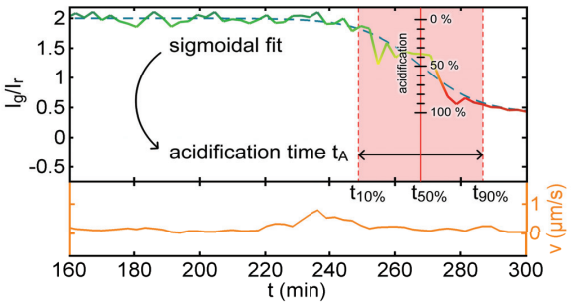

Figure S4 Capsule acidification time. The acidification time t_A is derived from a sigmoidal fit of the $I_g/I_r(t)$-trajectory data (upper part) and describes the duration of the acidification process. Furthermore, the velocity of each capsule is recorded.

References

1. Hartmann R, Weidenbach M, Neubauer M, Fery A, Parak WJ: **Stiffness-dependent in vitro uptake and lysosomal acidification of colloidal particles**. *Angew Chem Int Ed* 2015, 54 (8), 1365-1368
2. Gonzalez RC, Woods RE: **Digital Image Processing, 3rd Edition**. Upper Suddler River, New Jersey 07458: Prentice Hall Pearson Education, Inc; 2008.

Additional File 3:

Additional Trajectory pattern

As shown in Figure 4 (main manuscript), in some cases the acidification was not a continuous process. In 21 % of all analyzed trajectories temporary constant pH values at intermediate acidification levels occurred (see trajectories in Figure 4b, 4c and S5b). These trajectories were not considered for the evaluation shown in the box plot in Figure 4. In addition the table in Figure S5a shows the corresponding evaluation of the acidification times t_A including also these trajectories that showed an intermediate constant acidification level (exemplarily indicated for a selected trajectory with a white arrow in Figure S5b and S6b) with duration t_I (dark gray shaded area in Figure S6b). The statistics of the time span t_I was further examined for different clones as shown in Figure S6. Including node-containing trajectories into the analysis does not change the final conclusion of significantly lower acidification of lysosomal compartments inside cells of clone #1 in comparison to control cells. As visible from Figure S6 the duration of intermediate levels is also significantly increased in these cells indicating that the fusions frequency of acidic vesicles with the capsule-containing compartment might be reduced by overexpression of the V_1G_1 subunit.

a

All trajectories t_A (min)				
clone	**CTR#2**	**#1**	**#3**	**#7**
N	394	385	429	465
median	22.69	30.85	21.52	24.02
mean	30.45	42.25	28.45	32.92
Q1	12.83	17.95	13.14	12.55
Q3	38.81	52.79	34.95	42.51

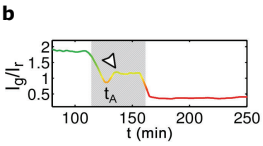

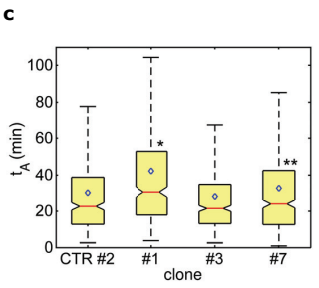

Figure S5 Duration of capsule acidification (all trajectories). All trajectories are considered including those with nodes. In a) the number of evaluated trajectories N, the mean/median values of the acidification time and the corresponding lower and upper quartiles (Q1 and Q3) are given. In b) a trajectory showing an intermediate constant acidification level (white arrow) is shown exemplarily. The corresponding t_A value corresponds to the gray shaded area. The boxplot in c) summarizes the table given in a). The blue diamonds correspond to the mean values. P-values were obtained from a two-tailed Wilcoxon–Mann–Whitney test: $p < 0.0001$ (*), $p < 0.36$ (**).

a

Plateau duration time t_I (min)				
clone	**CTR#2**	**#1**	**#3**	**#7**
%	24.1%	24.7%	16.1%	18.7%
median	22.67	41.01	20.44	33.53
mean	39.98	51.56	30.14	41.42
Q1	14.70	24.14	14.63	23.62
Q3	41.70	64.26	43.78	53.92

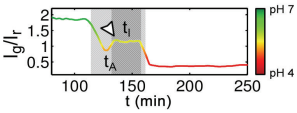

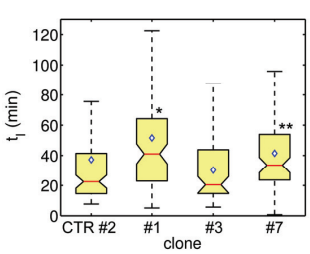

Figure S6 Duration of temporary constant intermediate pH-levels. The duration t_I was determined for all trajectories where nodes appeared. In a) the number of evaluated trajectories N, the mean/median values of the node duration and the corresponding lower and upper quartiles (Q1 and Q3) are given. In b) the node duration t_I is highlighted in dark gray in an exemplary trajectory showing an intermediate constant acidification level (white arrow). The boxplot in c) summarizes the table given in a). The blue diamonds correspond to the mean values. P-values were obtained from a two-tailed Wilcoxon–Mann–Whitney test. Additional significance levels: $p < 0.002$ (*), $p < 0.008$ (**).Mann–Whitney test: $p < 0.0001$ (*), $p < 0.36$ (**).

Additional File 4:

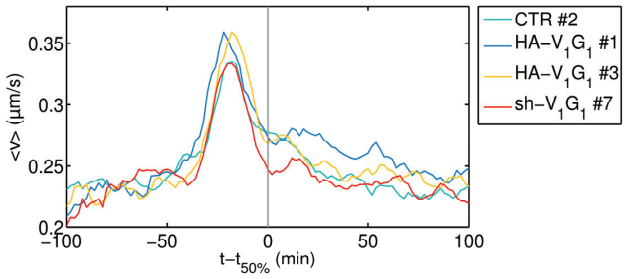

Figure S7 Mean velocity profile of capsule-based pH sensors during acidification.

Additional File 5:

Ultrastuctural Analysis via transmission electron microscopy

From the TEM images plenty of black dots that can be identified as glycogen, could be seen in all transfected cells, especially after 1 h (Figure 5 and Figures S8, S9, S10, and S11). The metabolism of glycogen provides the cell with energy in form of ATP. Figures S8b-c (CTR #1, 24 h), S10b and 5a.1 (CTR #2, 24 h), S11c-d, and 5f.1 (sh-V_1G_1, 24 h) show examples of how glycogen clearly co-localizes with lysosomes containing capsules. This new situation is reversible and should not interfere with the regular cell cycle. This is in agreement with other works [1, 2]. Transfected HA cells appeared more adapted to the presence of the capsules than sh cells as the reduction of the local accumulation of glycogen is slightly

more advanced in these cells after 24 h. Actually, the amount of glycogen in sh cells transfected with V_1G_1 plasmid (cells lacking this protein) after 24 h (Figures S11c-d and Figures 5f and 5f.1) is very similar to the amount found after 1 h (Figures S11a-b and Figures 5c and 5c.1).

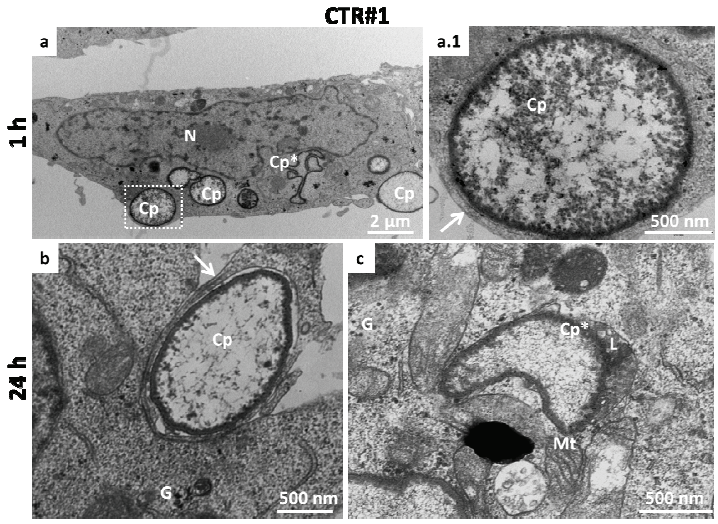

Figure S8 Morphological analysis of CTR #1 cells after 1 h (a, a.1) or 24 h (b, c) incubation with the capsules (Cp). N, Nucleus; Mt, Mitochondria; G, Glycogen; L, Lysosome. Stars, examples of deformed capsules. Dashed box, zoomed areas of representative capsules. Solid arrow, plasma membrane surrounding the capsules.

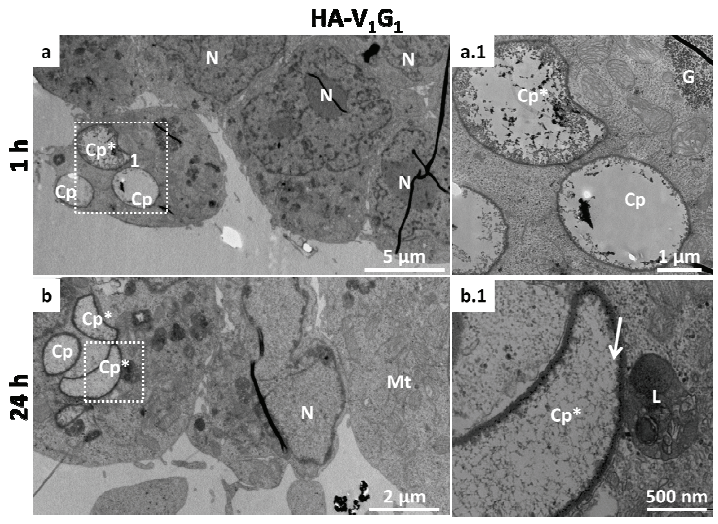

Figure S9 Morphological analysis of HA-V_1G_1 cells after 1 h (a, a.1) or 24 h (b, b.1) incubation with the capsules (Cp). N, Nucleus; Mt, Mitochondria; G, Glycogen; L, Lysosome. Stars, examples of deformed capsules. Dashed box, zoomed areas of representative capsules. Solid arrow, plasma membrane surrounding the capsules.

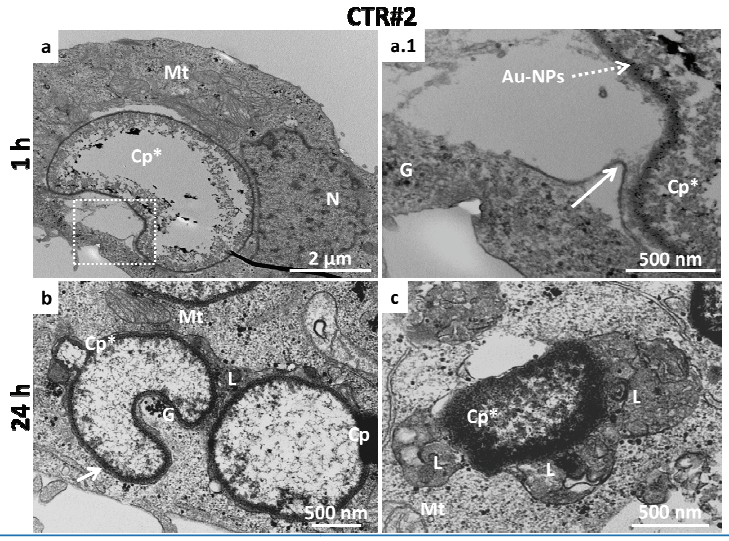

Figure S10 Morphological analysis of CTR#2 cells after 1 h (a, a.1) or 24 h (b, c) incubation with the capsules (Cp). N, Nucleus; Mt, Mitochondria; G, Glycogen; L, Lysosome. Stars, examples of deformed capsules. Dashed box, zoomed areas of representative capsules. Solid arrow, plasma membrane surrounding the capsules. Gold nanoparticles (Au-NPs, dashed arrow) of the capsule wall can be clearly seen.

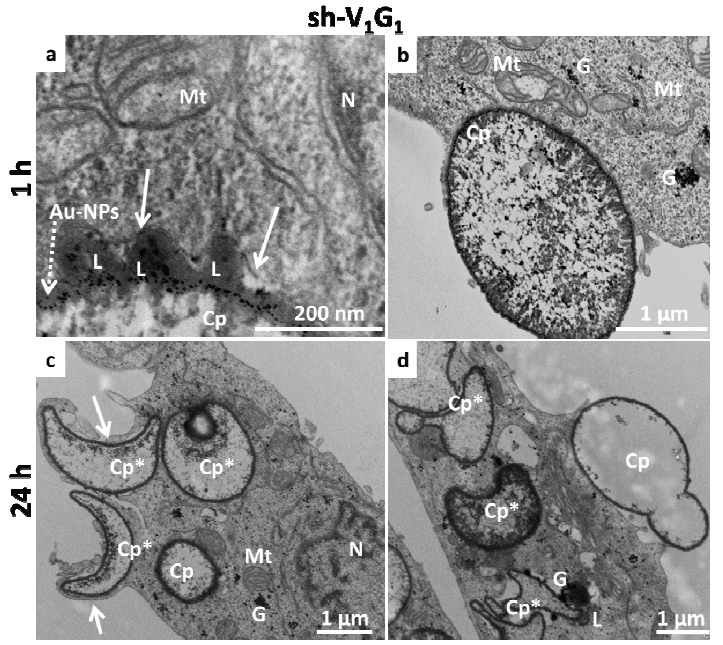

Figure S11 Morphological analysis of sh-V_1G_1 cells after 1 h (a, b) or 24 h (c, d) incubation with the capsules (Cp). N, Nucleus; Mt, Mitochondria; G, Glycogen; L, Lysosome. Stars, examples of deformed capsules. Dashed box, zoomed areas of representative capsules. Solid arrow, plasma membrane surrounding the capsules. Gold nanoparticles (Au-NPs, dashed arrow) of the capsule wall can be clearly seen.

References

1. Kastl L, Sasse D, Wulf V, Hartmann R, Mircheski J, Ranke C, Carregal-Romero S, Martinez-Lopez JA, Fernandez-Chacon R, Parak WJ *et al*: **Multiple Internalization Pathways of Polyelectrolyte Multilayer Capsules into Mammalian Cells**. *ACS Nano* 2013, **7**:6605-6618.
2. Rivera-Gil P, De Koker S, De Geest BG, Parak WJ: **Intracellular processing of proteins mediated by biodegradable polyelectrolyte capsules**. *Nano Lett* 2009, **9**:4398-4402.

Schweiger *et al. Journal of Nanobiotechnology* 2012, **10**:28
http://www.jnanobiotechnology.com/content/10/1/28

JOURNAL OF NANOBIOTECHNOLOGY

RESEARCH Open Access

Quantification of the internalization patterns of superparamagnetic iron oxide nanoparticles with opposite charge

Christoph Schweiger[1†], Raimo Hartmann[2†], Feng Zhang[2], Wolfgang J Parak[2], Thomas H Kissel[1] and Pilar Rivera Gil[2*]

Abstract

Time resolved quantitative colocalization analysis is a method based on confocal fluorescence microscopy allowing for a sophisticated characterization of nanomaterials with respect to their intracellular trafficking. This technique was applied to relate the internalization patterns of nanoparticles *i.e.* superparamagnetic iron oxide nanoparticles with distinct physicochemical characteristics with their uptake mechanism, rate and intracellular fate.

The physicochemical characterization of the nanoparticles showed particles of approximately the same size and shape as well as similar magnetic properties, only differing in charge due to different surface coatings. Incubation of the cells with both nanoparticles resulted in strong differences in the internalization rate and in the intracellular localization depending on the charge. Quantitative and qualitative analysis of nanoparticles organelle colocalization experiments revealed that positively charged particles were found to enter the cells faster using different endocytotic pathways than their negative counterparts. Nevertheless, both nanoparticles species were finally enriched inside lysosomal structures and their efficiency in agarose phantom relaxometry experiments was very similar.

This quantitative analysis demonstrates that charge is a key factor influencing the nanoparticle cell interactions, specially their intracellular accumulation. Despite differences in their physicochemical properties and intracellular distribution, the efficiencies of both nanoparticles as MRI agents were not significantly different.

Keywords: Superparamagnetic iron oxide nanoparticles (SPIONs), Intracellular distribution, Charge, Coating, Size, Quantitative correlation analysis, Colocalization

Background

The interaction of nanomaterials with cells and tissues is a key factor when considering their translation into clinical applications. Especially an effective accumulation of nanoparticles (NPs) inside certain tissues is beneficial for a great number of applications, such as hyperthermia, contrast enhancement in magnetic resonance imaging, cell tracking or theranostics [1-7]. Apart from colloidal stability, which is essential to ensure reproducibility as well as to influence the amount of cellular loading and toxicity, the surface chemistry/properties of the NPs control their cellular interactions [8]. Predominantly size, shape and surface charge of NPs influence their cellular internalization and distribution and thus their effective performance.

The overall uptake rate of nanoparticulate objects and their respective pathway of internalization can be manipulated by surface charge [9-11]. In general, cationic NPs have been found to display excellent properties for tracking applications as they enter cells with higher effectiveness [12] due to the interaction with the negatively charged glycocalix [13]. However, a higher degree of toxicity is often associated with these systems [14-17]. Nevertheless, also negatively charged NPs are massively incorporated by cells. In this respect it has to be mentioned that charged NPs strongly interact with serum proteins to form a protein corona [18-21], whose

* Correspondence: pilar.riveragil@physik.uniarburg.de
†Equal contributors
[2]Biophotonics Group and WZMW, Institute of Physics, Philipps University of Marburg, Renthof 7, Marburg D 35037, Germany
Full list of author information is available at the end of the article

formation also depends on the NP charge. The rate of NP uptake is important, as insufficient cellular accumulation of NPs *e.g.* magnetic NPs can lead to deficient usage for example as imaging probes [22].

Thus a precise knowledge of their internalization mechanisms, endosomal sorting and resulting intracellular pathways are crucial aspects governing their fate, efficiency or toxicity. So far most of the techniques employed to study NP-cells interactions are based on qualitative analysis; thus being prone to subjectivity or to errors in the interpretation of results.

Typically intracellular trafficking is studied using fluorescence microscopy. By comparing the fluorescent pattern of labeled and internalized NPs with the distribution of cellular organelles possible intracellular pathways can be derived for the material. Following endocytic uptake, NPs are generally trapped in vesicular compartments. The detection and imaging of typical proteins associated to those enclosed structures allows their identification and allocation in for example endosomes or lysosomes. If such image material is super-imposed with signal gained for example from labeled NPs, structures associated with NP uptake, transport and processing can be identified. To analyze the uptake and enrichment of NPs inside a certain organelle fluorescent labeling of both, the nanomaterial and the organelle is typically performed. The uptake study is based on the correlation of the emission of the labeled nanomaterial with fluorescence signal of the organelle. If both structures are colocalizing within the detection volume the overlay of the corresponding two fluorescence image channels (for example red and green) would result in a new color value (yellow). In a qualitative manner the degree of colocalization can be estimated by looking at the super-imposed image. As a matter of fact, any processing having impact on the image's histogram is influencing the "amount of yellow" in the overlay and altering the subjective impression of the degree of colocalization. For a sophisticated correlation of the image material of both structures, several approaches to perform a quantitative colocalization analysis exist. In intensity-based methods voxel or pixel intensities in both fluorescence channels are correlated by calculating for example Pearson's or Manders' colocalization coefficients [23,24]. In Li's approach the correlation between the variations of the intensity-distributions within both channels are analyzed [25]. In object-based approaches the imaged structures are transformed into binary objects and the overlap is quantified [24]. In live-cell imaging also methods for trajectory correlation of those binary objects have been introduced [26]. Nevertheless, as long as single nanoparticle detection and tracking is hard to realize by conventional confocal microscopy the relevance of trajectory correlation is quite low, although the results seem to bear good prospects due to the discrimination of false colocalization caused by low axial resolution.

In order to validate our analysis methodology as well as to correlate differences in the physicochemistry of the NPs to different cellular behavior, the NPs were synthesized according to different protocols to produce NPs with different physicochemical properties. Especially surface chemistry and thus an opposite charge was selected on purpose, to influence the internalization rates of the NPs and thus proof our methodology. Due to the different synthetic protocols used, the colloidal stability and the size distribution of both NPs were also altered. According to their great potential in biomedical applications [6,7,27,28], superparamagnetic iron oxide NPs (SPIONs) were selected as systems to investigate NP internalization patterns; firstly qualitatively *via* flow cytometry (Fluorescence-Activated Cell Sorting, FACS) and Confocal Laser Scanning Microscopy (CLSM) and then by quantitative correlation analysis. Additionally, possible alterations in the relaxation times in A549 lung carcinoma cells were quantitatively evaluated.

Results

Water-soluble SPIONs were synthesized either *via* aqueous coprecipitation [29] or *via* thermal decomposition of organometallic precursor molecules with subsequent phase transfer to aqueous solution [30-32]. Both methods lead to hydrophilic NPs suitable for biomedical applications.

The different synthesis strategies for formation of γ-Fe_2O_3 NPs clearly had an impact on the resulting NP morphology. Inorganic cores generated by aqueous co-precipitation following Massart's protocol [29] were found to be inhomogenously spherically-shaped. Those coming from thermal decomposition of organometallic precursor molecules in organic solvent had homogenous, almost spherical shape and better size distribution. Analysis of the Fe_2O_3 core diameters (*i.e.* the inorganic Fe_2O_3 part without the organic surface coating) on transmission electron microscopy (TEM) micrographs revealed mean diameters of 10.4 ± 2.4 nm and 10.8 ± 0.12 nm for the synthesis performed in aqueous and organic solution, respectively (see Additional file 1: Figure SI-1.c in the SI). Adsorptive attachment of poly(ethylene imine) (PEI) to stabilize the NPs in solution completed the synthesis of positively charged γ-Fe_2O_3-PEI NPs. In contrast, hydrophobic interaction *via* intercalation of polymer (poly(isobutylene-alt-maleic anhydride), PMA) strands between surfactant alkyl chains formed the final step in producing hydrophilic negatively charged γ-Fe_2O_3-PMA NPs [33]. It is important to point out that coupling PEI to the γ-Fe_2O_3 NPs turned out to be essential to stabilize the NPs generated by aqueous co-precipitation in solution. The absence of PEI led to strong agglomeration, making some kind of characterization procedure of the NPs (cf. Additional file 1: Figure SI-1.f) difficult. Hydrodynamic diameters for the two polymer-modified formulations, γ-Fe_2O_3-PEI and γ-Fe_2O_3-PMA NPs as measured by dynamic light scattering in

ultrapure water amounted to 16 ± 5 nm and 22 ± 7 nm, respectively (cf. Table 1). Both types of NP suspensions exhibited unimodal size distributions and zeta potentials of comparable absolute value, in numbers +53 ± 11 mV for γ-Fe_2O_3-PEI and −38 ± 6 mV for γ-Fe_2O_3-PMA (cf. Table 1). The impact of the preparation technology on magnetic features of the samples was investigated by monitoring the field-dependent magnetization with a SQUID (Superconducting QUantum Interference Device) system (cf. Table 1 and Additional file 1: Figure SI-2). All recorded curves showed lack of remanence and typical sigmoidal characteristics. The reader is referred to the SI (Additional file 1: § SI-1 and § SI-2) for a detailed description of the synthesis and physicochemical characterization of both NP formulations.

When incubating the lung carcinoma cell line A549 with fluorophore-bearing γ-Fe_2O_3 NPs, different uptake patterns were qualitatively observed for the two species. First of all it has to be remarked that due to a significant inferior colloidal stability of γ-Fe_2O_3-PEI-FITC NPs in growth medium (10 % serum-containing media) compared to γ-Fe_2O_3-PMA-Dy636 NPs it turned essential to establish a suitable exposure NP dose as well as the composition of the cell media, in which both NP systems had sufficient colloidal stability. An iron ([Fe]) concentration of 1 μg/ml in a 5 % serum-containing media turned out to be a good compromise between agglomeration, cell survival, and optical detection. Higher concentrations gave a better fluorescence signal (due to the fluorophores in the NP shell) but, in the case of γ-Fe_2O_3-PEI-FITC NPs suffered from strong agglomeration problems. NPs at lower concentrations were difficult to detect optically (cf. Additional file 1: Figure SI-6.a.i). It has to be pointed out that the concentrations are not absolutely comparable in terms of NPs per volume, as the mass comprises besides the inorganic Fe_2O_3 cores also the organic coating around their surface, which is different for both types of preparations. The quantity of serum proteins had to be lowered from 10 % (corresponding to the normal A549 growth media) to 5 % (cf. Additional file 1: Figure SI-6.a.ii and SI-6.a.iii). After having established the cell culture and NP incubation conditions the uptake of both formulations was studied with FACS and with CLSM. Positively γ-Fe_2O_3-PEI-FITC and negatively γ-Fe_2O_3-PMA-Dy636 charged NPs were internalized in a steady manner over the examined period of 24 hours. Nevertheless, the uptake of γ-Fe_2O_3-PEI-FITC NPs was taking place to an extent of about 40% within the first 4 h after incubation (cf. Figure 1). In contrast to that, γ-Fe$_2O_3$-PMA-Dy636 NPs were found to accumulate in cells only to a small extent within the first hours. The major fraction of these NPs was incorporated between time points 4 and 24 hours (cf. Figure 1), mostly after 8 h (cf. Additional file 1: Figure SI-6.b). Single-peaked mean fluorescence intensity signals indicated that there were no cell population subsets with lower degrees of NP incorporation. Incubation of the cells under the same circumstances as for FACS measurements and characterization by CLSM confirmed these results (cf. Additional file 1: Figure SI-6.b.i). Interestingly, negatively charged γ-Fe_2O_3-PMA-Dy636 NPs were faster incorporated by the cells in the presence of positively charged γ-Fe_2O_3-PEI-FITC NPs (cf. Additional file 1: Figure SI-6.b.i and SI-6.b.vi). These results suggest that upon concomitant incubation, complexes from positively and negatively charged NP were formed due to electrostatic interaction, finally leading to an increase in the uptake rate of the negatively charged NPs.

The impact of different charge and surface coating of both NP carriers on their intracellular pathways was analyzed by CLSM. For this purpose A549 cells, which were exposed to both NPs for different periods of time (individually or concomitantly) were stained for different organelles *i.e.* early endosomes, lysosomes, actin cytoskeleton and the plasma membrane (cf. Additional file 1: SI-6.b). Figure 2 shows the results of the intracellular localization of the NP complexes, whereby positively and negatively NPs were added simultaneously to the cells. In addition, the colocalization of each NP carrier with the different organelles upon time can be seen in Additional file 1: Figure SI-6.b. After 30 min the first fluorescent signal of γ-Fe_2O_3-PEI-FITC NPs was detectable. However the γ-Fe_2O_3-PMA-Dy636 NPs were firstly visualized after 60 min. Interestingly, at this early time points negatively charged γ-Fe_2O_3-PMA-Dy636 NPs clearly colocalized spatially with early endosomes near to the plasma membrane, whereas the positively charged counterparts, γ-Fe_2O_3-PEI-FITC NPs, were not found inside the endosomes. The endosomes migrate towards lysosomal structures wherein the first NPs were detectable after approximately 4 8 hours. After 24 h most of the NPs γ-Fe_2O_3-PEI-FITC as well as γ-Fe_2O_3-PMA-Dy636 were found inside the lysosomes. One can speculate that the absence of γ-Fe_2O_3-PEI-FITC NPs in the endosomes is due to the presence of PEI, which might manage to transfer the NPs out of the endosomes due to the proton-sponge effect [34]. In this case the NPs

Table 1 Physicochemical parameters of SPIONs as used in this work

	hydrodynamic diameter [nm]	polydispersity index	zeta potential [mV]	saturation magnetization [emu g^{-1}]
γ Fe_2O_3 PEI	16.2 ± 5.4	0.144 ± 0.019	+53.2 ± 11.0	23.7
γ Fe_2O_3 PMA	22.1 ± 7.1	0.321 ± 0.025	38.0 ± 5.6	16.4

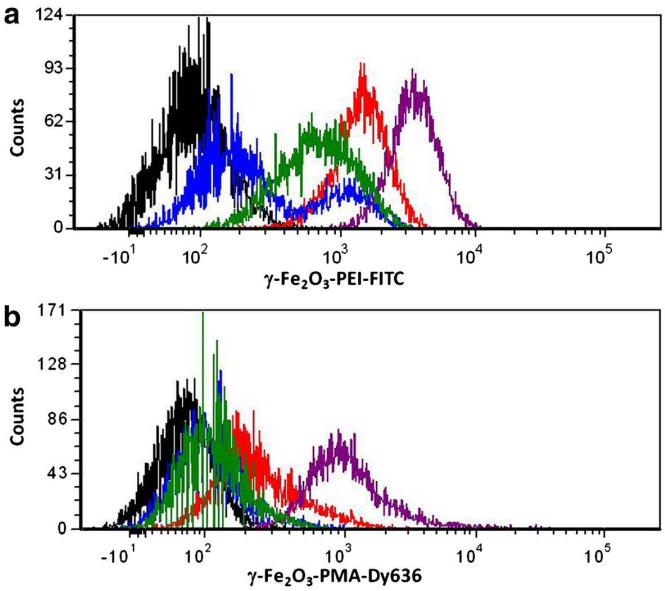

Figure 1 Cellular uptake kinetics of nanoparticle formulations (a) γ Fe_2O_3 PEI FITC and (b) γ Fe_2O_3 PMA Dy636. Cells were incubated with distinct amounts of the respective particle systems (1 μg/ml [Fe]) for time periods of 0 min (black line), 15 min (blue line), 60 min (green line), 4 h (red line), and 24 h (purple line). Fluorescence intensities were recorded by means of flow cytometry for a total of 10,000 events on channels FITC (excitation 488 nm) and APC A (630 nm).

should be found free in the cytosol of the cell. To confirm this assumption, the actin cytoskeleton was stained and the possible colocalization of the free NPs was studied. As can be seen in Figure 2 (see also Additional file 1: Figure SI-6.b.vii), γ-Fe_2O_3-PEI-FITC NPs were not found at detectable level in the cytosol of the cells. As expected γ-Fe_2O_3-PMA-Dy636 NPs were also not found there but rather inside vesicular structures as their counterparts, γ-Fe_2O_3-PEI-FITC NPs did.

Colocalization studies *via* CLSM images without further data treatment are merely qualitative in nature so that different labeling efficiencies of the two NP systems as well as the different optical properties of the fluorophores conjugated to the NPs can induce erroneous interpretations. In order to get absolute comparability between the intracellular localization of γ-Fe_2O_3-PEI-FITC and γ-Fe_2O_3-PMA-Dy636 NPs a quantitative colocalization analysis of both NPs with the different organelles was performed upon time (cf. Methods and Supporting Information) [35]. As can be seen in Figure 3, the results confirmed the qualitative analysis by looking at the overlay of the different fluorescence channels (cf. Figure 2). Immediately after addition of the NPs to the cells, γ-Fe_2O_3-PEI-FITC NPs did not colocalize with the endosomes (cf. Figure 3.a) though in contrast γ-Fe_2O_3-PMA-Dy636 NPs did to some extend (cf. Figure 3.b). Approximately 45 % of all γ-Fe_2O_3-PMA-Dy636 NP signal was overlapping with the endosomes but only 22 % of endosome signal was overlapping with the NPs at 4 h incubation time. At later points of time both NP types were found in the lysosomes (cf. Figure 3.c and 3.d). A significant fraction of γ-Fe_2O_3-PEI-FITC NPs colocalized with lysosomal structures after 8 h incubation time, but quite few lysosomes contained NPs. Interestingly, the analysis suggests that at early incubation times some γ-Fe_2O_3-PEI-FITC NPs were already in the lysosomes. After 24 h incubation time, a large fraction of γ-Fe_2O_3-PEI-FITC and γ-Fe_2O_3-PMA-Dy636 NPs colocalized with the lysosomes and a large fraction of lysosomes were containing NPs of both nature.

Finally, the impact of different charge and surface coatings of both NP carriers on their magnetic properties was studied. Relaxation parameters were gathered for agarose phantoms containing either freely dispersed NPs (γ-Fe_2O_3-PEI-FITC or γ-Fe_2O_3-PMA-Dy636) or cells loaded with certain amounts of SPIONs following incubation. Parameters of manufactured phantoms containing doped cells were dependent on the effective amounts of iron per cell. As expected, A549 incubation with high iron molarities caused non-proportional enhancement of intracellular accumulation. For γ-Fe_2O_3-PEI-FITC NPs, maximum incubation with a total of 100 μg [Fe] (as determined with ICP-OES) for instance led to intracellular iron levels of 6.9 pg per cell and subsequent relaxation rates R_2^* of 23.0 s^{-1}, where R_2^* is indicative of absolute proton relaxation and signal darkening level. An identical application scheme of

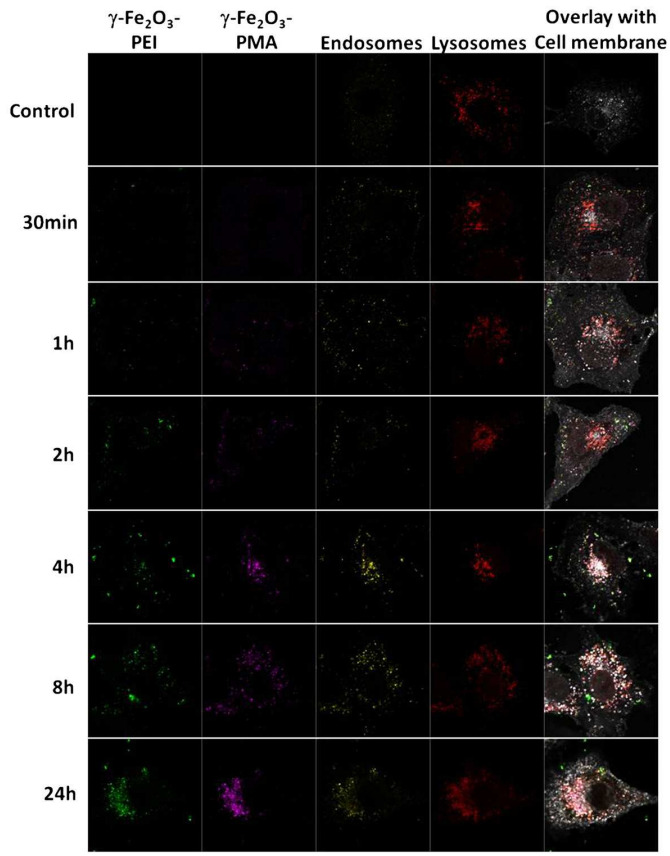

Figure 2 Intracellular localization of SPIONs. Cells were incubated concomitantly with both SPIONs (γ Fe_2O_3 PEI FITC and γ Fe_2O_3 PMA Dy636) at a final concentration of 1 μg/ml [Fe] for time periods of 30 min, 1 h, 2 h, 4 h, 8 h, and 24 h. Cells were then stained with wheat germ agglutinin, for EEA1 and for LAMP 1 to visualize the Plasma Membrane (white), the Endosomes (yellow) and the Lysosomes (red), respectively. Fluorescence images were recorded with a LSM. Additionally, the same experiments were performed with cells incubated with each NP system (see Additional file 1).

γ-Fe_2O_3-PMA-Dy636 NPs resulted in values of 1.4 pg per cell and R_2^* of 8.2 s^{-1}. In comparison to that, relaxation rates R_2^* reached 140 s^{-1} and 134 s^{-1} for freely dispersed PEI-FITC and PMA-Dy636 NPs at equal "incubation" levels (data not shown). Despite the discrepancy in absolute R_2^* numbers, the efficiency of both SPION set-ups in reducing transverse relaxation times, often denoted as relaxivity r_2^*, turned out to be almost equivalent as derived from comparison of the slopes of the best-fit lines: 1.70 μM^{-1} s^{-1} and 1.72 μM^{-1} s^{-1} for freely dispersed PEI-FITC and PMA-Dy636 NPs (data not shown), 1.61 μM^{-1} s^{-1} and 1.58 μM^{-1} s^{-1} for cell containing PEI-FITC and PMA-Dy636 NPs, respectively (cf. Figure 4).

Discussion

Several models are reported concerning the internalization of differently charged SPIONs [36]. However, only little efforts have been made so far to directly compare NP systems of equal dimensions and opposite charge with respect to their cellular uptake rate and intracellular fate. Especially a profound quantification of the colocalization of the NPs with different cellular structures is missing. Consequently, our approach consisted in eliminating size and shape as a key factor for NP uptake by keeping the dimensions of the two formulations constant. We hypothesized that, under these circumstances, the invasion into cells was predominantly dependent on the surface properties provided by the polymer coating, *i.e.* surface potential and the colloidal stability of incubated carriers.

Firstly, the synthesis strategy seems to affect the magnetic properties of the fabricated SPIONs. It is well-known that magnetization of inorganic colloids is determined primarily by their crystal diameter [37]. The results from TEM statistical analysis display a number-weighted and

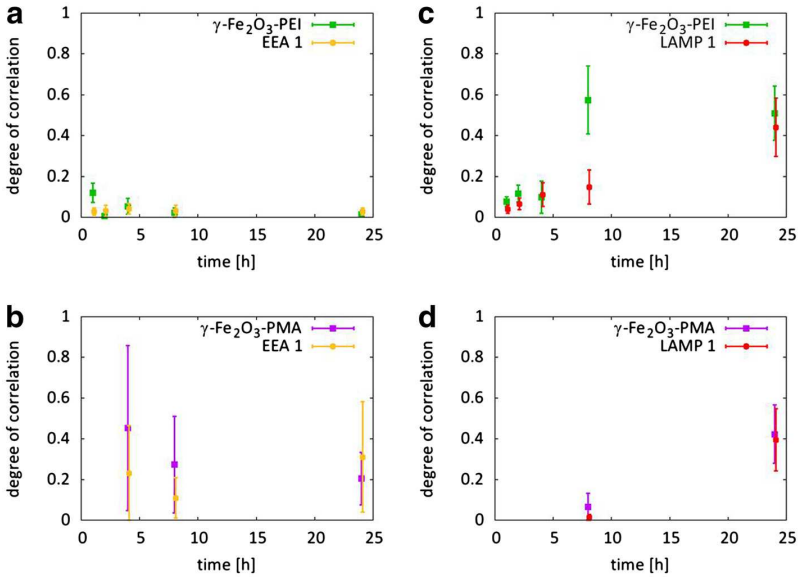

Figure 3 Quantification of colocalization. Manders' coefficients M_1 and M_2 represent the correlation between the intracellular locations of γ Fe_2O_3 PEI (green) and γ Fe_2O_3 PMA (pink) with early endosomes (yellow) and lysosomes (red), respectively.

therefore one-dimensional quantity (cf. the TEM data in Additional file 1: Figure SI-1.c). As the magnetic moment of nanoparticles depends on their volume, the relative contribution of particles with larger size to the overall magnetization is higher. A mathematical approximation of a volume-weighted mean for both samples gave values of 11.5 nm each. Since mean diameters are virtually equal, we speculate that microstructural features of the magnetic cores are responsible for the different saturation magnetizations. On the one hand, the crystalline domains in the γ-Fe_2O_3-PMA NPs might be smaller than those in the γ-Fe_2O_3-PEI NPs. Another explanation for the differing M_{sat} values might be the existence of a magnetically dead layer on the maghemite surface which does not contribute to the collective magnetic moment of γ-Fe_2O_3 NPs. The general reduction in magnetization with respect to bulk maghemite can be attributed to several mechanisms such as spin canting or spin-glass-like behavior of the surface spins, both of them being effects which become more and more important with decreasing particle size [38,39]. Polymer shielding of the naked Fe_2O_3 cores induced further lowering of gram-standardized saturation magnetizations, which becomes logical as the organic material does not add to the magnetic properties of the respective particle systems. As already pointed out, direct mass-correlated comparison of both types of NPs is complicated due to the fact that they have different surface coatings and thus mass contributions of organic material. Moreover, organic ligands used to stabilize SPIONs might lead to quenching of surface magnetic moments [40]. The sigmoidal curves displayed in the SI (Additional file 1: §2) are indicative for superparamagnetism of both γ-Fe_2O_3-PEI and γ-Fe_2O_3-PMA NPs. This feature is not only beneficial due to the availability of giant magnetic moments, but also due to the

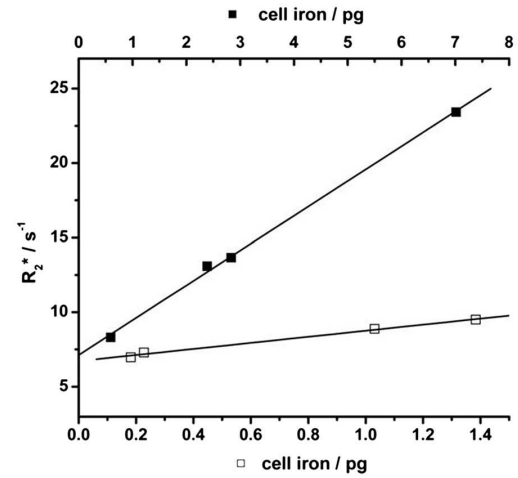

Figure 4 Relaxation rates R_2* of agarose phantoms containing 10^5 cells doped with SPIONs. Data points represent intracellular iron levels after incubation with increasing amounts of γ Fe_2O_3 PEI (■) and γ Fe_2O_3 PMA (□), respectively (1, 10, 30 and 50 μg [Fe]).

Schweiger et al. Journal of Nanobiotechnology 2012, 10:28
http://www.jnanobiotechnology.com/content/10/1/28

reduction in agglomeration tendency which is attributable to complete paramagnet-like loss of magnetization at zero external fields.

Secondly, differences in the charge of the NPs clearly affected their intracellular internalization route, rate and distribution. This statement was achieved by combination of the results obtained FACS and with CLSM followed by a time resolved quantitative analysis of the internalization patterns of both NP types. The conclusions drawn by eye-based interpretation of superimposed, fluorescent images presenting the distribution of NPs and certain cellular structures are strongly biased by any acquisition parameters and image processing. For a first impression or a proof of principle this method may be sufficient but the generalization of any observation has to be not taken literally. The averaging over colocalization data of several individual experiments and the imaging of various cells for each data point is needed. For quantification, the described procedure of time-resolved colocalization analysis is a well suited tool that certainly helps to retrace NP internalization in a reproducible manner.

The saturable, steady, but non-linear uptake pattern of positively charged γ-Fe_2O_3-PEI NPs strongly suggests adsorptive endocytosis as the main mechanism of cell uptake. This is supported by the fact that electrostatic interaction between the positively charged NPs and the negatively charged glycocalix certainly favors fast attachment to the cell membrane and subsequent ingestion of cationic species. It also goes along with the fact that the colloidal stability of the γ-Fe_2O_3-PEI NPs is limited. Furthermore, it has to be noted that positively charged NPs have been reported to interact differently with serum proteins at physiological pH than negatively charged NPs [21]. Different protein coronas are likely to influence cellular uptake. Finally, from the CLSM images of the cells incubated with positive γ-Fe_2O_3-PEI NPs over time and over different concentrations (cf. Additional file 1: Figure SI-6) it can be observed that accumulation of the positively charged NPs in the extracellular side of the cell membrane plays a key role, not only on the adsorption to the cell membrane (as commented before) but also on the fast rate of internalization. It appears that uptake of the positively charged NPs occurred only after membrane accumulation of the NPs, thus directly related to a specific NP concentration. These results suggested that there might be a concentration threshold responsible for the fast internalization as it happens for zwitterionic NPs [41]. Above the threshold NPs are rapidly internalized, however below this threshold NPs should be less efficiently internalized. Thus special attention should be paid to this insight. On the other hand, negatively charged γ-Fe_2O_3-PMA NPs seem to follow common endocytic internalization processes and even receptor-mediated endocytosis cannot be excluded. The uptake was steady and constant over time and more important, it was independent from membrane accumulation, thus excluding unnecessary thresholds. Furthermore, the negatively charged NPs strongly interact with serum proteins leading to the formation of a protein corona around the surface of the NPs [19-21]. Many of these proteins have specific ways of cellular entry. For example transferrin, which has been demonstrated to adsorb to the surface of negatively charged PMA-coated NPs [42] is well known to internalize *via* receptor-mediated endocytosis [43]. In this way, the uptake of these NPs may be controlled by the protein corona.

Sufficient and fast loading of certain cell types with SPIONs is for example desired for tracking purposes *via* magnetic resonance imaging [44]. The reason for this is the concentration-dependent enhancement of transverse proton relaxation in the vicinity of areas containing magnetic iron oxide NPs, thus leading to quick fading of MR signals and gain of contrast in T_2-weighted images [45]. Based on the quantification of the intracellular iron concentration *via* ICP-OES (cf. Additional file 1: Figure SI-5), γ-Fe_2O_3-PEI NPs accumulate to a higher degree inside the cells compared to the negative γ-Fe_2O_3-PMA NPs. Thus γ-Fe_2O_3-PEI NPs should perform better than their anionic counterpart when being used for cell tracking tasks. However, it has to be pointed out that despite an optimization of the cell culture media and NP dose (*i.e.* reduced serum quantity as well as adequate NP dose) to increase the stability of the γ-Fe_2O_3-PEI-FITC NPs, agglomeration was still observed for this formulation and the agglomerates were strongly attached to the cell membrane (cf. Additional file 1: Figure SI-6.a.ii and SI-6.a.iii). Trypsinization of the cells did not remove the agglomerates of γ-Fe_2O_3-PEI-FITC NPs attached to the cell membrane and thus signal could also result from γ-Fe_2O_3-PEI-FITC NPs only adherent to the outer cell membrane.

Finally, as an alternative way for probing the efficiency of both types of NPs as contrast agents for MRI, agarose phantoms containing NP-labeled cancer cells were subjected to MR measurement sequences. Phantom matrices act as versatile human tissue equivalents, as alteration of their basic composition allows for the imitation of specific intracorporal regions and appendant relaxation properties [46]. Most effective signal darkening in T_2-weighted MRI maps, denoted as high absolute relaxation rate values R_2^*, was observed for freely dispersed NPs and, to a lower extent, cell dispersions carrying large amounts of γ-Fe_2O_3-PEI NPs. As a more reliant measure of proton relaxation yield/efficiency, transversal relaxivity r_2^* values were calculated by normalization of the results to the iron concentration. The differences in relaxivity r_2^* between freely dispersed NPs and cell-confined NPs were relatively small and were supposed to result from less efficient proton spin interaction of magnetic NPs upon entrapment inside

cells or cell organelles. Thus, besides concentration of magnetic materials as the main factor for signal improvement, intracellular confinement plays a second, yet subordinate role in this context and has an impact on the detected proton relaxation times [47]. Coming back to the magnetization properties of the tested NP formulations, we predicted higher molar relaxivities for the system γ-Fe_2O_3-PEI due to enhanced magnetic interactions with surrounding proton spins. Surprisingly, the efficiencies of both tested NP formulations were found to be in the same range.

Conclusions

The physicochemical properties of the generated NPs (mainly charge and colloidal stability) were found to be a key factor governing the internalization into cells. The internalization patterns (i.e. uptake rates and intracellular localization) of SPIONs synthesized either directly in water or in organic solutions and with opposite charged, were completely different. The use of qualitative techniques like FACS and CLSM give interesting initial information in this regard however, a quantitative analysis is crucial to make statistically relevant conclusions. By real time quantitative correlation analysis the kinetic of NP internalization could be elucidated. Negatively charged SPIONs were found firstly in endosomes and lately in lysosomes whereas positively charged SPIONs were found exclusively inside lysosomes. Interestingly, not all the involved vesicles were found to be colocalizing with the NPs all over the time. Thus, elucidating dynamics in NPs trafficking inside the cells depending on their charge.

Methods

For a detailed description of the experimental procedure as well as for other additional experiments, the reader is referred to the supporting information (Additional file 1).

Nanoparticle synthesis

γ-Fe_2O_3 NPs were prepared following standard protocols since the acquirement of exact information about the crystalline structures of these kind of NPs is very controversial [48]. γ-Fe_2O_3 NPs were synthesized either *via* aqueous coprecipitation, according to the Massart protocol [29] or *via* thermal decomposition of organometallic precursor molecules following a published protocol by Hyeon and co-workers [30].

Physicochemical characterization

Hydrodynamic diameters and ζ-potentials of hydrophilic NPs after polymer functionalization were assessed by dynamic light scattering (DLS). For magnetization studies, the lyophilized NP materials were placed into a Magnetic Property Measurement System MPMS® equipped with a 5 T magnet (Quantum Design, San Diego, CA) using superconducting quantum interference device (SQUID) technology.

Cell culture and uptake studies

The human lung adenocarcinoma cell line A549 was maintained in Dulbecco's Modified Eagle Medium (DMEM) supplemented with 10 % serum. The uptake kinetics was analyzed with (1) flow cytometry and (2) CLSM. For (1), some cells were incubated with either γ-Fe_2O_3-PEI-FITC or with γ-Fe_2O_3-PMA-Dy636 NPs at fixed iron concentrations (1 μg/ml). The concentration of iron [Fe] was measured by ICP-OES (inductively coupled plasma - optical emission spectroscopy) (see Additional file 1: §1.g). Following determined incubation times (0 min, 15 min, 60 min, 4 h, 24 h), cells were analyzed with respect to their fluorescent intensity *via* FACS, using a FACSCanto II (BD Biosciences, San Jose, CA). For (2), the cells were incubated with each NP system as well as with both NP systems concomitantly (Additional file 1: Figure S6.b). Each NP species was diluted to a final iron concentration of 1 μg/ml and again the cells were incubated for different periods of time (30 min, 1 h, 2 h, 4 h, 8 h and 24 h). Cells were prepared for labeling as described in the supporting information. The cell membrane was stained with fluorescent wheat germ agglutinin and actin was colored applying fluorescent phalloidin (results are presented in the SI, Additional file 1: Figure SI-6). To visualize the metabolic pathways of the NPs, immunostainings of lysosomal structures and early endosomes were performed. Lysosomes were stained using monoclonal mouse anti-human LAMP1/CD107a antibodies (Developmental Studies Hybridoma Bank), while early endosomes were labeled with polyclonal rabbit anti-human EEA1 immunoglobulin (Cell Signaling). To excite and collect all fluorescence markers *i.e.* both types of NPs, cell membrane, actin cytoskeleton, lysosome and endosome simultaneously, the secondary antibodies used for the cellular structures had to be carefully chosen to minimize crosstalk, especially between the NPs and the cell membrane. Therefore the dyes conjugated to the antibodies were selected to absorb in the UV region of the spectra. In detail donkey anti-mouse DyLight405-ABs (Jackson ImmunoResearch) were used at 1 μg/ml to detect the LAMP1 specific primary antibodies while goat anti-rabbit AlexaFlour430 conjugated immunoglobulin (Invitrogen) was used as a secondary antibody for early endosomes at 30 μg/ml (both diluted in PBS containing 1 % BSA). For examination a LSM 510 Meta (Zeiss) microscope was used equipped with lasers emitting at 405, 488, 543 and 633 nm.

Quantitative analysis of colocalization studies

The intracellular distributions of both nanoparticle species were correlated with the locations of early endosomes and lysosomes over time to study the intracellular trafficking of both systems (see Additional file 1: SI, §7). Therefore, A549 adenocarcinoma cells were incubated with either γ-Fe_2O_3-PEI-FITC or with γ-Fe_2O_3-PMA-Dy636 NPs at fixed iron concentrations (1 μg/ml) for different periods of time followed by an immunostaining of either early endosomes or lysosomes, performed as described above. For each of the combinations given in Additional file 1: SI, §7, Table 1 at least 20 cells were imaged using a highly corrected CLSM. The degree of colocalization of fluorescence signal originating from nanoparticles and labeled endosomes (EEA1) or lysosomes (LAMP1) was quantified by calculating Manders' distinct colocalization coefficients M_1 and M_2 for the confocal image material: $M_1 = \frac{\sum R_{i,coloc}}{\sum Ri} \in [0,1]$ and $M_2 = \frac{\sum G_{i,coloc}}{\sum Gi} \in [0,1]$ R_i and G_i are the pixel intensities of pixel i in channel R (nanoparticles) and G (endosomes or lysosomes). "coloc" are pixels in which colocalization was observed. In our calculations M_1 represents the degree of colocalization of fluorescence signal from one nanoparticle species with signal coming either from stained endosomes or lysosomes while M_2 covers the situation with regard to the organelles. An image providing a high value of M_1 but a low value for M_2 can be interpreted as follows: Most of the detected particles are present in the particular cellular compartments but the largest fraction of these organelles is not including nanoparticles anyhow.

Agarose phantom relaxometry

A549 cells were plated at a density of 100,000 cells per well and were incubated with suspensions of SPIONs of different types γ-Fe_2O_3-PEI and γ-Fe_2O_3-PMA) and concentrations (1, 10, 30 and 50 μg/ml) for 24 hours. After PBS washing and trypsinization, cell numbers were counted using a Neubauer chamber. Quantification of cell-internalized iron was realized by ICP-OES after cell lysis in concentrated nitric acid (600 μl) for 4 hours. Phantoms for MR relaxometry were produced by dispersing 10^5 SPION-doped A549 cells in agarose (1 % w/v). Magnetic resonance (MR) imaging studies concerning the T_2 and T_2^* relaxation times of the respective phantoms were carried out on a 7 T Bruker ClinScan 70/30 USR (Bruker BioSpin, Rheinstetten, Germany). For measurements of transverse T_2 relaxation times, spin-echo multicontrast sequences were run at T_R values of 2000 ms, varying spin echo times T_E (10 120 ms with an increment of 10 ms), field of view 75x75 mm, matrix 128x128 and slice thickness 0.6 mm. Data quantification was achieved by evaluating such created DICOM images. Relaxation times T_2 could be derived by analyzing regions of interest (ROI) within T_2 maps generated by the overlay of successive spin-echo images, using a monoexponential fitting of the signal intensity (I) decay curve: $I(t) = I_0 \exp(-t/T_2)$, where I_0 is the signal magnitude at equilibrium and t the particular echo time. Effective transverse relaxation times (T_2^*) were calculated from T_2^*-weighted images taken with the following settings: gradient-echo multicontrast with $T_R = 350$ ms, multiple spin echo times T_E (3 32 ms), field of view 89x89 mm, matrix 128x128, slice thickness 0.5 mm. T_2^* values were obtained correspondingly by fitting the MRI signal intensities of the acquired maps versus echo times T_E.

Additional file

Additional file 1: Supporting Information.

Competing interests

We (the authors) wish to confirm that there are no known conflicts of interest associated with this publication and there has been no significant financial support for this work that could have influenced its outcome.

Authors' contributions

The concept was designed by WJP, THK, and PRG. Experiments and data analysis were performed by CS, RH, FZ, and PRG. All authors read and approved the final manuscript.

Authors' information

Dr. C. Schweiger studied Pharmacy and obtained his PhD under the supervision of Prof. Dr. T. H. Kissel in the Department of Pharmaceutical technology in the Philipps University of Marburg.
R. Hartmann studied Physics at the University of Marburg and is currently doing his PhD under the supervision of Dr. P. Rivera Gil and Prof. Dr. W. J. Parak.
Dr. F. Zhang received his bachelor degree in 2000 from Biology School of Inner Mongolia University and his Ph. D degree in 2006 from Shanghai Institute of Applied Physics, Chinese Academy of Sciences. After a postdoctoral stay in the group of Prof. Dr. W. J. Parak in the University of Marburg, Dr Zhang moved as a senior research fellow to Washington University (Bioengineering Dep.). He is currently employed as a professor and a Ph.D advisor in Biology School in Inner Mongolia Agricultural University.
Prof. Dr. W. J. Parak obtained his PhD in biophysics at the Ludwig Maximilians Universität München, Germany in 1999 in the group of Prof. Dr. Hermann Gaub. After a postdoctoral stay at the University of California, Berkeley, CA, USA in the group of Prof. Dr. Paul Alivisatos he returned 2002 to Munich as Assistant Professor. Since 2007 he is Full Professor at the Physics Department of the Philipps Universität Marburg, Germany.
Prof. Dr. T. H. Kissel is currently retired. Until August 2012, he was Professor of Pharmaceutics & Biopharmacy and Department Head at Philipps Universität Marburg, Germany, where he has been since 1991. He received his B.S. (Pharmacy) from Freiburg University (1971), his M. S. (Chemistry, 1974) and his Ph.D. (Medicinal Chemistry, 1976) from Marburg University.
Dr. P. Rivera Gil studied Pharmacy in Spain and obtained her PhD in Pharmacology at the Free University Berlin. She is currently a senior researcher in the group of Prof. Dr. W. J. Parak.

Acknowledgment

The authors thank Eva Mohr, Department of Pharmaceutics and Biopharmacy, Marburg, Germany for assistance in the cell culture lab and Clemens Pietzonka for helpful discussions concerning magnetic phenomena. The authors are grateful to Dr. Azhar Z. Abassi for the synthesis and TEM images of the γ Fe_2O_3 PMA NPs. This work was supported by the German Research Foundation (DFG, SPP1313, grant PA794/4 2 to WJP and PRG) and the European Commission (grant Nandiatream to WJP).

Author details
[1]Pharmaceutics and Biopharmacy, Faculty of Pharmacy, Philipps University of Marburg, Ketzerbach 63, Marburg D 35037, Germany. [2]Biophotonics Group and WZMW, Institute of Physics, Philipps University of Marburg, Renthof 7, Marburg D 35037, Germany.

Received: 2 April 2012 Accepted: 28 May 2012
Published: 10 July 2012

References

1. Jordan A, Scholz R, Wust P, Fahling H, Felix R: **Magnetic fluid hyperthermia (MFH): cancer treatment with AC magnetic field induced excitation of biocompatible superparamagnetic nanoparticles.** *J Magn Magn Mater* 1999, **201:**413 419.
2. Gonzales M, Krishnan KM: **Synthesis of magnetoliposomes with monodisperse iron oxide nanocrystal cores for hyperthermia.** *Journal of Magnetism and Magnetic Materials* 2005, **293:**265.
3. Nasongkla N, Bey E, Ren JM, Ai H, Khemtong C, Guthi JS, Chin SF, Sherry AD, Boothman DA, Gao JM: **Multifunctional polymeric micelles as cancer targeted, MRI ultrasensitive drug delivery systems.** *Nano Letters* 2006, **6:**2427 2430.
4. Huh YM, Jun YW, Song HT, Kim S, Choi JS, Lee JH, Yoon S, Kim KS, Shin JS, Suh JS, Cheon J: **In vivo magnetic resonance detection of cancer by using multifunctional magnetic nanocrystals.** *Journal Of The American Chemical Society* 2005, **127:**12387 12391.
5. Rivera Gil P, Yang F, Thomas H, Li L, Terfort A, Parak WJ: **Development of an assay based on cell counting with quantum dot labels for comparing cell adhesion within cocultures.** *Nano Today* 2011, **6:**20 27.
6. Jenkins SI, Pickard MR, Granger N, Chari DM: **Magnetic nanoparticle mediated gene transfer to oligodendrocyte precursor cell transplant populations is enhanced by magnetofection strategies.** *ACS Nano* 2011, **5:**6527 6538.
7. Cho HS, Dong Z, Pauletti GM, Zhang J, Xu H, Gu H, Wang L, Ewing RC, Huth C, Wang F, Shi D: **Fluorescent, superparamagnetic nanospheres for drug storage, targeting, and imaging: a multifunctional nanocarrier system for cancer diagnosis and treatment.** *ACS Nano* 2010, **4:**5398 5404.
8. Mailander V, Landfester K: **Interaction of Nanoparticles with Cells.** *Biomacromolecules* 2009, **10:**2379 2400.
9. Harush Frenkel O, Rozentur E, Benita S, Altschuler Y: **Surface charge of nanoparticles determines their endocytic and transcytotic pathway in polarized MDCK cells.** *Biomacromolecules* 2008, **9:**435 443.
10. Chung YI, Kim JC, Kim YH, Tae G, Lee SY, Kim K, Kwon IC: **The effect of surface functionalization of PLGA nanoparticles by heparin or chitosan conjugated Pluronic on tumor targeting.** *Journal Of Controlled Release*, **143:**374 382.
11. Ge YQ, Zhang Y, Xia JG, Ma M, He SY, Nie F, Gu N: **Effect of surface charge and agglomerate degree of magnetic iron oxide nanoparticles on KB cellular uptake in vitro.** *Colloids And Surfaces B Biointerfaces* 2009, **73:**294 301.
12. Villanueva A, Canete M, Roca AG, Calero M, Veintemillas Verdaguer S, Serna CJ, Morales MD, Miranda R: **The influence of surface functionalization on the enhanced internalization of magnetic nanoparticles in cancer cells.** *Nanotechnology* 2009, **20**.
13. Martin AL, Bernas LM, Rutt BK, Foster PJ, Gillies ER: **Enhanced Cell Uptake of Superparamagnetic Iron Oxide Nanoparticles Functionalized with Dendritic Guanidines.** *Bioconjugate Chemistry* 2008, **19:**2375 2384.
14. Luo JT, Xiao K, Li YP, Lee JS, Xiao WW, Gonik AM, Agarwal RG, Lam KS: **The effect of surface charge on in vivo biodistribution of PEG oligocholic acid based micellar nanoparticles.** *Biomaterials* 2011, **32:**3435 3446.
15. Xia T, Kovochich M, Liong M, Zink JI, Nel AE: **Cationic polystyrene nanosphere toxicity depends on cell specific endocytic and mitochondrial injury pathways.** *ACS Nano* 2008, **2:**85 96.
16. Breunig M, Lungwitz U, Klar J, Kurtz A, Blunk T, Goepferich A: **Polyplexes of polyethylenimine and per N methylated polyethylenimine cytotoxicity and transfection efficiency.** *Journal Of Nanoscience And Nanotechnology* 2004, **4:**512 520.
17. Petersen H, Fechner PM, Martin AL, Kunath K, Stolnik S, Roberts CJ, Fischer D, Davies MC, Kissel T: **Polyethylenimine graft poly(ethylene glycol) copolymers: Influence of copolymer block structure on DNA complexation and biological activities as gene delivery system.** *Bioconjugate Chemistry* 2002, **13:**845 854.
18. Walczyk D, Bombelli FB, Monopoli MP, Lynch I, Dawson KA: **What the Cell "Sees" in Bionanoscience.** *Journal of the American Chemical Society* 2010, **132:**5761 5768.
19. Röcker C, Pötzl M, Zhang F, Parak WJ, Nienhaus GU: **A Quantitative Fluorescence Study of Protein Monolayer Formation on Colloidal Nanoparticles.** *Nature Nanotechnology* 2009, **4:**577 580.
20. Cedervall T, Lynch I, Lindman S, Berggård T, Thulin E, Nilsson H, Dawson KA, Linse S: **Understanding the nanoparticle protein corona using methods to quantify exchange rates and affinities of proteins for nanoparticles.** *Proceedings of the National Academy of Sciences of the United States of America* 2007, **104:**2050 2055.
21. Lundqvist M, Stigler J, Elia G, Lynch I, Cedervall T, Dawson KA: **Nanoparticle size and surface properties determine the protein corona with possible implications for biological impacts.** *Proceedings of the National Academy of Sciences of the United States of America* 2008, **105:**14265 14270.
22. Huang HC, Chang PY, Chang K, Chen CY, Lin CW, Chen JH, Mou CY, Chang ZF, Chang FH: **Formulation of novel lipid coated magnetic nanoparticles as the probe for in vivo imaging.** *Journal Of Biomedical Science* 2009, **16:**86.
23. Gonzalez RC, Woods RE: *Digital Image Processing*. 3rd edition. Upper Saddle River, NJ: Prentice Hall; 2008.
24. Manders EMM, Verbeek FJ, Aten JA: **Measurement Of Colocalization Of Objects In Dual Color Confocal Images.** *Journal Of Microscopy Oxford* 1993, **169:**375 382.
25. Li Q, Lau A, Morris TJ, Guo L, Fordyce CB, Stanley EF: **A Syntaxin 1, Galpha (o), and N Type Calcium Channel Complex at a Presynaptic Nerve Terminal: Analysis by Quantitative Immunocolocalization.** *The Journal of Neuroscience* 2004, **24:**4070 4081.
26. Vercauteren D, Deschout H, Remaut K, Engbersen JFJ, Jones AT, Demeester J, De Smedt SC, Braeckmans K: **Dynamic Colocalization Microscopy To Characterize Intracellular Trafficking of Nanomedicines.** *Acs Nano* 2011, **5:**7874 7884.
27. Pankhurst QA, Connolly J, Jones SK, Dobson J: **Applications of magnetic nanoparticles in biomedicine.** *Journal Of Physics D Applied Physics* 2003, **36:** R167 R181.
28. Rivera Gil P, Hühn D, del Mercato LL, Sasse D, Parak WJ: **Nanopharmacy: Inorganic nanoscale devices as vectors and active compounds.** *Pharmacological Research* 2010, **62:**115 125.
29. Bee A, Massart R, Neveu S: **Synthesis of Very Fine Maghemite Particles.** *Journal of Magnetism and Magnetic Materials* 1995, **149:**6 9.
30. Hyeon T: **Chemical synthesis of magnetic nanoparticles.** *Chem Commun* 2003, **8:**927 934.
31. Casula MF, Jun YW, Zaziski DJ, Chan EM, Corrias A, Alivisatos AP: **The Concept of Delayed Nucleation in Nanocrystal Growth Demonstrated for the Case of Iron Oxide Nanodisks.** *Journal of the American Chemical Society* 2006, **128:**1675 1682.
32. Casula MF, Floris P, Innocenti C, Lascialfari A, Marinone M, Corti M, Sperling RA, Parak WJ, Sangregorio C: **Magnetic Resonance Imaging Contrast Agents Based on Iron Oxide Superparamagnetic Ferrofluids.** *Chemistry Of Materials* 2010, **22:**1739 1748.
33. Lin C AJ, Sperling RA, Li JK, Yang T Y, Li P Y, Zanella M, Chang WH, Parak WJ: **Design of an amphiphilic polymer for nanoparticle coating and functionalization.** *Small* 2008, **4:**334 341.
34. Akinc A, Thomas M, Klibanov AM, Langer R: **Exploring polyethylenimine mediated DNA transfection and the proton sponge hypothesis.** *Journal of Gene Medicine* 2005, **7:**657 663.
35. Zinchuk V, Zinchuk O, Okada T: **Quantitative Colocalization Analysis of Multicolor Confocal Immunofluorescence Microscopy Images: Pushing Pixels to Explore Biological Phenomena.** *Acta Histochemica et Cytochemica* 2007, **40:**101.
36. He C, Hu Y, Yin L, Tang C, Yin C: **Effects of particle size and surface charge on cellular uptake and biodistribution of polymeric nanoparticles.** *Biomaterials*, **31:**3657 3666.
37. Kneller EF, Luborsky FE: **Particle Size Dependence of Coercivity and Remanence of Single Domain Particles.** *Journal of Applied Physics* 1963, **34:**656.
38. Lu AH, Salabas EL, Schuth F: **Magnetic nanoparticles: Synthesis, protection, functionalization, and application.** *Angewandte Chemie International Edition* 2007, **46:**1222 1244.
39. Fiorani D, Testa AM, Lucari F, D'Orazio F, Romero H: **Magnetic properties of maghemite nanoparticle systems: surface anisotropy and interparticle interaction effects.** *Physica B Condensed Matter* 2002, **320:**122 126.
40. Paulus PM, Bonnemann H, van der Kraan AM, Luis F, Sinzig J, de Jongh LJ: **Magnetic properties of nanosized transition metal colloids: the influence of noble metal coating.** *European Physical Journal D* 1999, **9:**501 504.
41. Jiang X, Röcker C, Hafner M, Nienhaus GU: **Endo and Exocytosis of Zwitterionic Quantum Dot Nanoparticles by Living Cells.** *ACS Nano*, **4:**6787 6797.

42. Jiang X, Weise S, Hafner M, Röcker C, Zhang F, Parak WJ, Nienhaus GU: **Quantitative Analysis of the Protein Corona on FePt Nanoparticles formed by Transferrin Binding.** *J R Soc Interface* 2010, **7:**S5 S13.
43. Karin M, Mintz B: **Receptor Mediated Endocytosis of Transferrin in Developmentally Totipotent Mouse Teratocarcinoma Stem Cells.** *Journal of Biological Chemistry* 1981, **256:**3245 3252.
44. Himmelreich U, Dresselaers T: **Cell labeling and tracking for experimental models using Magnetic Resonance Imaging.** *Methods* 2009, **48:**112 124.
45. Laurent S, Boutry S, Mahieu I, Vander Elst L, Muller RN: **Iron Oxide Based MR Contrast Agents: from Chemistry to Cell Labeling.** *Current Medicinal Chemistry* 2009, **16:**4712 4727.
46. Park SM, Nyenhuis JA, Smith CD, Lim EJ, Foster KS, Baker KB, Hrdlicka G, Rezai AR, Ruggieri P, Sharan A, *et al*: **Gelled versus nongelled phantom material for measurement of MRI induced temperature increases with bioimplants.** *Ieee Transactions on Magnetics* 2003, **39:**3367 3371.
47. Tanimoto A, Oshio K, Suematsu M, Pouliquen D, Stark DD: **Relaxation effects of clustered particles.** *Journal of Magnetic Resonance Imaging* 2001, **14:**72 77.
48. Corrias A, Mountjoy G, Loche D, Puntes V, Falqui A, Zanella M, Parak WJ, Casula MF: **Identifying Spinel Phases in Nearly Monodisperse Iron Oxide Colloidal Nanocrystal.** *J Phys Chem C* 2009, **113:**18667 18675.

doi:10.1186/1477 3155 10 28
Cite this article as: Schweiger *et al.*: Quantification of the internalization patterns of superparamagnetic iron oxide nanoparticles with opposite charge. *Journal of Nanobiotechnology* 2012 **10**:28.

Submitted to Nano Today, DRAFT ONLY

REVIEW

Colloidal nanoparticles induce changes in cellular morphology

Xiaowei Ma[a,b*], Raimo Hartmann[a*], Dorleta Jimenez de Aberasturi[a,c], Fang Yang[d,e], Stefaan J. Soenen[f], Bella Manshian[f], Jonas Franz[g], Daniel Valdeperez[a], Beatriz Pelaz[a], Norbert Hampp[d,e], Christoph Riethmüller[h], Henning Vieker[i], Natalie Freese[i], Armin Gölzhäuser[i], Michael Simonich[j], Robert Tanguay[j], Xing-Jie Liang[b#], Wolfgang J. Parak[a,c#]

[a] Fachbereich Physik, Philipps Universität Marburg, Marburg, Germany
[b] Chinese Academy of Sciences (CAS) Key Laboratory for Biological Effects of Nanomaterials and Nanosafety, National Center for Nanoscience and Technology, Beijing, China
[c] CIC Biomagune, San Sebastian, Spain
[d] Fachbereich Chemie, Philipps Universität Marburg, Marburg, Germany
[e] Material Science Center, Philipps Universität Marburg, Marburg, Germany
[f] Biomedical MRI Unit/MoSAIC, Catholic University of Leuven, Leuven, Belgium
[g] nAnostic Institute, Center for Nanotechnology, University of Münster, Germany
[h] Serend-ip GmbH, Center for Nanotechnology, Münster, Germany
[i] Fakultät für Physik, Universität Bielefeld, Bielefeld, Germany
[j] OSU Sinnhuber Aquatic Research Laboratory (SARL), Oregon, USA

[*] both authors contributed equally to this work
[#] corresponding authors: liangxj@nanoctr.cn; wolfgang.parak@physik.uni-marburg.de

Received 9 December 2014, in revision

KEYWORDS
Nanoparticles;
Au NPs;
Cellular morphology;
Cytotoxicity;
Viability;
Cellular response

Summary Exposure of cells to colloidal nanoparticles (NPs) can have concentration-dependent harmful effects. Mostly, such effects are monitored with biochemical assays or probes from molecular biology, *i.e.* viability assays, gene expression profiles, *etc.*, neglecting that the presence of NPs can also drastically affect cellular morphology. In the case of polymer-coated Au NPs we demonstrate that upon NP internalization, cells undergo lysosomal swelling, alterations in mitochondrial morphology, disturbances in actin and tubulin cytoskeleton and associated signaling, reduction of focal adhesion contact area and number of filopodia. Appropriate imaging and data treatment techniques allow for quantitative analyses of these concentration-dependent changes. Abnormalities in morphology occur at similar nanoparticle concentrations as the onset of reduced cellular viability. Cellular morphology is thus an important quantitative indicator to verify harmful effects of NPs to cells, without requiring biochemical assays but relying on appropriate staining and imaging techniques.

Introduction

Colloidal nanoparticles (NPs) are incorporated by living cells, regardless of whether this is intended for certain delivery applications (*i.e.* tumor targeting), or not due to leakage of NPs into the environment (*i.e.* air, water) [1]. Once in contact with cells, the

typical uptake scenario involves endocytosis [2-4]. Interaction of NPs with cells has been demonstrated to trigger dose-dependent effects in cells (which obviously strongly depend on the nature of NPs and on the type of cells), which can ultimately lead to cell death. Details about the uptake mechanisms of NPs by cells, as well as the molecular signaling cascades which are being triggered also involving molecular mechanisms for toxic effects are well described in the literature [5-7]. Most of these studies aim at understanding the interaction of NPs with cells at a molecular level. However, effects of the NPs on cells are also manifested at the level of cell morphology.

In multiple studies the disruption of organelles and other subcellular structures caused by NPs have been reported. Gold NPs for example have been described to have a profound effect on several intracellular organelles/structures and functions associated with morphological changes. First, this applies to mitochondria. Mitochondria are one of the most important organelles in cells. Disruption of mitochondria can result in a wide range of diseases and disorders. It has been reported that the decrease of mitochondrial activity reflects acute cytotoxicity of colloidal NPs. Many studies have found that exposure of cells to Au NPs was accompanied by an increased level of reactive oxygen species (ROS), which is associated with malfunctioned mitochondria. Pan *et al.* observed that Au NPs of an average diameter of 1.4 nm induce cytotoxicity by oxidative stress, which is indicated by endogenous ROS production, compromised mitochondrial potential, integrity, and mitochondrial substrate reduction [8]. Interestingly, Chompoosor *et al.* reported that 2 nm Au NPs with different hydrophobic alkyl tails could generate significant amount of ROS at concentrations that do not even affect mitochondrial activity [9]. Wang *et al.* speculated that the selective targeting and damaging effects of Au nanorods to the mitochondria of cancer cells could be used in tumor therapy, while normal cells maintain intact mitochondria [10]. Second, effects on lysosomes have been reported. Most NPs will eventually be accumulated inside acidic organelles after following their endocytic pathway. Being the major degradative compartment of eukaryotic cells, the lysosome is a high capacity organelle responsible for macromolecular homeostasis. Previous work has shown that large amounts of Au NPs aggregated in the lysosomes can lead to lysosome alkalinization. This is associated with the impairment of vacuolar V-ATPases, which regulate lysosome acidification. Consequently, the lysosome-based degradative pathway-autophagy is affected, which leads to a disruption of cellular homeostasis [11]. Swelling of lysosomes upon NP enrichment has also been reported [12, 13]. Third, NPs have been shown to interfere with the cellular cytoskeleton. The cytoskeleton is responsible for anchoring organelles, maintaining cell morphology, and intercellular connections. Previous findings by Pernodet *et al.* indicate that the diameter, the stretching state, and the density of actin filaments in human dermal fibroblasts were affected in a concentration-dependent manner upon treatment with Au NPs. These effects might cause major changes in cell shape, cell spreading, cell adhesion, and cell growth [14, 15]. The same group also found that different sized Au NPs (13 or 45 nm) can induce cytoskeletal filament disruption to a different extent, without changing actin or beta-tubulin protein levels [16]. A further study by Yang *et al.* showed that the actin F-fibers were disrupted to various extents depending on the aggregation state of Au NPs. The authors reported varying decrease in F-actin fiber intensity and thickness and the appearance of actin dots. The lack of actin-fiber formation and the appearance of actin dots rather than long fibers were correlated with the presence of Au NPs in the cytosol which were thought to cause depolymerization of actin [17]. Furthermore, the morphology of cell junctions may be subject to changes [18] following NP exposure. The intracellular disruption of the cytoskeletal network caused by Au NPs has been found to be associated with the disruption of cell-cell adhesion. It was found that exposure to highly concentrated Au NPs will significantly reduce the area of focal adhesion complexes (FACs) which leads to an increase in the amount of free vinculin, a major structural component of FACs [19]. Lin *et al.* also found different sized Au NPs could cause loosening of the intercellular tight junctions that are joining individual cells [20]. Finally, NP impact on the cytoskeleton may influence cellular migration. Rafailovich's group found that the presence of Au NPs in human adipose-derived stromal cells could result in a concentration-dependent increase in population doubling times, a decrease in cell motility, and cell-mediated collagen contraction [21]. Considering that cell migration plays a crucial role in tumor growth and metastasis, therefore, NPs that can impede the mobility of tumor cells are of great interest in preclinical research. In summary, there is clear evidence that the uptake of Au NPs by cells has a (concentration-dependent) effect on their morphology.

In the present work, we provide a comprehensive study on how *in vitro* uptake of Au NPs affects cellular morphology and intracellular organelles/structures. Thus, the focus of this work is not on signal pathways, but rather on morphological changes.

Polymer-coated, anionic Au NPs were chosen for this study [22-24]. These NPs have been fully characterized for their colloidal properties and interaction with cells within the last 10 years. They are colloidally stable with a narrow size distribution (4.8 ± 0.7 nm core diameter) [25, 26]. These NPs are incorporated by cells *via* endocytic pathways and accumulated inside acidic intracellular vesicles, in particular lysosomes [27-29]. In contrast to other NPs such as cadmium selenide (CdSe) or silver (Ag) NPs

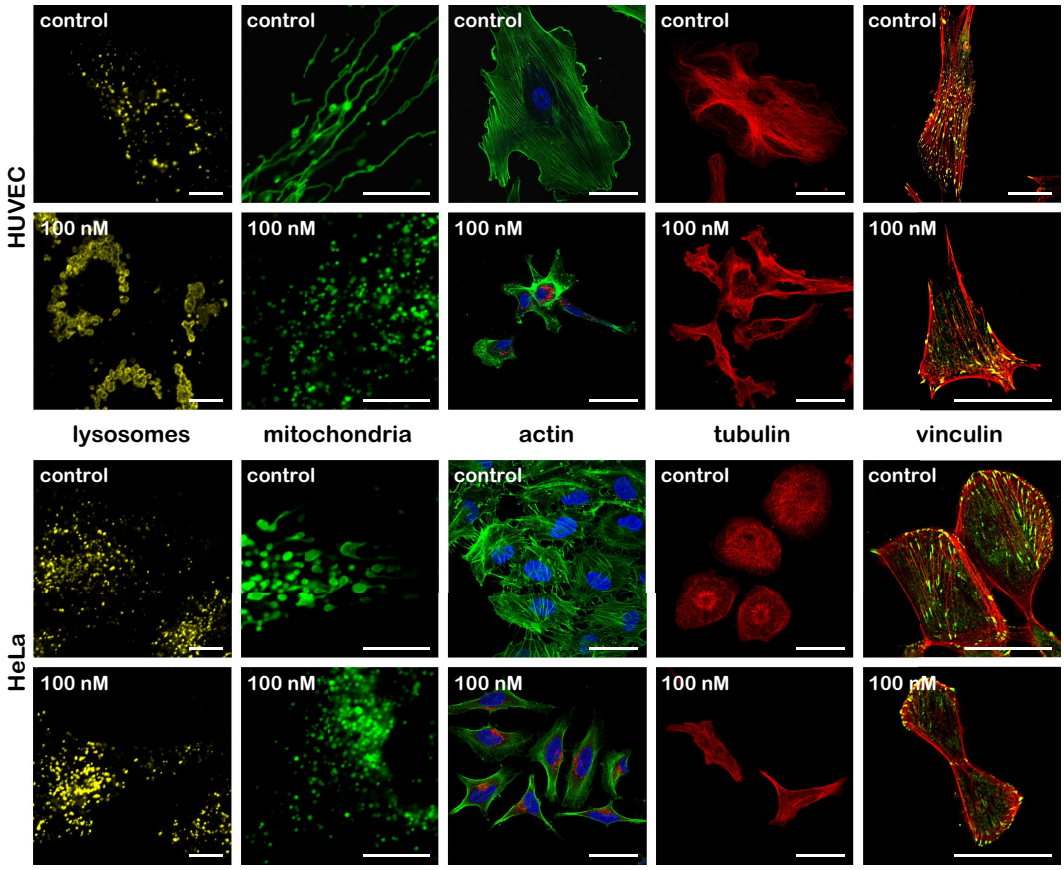

Figure 1 Morphological changes of different cellular structures without and after c_{NP} = 100 nM Au NP treatment in HUVECs and HeLa cells. All scale bars correspond to 50 µm except for lysosomes and mitochondria (10 µm). Lysosomes were stained with anti-lysosomal associated protein 1 (LAMP1) antibodies (shown here in yellow false colors). Mitochondria were stained by expressing green fluorescent protein GFP-labeled E1 alpha pyruvate dehydrogenase in the cells (shown in green). Actin fibers were stained by phalloidin (shown in green), nuclei stained with DAPI (shown in blue), together with the red fluorescence of incorporated NPs. Tubulin was stained using an anti-alpha tubulin antibody (shown here in red). Vinculin was stained with an anti-vinculin mouse monoclonal antibody (shown in green), together with actin staining with phalloidin (shown in red).

the Au NPs are not composed of an intrinsically toxic material such as Ag or CdSe NPs, yet several concentration-dependent cytotoxic responses such as production of ROS have been described *in vitro* [19, 30]. Reported IC_{50} concentration values for particles of similar size distribution vary between a few hundred nM [19, 31] and a few µM or even mM [32, 33] depending on surface coating, the cell types used and incubation conditions. The NPs used in the present study are bigger than the ultra-small clusters of 1.3 nm core size Au NPs for which size-specific effects have been reported [8]. In the case of the here used 4-5 nm core diameter NPs toxic effects do not only originate from their surface coating, but also due to the Au core [30], which possesses some catalytic activity. For this study two well established and commonly used mammalian cell lines were used. These were the human umbilical vein endothelial cells (HUVECs) and the human cervical cancer cell line (HeLa).

Materials and Methods

Polymer-coated Au NPs [22-24] with a core diameter of d_c = 4 ± 1 nm (as determined by transmission electron microscopy (TEM)), a hydrodynamic diameter of d_h = 12 ± 3 nm (as determined from the number distribution of dynamic light scattering (DLS) in water), and a zeta-potential of ζ = -30 ± 2 nm (as determined from laser Doppler anemometry (LDA) in water) were used, *cf.* the Supporting Information for the raw data. Due to a fluorophore which is located inside the inner hydrophobic polymer shell [34], and thus in first order not present at the NP surface, these NPs are fluorescent and thus can be visualized with confocal microscopy. HUVECs and HeLa cells were exposed to the NPs at concentrations ranging from 0.1 - 200 nM (in serum containing medium, for details *cf.* the Supporting Information). Their uptake

was quantified by confocal microscopy and standard viability and proliferation assays (Live/Dead Viability Assay [35], Cell Proliferation Assay [36], Resazurin Assay [37], and MTT Assay [38]). Different cellular structures (lysosomes, mitochondria, actin and microtubule network, vinculin, and filopodia) were optionally labeled by immunostaining or transfection, and changes in their geometry, as well as changes in the morphology of the whole cell (*i.e.* cell spreading) were analyzed from fluorescence or atomic force microscopy (AFM) images by digital image analysis tools. In addition, the effects of the NPs on expression of genes related to the cytoskeleton, as well as actin- and tubulin polymerization assays were carried out [39, 40].

Results and Discussion

1. Au NP location and internalization rate

As expected the Au NPs were internalized by both HeLa cells and HUVECs. While we did not make attempts to unravel the detailed uptake pathways (*i.e.* by blocking of certain pathways by specific inhibitors or by colocalization experiments with objects of known pathways of internalization) it is known from previous experiments with NPs of similar surface chemistry that they are endocytosed by cells [19]. Experiments have shown contribution of macropinocytosis (see for example the formation of macropinocytic cups upon NP internalization, *cf.* TEM images in the Supporting Information) as well as caveolin-mediated endocytosis [28]. Presence of the Au NPs in the lysosomes after cellular internalization was proven by colocalization of the fluorescence-labeled NPs with green fluorescent protein (GFP)-labeled lysosomal associated protein 1 (LAMP1), employing confocal laser scanning microscopy. LAMP1 which was expressed in HUVEC and HeLa cells as a marker for lysosomal membranes (*cf.* the Supporting Information for data). Quantification of internalized NPs demonstrate that the uptake rate was higher and that transport of the Au NPs into the lysosomes (25, 50, 100 nM) by HUVECs (in 2% serum supplemented medium) was faster than by HeLa cells (in 10% serum supplemented medium). In case of HUVECs saturation of cells with NPs was already seen after less than 5 hours, whereas in HeLa cells the amount of internalized NPs still increased after 15 hours. After 24 hours of incubating cells with NPs at concentrations c_{NP} > 5 nM (at lower concentrations the signal of the fluorescently-labeled Au NPs was too weak for reliable quantitative analysis, *i.e.* in the range of the auto-fluorescence of cells). In the case of HUVECs incubation with the double amount of NPs (from 25 to 50 nM) resulted also in more or less the double amount of internalized NPs while this was not observed for HeLa cells where the internalization rate slightly decreases with increasing concentration of NPs. This again points out that internalization of the Au NPs by HeLa cells is less effective. Even within 24 hours of exposure HeLa cells were not saturated with Au NPs at the used concentrations. Uptake of the Au NPs by HeLa cells thus follow a much slower kinetics compared to the HUVECs (all raw data are shown in the Supporting Information). We have also noted that differences in the amount of serum in the culture medium may play a role in the NP uptake, as serum in general reduces NP uptake [26].

2. Effect of Au NPs on cell viability, proliferation, and other indicators

It is well known that even inert Au NPs can cause cytotoxic effects on cells at elevated exposure concentrations and times. In order to investigate a useful range of concentrations we took into account two considerations. First, in case of biological *in vitro* labeling experiments NP concentrations are typically chosen in the range of a few to a few tens of nM, in order to provide sufficient effect. Second, as according to Paracelsus everything at high enough concentration is toxic, we performed *in vivo* toxicity experiments with zebra fish embryos. Exposure of zebrafish embryos to NP concentrations up to 700 nM was not significantly associated with mortality or any morphological abnormality (data are presented in the Supporting Information), which demonstrates the relatively low toxic profile of the here used Au NPs. Guided by these two considerations we decided to investigate NP concentrations in the range from 0.1 to 100 nM, which covers the range of typical *in vitro* applications, but does not cause any acute abnormality *in vivo*. Using this range of concentrations we performed several standard biochemical assays to investigate the concentration-dependent effect of Au NPs on HUVECs and HeLa cells. As exposure time for all following experiments we chose 24 h. In a first set of assays effects on cellular enzymatic activity were probed: i) oxidation of resazurin/Alamar blue by cellular dehydrogenases (Resazurin assay/Alamar blue assay), likely by mitochondrial enzymes, ii) reduction of 3-(4,5-dimethylthiazol-2-yl)-2,5-diphenyltetrazolium bromide (MTT) by oxidoreductases (MTT assay), and iii) conversion of cell permeable calcein acetoxymethyl (AM) by esterases (first part of a commercial Live/Dead assay). In HUVECs the resazurin as well as the MTT assays showed reduction of cell viability at around $c_{NP,50} \approx 10$ nM (all raw data can be found in the Supporting Information, a summary of all effects is shown in Table 1), whereas in case of the Alamar blue and the “Live” assay these effects were detected at higher concentrations of NPs. In the case of HeLa cells effect of NPs on cell viability was much lower, and exposure with NPs up to concentrations of 100 nM could in most assays not reduce viability to its half. Still, also in HeLa cells concentration

Table 1 Summary of the experimental results, in which cellular reaction to exposure to Au NPs was probed. Reactions are shown in the trend column. $c_{NP,50}$ describes the NP concentration at which half of the maximum effect was obtained. If a sigmoidal fit could be applied to the data the uncertainty is given in addition. The full data sets corresponding to this table are shown in the supporting information. Ab = antibody.

				Trend		$c_{NP,50}$ range [nM]	
Feature	**Parameter**	**Variable**	**Derived from**	***HUVEC***	***HeLa***	***HUVEC***	***HeLa***
NP uptake	Integrated intensity	I_{NP}	NP fluorescence	+++	+		
Viability	Viability	V_{res}	Resazurin	--	-	3.5-**11**-33	
		V_{AB}	Alamar blue	--	o	55-**65**-77	
		V_{MTT}	MTT	--	-	2.7-**8.4**-27	
	Dead/Live	D	Live/Dead stain	+	+	30+	80+
	Proliferation rate	p	DNA synthesis	--	-	0.49-**0.54**-0.59	0.073-**0.12**-0.20
	ROS	R	Pyocyanin/N-acetyl-L-cysteine	++	+	10+	10+
Cell morphology	Area	A_{cell}	CellMask blue	--	-	18-**26**-37	39-**49**-61
			Actin (phalloidin)	--	-	2+	10+
	Form factor	F_{cell}		o	-		8+
Lysosomes	Area	A_{lyso}	LAMP1 (Ab)	+++	o	5+	
	Fraction of cell area	A_{lyso}/A_{cell}	LAMP1 (Ab) / actin (phalloidin)	++	++	30+	10+
	Intensity	I_{lyso}	LAMP1 (Ab)	o	+		10+
Mitochondria	Form factor	F_{mito}	CellLight - mitochondria	++	++	3.0-**4.7**-7.3	2.0-**2.5**-3.1
	Zernike 0^{th} order	Z^{0}_{mito}		+++	+	2.9-**4.4**-6.8	1.8-**2.3**-2.9
Cytoskeleton	Filopodia: Area	A_{vinc}	Vinculin (Ab)	--	-	50+	50+
		A_{filo}	AFM	--	o/-	2+	25+
	Filopodia: Number	N_{filo}		--	-	2+	50+
	Filopodia: Volume	V_{filo}		-	-	2+	25+
	Filopodia: Height	h_{filo}		o	o		
	Actin: Texture contrast	$T_{act,cont}$	Actin (phalloidin)	+	--	5+	1.7-**3.3**-6.3
	Actin: Texture correlation	$T_{act,corr}$		+	-	5+	5+
	Tubulin: Texture contrast	$T_{tub,cont}$	Tubulin (Ab)	+	/	50+	/
	Tubulin: Texture correlation	$T_{tub,corr}$		-	/	10+	/
	Gene expression	CALD1	RT-PCR array	+	+	12+	25+
		CCNA1		+	+	50+	25+
		CYFIP2		++	++	25+	25+
		IQGAP2		+	++	50+	12+
		MAPK13		+++	+	25+	50+
		MAPT		++	o	25+	
		PPP1R12A		+	o	50+	
		PPP1R12B		+	++	50+	12+
		TIAM1		+	++	50+	12+
		VASP		o	+		(50+)

dependent reduction in cell viability was observed. In a second assay format cellular proliferation was probed in terms of measuring DNA synthesis (see the Supporting Information for the details and the data). For both cell lines inhibition of proliferation was already caused by NP concentrations well below 1 nM. Cellular proliferation thus is at least sensitive to one order of magnitude lower NP concentrations than cellular viability. In a third assay we probed for direct damage: In the "Live/Dead" assay a cell-impermeable ethidium homodimer only stains cellular nuclei in case their membrane is damaged in the form of perforation. Altogether the $c_{NP,50}$ values obtained from the Live/Dead assay were in the range of a few tens of nM. Images of the outer cell membrane with Helium Ion Microscopy also show disruption of the cellular plasma membrane at high NP concentrations (see the Supporting Information for images). In a fourth assay type we probed for the generation of reactive oxygen species (ROS), which are typically associated with cytotoxic effects, using CellROX Green as the probe. For both cell types we found $c_{NP,50}$ values of around 10 nM.

First, these data (*cf*. Table 1) show that significant reduction in cellular proliferation starts already at least at one order of magnitude lower Au NP concentrations, which corresponds to the concentration at which cellular viability is affected. Second, viability of HeLa cells is less influenced by the exposure to Au NPs than HUVECs. Onset of oxidative stress (production of ROS) starts at similar NP concentrations as required to reduce cell viability. More dramatic effects such as permeation of nuclear membranes occur at even higher NP concentrations. Summing up, these data indicate that first toxic effects of Au NPs can be already noted at NP concentrations well below 1 nM (proliferation), whereas typical onset of drastic reduction in cell viability requires exposure concentrations in the order of 10 nM.

3. Lysosomal swelling caused by endocytosed Au NPs

Staining of the lysosomes (yellow stain in the corresponding image in Figure 1) as well as of the cytoskeleton allows for relating the average sectional area of lysosomes A_{lyso} to the cell cross-section area A_{cell} in a defined intracellular plane. Thereby, a useful measure, the fraction of cell area which is occupied by lysosomes A_{lyso}/A_{cell} can be derived. The results clearly indicate that lysosomes start to swell, *i.e.* increase their size, upon exposure of cells to NPs, whereby the effect was higher for HUVECs than for HeLa cells (*cf*. Table 1). Just looking at the size of lysosomes already allows for pre-estimating whether NPs are present. $c_{NP,50}$ values, *e.g.* the required NP concentration at which half of the effect is observed, are in the order of 10 nM. In summary, exposure of cells to NPs causes swelling of lysosomes and thus leading to an increased fraction of intracellular space which is occupied by lysosomes.

4. Loss of mitochondrial structure caused by NPs

Staining of the mitochondria (green stain in the corresponding image in Figure 1) allowed for observing changes in the morphology of the mitochondria upon cellular exposure to Au NPs. Data show that upon presence of NPs there is a significant shape change from more thread-like elongated to smaller spherical structures. This can be quantified by calculating the form factor F_{mito} and the Zernike moment of 0^{th} order Z^0_{mito}, *cf*. Table 1 and the Supporting Information. Both measures describe the transition from an indefinitely extended object (F, Z_0 = 0) to a spherical object (F, Z_0 = 1) [41], *cf*. the Supporting Information. The results clearly indicate dramatic changes in mitochondrial morphology upon exposure to NPs. As mitochondria are the "power plant" of cells thus energy availability might be affected. For both investigated cell types the $c_{NP,50}$ values were between 1 and 10 nM, and thus well below NP concentrations in which reduction of cellular viability was detected. Thus, reduction in cellular viability might be interpreted as a consequence of mitochondrial impairment.

5. Distortion of the cytoskeleton caused by NPs

Staining of several components of the cytoskeleton was performed, *cf*. Figure 1. Actin was stained with fluorescence-labeled phalloidin, while specific antibodies were used for tubulin and vinculin staining procedures. Even by microscopic inspection with the naked eye striking effects of the NPs on the morphology of the cells were visible. Presence of NPs strongly reduced the cellular cross-section area A_{cell}. In the case of HeLa cells NP exposure induced a more elongated, stretched cell shape, manifested by a reduction in the form factor F_{cell}, *cf*. Table 1. Actin fibers were directly affected by exposure to the NPs. In the case of HUVECs the elongated actin fiber bundles shortened and rounded up. In the case of HeLa cells the actin fibers appeared smoother, indicated by a decreasing texture contrast $T_{act,cont}$ [42]. For tubulin an increase in texture contrast $T_{tub,cont}$ and decrease in texture correlation $T_{tub,corr}$ was observed in case of HUVECs. Under high NP doses tubulin fibers were arranged less compactly and became thinner and longer. Visual inspection with the naked eye however leads to the conclusion that the tubulin network is less affected than the actin network by the presence of NPs. The cytoskeleton stabilizes cells in a dynamic way, based on continuous polymerization and depolymerization of fibers. For this reason control experiments without involving cells were performed, in which reduction of actin and tubulin polymerization upon presence of NPs was determined with biochemical assays. Data indicate that already NP concentrations below 1 nM significantly reduce polymerization of both, actin and

tubulin, *cf*. the Supporting Information. Staining of vinculin indicated a reduction in focal adhesion contact areas A_{vinc}. Additionally, atomic force microscopy (AFM) data showed that, in particular, for HUVECs the number N_{filo} and area A_{filo} of filopodia decreased upon exposure to NPs. Here again a clear difference between both cell types could be seen. Accompanying gene expression assays revealed the upregulation of several genes which are related to the cellular cytoskeleton, *cf*. Table 1. Taken together the data demonstrate that NPs clearly have an impact on the cellular cytoskeleton, whereby detailed effects and in particular related NP doses vary between the investigated cell lines. In general HUVECs seem to be more affected than HeLa cells. Morphology changes occur at NP concentrations around $c_{NP,50} \approx 10$ nM, though this number can be seen only as an indicator for the order of magnitude. In contrast, it is safe to suggest that changes in gene expression are detected only at much higher NP concentrations than changes in morphology.

Conclusions

There are many published records in which cytotoxic effects of NPs on cells have been observed. Many of these reports focus on biochemical assays, probing cell viability or measuring gene expression levels. In this work we demonstrate that effects are also directly visible by changes in cellular morphology. Though there is an impressive amount of studies available in literature, quantitative comparison is hindered by the fact that on the one hand toxicity strongly depends on the type of NPs and on the other hand the type of cells which have been used. In our study we performed many different assays with the same NP on two different types of cells, which allows a quantitative comparison. In general, first effects upon exposure to NPs can be seen by a reduction in cellular proliferation rates. This effect already happens at NP concentrations one order of magnitude lower than the effects can be observed with standard cell viability assays. Also, changes in mitochondrial morphology are an early indicator of NP induced cellular damage. Then again lysosomal swelling and changes in cytoskeleton morphology occur at the same order of NP concentrations that cause significant reduction in cell viability. On the contrary, ROS production sets-on prominently only at even higher concentrations. These data suggest that not all indicators for NP toxicity have the same sensitivity. Cellular proliferation clearly is an early indicator. Prior to changes in cellular viability are observable there are already detectable changes in (sub-) cellular morphology. Geometrical changes in certain cellular compartments occur already at surprisingly low NP concentrations, in particular in mitochondria. In this way, just by visual inspection of cells (upon appropriate immunostaining) NP-related toxicity can be observed *via* morphological analysis. In our case of polymer-coated Au NPs, even at NP concentrations where no significant oxidative stress (ROS production) can be detected morphology can already be altered significantly. These morphological changes provide a reliable assessment for the effect of NPs on the cellular homeostasis. Therefore, the determination of toxic effects of NP exposure based on morphological features may be an attractive alternative methodology for situations in which fixed samples, such as tissue sample from a biopsy have to be inspected, and in which case the use of biochemical assays can no longer be applied.

Acknowledgements

This work was supported by HSFP (project RGP0052/2012 to WJP). The authors are grateful to Andre Beyer for technical assistance with helium ion microscopy.

Contributions

X. M. was responsible for cell culture and involved in CLSM and TEM imaging. R. H. performed parts of the microscopic imaging and the major part of the image processing and data analysis. D. J. de A. and B. P. prepared and characterized the nanoparticles. S. J. S. and B. A. performed several cyto/genotoxocity assays. F. Y., J. F. and C. R. did AFM imaging while H. V. and N. F. performed HIM imaging. M. S. and R. T. did the *in vivo* zebrafish experiments. D. V. conducted the actin/tubulin polymerization assays. N. H., A. G., X.-J. L., and W. J. P. designed the experiments. All authors discussed the results and implications and commented on the manuscript at all stages.

References

[1] M. Auffan, J. Rose, J.-Y. Bottero, G.V. Lowry, J.-P. Jolivet, M.R. Wiesner, Nat. Nanotechnol., 4 (2009) 634-641.
[2] A. Alkilany, C. Murphy, J. Nanopart. Res., 12 (2010) 2313-2333.
[3] I. Canton, G. Battaglia, Chem. Soc. Rev., 41 (2012) 2718-2739.
[4] M. Nazarenus, Q. Zhang, M.G. Soliman, P. del Pino, B. Pelaz, S. Carregal_Romero, J. Rejman, B. Rothen-Ruthishauser, M.J.D. Clift, R. Zellner, G.U. Nienhaus, J.B. Delehanty, I.L. Medintz, W.J. Parak, Beilstein J. Nanotechnol., 5 (2014) 1477-1490.
[5] A.E. Nel, L. Madler, D. Velegol, T. Xia, E.M.V. Hoek, P. Somasundaran, F. Klaessig, V. Castranova, M. Thompson, Nat. Mater., 8 (2009) 543-557.
[6] T. Xia, L. Rome, A. Nel, Nat. Mater., 7 (2008) 519-520.
[7] M.I. Setyawati, P.K.S. Khoo, B.H. Eng, S. Xiong, X. Zhao, G.K. Das, T.T.-Y. Tan, J.S.C. Loo, D.T. Leong, K.W. Ng, J. Biomed. Mater. Res., Part A, 101A (2012) 633-640.
[8] Y. Pan, A. Leifert, D. Ruau, S. Neuss, J. Bornemann, G. Schmid, W. Brandau, U. Simon, W. Jahnen-Dechent, Small, 5 (2009) 2067-2076.
[9] A. Chompoosor, K. Saha, P.S. Ghosh, D.J. Macarthy,

O.R. Miranda, Z.J. Zhu, K.F. Arcaro, V.M. Rotello, Small, 6 (2010) 2246-2249.
[10] L. Wang, Y. Liu, W. Li, X. Jiang, Y. Ji, X. Wu, L. Xu, Y. Qiu, K. Zhao, T. Wei, Y. Li, Y. Zhao, C. Chen, Nano Lett., 11 (2011) 772-780.
[11] X. Ma, Y. Wu, S. Jin, Y. Tian, X. Zhang, Y. Zhao, L. Yu, X.-J. Liang, ACS Nano, 5 (2011) 8629-8639.
[12] M. Mahmoudi, A.M. Abdelmonem, S. Behzadi, J.H. Clement, S. Dutz, M.R. Ejtehadi, R. Hartmann, K. Kantner, U. Linne, P. Maffre, S. Metzler, M.K. Moghadam, C. Pfeiffer, M. Rezaei, P. Ruiz-Lozano, V. Serpooshan, M.A. Shokrgozar, G.U. Nienhaus, W.J. Parak, ACS Nano, 7 (2013) 6555-6562.
[13] A. Ott, X. Yu, R. Hartmann, J. Rejman, A. Schütz, M. Ochs, W.J. Parak, S. Carregal-Romero, Chem. Mater., in revision.
[14] N. Pernodet, X.H. Fang, Y. Sun, A. Bakhtina, A. Ramakrishnan, J. Sokolov, A. Ulman, M. Rafailovich, Small, 2 (2006) 766-773.
[15] Y.-L. Wu, N. Putcha, K.W. Ng, D.T. Leong, C.T. Lim, S.C.J. Loo, X. Chen, Acc. Chem. Res., 46 (2013) 782-791.
[16] T. Mironava, M. Hadjiargyrou, M. Simon, V. Jurukovski, M.H. Rafailovich, Nanotoxicology, 4 (2010) 120-137.
[17] J.A. Yang, S.E. Lohse, C.J. Murphy, Small, 10 (2013) 1642-1651.
[18] M.I. Setyawati, C.Y. Tay, S.L. Chia, S.L. Goh, W. Fang, M.J. Neo, H.C. Chong, S.M. Tan, S.C.J. Loo, K.W. Ng, J.P. Xie, C.N. Ong, N.S. Tan, D.T. Leong, Nat. Commun., 4 (2013) 1673.
[19] S.J. Soenen, B. Manshian, J.M. Montenegro, F. Amin, B. Meermann, T. Thiron, M. Cornelissen, F. Vanhaecke, D. Shareen, W.J. Parak, S. De Smedt, K. Braeckmans, ACS Nano, 6 (2012) 5767-5783.
[20] I.C. Lin, M. Liang, T.-Y. Liu, Z.M. Ziora, M.J. Monteiro, I. Toth, Biomacromolecules, 12 (2011) 1339-1348.
[21] T. Mironava, M. Hadjiargyrou, M. Simon, M.H. Rafailovich, Nanotoxicology, 8 (2014) 189-201.
[22] T. Pellegrino, L. Manna, S. Kudera, T. Liedl, D. Koktysh, A.L. Rogach, S. Keller, J. Rädler, G. Natile, W.J. Parak, Nano Lett., 4 (2004) 703-707.
[23] C.-A.J. Lin, R.A. Sperling, J.K. Li, T.-Y. Yang, P.-Y. Li, M. Zanella, W.H. Chang, W.J. Parak, Small, 4 (2008) 334-341.
[24] F. Zhang, E. Lees, F. Amin, P. Rivera_Gil, F. Yang, P. Mulvaney, W.J. Parak, Small, 7 (2011) 3113-3127.
[25] G. Charron, D. Hühn, A. Perrier, L. Cordier, C.J. Pickett, T. Nann, W.J. Parak, Langmuir, 28 (2012) 15141-15149.
[26] D. Hühn, K. Kantner, C. Geidel, S. Brandholt, I. De Cock, S.J.H. Soenen, P. Rivera Gil, J.-M. Montenegro, K. Braeckmans, K. Müllen, G.U. Nienhaus, M. Klapper, W.J. Parak, ACS Nano, 7 (2013) 3253-3263.
[27] S. Harakeh, R.M. Abdel-Massih, P. Rivera_Gil, R.A. Sperling, A. Meinhardt, A. Niedwiecki, M. Rath, W.J. Parak, E. Baydoun, Nanotoxicology, 4 (2010) 177-185.
[28] B. Rothen-Rutishauser, D.A. Kuhn, Z. Ali, M. Gasser, F. Amin, W.J. Parak, D. Vanhecke, A. Fink, P. Gehr, C. Brandenberger, Nanomedicine, 9 (2014) 607-621.
[29] C. Schweiger, R. Hartmann, F. Zhang, W.J. Parak, T. Kissel, P. Rivera Gil, J. Nanobiotechnol., 10 (2012) 28.
[30] A.D. Lehmann, W.J. Parak, F. Zhang, Z. Ali, C. Röcker, G.U. Nienhaus, P. Gehr, B. Rothen-Rutishauser, Small, 6 (2010) 753-762.
[31] S.J. Soenen, B.B. Manshian, A.M. Abdelmonem, J.-M. Montenegro, S. Tan, L. Balcaen, F. Vanhaecke, A.R. Brisson, W.J. Parak, S.C.D. Smedt, K. Braeckmans, Part. Part. Syst. Charact., 31 (2014) 794-800.
[32] Y. Pan, S. Neuss, A. Leifert, M. Fischler, F. Wen, U. Simon, G. Schmid, W. Brandau, W. Jahnen-Dechent, Small, 3 (2007) 1941-1949.
[33] R. Shukla, V. Bansal, M. Chaudhary, A. Basu, R.R. Bhonde, M. Sastry, Langmuir, 21 (2005) 10644-10654.
[34] F. Amin, D.A. Yushchenko, J.M. Montenegro, W.J. Parak, ChemPhysChem, 13 (2012) 1030-1035.
[35] N.G. Papadopoulos, G.V.Z. Dedoussis, G. Spanakos, A.D. Gritzapis, C.N. Baxevanis, M. Papamichail, J. Immunol. Methods, 177 (1994) 101-111.
[36] A. Salic, T.J. Mitchison, Proc. Natl. Acad. Sci. U. S. A., 105 (2008) 2415-2420.
[37] M.P. Singh, T.M. Atkins, E. Muthuswamy, S. Kamali, C. Tu, A.Y. Louie, S.M. Kauzlarich, ACS Nano, 6 (2012) 5596-5604.
[38] A. Magrez, L. Horvath, R. Smajda, V. Salicio, N. Pasquier, L. Forro, B. Schwaller, ACS Nano, 3 (2009) 2274-2280.
[39] T. Kouyama, K. Mihashi, Eur. J. Biochem., 114 (1981) 33-38.
[40] D. Bonne, C. Heuséle, C. Simon, D. Pantaloni, J. Biol. Chem., 260 (1985) 2819-2825.
[41] M.V. Boland, M.K. Markey, R.F. Murphy, Cytometry, 33 (1998) 366-375.
[42] R.M. Haralick, Proc. IEEE, 67 (1979) 786-804.

1

Colloidal Nanoparticles Induce Changes in Cellular Morphology

SUPPORTING INFORMATION

I) Nanoparticle synthesis

I.1) Synthesis of gold nanoparticles (Au NPs)

I.2) Synthesis of amphiphilic polymer functionalized with TMR-cadaverine

I.3) Polymer coating of Au NPs

I.1) Synthesis of gold nanoparticles (Au NPs)

Gold nanoparticles (Au NPs) were synthesized following the Brust method [1] according to previously published protocols [2, 3]. Briefly, 0.300 g (0.9 mmol) of hydrogen tetrachloroaurate (III) (99.9 %, Alfa Aesar, #12325) was dissolved as aqueous gold precursor in 25 mL of Milli-Q water. This solution was mixed with a solution of 2.170 g (3.9 mmol) of tetraoctylammonium bromide (TOAB, Sigma-Aldrich, #294136) dissolved in 80 mL of toluene (Fluka, #89682). The mixture of both solutions was shaken vigorously for about 5 min. Hereby $AuCl_4^-$ ions were gradually transferred from the aqueous into the organic phase (toluene) through the formation of tetraoctylammonium-gold tetrachloroaurate ion pairs.

$AuCl_4^-$ (aq) + $N(C_8H_{17})_4^+$ (tol) → $N(C_8H_{17})_4^+AuCl_4^-$ (tol)

Afterwards, the aqueous solution was discarded and the toluene solution containing the $AuCl_4^-$ ions was transferred to a 250 mL round bottom flask. A solution of 0.334 g (8.8 mmol) sodium borohydride ($NaBH_4$, Sigma-Aldrich, #452882) in 25 mL of Milli-Q water was added drop-wise to the vigorously stirred solution of gold precursor in toluene. The gold started to be reduced after a few seconds by sodium borohydride resulting in a change of colour from orange to violet.

$nAuCl_4^-$ (tol) + $3ne^-$ → $4nCl^-$ (aq) + Au_n

Then the growth of NPs was mediated by the residue of sodium borohydride, which reduced the remaining gold ions. After one-hour stirring, the solution was transferred to a separation funnel and the NPs were washed several times. The first washing step was performed with 25 mL of 0.01 M HCl, in order to remove the excess sodium borohydride. The second step was done with 25 mL of 0.01 M NaOH to remove the excess acid. Finally, four times washing with 25 mL of Milli-Q water was performed to remove salt residues from the HCl and NaOH washing steps. The resulting organic solution was transferred to a 250 mL round-bottomed flask and was stirred overnight to allow the NPs to reach a thermodynamically stable size distribution (Ostwald

ripening process [4]). Next day, ı ligand exchange was carried out by adding 10 mL (8.450 g, 41.7 mmol) of 1-dodecanethiol (Sigma-Aldrich, #471364) and heating the solution up to 65 °C for 3 hours. Hereby the dodecanethiol displaces the Br^- ions from the NP surface due t the high binding affinity of thiol groups to gold [5]. Large agglomerates were first removed y centrifugation at 700 rcf whereby the supernatant w s collected, and the precipitate containing the agglome ıtes was discarded. Then the obtained NPs were precipitated with methanol undergoing a selective size precipitation process by centrifugation. After discarding the supernatant the NP precipitate containing the hydrophobic Au NPs was dissolved in chloroform to a final concentration of 4 µM.

I.2) Synthesis of amphiphilic pol mer functionalized with TMR-cadaverine

First, following the previously reported synthesis procedure [6-9], an amphiphilic polymer, poly(isobutylene–*alt*–maleic anhydride)–*graft*–dodecylamine (PMA), was prepared. The amphiphilic polymer is not only useful to transfer the hydrophobic NPs to aqueous solution [6, 10], but it also allows the attachment of other molecules containing free amino groups directly *via* amide bonds to its maleic anhydride rings [7, 9, 11]. The polymer consists of a polyisobutylene-*alt*-maleic anhydride hydrophilic backbone ($M_w \approx 6$ kDa, Sigma-Aldrich, #531278) modified with dodecylamine hydrophobic side chains. 75 % of the anhydride rings of the polymer backbone are covalently linked *via* amide bonds to the amine groups of hydrophobic chains. Figure SI-I.1 shows the structure of the polymer in detail. The synthesis is described in detail in Lin *et al.* [7]

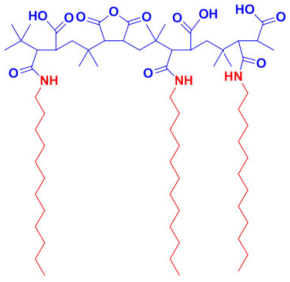

Figure SI-I.1: *Structure of the synthesized amphiphilic polymer (PMA). Polyisobutylene-alt-maleic anhydride hydrophilic backbone (blue) modified with dodecylamine hydrophobic side chains (red).*

In order to attach the tetramethylrhodamine cadaverine dye (TMR-cadaverine, λ_{ex} = 544 nm, λ_{em} = 571 nm, Molecular Probes, ıife Technologies, #A1318) to the polymer, 2 % of the total anhydride rings of the amphiphilic polymer were modified by the reaction of the maleic anhydride rings with the amino group of the dye, leaving in total 23 % of the anhydride rings free (75 % are occupied by the linked dodecylamine side chains). Briefly, 2 mg of the dye dissolved in chloroform wer mixed with 400 µL of 0.5 M (in terms of monomer concentration [7]) of the prepared amphiphilic polymer solution. The reaction mixture was refluxed overnight at room temperature. Then, the solvent mixture was evaporated and the dye-modified polymer was redissolved in anhydrous chloroform to obtain a final (monomer) concentration of c_P = 0.05 M (*cf.* Figure SI-I.2).

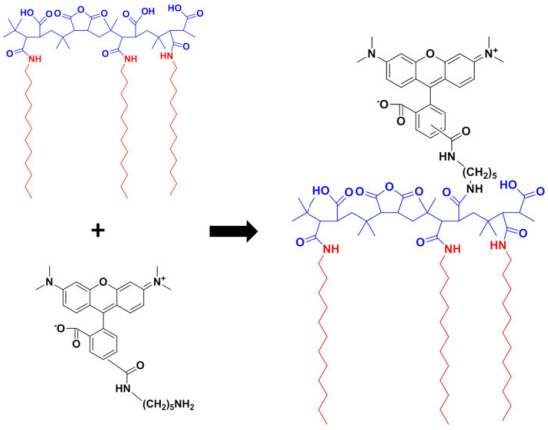

Figure SI-I.2: *Scheme of the linkage of the TMR-cadaverine dye 590 (black) via amide bonds to the anhydride rings of the hydrophilic backbone of the amphiphilic polymer (blue). The -NH_2 group of the dye is used for linkage to the PMA backbone.*

I.3) Polymer coating of Au N ;

To calculate the amount required to coat the synthesized NPs with the prepared amphiphilic polymer Eq. SI-I.1 was used , 12, 13].

$$V_p = \frac{\pi \cdot c_{NP} \cdot V \cdot d_{eff}^2 \cdot R_{p/area}}{c_p} \qquad \text{Eq. SI-I.1}$$

The variable c_{NP} corresponds to the NP concentration and V corresponds to the volume of the NP solution. c_p is the monomer concentration of the amphiphilic polymer dissolved in chloroform while V_p represents the volume of the polymer solution. d_{eff} corresponds to the effective diameter of the NPs: $d_{eff} = d_c + 2 \cdot l_{surfactant}$, which is the sum of the diameter of the inorganic core (d_c) plus two times the assumed thickness of the surfactant shell that corresponds to $l_{surfactant} \approx 1.2$ nm. $R_{p/area}$ is the number of polymer monomers which need to be added per surface area $A_{eff} = 4\pi \cdot (d_{eff}/2)^2$ of NP in monomer units/nm^2.

Thus, for all the experiments, several batches of polymer coated NPs were prepared with the following procedure: Au NPs (d_c = 4.8 nm $\Rightarrow$ d_{eff} = 4.8 nm + 2·1.2 nm = 7.2 nm; V = 1000 µL, c_{NP} = 4 µM in chloroform) ere mixed with PMA

functionalized with TMR cadaverine dye in chloroform (V_P = 515 µL, c_P = 0.05 M, $R_{p/area}$ = 50 nm^{-2}) in a 10 mL round-bottomed flask. The mixture was stirred and the solvent was slowly evaporated. Then the NP powder was dissolved in 50 mM sodium borate buffer at pH 12 (SBB 12). The basic pH of the buffer opens the remaining anhydride rings, leading to negatively charged carboxyl groups at that pH, which increases the surface charge and renders the NPs water-soluble.

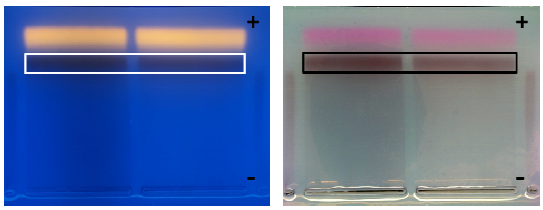

Figure SI-I.3: *Images of agarose gels on which the Au NPs with TMR-cadaverine in their polymer shell had been run for 1 h in an electric field of 15 V·cm^{-1} under white-light (left) and UV (right) illumination. Images of the gels were taken after 60 min. "+" and "-" indicate the direction of the electric field. The marked sections correspond to the NP-containing bands that were cut to extract the Au NPs.*

Gel electrophoresis was used after the polymer coating procedure in order to purify the sample and to eliminate empty polymer micelles [6]. For this purpose, a 2 % agarose gel was prepared by mixing the agarose (2 g) with Tris-Borate-EDTA buffer (TBE; 0.5x, 98 mL corresponding to 98 g). In addition, the polymer-coated Au NPs were mixed with glycerol (in order to increase the density of the sample) and with Orange G dye (in order to label the sample mixture which is loaded on the gel) [14]. The mixture was then placed into the cavity of the prepared gel. Applying an electric field of 15 V·cm^{-1}, the negatively charged NPs will move to the plus pole. After one hour, the polymer-coated NPs form a band which can be distinguished from empty micelles and free dye molecules that move faster, as they are smaller [6]. The band which contains the NPs was cut and placed into a dialysis membrane (50 kDa molecular weight cut-off (MWCO)) filled with TBE buffer. Applying again an electric field of 10 V·cm^{-1} for *ca.* 20 min, which caused the NPs to move out of the gel, whereby they stayed trapped inside the dialysis membrane. In order to be sure that all empty micelles were removed this procedure was applied twice. Examples are shown in Figure SI-I.3.

II) Nanoparticle characterization

The polymer-coated NPs were characterized with different methods. First, the inorganic core diameter d_c was derived from transmission electron microscopy (TEM) images, *cf.* Figure SI-II.1. For this purpose a drop of the NP solution was dried on a TEM grid, and low resolution TEM images were recorded. Note that only the Au core, but not the organic molecules around the NP surface (dodecanethiol, amphiphilic polymer) provide contrast [15, 16]. A histogram of the NP diameter d_c was generated from these images using a standard image analysis software. The average diameter of the inorganic core d_c of the Au NPs obtained was determined to be 4.79 ± 0.70 nm (*cf.* Figure SI-II.1).

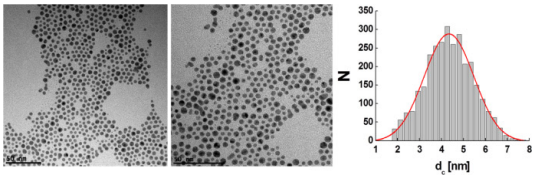

Figure SI-II.1: *TEM images of a solution of dried polymer coated NPs. The scale bar corresponds to 50 nm. From these images a histogram of the distribution N(d_c) of the Au core diameter of the NPs was obtained.*

For measuring the hydrodynamic diameter d_h with dynamic light scattering (DLS; d_h = 12 ± 3 nm, *cf.* Figure SI-II.2) and the zeta-potential ζ with laser Doppler anemometry (LDA; ζ = -30 ± 2 nm, *cf.* Figure SI-II.3) a Malvern Zetasizer Nano ZS with a red laser (632.8 nm) as light source was used in 173° backscatter detection mode. All the NP samples were measured in Milli-Q water using polystyrene cuvettes as described previously [13].

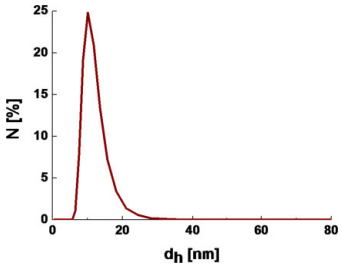

Figure SI-II.2: *Number distribution N(d_h) of the hydrodynamic diameter of polymer coated Au NPs dispersed in water.*

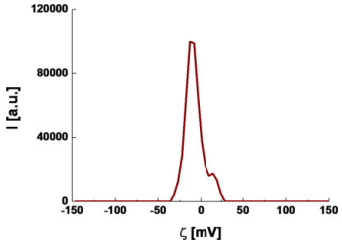

Figure SI-II.3: *Distribution of the zeta potential I(ζ) of polymer coated Au NPs dispersed in water.*

UV/vis absorption (*cf.* Figure SI-II.4) and fluorescence (*cf.* Figure SI-II.5) spectra of the Au NP samples dispersed in water were recorded. From the

absorption spectra A(λ) the NP concentration c_{NP} was calculated using the Lambert Beer law:

$$A_{max} = c_{NP} \cdot \varepsilon_{NP} \cdot l \qquad \text{Eq. SI-II.1}$$

Hereby, A_{max} is the absorpti maximum at the surface plasmon resonance peak of the Au NPs, c_{NP} the NP concentration, l is the path length of the cuvette in which measurements w re performed, and ε_{NP} is the molar extinction coefficient of the NPs at the wavelength of the absorption peak, which was assumed to be $\varepsilon_{NP} = 8.7 \cdot 10^6\ M^{-1}cm^{-1}$. The fluorescence of the NPs was measured with a Horiba FluoroLog fluorimeter upo excitation at λ_{ex} = 544 nm.

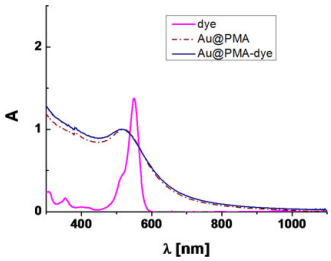

Figure SI-II.4: *UV/vis absorption spectra as recorded in aqueous solution of free TMR-cadaverine ("dye"), and polymer-coated Au NPs without ("Au@PMA") and with TMR-cadaverine ("Au@PMA-dye") in their polymer shell, respectively.*

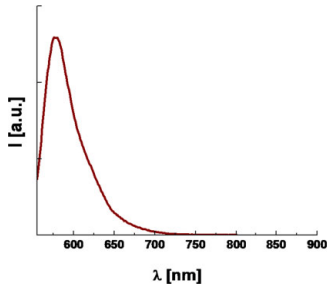

Figure SI-II.5: *Fluorescence spectrum of polymer-coated Au NPs with TMR-cadaverine in their polymer shell.*

III) Cell culture and nanoparticle exposure

HeLa cells (derived from cervical cancer cells taken from Henrietta Lacks) were cultured in Minimum Essential Medium (MEM, Sigma-Aldrich, #M4655) and Human Umbilical Vein Endothelial Cells (HUVECs) were cultured in Endothelial Cell Growth Medium (ECGM, Promo ell, Germany, #C-22010). MEM medium was supplemented with 10 % fetal bovine serum (Biochrom, Germany, #S0615), and 1 % penicillin/streptomycin (P/S, Sigma-Aldrich, #P4333). ECGM was supplemented with ECGM supplement mix (PromoCell, #C-39215), and 1 % P/S. HeLa cells or HUVECs were added to 8 well µ-slides (1 cm^2 per well, Ibidi, Germany, #80826) and incubated at 37 °C and 5 % CO_2 (all incubation steps are at 37 °C; only pre-warm l media were added to the cells). After 24 h, the particular growth medium was replaced by Au NP-containing medium for additional 24 h unless otherwise stated.

IV) Transmission electron microscopy of cells

Cells (grown on 35 mm corning culture dishes, #ym-2011A) were rinsed in phosphate buffered saline (PBS) for 3 times and then fixed in 2.5 % glutaraldehyde (8 %, EMS, USA, #16010) in 0.1 M 3-(N-morpholino)propanesulfonic acid (MOPS) buffer (pH 7.0) for 10 h at room temperature. This was followed by secondary fixation with 1 % osmium tetraoxide for 1 h. Then, the specimens were dehydrated through a graded ethanol series (50 %, 70 %, 80 %, 90 % and 100 % and infiltrated through propylene oxide, and embedded in epoxy resin. Ultrathin sections (80 nm) were cut with a diamond knife using a Leica Ultracut JCT microtome (Leica EM UC6, Stockach, Germany). The sections were placed on 300 mesh copper grids and post-stained with uranyl acetate and lead citrate for observation under the transmission electron microscope (Hitachi, H-7650B).

Transmission electron microscopy (TEM) images of HUVECs and HeLa cells with incorporated NPs are shown in Figure SI-IV.1. As Figure SI-IV.1 shows, in HUVECs as well as HeLa cells, Au NPs along with some other substances outside the cells form loose clusters around 200 nm in diameter. Presumably macropinocytosis plays a role in internalization of the Au NPs, as it can be seen om the pictures that a macropinocytic cup wraps the Au NP cluster. After Au NPs are taken up into the cells, they appear to accumulate in lysosomes (*cf.* Figure SI-IV.1, yellow arrows, as well the discussion in § XI.1).

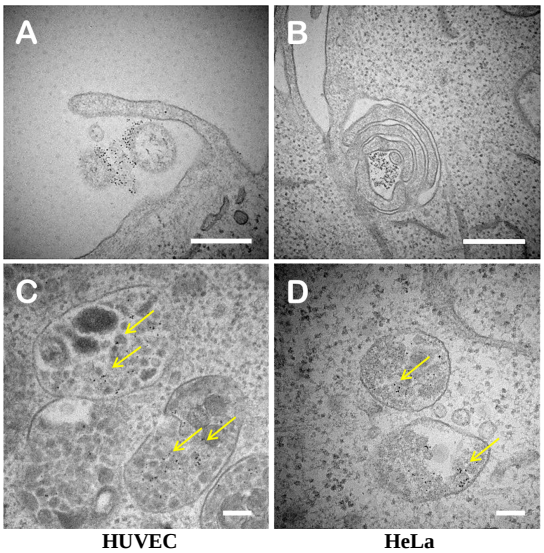

HUVEC **HeLa**

Figure SI-IV.1: *TEM images of HUVECs and HeLa cells after having been incubated with Au NPs at a final NP concentration of c_{NP} = 25 nM for 24 h. The scale bars correspond to 500 nm for A and B, 100 nm for C and D. Yellow arrows indicate Au NPs present in lysosomes.*

V) Atomic force microscopy of cells

After incubation with Au NPs, cells were imaged with atomic force microscopy (Nanoscope IV, Veeco, Santa Barbara, CA). Contact Mode (CM) was utilized for topological imaging, which was performed in phosphate buffered saline (PBS), using a silicon-tip on nitride lever cantilever (SNL spring constant k = 0.08 $N \cdot m^{-1}$, resonance frequency f = 12-24 kHz, Bruker, Karlsruhe, Germany). The deflection set point was adjusted to 0.8 V. The scanning area was chosen to be 40x40 μm^2 for imaging the whole cell, and the scan angle was set to 90^o.

VI) Helium ion microscopy

For helium ion microscopy (HIM) cells were seeded on glass cover slips (d = 15 mm, Roth, Germany, #P231.1). After 24 h the cells were exposed to the NPs at concentrations between 0 and 100 nM. After additional 24 h the cells were fixed with 1 % glutaraldehyde (8 %, EMS, USA, 16010), which was added directly to the cell medium for 10 min, followed by three washing steps with PB Subsequently, the samples were treated with 2 % glutaraldehyde and 4 % paraformaldehyde (8 %, EMS, USA, #157-8-100) in 0.1 M sodium cacodylate buffer (pH 7.2, Sigma-Aldrich, #20840) for 90 min and dehydrated in ethanol-water mixtures with increasing ethanol content (30 %, 50 %; 70 %, 95 %, and 3 x 100 %) for 10 min per step. Finally critical point drying was performed using a Polaron E3000 (Quorum Technologies, UK). The samples were imaged with a HIM ORION PLUS from Zeiss at a working distance of 19.5 mm, with an accelerating voltage of 36.5 keV, and a beam current of 0.8-0.9 pA. A flood gun was used to compensate charging. Images show the distribution of secondary electrons or Rutherford backscattered helium ions. The latter images highlight materials with high atomic numbers such as Au.

As visible in Figure SI-VI.1 local membrane disruptions occur in case of HUVECs, which may be attributed to the exposure to Au NPs. In addition, this interpretation is strengthened by Rutherford backscattering images of such structures (*cf.* Figure SI-VI.2) which show an increased level of backscattered ions probably due to the presence of Au NPs.

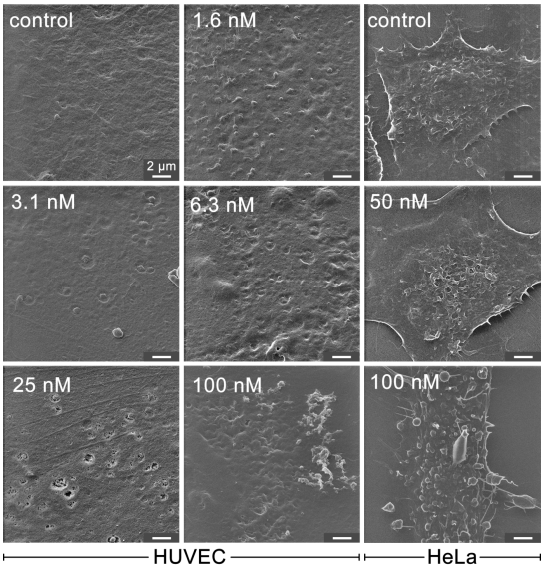

Figure SI-VI.1: *HIM images (secondary electrons) of HUVEC and HeLa cells after exposure to Au NPs. In case of HUVECs the surface becomes locally disrupted.*

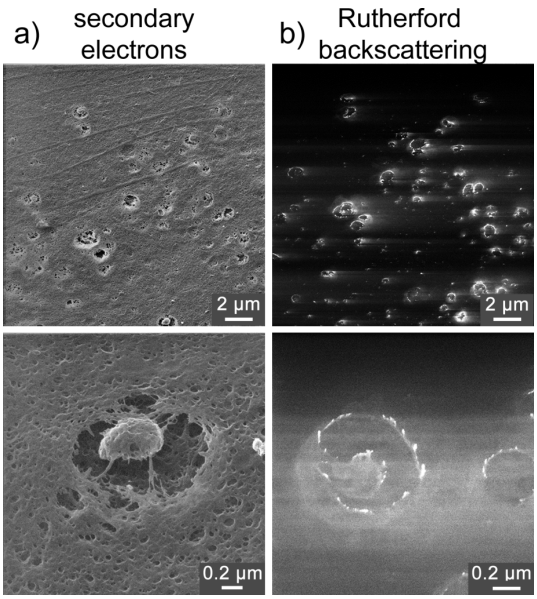

Figure SI-VI.2: *Rutherford backscattering at membrane disruptions (HUVECs, c_{NP} = 25 nM).*

VII) Confocal microscopy of cells

Imaging was performed with a confocal laser scanning microscope (CLSM 510 Meta) from Zeiss, equipped with lasers allowing excitation at 405, 488, 543, and 633 nm. Details regarding the imaging are given in the descriptions of the corresponding assays.

VIII) Data analysis of geometrical features from fluorescence images

VIII.1) Cells

VIII.2) Subcellular structures (mitochondria/lysosomes)

VIII.3) Geometrical features

VIII.4) NP uptake

To extract geometrical features, texture information and NP uptake from fluorescence images in a high throughput manner CellProfiler [17] and Matlab (Mathworks) were used.

VIII.1) Cells

To quantify the effect of NP exposure on cell morphology several geometrical features were calculated, based on cross-sections of hundreds of individual cells. Cells were automatically identified from 2D fluorescence images in low magnification, based on the fluorescent pattern of the cytoskeleton and nuclei. The identification of clumpy cells turned out to be quite challenging. Therefore, nuclei (primary objects) were identified first, in order to obtain the outlines of the whole cells (secondary objects) more easily in a second step [17]. Thus, image processing was performed as follows: First, cell nuclei were segmented based on their DAPI-staining pattern (Figure SI-VIII.1.1, a) by thresholding and identified as primary objects. Around each nucleus the corresponding cell body (secondary object) was derived from actin-staining (Figure SI-VIII.1.1, b), by using the "propagation"-algorithm [18] provided by CellProfiler. Manual post-processing (removal of dead cells and correction of erroneous segmentation results) was performed with a graphical user interface written in Matlab (Mathworks). The obtained shapes were converted into binary images and several geometrical parameters were calculated (listed below) (Figure SI-VIII.1, c-d).

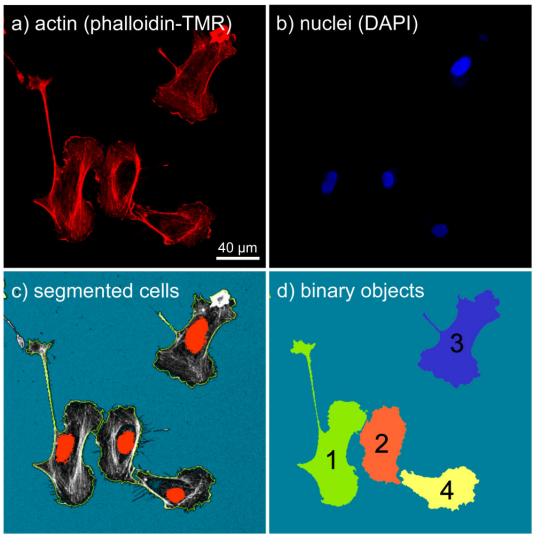

Figure SI-VIII.1: *Cell segmentation example. Fluorescence image of non-treated HUVECs, showing (a) the cytoskeleton (phalloidin-TMR) in the red channel and (b) the nuclei (DAPI) in the blue channel. (c) The outcome of the segmentation procedure is shown. (d) The resulting objects which were used to derive all geometrical features are shown.*

VIII.2) Subcellular structures (mitochondria/lysosomes)

The segmentation of subcellular structures was difficult, as shapes can vary from spindle like objects (*e.g.* mitochondria of untreated cells) over polliwog shaped forms (*e.g.* mitochondria of cells exposed to increasing concentration of NPs) to simple round objects (*e.g.* lysosomes, damaged mitochondria). Object identification was performed based on fluorescence confocal microscopy 2D slices (*cf.* Figure SI-VIII.2, a). In case of mitochondria the image quality was enhanced by employing a classical maximum likelihood estimation deconvolution algorithm, using a theoretical point spread function. Apart from being able to cope with different shapes, the segmentation routine should be able to handle staining intensity variations. In addition the background in an intracellular region is not dark (unfocussed structures), especially in the perinuclear region, where the lysosomal and mitochondrial density is significantly higher than in outer regions of the cell. To obtain satisfactory results multiple thresholding steps were performed: First, the image was roughly segmented by adaptive two-class thresholding following the Otsu-method [19] (*cf.* Figure SI-VIII.2, b). This step was applied to separate scattered structures in the outer region of the cell from clumpy structures in the perinuclear region. The obtained objects were processed again with an object based thresholding approach using the MoG (Mixture

of Gaussian) algorithm provided by CellProfiler [17] (*cf.* Figure SI-VIII.2c). Third, to indentify objects which were still including more than one structure, the objects were classified with respect to texture entropy and area (*cf.* Figure SI-VIII.2, d). Correctly segmented objects with only one structure of interest are smaller and show a much lesser texture entropy than objects including more than one or clumpy structures. Fourth, objects which showed a high texture entropy were segmented a third time, again following the adaptive two-class thresholding approac using the Otsu-method [19], which was used already for the initial segmentation step (*cf.* Figure SI-VIII.2, e). Fifth, the size distribution of all resulting o ects was analyzed and large objects very excluded from the analysis. Finally, texture and intensity of all individual objects was determined and several geometrical features were calculated based on their shape features are listed below) (*cf.* Figure SI-VIII.2, f).

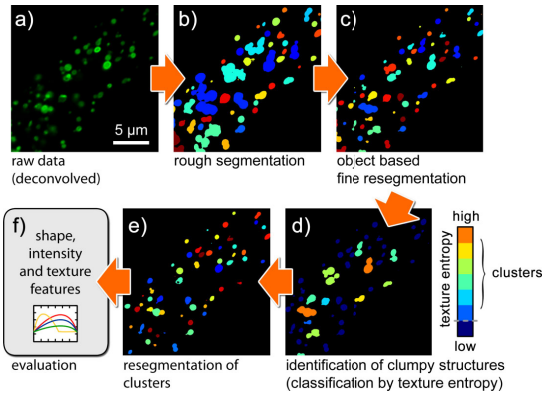

Figure SI-VIII.2: *Segmentation of mitochondria. A fluorescence image of HUVECs treated with NPs at 12.5 nM showing mitochondria (CellLight Mitochondria-GFP) in the green channel (a) after deconvolution and (b-f) after subsequent segmentation procedure steps .*

VIII.3) Geometrical features

Form factor: For the identified objects their area A [µm^2], as well as their perimeter P [µm] was determined. From these parameter the form factor F was calculated. Examples are given in Table SI-VIII.1.

$$F = 4 \cdot \pi \cdot A/P^2 \qquad \text{Eq. SI-VIII.1}$$

Zernike moments: Zernike moments are commonly used for automatic recognition of pattern characteristics in fluorescence aging [20]. They describe the decomposition of an image object onto an orthogonal set of polynomials similar to the way that Fourier coefficients are used to decompose a time series. In this work only the 0th m ment Z^0 was used to describe whether a shape is similar to a disk ($Z^0 = 1$) or more spindle like ($Z^0 = 0$). Examples are given in Table SI-VIII.3.

Feature	Perimeter d=1µm	0.5µm	0.25µm	0µm
A [µm²]	0.78	0.39	0.2	0
P [µm]	3.1	2.5	2.2	2
F	1	0.76	0.5	0
Z0	1	0.5	0.25	0

Table SI-VIII.3: *Features used to describe cell, mitochondria, and lysosomal shapes upon exposure to NPs. A = area, P = perimeter, F = form factor, Z^0 = Zernike moment of order 0, d corresponds to the semi-minor axis of the example shapes, if being represented by an ellipse.*

Lysosomal fraction: To investigate lysosomal swelling upon exposure to NPs the total area A_{lyso} of all lysosomes in a confocal 2D-slide was divided by the cell area A_{cell}, *cf.* Figure SI-VIII.4. The area occupied by lysosomes was obtained by binarizing the image containing the fluorescence information of stained lysosomes using ma al thresholding. Along the obtained shape of each cell (as described in § VIII.1) the number of positive pixels in the corresponding binary image was determined and divided by the total cell area.

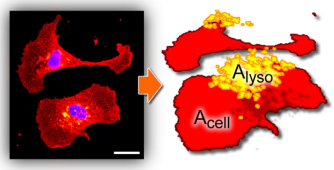

Figure SI-VIII.4: *The lysosomal fraction is calculated by dividing the area occupied by lysosomes (A_{lyso}) by the area of the whole cell (A_{cell}). Left image: blue: nuclei, red: plasma membrane, scale bar: 20 µm.*

Texture: To quantify the texture of actin or tubulin staining, several Haralick texture features were calculated [21]. These features are derived from the co-occurrence matrix, containing information about how pixel intensities or correlated spatially in horizontal orientation. Examples are given in Table SI-VIII.5.

Texture					
T_{cont} [a.u.]	36	4.2	0.6	0	7.8
T_{corr} [a.u.]	-0.5	-0.6	0.3	0	0.7

Table SI-VIII.5: *Features used to describe the texture of actin and tubulin staining of cells treated with NPs. T_{cont} = texture contrast, T_{corr} = texture correlation.*

VIII.4) NP uptake

The relative amount of fluorescent NPs taken up by individual cells was estimated from fluorescence images. In addition to the fluorescence information of nuclei and cytoskeleton the signal of the NPs was

recorded in a third channel. Along the area of each cell obtained in § VIII.1 the fluorescence intensity of the internalized NPs was summed up, yielding the integrated intensity I_{NP} per cell [22].

IX) Cell viability, proliferation, etc.

IX.1) Resazurin assay

IX.2) Alamar blue assay

IX.3) MTT assay

IX.4) Live/dead assay

IX.5) Proliferation assay

IX.6) Oxidative stress

A selection of standard assays used for analysis of cytotoxic effects of NPs on cells in vitro was applied. These data show the different concentration ranges at which effects occur.

IX.1) Resazurin assay

First, cell viability in the presence of NPs was investigated with resazurin assays. HUVECs and HeLa cells were seeded in 96-well plates (Sigma Aldrich, #CLS3603) at a density of 5000 cells in 300 µL medium per well (each well had an area of 0.3 cm^2), and were grown for 24 h in cell growth medium. Then the cells were rinsed with PBS and supplemented cell growth medium containing Au NPs at different resulting concentrations c_{NP} was added to the wells (100 µL medium per well). Concentrations were adjusted in a way that a wide range of concentrations was covered. The cells were incubated at 37 °C and 5 % CO_2 for 24 h. After that, the cells were rinsed with PBS and a freshly prepared solution of 90 % medium and 10 % resazurin (Sigma-Aldrich, #TOX8) was added to the wells. The cells were incubated for 3 h at 37 °C and 5 % CO_2.

Non-fluorescent resazurin is oxidized by living cells to fluorescent resorufin. Therefore, the fluorescence intensity is a measure of the viability of the cells. After incubation, the fluorescence emission spectrum $I(\lambda, c_{NP})$ of the solution was recorded with a fluorometer (Fluorolog-3, Horiba Jobin Yvon). Hereby, the wells were excited at λ_{ex} = 560 nm, and fluorescence emission was recorded from 572 to 650 nm, *cf.* Figure SI-IX.1.

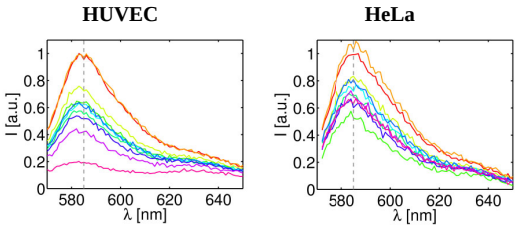

Figure SI-IX.1: *Resorufin fluorescence spectra as recorded on cells incubated with different concentrations c_{NP} of NPs and resazurin for (a) HUVECs, and (b) HeLa cells.*

The intensities between 640 to 650 nm were averaged and subtracted as background from the intensity average between 583 to 587 nm, which was the maximum of the emission spectrum. The background corrected averaged intensity maxima $I(c_{NP})$ were plotted versus the concentration c_{NP}, *cf.* Figure SI-IX.2. The cell viability V_{res} was hereby defined as normalized intensity maxima, *cf.* Eq. SI-IX.1.

$$V_{res}(c_{NP}) = I(c_{NP}) / I(c_{NP} = 0) \qquad \text{Eq. SI-IX.1}$$

The concentration-dependent fluorescence intensities $I(c_{NP})$ were then fitted using the sigmoidal function shown in Eq. SI-IX.2, with the fit parameters $c_{NP,50}$, I_{min}, I_{max}, and p. Hereby, $c_{NP,50}$ is the NP concentration at which viability of cells has been reduced to half of its activity, and are I_{min} and I_{max} the minimum and the maximum of the concentration-dependent intensity maxima $I(c_{NP})$.

$$I(c_{NP}) = \frac{I_{max} - I_{min}}{1 + \left(\frac{c_{NP}}{c_{NP,50}}\right)^{p}} + I_{min} \qquad \text{Eq. SI-IX.2}$$

The resulting viability data are shown in Figure SI-IX.2. As expected, upon a certain NP concentration cell viability is reduced. HUVECs are more sensitive than HeLa cells to incubation with the NPs.

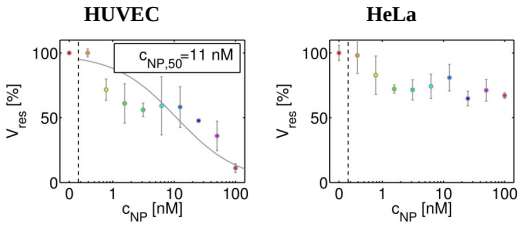

Figure SI-IX.2: *Cell viability V_{res}, as determined with the resazurin test, in dependence of the NP concentration c_{NP}. The results are presented as mean value ± standard deviation (SD).*

IX.2) Alamar blue assay

Second, as an additional assay probing cell viability, the commercially available Alamar blue test was used. Regarding the probing principles the Alamar blue assay is very similar to the resazurin assay [23].

HeLa cells or HUVECs were seeded at 5000 cells/well in black, clear-bottom 96-well plates and were allowed to settle overnight. Cells were then incubated for 24 h with the Au NPs at the indicated concentrations (from c_{NP} = 0 to 100 nM), after which the Alamar Blue assay (Molecular Probes, life

technologies, #DAL1025) was performed according to the manufacturer's protocol. Fluorescence readouts were performed using an Optima FluoStar plate reader instrument (λ_{ex} = 560 nm; λ_{em} = 590 nm). Data analysis was performed as described in § IX.1. Data are expressed as mean ± SD (*n* = 4).

The results of the Alamar blue test are reported in Figure SI-IX.3. For the HUVECs, the NPs resulted in a reduction of cell viability at high NP concentrations, with the cell viability being significantly reduced at c_{NP} = 100 nM. For the HeLa cells, no significant toxic effects were observed for NP concentrations up to 100 nM.

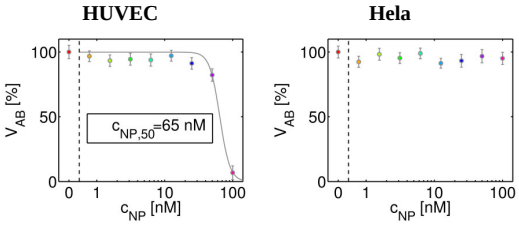

Figure SI-IX.3: *Cell viability V_{AB}, as determined with the Alamar blue test, in dependence of the NP concentration c_{NP}. The results are presented as mean ± SD for 4 independent measurements.*

IX.3) MTT assay

Third, cell viability was probed with the 3-(4,5-dimethylthiazol-2-yl)-2,5-diphenyltetrazolium bromide (MTT) assay. For the assay HUVECs and HeLa cells were seeded in 24-well plates (Greiner Bio-One, #662160) at a density of 50000 cells per well (1 mL/well, 1.9 cm^2 area per well) one day prior the planed experiments. Cells were then incubated with the Au NPs for 24 h at the indicated concentrations (from 0 to 200 nM). After extensive washing an MTT cell proliferation assay (Roche, #11465007001) was performed according to the manufacturer´s instructions. Briefly, 500 µL of regular cell media were added to the cells and then supplemented with 50 µL MTT1 solution. After 4 hours 500 µL of solubilization solution (MTT2) were added. An analysis of the absorbance maximum A_{max} at 590 nm wavelength in an Agilent Technologies 8453 UV-Vis spectrophotometer was done after an overnight incubation. The MTT test is based on the cleavage of the yellow tetrazolium salt MTT in the presence of an electron-coupling reagent [24]. NAD(P)H-dependent cellular oxidoreductase enzymes are capable of reducing the tetrazolium salt MTT to insoluble formazan, that has a purple color, which can be analyzed by measuring absorbance at 590 nm. This bioreduction occurs only in viable cells, and is related to NAD(P)H production through glycolysis. Therefore, the amount of formed formazan dye, directly correlates to the number of metabolically active cells in the culture. The cell viability was defined as

$$V_{MTT}(c_{NP}) = A_{max}(c_{NP})/A_{max}(c_{NP} = 0)$$

The cell viability V_{MTT} was plotted against the NP concentration c_{NP}, *cf.* Figure SI-IX.4. The resulting viability data $V_{MTT}(c_{NP})$ as obtained from the MTT test are displayed in Figure SI-IX.4. The data demonstrate that HUVECs are more sensitive to exposure with NPs than HeLa cells.

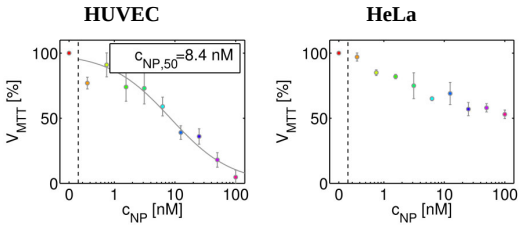

Figure SI-IX.4: *Cell viability V_{MTT}, as determined with the MTT test, in dependence of the NP concentration c_{NP}. The results are presented as mean ± SD for n = 3 independent measurements.*

IX.4) Live/dead assay

Forth, a commercially available live/dead assay was performed. Cell viability upon exposure to NPs was assessed by discriminating live and dead cells in fluorescence micrographs, using the LIVE/DEAD Viability/Cytotoxicity Kit (Molecular Probes, life technologies, #L3224). The kit contains two dyes: i) non-fluorescent cell-permeant calcein acetoxymethyl (AM) which enters live cells and is enzymatically converted into fluorescent calcein by intracellular esterases. ii) upon binding to DNA the fluorescence of live cell-impermeant ethidium homodimer (EthD-1) is strongly increased. The latter stains dead cells. Additionally, the nuclei of all cells (live and dead) were stained with Hoechst 33342 which is specific to DNA to allow automatic segmentation to simplify the readout of the assay.

Briefly, cells were seeded into an 8-well Ibidy µ-slide (12,500 cells/well). After 24 h NPs were added at various concentrations (c_{NP} = 0 - 100 nM). After an additional 24 h incubation cells were washed twice with PBS and stained referring to the instructions of the kit. Living cells were stained with calcein AM at a concentration of 12.5 µM, while EthD-1 was used at 40 µM (HeLa cells) and 200 µM (HUVECs) to stain dead cells. In addition, all nuclei were counterstained by Hoechst 33342 (Molecular Probes, life technology, #H1399) at 30 µg/mL. After 10 min incubation time imaging was started while the staining solution remained on the sample.

Imaging was performed with a fluorescent

widefield microscope (Zeiss, Axiovert 200M). Calcein was excited at λ_{ex} = nm (30 nm width band-pass filter) and emission was recorded at λ_{em} = 535 nm (40 nm width band-pass filter: green channel). Excitation of EthD-1 was perfor ed at λ_{ex} = 555 nm (50 nm width band-pass filter) while emitted photons were detected using a λ_{em} = 615 nm long-pass filter (red channel). Hoechst 33342 was excited around λ_{ex} = 365 nm and the emission was detected at λ_{em} = 440 nm (20 nm width ba l-pass filter: blue channel).

A total area of 10 mm^2 was im ıged for each well, allowing the analysis of 3000-6000 cells (*cf.* Figure SI-IX.5). For evaluation the micrographs were processed using MATLAB (Mathworks) and CellProfiler [17] in the following way: To identify whether a cell was stained green or red all nuclei were segmented based on the Hoechst stain. Along the area of each nucleus the corresponding mean intensities in the green and red channel were calculated. For live *vs.* dead cells two distinct populations appear when the mean intensity of calcein ($I_{Calcein}$) is plotted against the mean intensity of EthD-1 (I_{EthD-1}) in logarithmic scale (*cf.* Figure SI-IX.5, b-c). Those scatter plots allowed gating of individual populations and simplified the calculation of the ratio D of dead to living cells, defined as the ratio of the ave a ge number of red fluorescent cells to the average number of green fluorescent cells. The resulting data (mean values of three individual experiments ± SD) is given in Figure SI-IX.6.

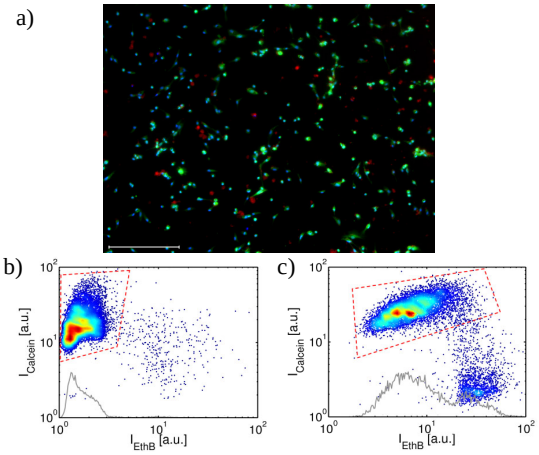

Figure SI-IX.5: *Cell viability assessed by calculating the ratio of dead/live cells. In a) a typical fluorescence image is shown after staining live cells with Calcein AM (green), dead cells with EthD-1 (red), and nuclei with Hoechst 33342 in blue. The scale bar corresponds to 50 µm. The scatter plots are showing gated populations of living (surrounded by red dashed line), and dead cells for HUVECs (b) in growth medium only, and (c) exposed to NPs at a concentration of c_{NP} = 100 nM for 24 h (c).*

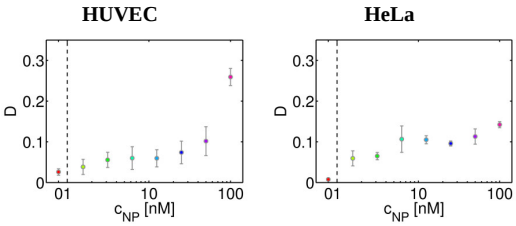

Figure SI-IX.6: *Rate of dead vs. live cells D, as derived from a fluorescence cell staining specific for live and dead cells, respectively. The results are presented as mean ± SD for 3 independent measurements.*

IX.5) Proliferation assay

The effect of the Au NPs on cell proliferation was investigated by directly measuring DNA synthesis, as monitored by the incorporation of the thymidine-analog EdU (5-ethynyl-2´-deoxyuridine). EdU can be detected by a copper-catalyzed click-reaction between its alkyne group and an azide group-containing fluorescent dye [25].

Briefly, cells were seeded into an 8-well Ibidy µ-slide (12,500 cells/well). A ter 24 h the growth medium was exchanged with medium containing 10 µM EdU (Molecular Probes, life technologies, #A10044) and NPs were added at various concentrations (c_{NP} = 0 - 1) nM). As a negative control .59cine (Sigma Aldric , #C3915) was added at a concentration of 5 µM (HUVECs) and 10 µM (HeLa cells). Cholchicine is an inhibitor of chromosome segregation during mitosi and suppresses cell proliferation. After additional 24 h of incubation the cells were fixated and permeabilized. Incorporated EdU was labelled with AlexaFluor 488 azide (Molecular Probes, life technologies, #A10266) by following the protocol of Salic *et al.* [25]. Briefly, the reaction cocktail for one µ-slide was prepared by mixing 800 µL ddH_20 with 200 µL of 1.7 M Tris (Sigma Aldrich, #T1503) buffer pH 8.5, 10 µL 100 mM $CuSO_4$ (Sigma Aldrich, #61230), 5 µL 10 mM AlexaFlour azide, and 200 µL 0.5 M ascorbic acid (Sigma Aldrich, #255564) and applied for 30 min. Additionally, the nuclei of all cells were labelled with Hoechst 33342 (Molecular Probes, life technologies, #H1399) for 30 min at 10 µg/mL.

Imaging was performed with a fluorescent widefield microscope (Zeiss, Axiovert 200M). EdU-AlexaFluor 488 was exited at λ_{ex} = 480 nm (30 nm width band-pass filter) and emission was recorded at λ_{em} = 535 nm (40 nm width band-pass filter: green channel). Hoechst 33342 was excited around λ_{ex} = 365 nm and the emission was gated at λ_{em} = 440 nm (20 nm width band-pass filter: blue channel).

A total area of 10 mm^2 w s imaged for each well,

allowing for the analysis of 3000-6000 cells (*cf.* Figure SI-IX.7). To determine the proliferation rate p the micrographs were processed using MATLAB (Mathworks) and CellProfiler [17] in the following way: First, the Hoechst-stained nuclei were segmented, representing all cells (proliferated and non-proliferated) present in the current frame. Second, the mean fluorescence intensity in the blue channel ($I_{Hoechst}$) per nuclei was determined, as well as the mean intensity of EdU-Alex Flour 488 in the corresponding green channel ($I_{EdU\text{-}AF488}$). For each nucleus the logarithm of both i ensity values was plotted in a scatter plot to allow for identification and gating of proliferated cells from non-proliferated ones, similar to analyzing flow cytometry data (*cf.* Figure SI-IX.7, b-c). Finally the fraction p of proliferated cells from all cells was calculated for each image and averaged for each concentration. Figure SI-IX.8 shows the mean values ± SD resulting from three individual experiments.

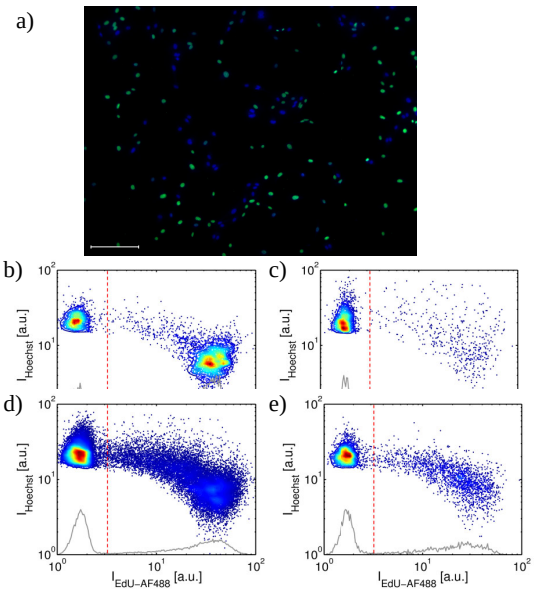

Figure SI-IX.7: *Cell proliferation assay. In a) a typical fluorescence image is shown for HUVECs used to derive quantitative results (scale bar: 100 µm). The nuclei of all cells are stained with Hoechst 33342 (blue), while only proliferated cells show green fluorescence in addition. The scatter plots are showing two populations divided by a dashed red line: the left spot in each plot is representing non-proliferated cells, while the right population is generated by proliferated cells. Shown are the data for (b) the positive control, (c) the negative control, (d) all cells analyzed, and (e) cells being exposed to NPs at c_{NP} = 0.59 nM.*

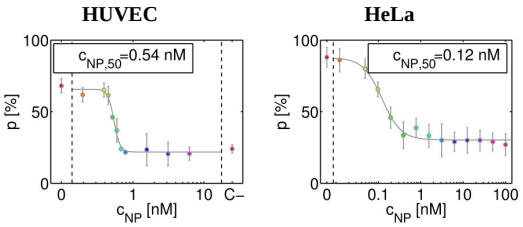

Figure SI-IX.8: *Proliferation rate p, as derived freshly synthesized DNA of cells after 24 h of NP exposure. The results are presented as mean ± SD for 3 independent measurements.*

IX.6) Oxidative stress

Sixth, oxidative stress was measured using CellROX as the probe. HeLa cells and HUVECs were seeded at 20000 cells/well in non-transparent 96 well plates (Greiner Bio One, Wemmel, Belgium) and were allowed to settle overnight, after which the cells were incubated with Au NPs at c_{NP} = 0 - 100 nM for 24 h. Then, the cells were washe 3 times with PBS and incubated with 10 µM CellROX Green (Molecular Probes, life technologies, #C10444) for 45 min. Cells were then washed 3 times with PBS, followed by an additional incubation for 30 min in full culture medium. Then, the cells were washed twice with PBS, and the fluorescence signal was measured using a Wallac Envision plate reader instrument with an excitation filter at λ_{ex} = 480 nm and an emission filter at λ_{ex} = 540 nm. As a positive control, cells were incubated with 0.5 % H_2O_2 f 1 h prior to incubation with CellROX Green. Data are expressed relative to untreated control cells (= 100 %) as mean + SD (n = 4). As toxic effects occurred, the data obtained for oxidative stress have been normalized for 20000 cells based on the ce viability data from the Alamar Blue assay (*cf.* Figure SI-IX.3).

The relative level R of ROS as calculated from the measurements is shown in Figure SI-IX.9. For HUVECs, an increase in ROS can be seen at higher NP concentrations. For HeLa cells, the level of ROS is increasing at higher NP concentrations, but the values themselves are not very high and significantly lower than those of HUVECs. This may in part explain the lower toxicity of the NPs to HeLa cells as compared to HUVECs.

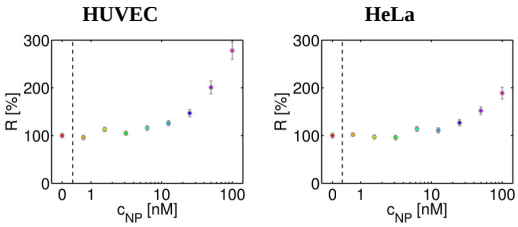

Figure SI-IX.9: *ROS levels R after exposure to NPs. Results are presented as mean value ± SD for n = 4 independent measurements.*

X) Analysis of general cell morphology

Concerning cell morphology first the mean area A_{cell} of each cell was determined. After cell exposure to the NPs for 24 h, cells were washed twice with PBS and fixed for 15 min at room temperature with 4 % paraformaldehyde. The fixative was then aspirated, cells were washed twice with PBS (500 µL/well), after which cells were permeabilized ith 250 µL/well of Triton X-100 (1 %) for 10 min at room temperature. Cells were then blocked with 10 % serum-containing PBS for 30 min at room temperature, followed by the addition of primary murine anti-α-tubulin (Abcam, Cambridge, UK, #ab80779) IgG antibody (Ab, 1 µg/mL in blocking buffer) at a total volume of 200 µL/well, and were incubated in the dark for 1.5 h at room temperature. Cells were washed twice with PBS, followed by addition of the secondary AF488-coupled secondary goat anti-murine IgG Ab (Molecular Probes, life technologies, #A-11029) (1/500 dilution in blocking buffer) and 15 µL (1/100 dilution) Acti-Stain 555 (Tebu-Bio, Belgium) per mL of blocking buffer to a total volume of 200 µL/well. Cells were incubated for 1 h at room temperature in the dark. The latter solution was removed and cells were washed once with PBS and incubated with CellMask Blue (Molecular Probes, life technologies, #H32720) at 5 µg/mL in PBS for 10 min in the dark. Finally, cells were washed twice with PBS, 500 µL fresh PBS was added to each well, and plates were analyzed on the InCell analyser 2000, where phase contrast and fluorescence-based images for the blue (CellMask Blue), green (α-tubulin), and red (F-actin) channel were collected at minimum 2000 cells/well. Data analysis was performed with the InCell Investigator software (GE Healthcare Life Sciences, Belgium) using in-house develo ed protocols. The size of the cells was calculated as follows: First, cell nuclei were segmented based o the blue channel (CellMask Blue stains the entire cytoplasm, but in permeabilized cells, the nucleus is preferentially stained and has a higher intensity). Using the green and red channel, cells were then segmented, where any holes in the cells were filled up and included and any cells on the border of the field of view were excluded from the analysis. The segmentation was based on the blue channel as seed channel for the nucleus. The total area of every individual cell was then determined. Images are shown in Figure SI-X.1 and Figure SI-X.2 for HUVECs and HeLa cells, respectively.

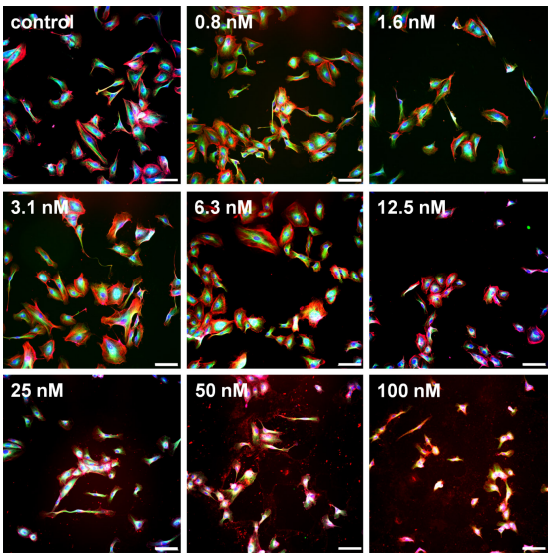

Figure SI-X.1: *Representative ages of HUVECs treated with Au NPs at different NP concentrations c_{NP}. Cells were stained for actin (red), tubulin (green), and CellMask (blue). The scale bar corresponds to 100 m.*

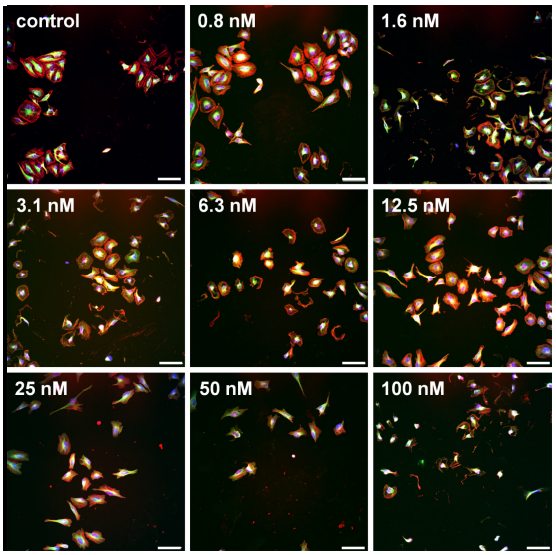

Figure SI-X.2: *Representative images of HeLa cells treated with Au NPs at different concentrations c_{NP}. Cells were stained for actin (red), tubulin (green), and CellMask (blue). The scale bar corresponds to 100 m.*

The results for the cell spreading experiments are summarized in Figure SI-X.3. The data demonstrate that upon exposure to NPs the cell area A_{cell} is reduced. For HUVECs the effects are far more

outspoken as in comparison to HeLa cells.

Cell spreading was investigated also from an additional data set, which was derived by actin-staining, as described in § VIII.1 and § XIII. The data set shown in Figure SI-XIII.1 and Figure SI-XIII.2 was also used for estimating the area per cell, in this case in terms of area of stained actin fibers per cell. The resulting values are shown in Figure SI-X.4.

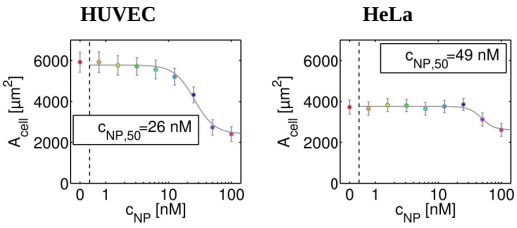

Figure SI-X.3: *Mean cross section area per cell A_{cell} of HUVECs (left) and HeLa cells (right) which had been incorporated for 24 h with Au NPs at different concentrations c_{NP}. Error bars indicate standard deviation for 3 independent sets of over 2000 cells evaluated per condition.*

In agreement with Figure SI-X.3 the data demonstrate that with increasing of the Au NP concentration the cell area decreases concentration dependently in both of the cells. Under the highest Au NP exposure concentration the area of HUVECs is reduced by a factor of two, whereas HeLa cells only loose 20 % of the cell area (as quantified in terms of stained actin). From the same data also the form factor F_{cell} of cells was determined, which shows that not only spreading area, but also shape of the cells upon exposure to NPs changed.

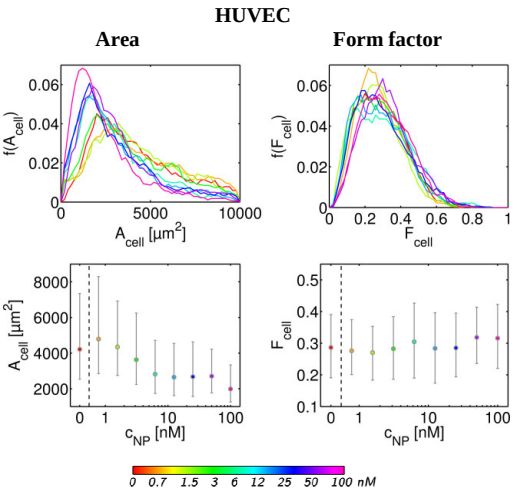

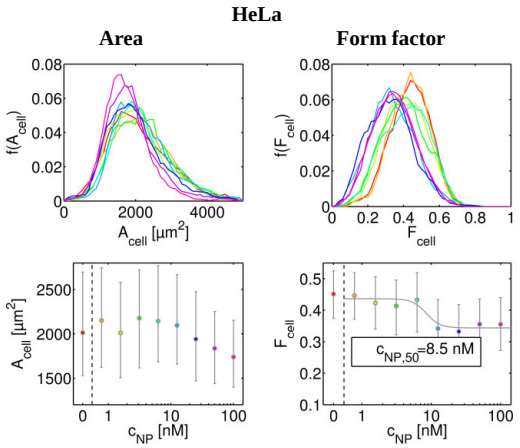

Figure SI-X.4: *The normalized probability distribution $f(A_{cell})$ and $f(F_{cell})$ of the frequency of cells found with an area A_{cell} and with form factor F_{cell}, respectively, as derived from stained actin per cell, is plotted for different Au NP concentrations c_{NP}. The results are presented as normalized probability distributions (first row) and median ± lower/upper quartile for 500 - 1000 cells/condition.*

As a second parameter describing cell morphology, filopodia of the two cell types were investigated. For this purpose, AFM analysis was performed on cells, which had been incubated for 24 h with NPs. Resulting images are presented in Figure SI-X.5 and Figure SI-X.6.

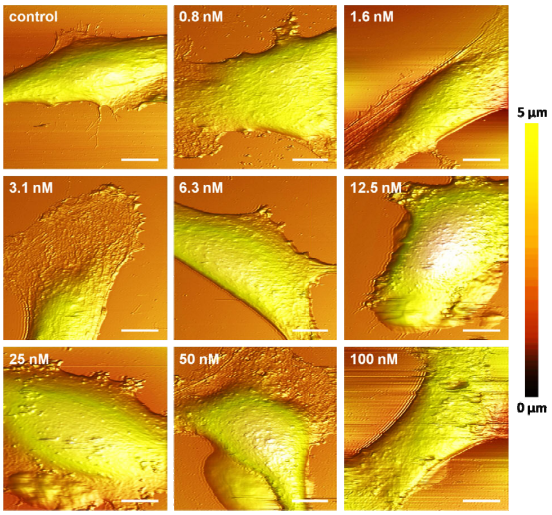

Figure SI-X.5: *AFM images (contact mode) of HUVECs which have been exposed to Au NPs at different concentrations c_{NP}. All samples were imaged on a glass-slide substrate. The scale bars correspond to 10 µm.*

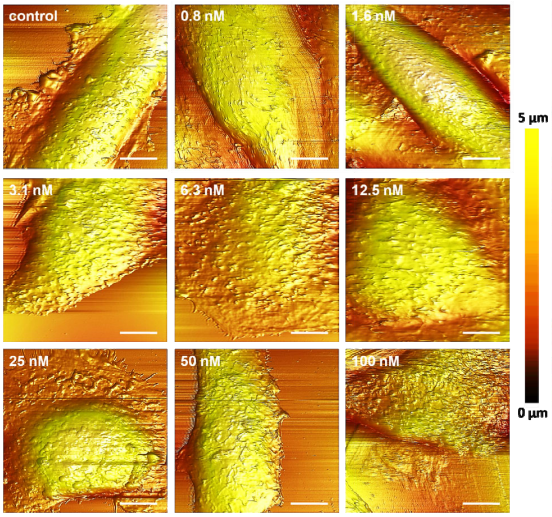

Figure SI-X.6: *AFM images (contact mode) of HeLa cells which have been exposed to Au NPs at different concentrations. All samples were examined on a glass-slide substrate. The scale bars correspond to 10 µm.*

From these images quantitati e data concerning filopodia were derived. Computer vision for the counting of surface objects (nAnosticTM method) was done using proprietary algorithms (Serend-ip GmbH, Münster, Germany), which are optimized for AFM-images. Basically, the experimenters label manually the objects of interest and feed an artificial neuronal network with these examples (machine learning). The computer then searches similar structures, *cf.* Figure SI-X.7 and Figure SI-X.8. Of each sample 10 images at arbitrarily chosen positions were recorded. The following parameters were extracted: the number of counted filopodia N_{fiolo} found on a cell within an imaging area of 20x20 µm^2, the total area A_{filo} occupied by filopodia within an imaging area of 20x20 µm^2, the average filopodia height h_{filo}, and the sum of the local deviational volumes V_{filo} occupied by filopodia within an imaging area of 20x20 µm^2. The local deviational volume of each filopodium was calculated by summation of the height values corrected by a local plane fit for each filopodium [26]. Both cell types HUVECs and eLa cells show a decreasing number, area and local ɨeviational volume of filopodia per image within an increasing concentration of Au NPs. In contrast the height increases at higher concentrations of Au NPs. Comparing HUVECs and HeLa cells demonstrates that the morphology of HUVECs is altered at lower concentrations of Au NPs. The resulting data are presented in Figure SI-X.9.

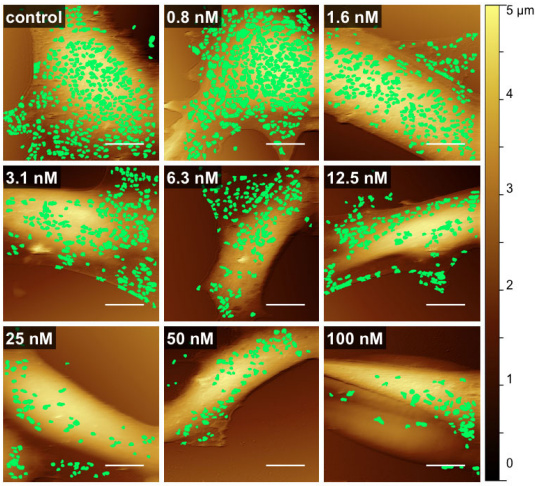

Figure SI-X.7: *Results of computer vision are displayed as green overlays demonstrating the decreasing number of filopodia in HUVECs exposed to increasing concentrations of Au NPs. The scale bars correspond to 10 µm.*

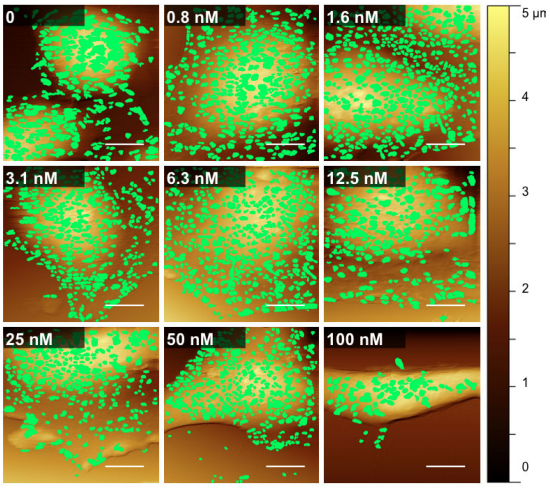

Figure SI-X.8*: Results of computer vision are displayed as green overlays demonstrating the decreasing number of filopodia in HeLa cells exposed to increasing concentrations of Au NPs. The scale bars correspond to 10 µm.*

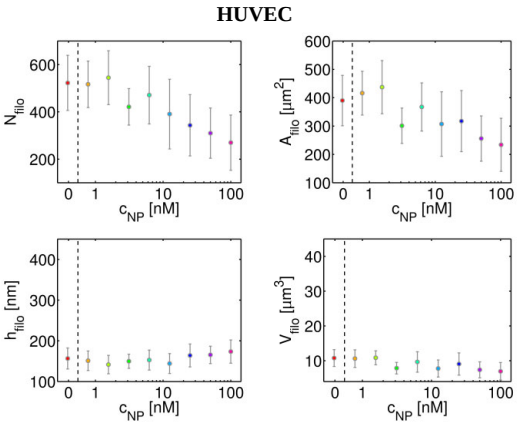

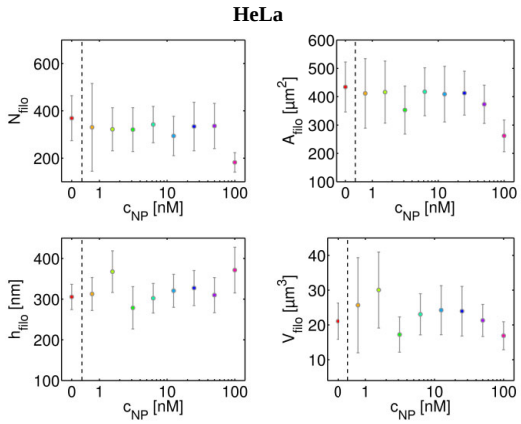

Figure SI-X.9: *Mean number of counted filopodia N_{fiolo}, the total area A_{filo} occupied by filopodia, the average filopodia height h_{filo}, and the total volume V_{filo} occupied by filopodia within an imaging area of 20x20 µm², as determined by data analysis of AFM images, in dependence of the Au NPs concentration. The results are presented as mean ± SD for 3 individual experiments.*

XI) Analysis of nanoparticle uptake and morphology of the lysosomes

XI.1) Quantification of NP uptake

XI.2) Assessment of NP-induced changes in lysosome morphology

XI.1) Quantification of NP uptake

First, we first investigated the endocytosis of Au NPs. In agreement with previous reports we assume that macropinocytosis plays a role in the uptake pathway, as in Figure SI-IV.1 one can see a macropinocytic cup which wraps around an assembly of Au NPs. However, studies on uptake of bigger Au NPs with similar surface chemistry showed a dominant *via* caveolin-mediated endocytosis [27].

In order to trace the intracel ular location of the NPs, green fluorescent protein (GFP)-labeled lysosomal associated protein 1 (LAMP1) was expressed in HUVECs and HeL cells to allow for simultaneous live-imaging o lysosomes and fluorescence-labeled NPs [22].

HeLa cells (2500 cells/per well, in 200 µL) or HUVECs (5000 cells/per well, in 200 µL) were added to µ-Slide 8 well-ibiTreat chambers (1 cm^2 per well, Ibidi, Germany) and incubated over night at 37 °C. Next, the cells were transfected with CellLight lysosome-GFP (Molecular Probes, life technologies, #C10596), 1 µL and 2 µL per we for HeLa cells and HUVECs, respectively. After 24 h the µ-slide was mounted into a portable microscope incubator system (PeCon, Germany) on the CLSM to allow for live cell imaging at 37 °C and 5 % CO_2. After equilibration NPs were added (c_{NP} = 25 - 100 nM) and imaging was started using an Apochromat 63x/1.40 Oil DIC M27 objective. For each concentration 10 positions (2800 µm², approx. 30-50 cells) were imaged at a lateral sampling frequency o 140 µm (pinhole size: 1 AU) and a temporal resolution of 45 min. The focus position was adjusted to be 0.5 µm above the substrate. GFP was excited at λ_{ex} = 488 nm and the emission was detected between λ_{em} = 505 and 530 nm (band-pass, green channel). Fluorescence-labeled NPs were excited at λ_{ex} = 543 nm and emitted photons were gated using a long-pa s filter at λ_{em} = 560 nm filter (red channel). From the obtained time image series the NP intensity inside lysosomes (density of NPs) was calculated: For each time point and for each position the fluorescence signal originating from the lysosomes (green channel) was used to mask the signal derived from the NPs (red channel) spatially. Thereto the green channel containing the signal of the lysosomes was carefully thresholded followed by median-filtering to remove background noise. Then, the signal was binarized by adjusting all pixel intensities above zero to 1. Subsequently, the obtained mask was deconvolved w th the related image containing the NP intensities (red channel). In other words, only the NP signal at positions colocalizing with lysosomes was considered. Due to the high axial resolution of a CLSM almost all NP-signal which is not originating from NPs being present in structures associated with LAMP1 is suppressed. Finally for each time point the mean of the masked NP intensity I_{NP}(lyso) was calculated and plotted *versus* time (Figure SI-XI.2).

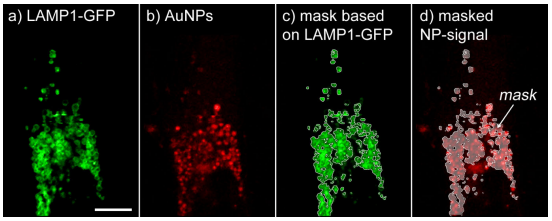

Figure SI-XI.1: *Confocal micrographs of a time lapse series showing parts of a HUVEC which has been exposed to NPs for 16 h at c_{NP} = 50 nM. (a) The signal of stained lysosomes is used to create a mask. (b) Shows the channel of fluorescence labeled NPs. (c) Mask based on LAMP1-GFP signal. (d) Mean intensity I_{NP}(lyso) of NPs inside the lysosomal mask. The scale bar corresponds to 10 µm.*

Although the absolute intensity values cannot be compared for HUVECs an HeLa cells (the total uptake by HUVECs is much higher as compared to HeLa cells, *cf.* Figure SI-XI.3), the results highlight the different uptake/transport kinetics of the NPs in HUVECs and HeLa cells. Regarding HUVECs, the largest fraction of NPs is transported into lysosomes within the first 4 hours of incubation, while in HeLa

cells the lysosomal enrichment takes place more linearly.

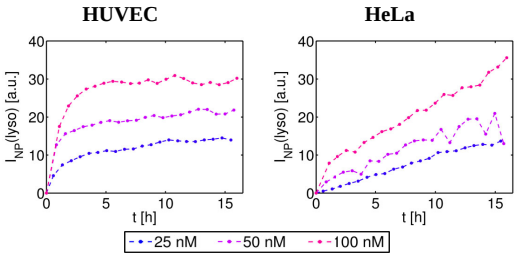

Figure SI-XI.2: *Mean NP-intensity I_{NP}(lyso) measured inside lysosomal structures at different NP concentrations c_{NP} = 25, 50 and 100 nM. I_{NP}(lyso) is proportional to the average lysosomal Au NPs density. The intensities are not comparable between HUVECs and HeLa cells as the uptake rate of HeLa cells was much lower.*

HeLa cells (3000 cells/per well, in 200 µL) or HUVECs (6000 cells/per well, in 200 µL) were added to 8 well µ-Slide chambers (1 cm^2 per well, Ibidi, Germany, #80826) and incubated over night at 37 °C. Next, the cells were incubated with Au NPs at c_{NP} = 0-100 nM for 24 h at 37 °C and 5 % CO_2.The cells were then fixed for 20 min in 4 % paraformaldehyde, after which the cells were washed 3 times with Hank's balanced salt solution (HBSS). Cells were stained with Wheat Germ Agglutinin (WGA)-AlexaFluor 488 conjugate (Molecular Probes, Life technologies, USA, #W11261**)** solution (15 µg/mL in HBSS) for 15 minutes. Then the cells were washed 2 times in HBSS, followed by 2 times in PBS. Next, the cells were permeabilized (5 mg/mL glycine, Roth, Germany, #3908.1), 0.5 mg/mL saponin (Sigma-Aldrich, #S7900) in PBS for 5 min and incubated in blocking solution (PBS with 2 % BSA (bovine serum albumin, Jackson ImmunoResearch Laboratories, #001-000-161)). Afterwards, the cells were stained with murine anti-LAMP-1 antibodies (Developmental Studies Hybridoma Bank, USA, #H4A3) at 2 µg/mL at 4 °C overnight. Then, the cells were washed three times with PBS and stained with 1.25 µg/mL secondary antibody DyLight 649 donkey anti-mouse IgG (H+L) antibody (Jackson ImmunoResearch Laboratories, #715-495-150) at 37 °C for 30 minutes. After that, the cells were stained with 50 µM DAPI (Molecular Probes, life technologies, #D1306) and incubated for 5 min at room temperature. Cells were then washed three times with PBS and stored in 200 µL PBS/well at 4 °C, followed by analysis using a CLSM.

Images were recorded using a Plan-Apochromat 20x/0.8 M27 objective and a pinhole-size of around four airy units (AU). The focus position was determined automatically 3 µm above the substrate for each position. The emission of DAPI (λ_{ex} = 405 nm) was detected using a 420-490 nm band-pass, AlexaFluor 488 was excited at λ_{ex} = 488 nm. Emission was detected at λ_{em} = 525 (±50) nm with a 40 nm bandwidth band-pass filter). DyLight 649 was excited at λ_{ex} = 633 nm and emission was filtered using a λ_{em} =650 nm long-pass. Around 500 - 1000 cells were imaged per condition.

The data shown in Figure SI-XI.1 suggest that the internalized Au NPs accumulate inside lysosomes. The number of internalized NPs per cell (as measured in average integrated fluorescence intensity I_{NP} of the NP-signal in one cell, *cf.* § VIII.4) is display in Figure SI-XI.3.

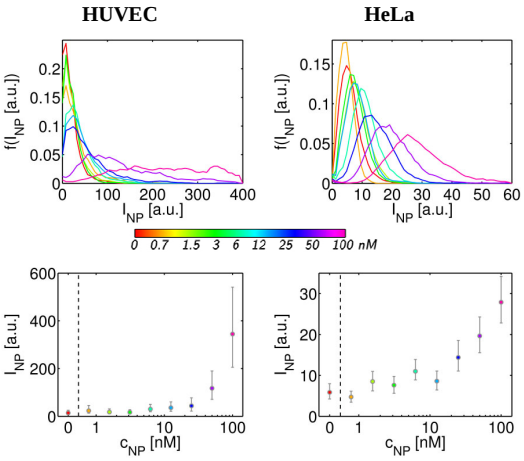

Figure SI-XI.3: *Integrated fluorescence intensity of internalized Au NPs per cell (I_{NP}). The results are presented as normalized probability distributions (first row) and median ± lower/upper quartile for 500 - 1000 cells/condition.*

XI.2) Assessment of NP-induced changes in lysosome morphology

Eventually, we investigated the effects of Au NPs on the morphology of the lysosomes (§ VIII.3, *lysosomal fraction*). The fraction of the area within the cells, which is occupied by lysosomes A_{lyso}/A_{cell} (an example is given in Figure -VIII.4) as well as the amount of lysosomes in terms of lysosome fluorescence I_{lyso} per cell was determined, *cf.* Figure SI-XI.4.

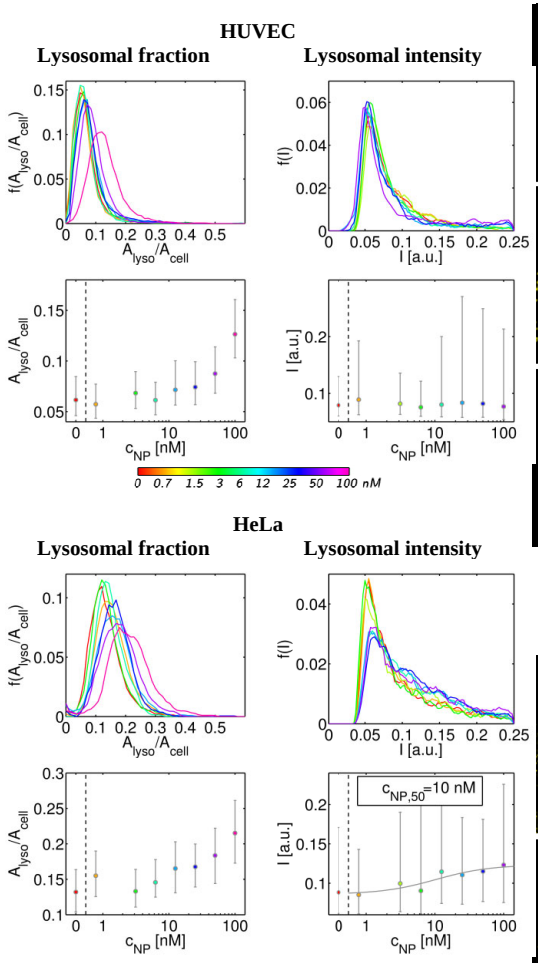

Figure SI-XI.4: *Fraction of cross section area occupied by lysosomes A_{lyso}/A_{cell}, as derived by dividing the lysosome area (yellow stain in Figure SI-VIII.4) by the total area of each cell (red stain in Figure SI-VIII.4). In addition, the amount of lysosomes per cell as determined by their fluorescence intensity I_{lyso} is depicted. The results are presented as normalized probability distributions (first row) and median ± lower/upper quartile for 400 - 1000 cells/condition.*

In an additional set of data we investigated lysosome swelling, *i.e.* the change in size distribution of the lysosomes upon exposure to Au NPs. Imaging was performed at higher magnification, using a Plan-Apochromat 63x/1.40 Oil DIC M27 objective and a lateral sampling frequency of 90 nm. In Figure SI-XI.5 and Figure SI-XI.6 images were obtained at different exposure concentrations c_{NP} are displayed for HUVECs as well as for HeLa cells.

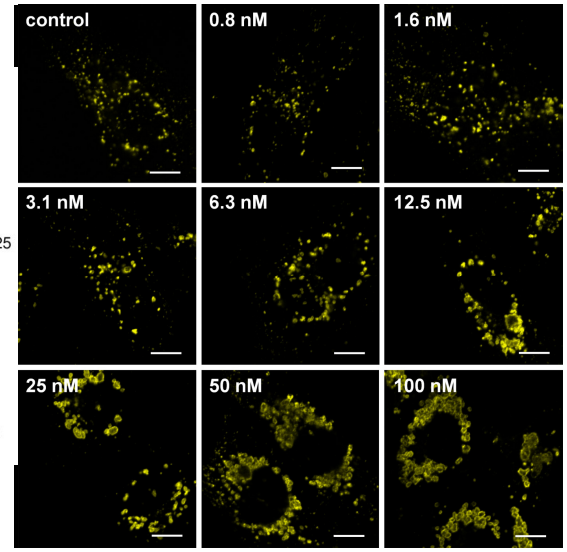

Figure SI-XI.5: *Change in lysosome morphology of HUVECs exposed to c_{NP} = 1-100 nM of Au NPs (scale bar: 10 µm).*

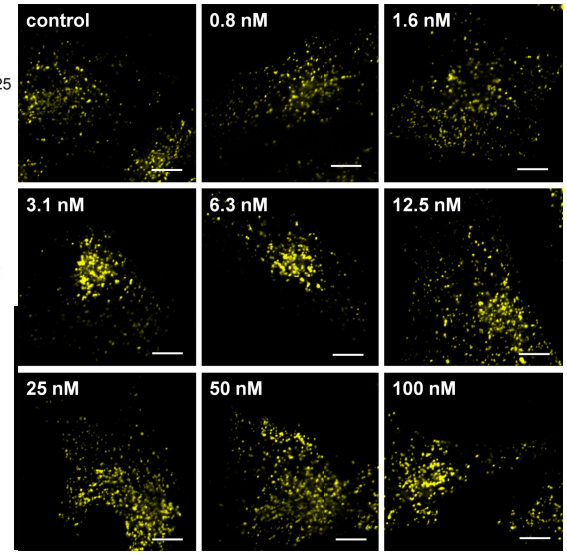

Figure SI-XI.6: *Change in lysosome morphology of HeLa cells exposed to c_{NP} = 1 - 100 nM of Au NPs (scale bar: 10 µm).*

The average area of an individual lysosome A_{lyso} is shown for the different NP concentrations in Figure SI-XI.7. It can be seen that lysosome swelling, *i.e.* increase of lysosome size upon increasing NP concentrations, is very intense in HUVECs, but the change of lysosome morphology not so obvious in HeLa cells. Therefore, the increase of the fraction occupied by lysosomes A_{lyso}/A_c as displayed in Figure SI-XI.4 has more relevance for indicating morphology changes of the lysosome. Anchoring organelles is an important function of cytoskeleton. Therefore, the change in lysosome occupation fraction should be also a reflection of cytoskeletal disruption, *cf.* § XIII.

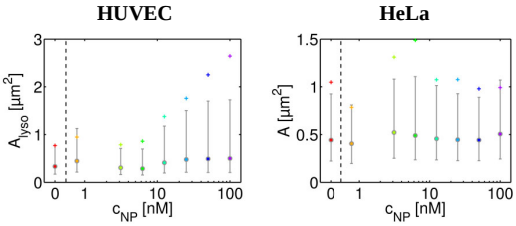

Figure SI-XI.7: *Size of individual lysosomes. The results are presented as median (o) ± lower/upper quartile for 1800-4000 lysosomes/condition. The mean values are represented as crosses (+).*

XII) Analysis of the morphology of the mitochondria

We also investigated the effects of Au NPs on mitochondrial morphology. Mitochondrial morphology is a very sensitive parameter for cellular stress. In order to image individual mitochondria, green fluorescent protein GFP-labeled E1 alpha pyruvate dehydrogenase was expressed in HUVECs and HeLa cells, to allow for simultaneous live-imaging of mitochondria and fluorescence-labeled NPs.

HeLa cells (2500 cells/per well, in 200 µL) or HUVECs (5000 cells/per well, in 200 µL) were added to 8 well µ-slides (1 cm^2 per well, Ibidi, Germany, #80826) and incubated over night at 37 °C. Next, the cells were transfected with CellLight Mitochondria-GFP (Molecular Probes, Life Technologies, #C10600), 1.5 µL and 3 µL reagent per well for HeLa cells and HUVECs, respectively. After 24 hours, the cells were incubated with Au NPs at c_{NP} = 0 - 100 nM for 24 h at 37 °C and 5 % CO_2. Then, the cells were fixed for 20 min in 4 % paraformaldehyde, after which they were washed three times with PBS. Cells were stored in 200 µL PBS/well at 4 °C, followed by analysis using a CLSM. The fluorescence of GFP was excited at λ_{ex} = 488 nm. Emission was detected at λ_{em} = 52 (40 nm bandwidth band-pass). Imaging was performed using a Plan-Apochromat 63x/1.40 Oil DIC M27 objective and a lateral sampling frequency of 30 nm.

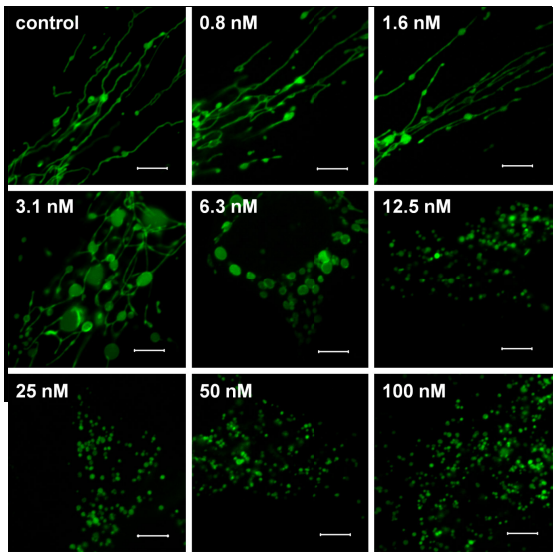

Figure SI-XII.1: *Mitochondria morphology change of HUVECs after Au NP-treatment at different concentrations c_{NP}. (Scale bar: 5 µm)*

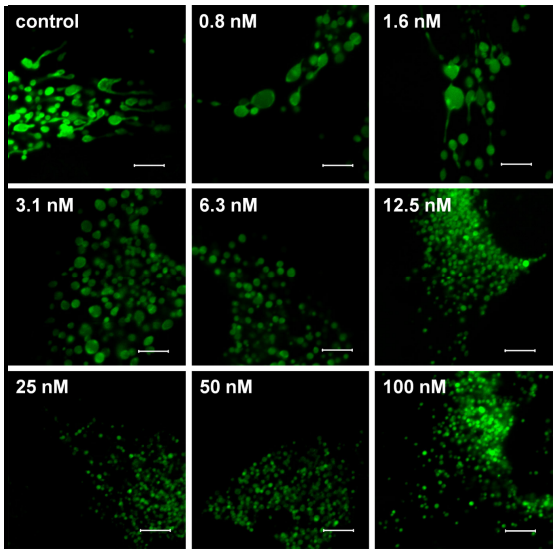

Figure SI-XII.2: *Mitochondria morphology change of HeLa cells after Au NP-treatment. (Scale bar: 5 µm)*

In the HUVECs the mitochondria are long thread-like structures in the control group (*i.e.* without NP exposure) and at low concentrations of Au NPs, *cf.* Figure SI-XII.1. With an increase of the Au NP concentration the morphology of the mitochondria changed from polliwog-like structures to large dots and finally to small spots. This can be seen in the form factor F_{mito}, which would be equal to 1 in case the mitochondria had perfect spherical shape. Looking at the HeLa cells, the mitochondria without or with exposure to low NP concentrations are longer,

however, not as long as the o es which can be observed in HUVECs. Thread and polliwog structures co-exist in the control group and cells exposed to low concentrations of Au NPs, *cf.* Figure SI-XII.2. The mitochondria become smaller and smaller with the increase of the Au NPs concentration. Although the change of mitochondria morphology is more obvious in HUVECs than in HeLa cells, the latter ones are more sensitive at low NP concentrations. The mitochondria begin to become round-shaped already at c_{NP} = 6.2 nM in HUVECs, but in HeLa cells, the change starts already at concentrations as low as c_{NP} = 3.1 nM, *cf.* Figure SI-XII.3.

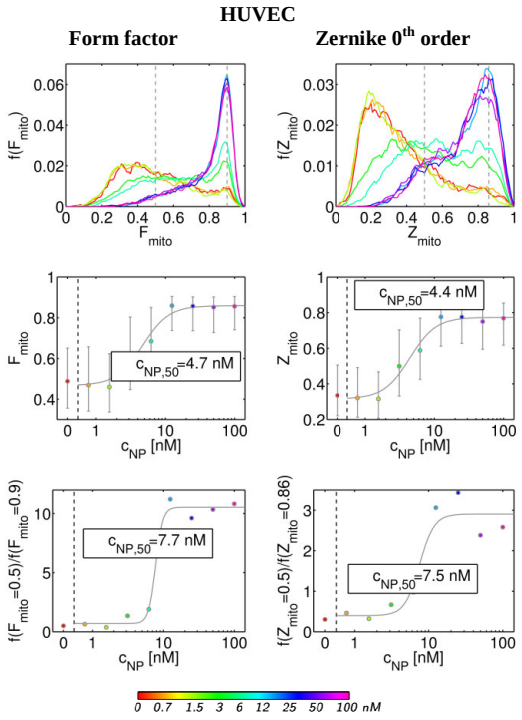

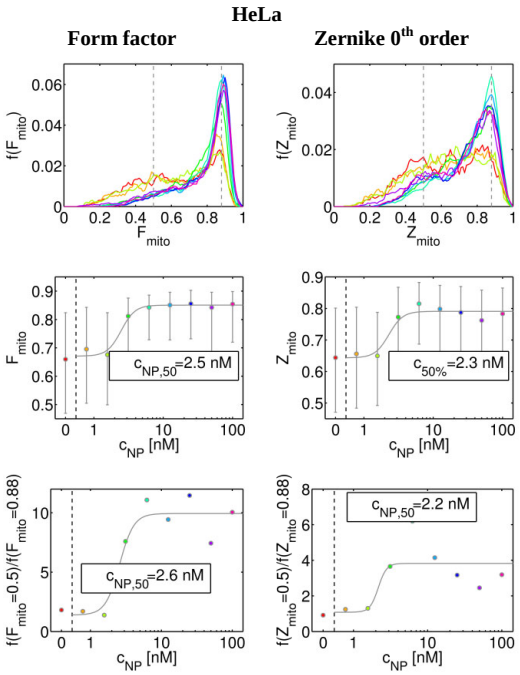

Figure SI-XII.3: *Geometrical features of mitochondria upon exposure to Au NPs. The results are presented as normalized probability distributions (first row) and median ± lower/upper quartile for 1700-5000 mitochondria/condition (second row). In the last row the ratios of the corresponding values at the dotted lines were derived from the probability distributions.*

XIII) Analysis of the morphology of the cytoskeleton

XIII.1) Assessment of changes in actin morphology

XIII.2) Assessment of changes in tubulin morphology

XIII.3) Assessment of focal adhesions

The cytoskeleton provides support and shape to the cell and anchors the organelles to their designated place. It also helps in movement of materials in and out of cells. Once the solid Au NPs are endocytosed and accumulate in cells, they may occupy significant space and therefore the cytoskeleton may be affected. We investigated the change o actin and tubulin fibers.

XIII.1) Assessment of change in actin morphology

HeLa cells (3000 cells/per well, in 200 µL) or HUVECs (6000 cells/per well, in 200 µL) were added to 8 well µ-Slide (1 cm^2 per well, Ibidi, Germany, #80826) and incubated over night at 37 °C. Next, the cells were incubated with Au NPs at c_{NP} = 0 - 100 nM for 24 h at 37 °C and 5 % CO_2. The cells were then fixed for 20 min in 4 % paraf maldehyde, after which the cells were washed with PBS for 3 times. Next, the

cells were permeabilized with 5 mg/mL glycine (Roth, Germany, #3908.1) and 0.5 mg/mL saponin (Sigma-Aldrich, #S7900) in PB for 5 min, followed by incubation in blocking solution (3S with 2 % BSA (Jackson ImmunoResearch Laboratories, #001-000-161)). Then, the cells were stained with 165 nM AlexaFluor 488-phalloidin (Molecular Probes, Life technologies, USA, #A12379) and incubated at room temperature for 20 min. After that, the cells were stained with 50 µM DAPI (Molecular Probes, life technologies, #D1306) and incubated for 5 min at room temperature. The cells were washed three times with PBS and stored in 200 µL PBS/well at 4 °C, followed by analysis using a CLSM. The emission of DAPI (λ_{ex} = 405 nm) was detected using a λ_{em} = 420 - 490 nm band-pass. The fluorescence of AlexaFluor 488-phalloidin was excited at λ_{ex} = 488 nm. Emission was detected at λ_{em} = 525 nm (40 nm width band-pass). Imaging was performed using a Plan-Apochromat 20x/0.8 M27 objective. Actin texture features were calculated as described in § VIII.3 with a correlation length 1.8 µm.

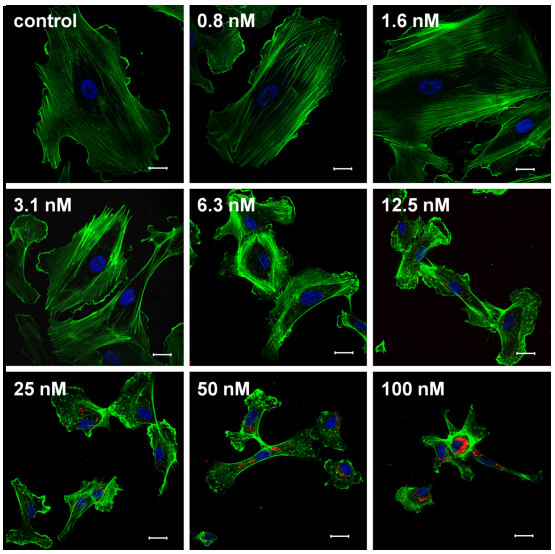

Figure SI-XIII.1: *Actin morphology change of HUVECs under different concentrations of Au NPs (scale bars: 20 µm). Blue channel: nuclei, red channel: Au NPs, green channel: actin fibers.*

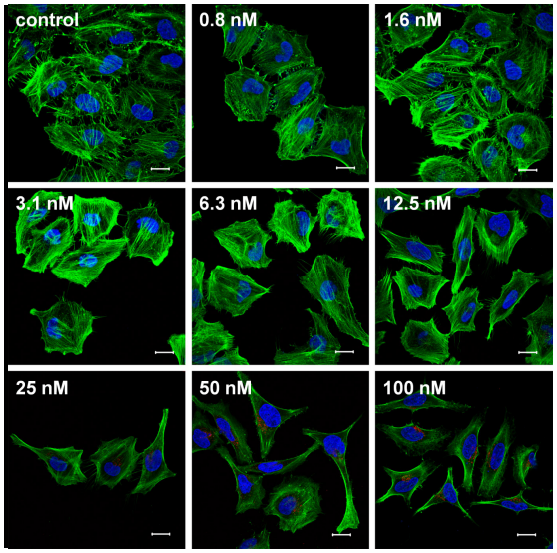

Figure SI-XIII.2: *Actin morphology change of HeLa cells under different concentrations of Au NPs (scale bars: 20 µm). Nuclei are shown in blue, Au NPs in red, and actin fibers in green.*

In the HUVECs, with increasing concentration of Au NPs, the long thread like structure of actin was partially lost, and more and more dot-like structures appeared, *cf.* Figure SI-XIII.1. From the analysis of actin texture change, we found that in HUVECs the texture contrast increased after Au NP treatment, which is correlated with an increase of dot-like structures and a decrease of thread-like structures in HUVECs (*cf.* Table SI-VIII.5 Figure SI-XIII.3). This is different with HeLa cells. In this case the appearing of dot-like structures was not observed, *cf.* Figure SI-XIII.2). Here the texture variance decreased after Au NP treatment. This is correlated with the cell surface actin fibers becoming smoother after Au NP treatment. In HeLa cells, the edge of the cells changed significantly, *i.e.* the edge of the cells was "kiwi"-like in the control group (c_{NP} = 0 nM), and the actin fibers tightly connect the neighboring cells. The cell surface became smoother after Au NP treatment. This involves that the cells might lose connection and communications with each other after exposure to Au NPs. In addition, round-shaped cells became long and narrow after Au NPs treatment, which suggests that the adhesion of the cells to the culture dish is not as tight anymore after exposure to Au NPs. High intracellular numbers of non-degradable solid Au NPs are clustered in endosomal structures, which are located in the perinuclear region and near the microtubule organizing center *cf.* § IX. Thus the NPs may hinder existing or newly forming cytoskeletal structures.

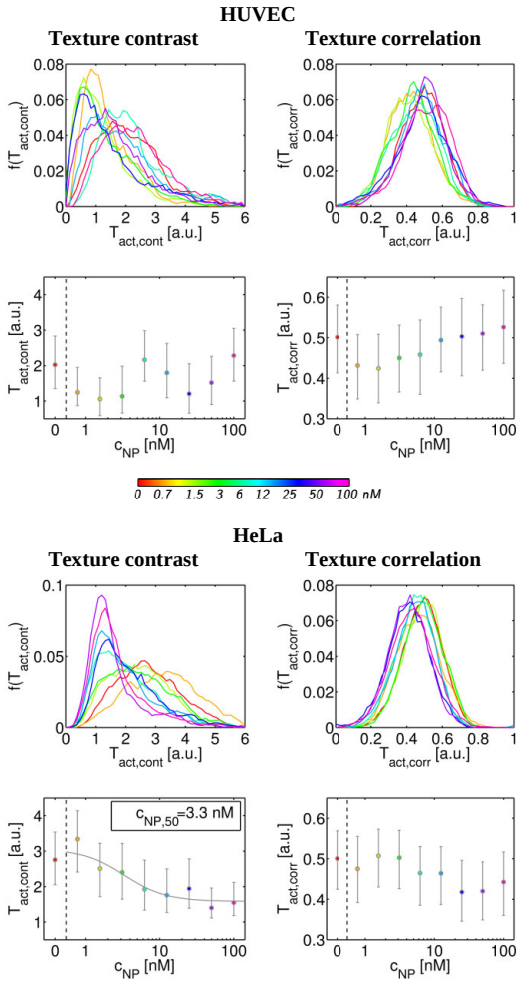

Figure SI-XIII.3: *Change of actin texture features (contrast $T_{tub,cont}$, correlation $T_{tub,corr}$) upon exposure of cells to Au NPs. The results are presented as normalized probability distributions (first row) and median ± lower/upper quartile for 600 - 1000 cells/condition.*

XIII.2) Assessment of changes in tubulin morphology

HeLa cells (3000 cells/per well, in 200 µL) or HUVECs (6000 cells/per well, in 200 µL) were added to 8 well µ-Slide chambers (1 cm^2 per well, Ibidi, Germany) and incubated over nig at 37 °C. Next, the cells were incubated with Au NPs at c_{NP} = 0 - 100 nM for 24 h at 37 °C and 5 % CO_2. ıen, the cells were fixed for 20 min in 4 % paraformaldehyde, after which the cells were washed with PBS for 3 times. Next, the cells were permeabilized (5 mg ıL glycine (Roth, Germany, #3908.1), 0.5 mg/mL saponin (Sigma-Aldrich, #S7900) in PBS) for 5 m ı and incubated in blocking solution (PBS with 2 % BSA (Jackson ImmunoResearch Laboratories, #001-000-161)). The cells were stained with goat anti-alpha tubulin antibody (abcam, UK, #ab18251) at the concentration of 1 µg/mL at 4 °C overnight. Then, the cells were washed three times with BS and stained with 20 µg/mL secondary antibody (Ab) AlexaFluor 430 goat anti-rabbit IgG (H+L) antibody (Molecular Probes, Life technologies, USA, #A11064) at 37 °C for 30 minutes. After that, the cells were washed three times with PBS and stored in 200 µL PBS/well at 4 °C, until they were analyzed using a CLSM. The fluorescence of AlexaFluor 488 was excited at λ_{ex} = 488 nm. Emission was detected at λ_{ex} = 525 nm (40 nm width band-pass). Imaging was performed using a Plan-Apochromat 63x/1.40 Oil DIC M27 objective and a lateral sampling frequency of 200 nm. Tubulin texture features were calculated as described in § VIII.3 with a correlation ngth of 1.2 µm.

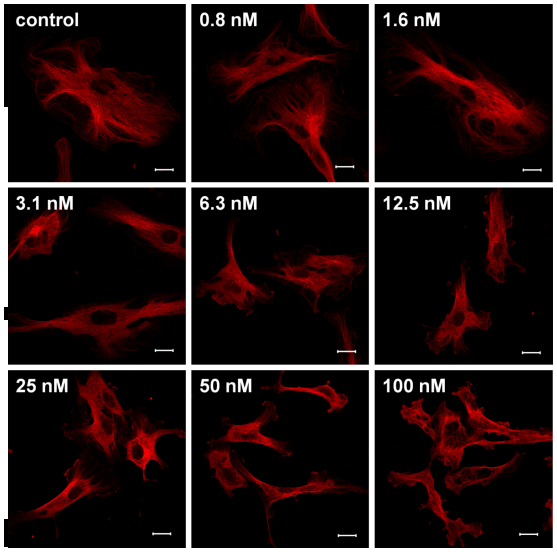

Figure SI-XIII.4: *Tubulin morphology change of HUVECs under exposure to different concentrations of Au NPs (scale bars: 20 µm)*

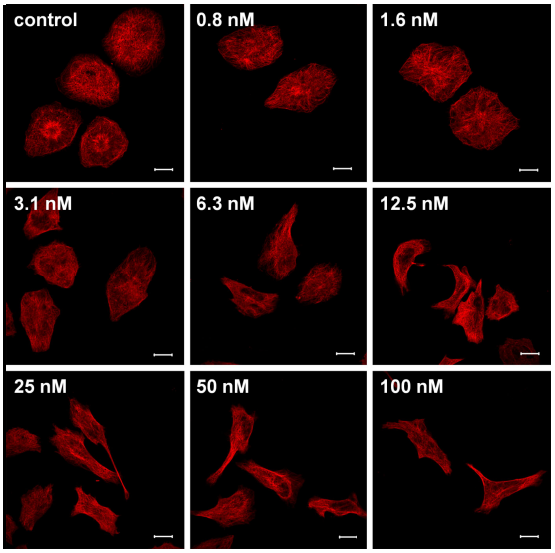

Figure SI-XIII.5: Tubulin morphology change of HeLa cells under Au NP-treatment (scale bars: 20 µm)

In HUVECs we found a clear loss of tubulin network at high Au NP concentrations, *cf.* Figure SI-XIII.6. The tubulin fibers are compactly arranged in the control group (c_{NP} = 0 nM), b t big holes can be found in cells treated with c_{NP} = 100 nM. In HeLa cells, the tubulin network was originally circularly arranged in the control (c_{NP} = 0 nM) and at low concentrations of Au NPs. Upon increasing NP concentrations the tubulin network became thin and long. The deformation of the actin cytoskeleton is more serious than the one of the tubulin network, suggesting that the actin fibers are more sensitive to the NP-induced deformations, *cf.* § XIV.

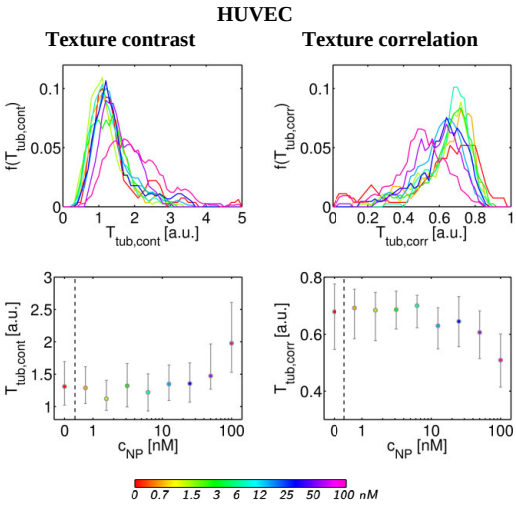

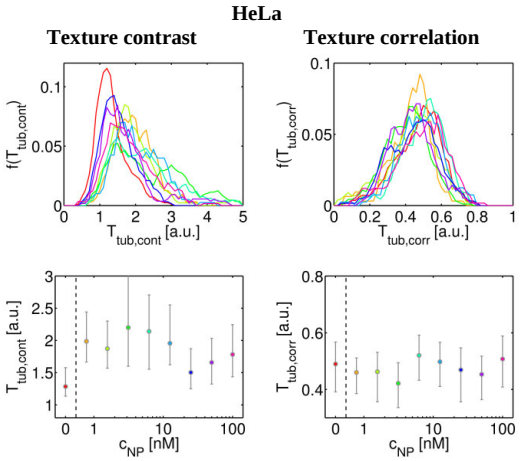

Figure SI-XIII.7: *Change of tubulin texture features (contrast $T_{tub,cont}$, correlation $T_{tub,corr}$) upon exposure of cells to Au NPs. The results are presented as normalized probability distributions (first row) and median ± lower/upper quartile for 60 - 150 cells/condition.*

XIII.3) Assessment of focal adhesions

Focal adhesions are important mediators in cell signaling along actin fibers, a d represent the integrity of contact of the cell cytoskeleton with cell surface located receptors that regulates signaling. For this reason we performed a co-staining of the actin network as well as vinculin. o analyze the effects of the Au NPs on focal adhesions, HUVECs and HeLa cells were seeded in MatTek glass bottom microscopy culture dishes (MatTek, USA, #P35G-1.5-10-C) at $2 \cdot 10^4$ cells/dish and allowed to settle overnight. Cells were then labeled with the Au NPs at c_{NP} = 0 - 100 nM for 24 h. Then, media were removed, and cells were washed 3 times with PBS (500 µL/dish). Then cells were fixed (2 % paraformaldehyde for 15 min), permeabilized (1 % Triton X-100 for 15 min), and blocked for 30 min in PBS containing 10 % goat serum (Gibco, life technologies, #PCN5000) and 2 % BSA. Cells were then incubated with primary antibody in b cking solution: mouse anti-vinculin monoclonal Ab (1:200, Abcam, Cambridge, UK, #ab18058) for 2 h at ambient temperature, followed by 1 h incubation at ambient temperature with secondary AlexaFluor 488-conjugated goat anti-mo e antibody (1:250, Molecular Probes, life technologies, #H32720), and AlexaFluor 546-conjugated phalloidin (Molecular Probes, life technologies, # .22283). Subsequently, cells were washed three times with blocking solution and mounted on microscope slides prior to being analyzed by confocal laser scanning microscopy (LSM710, Zeiss, Germany). For analysis of focal adhesion areas, confocal images displaying vinculin were background-corrected, and thresholded. Focal

adhesions were identified and the total areas per cell were calculated for 40 cells per condition. Images are shown in Figure SI-XIII.8 and Figure SI-XIII.9.

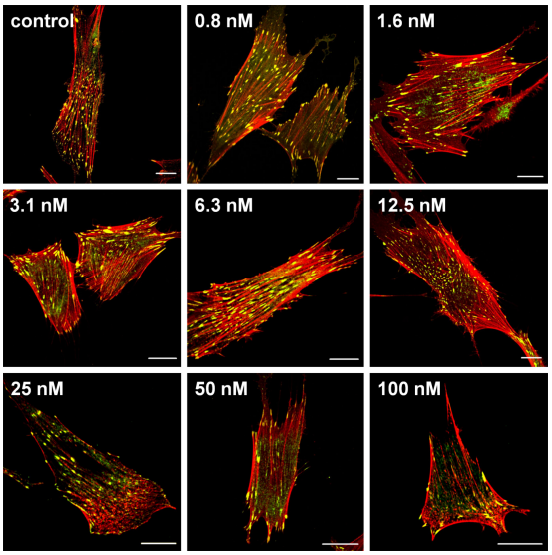

Figure SI-XIII.8: *Confocal microscopy images of HUVECs treated with Au NPs at the indicated concentrations for 24 h. Cells were then stained for F-actin (red) and vinculin (green). Scale bars: 25 µm.*

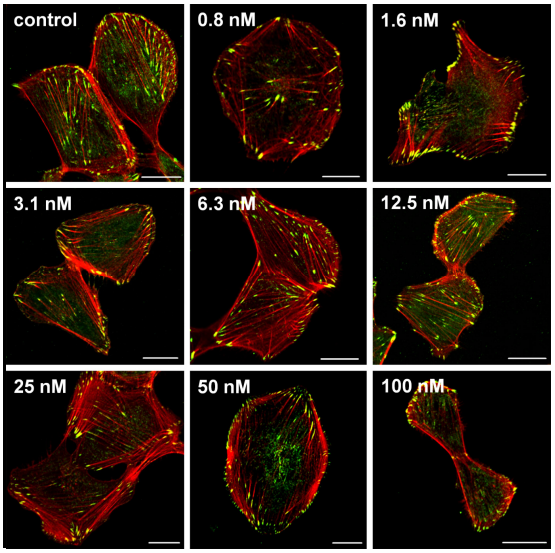

Figure SI-XIII.9: *Confocal microscopy images of HeLa cells treated with Au NPs for 24 h at different NP concentrations c_{NP}. Cells were then stained for F-actin (red) and vinculin (green). Scale bars: 25 µ .*

For HUVECs, the overall size of focal adhesions (as determined in the area of vinculin staining A_{vinc}) is much higher and the effects are much more outspoken and significant at higher NP concentrations, as compared to HeLa cells, *cf.* Figure SI-XIII.10. With HeLa cells, only minor effects can be seen, but at higher NP concentrations, the total vinculin area A_{vinc} per cell goes down. These results indicate that as the cell cytoskeleton is affected, as is actin-mediated signaling (which affects man different pathways such as cell division, cell death, *etc.*…).

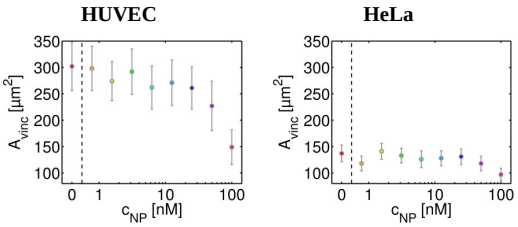

Figure SI-XIII.10: *Focal adhesion area A_{vinc} after exposure of cells to Au NPs. The results are presented as mean ± SD for 30 cells/condition.*

XIV) Biochemical influence of nanoparticle exposure to the cytoskeleton

XIV.1) Gene expression assay
XIV.2) Polymerization of cytoskeletal fibers

XIV.1) Gene expression assay

To have a look into the precise mechanisms causing the effects on cell cytoskeleton, the effect of the presence of Au NPs on gene expression related to the cytoskeleton was investigated. Reat Time Polymerase chain reaction (RT-PCR) arrays involving the cytoskeletal regulator pathway (Qiagen Benelux BV, Netherlands, #PAHS-088Z) were run in which the expression of 84 genes involved with actin and tubulin cytoskeleton were probed. HUVECs or HeLa cells were seeded at $1.5 \cdot 10^5$ cells/mL and allowed to settle overnight. Then, cells were either left untreated (controls) or incubated for 24 h with the Au NPs at various concentrations (c_{NP} = 6.3 100 nM). Next, cells were washed twice with PBS and harvested into centrifuge tubes. RNA was extracted using the Qiagen RNeasy Mini Kit (Qiagen, Benelux BV, Netherlands, #74104) according to the manufacturer's instructions. Every RNA sample underwent DNase digestion to eliminate genomic DNA c ntamination using the RNase-Free DNase Set (Qiagen, Benelux BV, Netherlands). RNA samples were converted into first strand cDNA using the RT2 First Strand Kit (Qiagen Benelux BV, Netherlands), where Genomic DNA Elimination Mixture was applied according to the manufacturer's instructions and samples were amplified by PCR. First strand cDNA was then used in the RT-PCR after samples were added to the RT2 qPCR Master Mix plus Sybr Green (Qiagen Benelux BV, Netherlands). RT-PCR was performed on the iCycler iQ5 Thermal Cycler (Bio-Rad Laboratories N.V., Belgium). PCR array data were analyzed using the ΔΔCt method *via* the SABiosciences web portal (www.SABiosciences.com/pcrarraydataanalysis.php). The data shown in Figure SI-XIV.1 reveal those genes

where high levels of upregulation > 4.5-fold increase compared to control) were noticed. Overall, there are clear NP concentration-dependent effects noticeable for several of the investigated genes. For the genes most affected (the ones shown i Figure SI-XIV.1), the effects are also clearly highest for the highest NP doses. Some genes such as MAPK13 and CCNA1 were strongly up-regulated in both cell types, indicating that these are quite essential for the general effect. The differences noted between the two cell types can then be explained by differences in intrinsic gene expression levels.

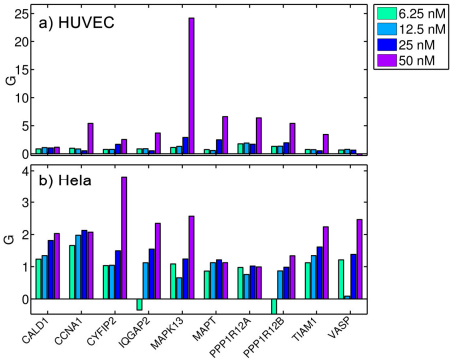

Figure SI-XIV.1: *Gene expression level G (normalized to c_{NP} = 0 nM) for cytoskeleton-related genes. The data shown reveal the fold-change expression level of genes in treated cells compared to the expression level of the corresponding genes in the untreated control cells. Only those genes are shown where a difference of 4.5-fold change in relative gene expression level was observed for any of the samples.*

XIV.2) Polymerization of cytoskeletal fibers

In order to unravel the effects of Au NPs on the formation of actin and tubulin fibers, actin and tubulin polymerization assays were performed. Both proteins polymerization processes follow a polymerization curve with three different phases: nucleation (phase I), growth (phase II), and steady state equilibrium (phase III) (*cf.* Figure SI-XIV.2). Under physiological conditions inside cells, globular-actin readily polymerizes to form filamentous-actin, which in return forms double-helical filaments. Effect of Au NPs on this polymerization was probed with a fluorescence-based commercial assay.

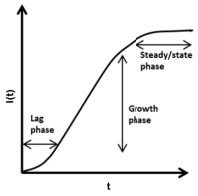

Figure SI-XIV.2: *Actin/tubulin polymerization as determined by time-dependent fluorescence intensity I(t) follows three phases, divided in a lag phase, and a growth- and steady state.*

To investigate the effect of Au NPs on actin fiber polymerization, the Actin Polymerization Biochem Kit (Cytoskeleton Inc., USA, #BK003) was used. The kit makes use of the enhanced fluorescence of pyrene-conjugated actin obtained d ring the polymerization process. This reaction is foll wed by an increase in fluorescence emission, λ_{em}, in the range of λ_{em} = 395 - 440 nm over a period of 60 minutes at room temperature (excitation in the range of λ_{ex} = 340 - 380 nm). Here, at physiological conditions double-helically structured ac n (filamentous-actin) is obtained by the polymerization of pyrene globular-actin (monomer), involving ATP hydrolysis. Actin requires ATP and divalent cat ns for stability.

The experiment was performed in a 96-well plate in which triplicates of all the samples were prepared. First, an adenosine triphosphate (ATP) solution in Tris-HCl pH 7.5, was diluted in 5 mM Tris-HCl, 0.2 mM $CaCl_2$ pH 8.0 buffer to obtain a final concentration of 0.2 mM A P (ATP-buffer). Next, lyophilized pyrene-labeled muscle actin was dissolved in this ATP-buffer at 0.4 mg/mL and left on ice to avoid the start of polymerization process. Eventually, 100 µL of actin-ATP-buffer was added into each well. As negative control, 100 µL ATP-buffer were used. The 96-well plate was shaken for 5 seconds and placed into a fluorometer (FluoroLog, Horiba). The emission was recorded over 3 min to obtain a baseline emission signal for the samp s. After this, 10 µL Au NPs in Milli-Q water were dded to obtain loading concentrations between c_{NP} = 0 - 100 nM, and the emission intensity was recorded with a temporal resolution of 60 s for about 20 min, to ensure that Au NPs themselves do not enhance actin polymerization without ATP present.

After 20 minutes, 10 µL 10 mM ATP, 500 mM KCl, 20 mM $MgCl_2$ in 0.05 M guanidine carbonate pH 7.5 (Actin Polymerization Buffer) were added into each well to start the polymerization reaction. Fluorescence readouts were performed every 60 s. The normalized emission results I(t) are shown in Figure SI-XIV.3.

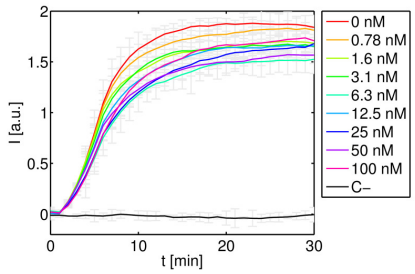

Figure SI-XIV.3: *Normalized emission I(t) of pyrene-conjugated actin (λ_{ex} = 355 nm, λ_{em} = 410), indicating the amount of polymerized fibers upon addition of Au NPs at c_{NP} = 0 - 100 nM.*

The data presented in Figure SI-XIV.3 show that the presence of high Au NP-concentration slightly affected the polymerization process of actin. This is probably due to the binding of actin monomers to the Au NPs, hampering actin polymerization. These results correlate with the changes in actin morphology of HUVECs and HeLa cells exposed to high concentrations of Au NPs (*cf.* Figure SI-XIII.1 and Figure SI-XIII.2). For quantitative evaluation the I(t) values were from Figure SI-XIV.3 were fitted with the following function: $I(t) = 1 - \exp(-k_{act} \cdot t)$, with the actin polymerization rate k_{act} as fit parameter. The NP-exposure dependent actin polymerization rate is shown in Figure SI-XIV.4.

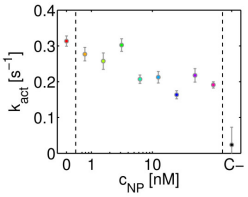

Figure SI-XIV.4: *Actin polymerization rate k_{act} during actin growth in the presence of Au NPs at indicated concentrations c_{NP}.*

It can be stated that Au NPs influence the actin polymerization growth phase, since different maximum slope values are shown in Figure SI-XIV.3. The higher the Au NP concentration in the media, the higher the obtained k_{act}. No influence was observed on the other process phases.

The effect of Au NPs on tubulin fiber polymerization was investigated using the Tubulin Polymerization Assay Kit (Cytoskeleton Inc., USA, #BK006P). Tubulin polymerizes forming microtubules. During the polymerization process, fluorescence is increased due to the incorporation of a fluorescent dye into microtubules. Au NPs may alter any of the three phases of polymerization described earlier. During polymerization, fluorescence is increased due to the incorporation of a fluorescent reporter dye into microtubules. Au NPs may alter any of the three phases of polymerization.

As positive control, the anti-mitotic drug paclitaxel was used at a final concentration of 0.03 mM in Milli-Q water, since this compound removes the nucleation process (phase I) and enhances the maximum slope of the growth phase (phase II). In addition to this, 5 mM $CaCl_2$ solution in working buffer was used as negative control, since the calcium inhibits tubulin polymerization. First, a 96 well plate was pre-warmed to 37 °C. 972 µL of buffer 1, composed of 80 mM piperazine-N,N'-bis[2-ethanesulfonic acid] sequisodium salt, 2 mM $MgCl_2$, 0.5 mM ethylene glycol-bis(b-amino-ethyl ether) N,N,N',N'-tetra-acetic acid, pH 6.9, and 10 µM fluorescence reporter were mixed with 448 µL of the tubulin glycerol buffer, composed of 80 mM piperazine-N,N'-bis[2-ethanesulfonic acid] sequisodium salt, 2 mM $MgCl_2$, 0.5 mM ethyleneglycol-bis(b-amino-ethyl ether) N,N,N',N'-tetra-acetic acid in 60 % v/v glycerol at pH 6.9. Quickly, 17.7 µL of 100 mM guanosine triphosphate (GTP), required for tubulin polymerization, dissolved in Milli-Q water, and 340 µL of 10 mg/mL tubulin stock solution in buffer 1 were added to the previous mixture. The obtained "Tubulin Reaction Mix" was placed on ice to avoid the start of the reaction at room temperature.

Once prepared, 5 µL of the Au NPs samples at a 10x concentration (0-1 µM) were added to their respective wells, leading to final NP concentrations c_{NP} = 0 - 100 nM. Paclitaxel and $CaCl_2$ solutions were also added in control wells. Then, the plate was placed at 37 °C for 1 min. After this, 50 µL of the Tubulin Reaction Mix were added to every well of the plate and fluorescence emission I(t) (λ_{ex} = 360 nm, λ_{em} = 420 nm) was recorded at a temporal resolution of 60 s for 2 h. Normalized results are shown in Figure SI-XIV.5.

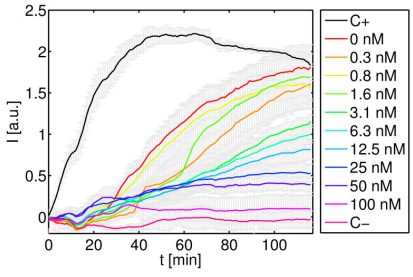

Figure SI-XIV.5: *Normalized emission I(t) of the tubulin polymerization process (λ_{ex} = 360 nm, λ_{em} = 420 nm). The reaction starting point values have been taken for normalization. C+ is the positive control (paclitaxel), and C- is the $CaCl_2$ solution acting as negative control.*

Obviously, Au NPs do not only clearly inhibit tubulin polymerization in the growth phase (phase II), but also influence the steady state phase (phase I). The increase in Au NP-concentration leads to a diminution

of the maximum slope of the mic otubules formation and thus, having a clear effect on the polymerization process. For quantification we defined the normalized amount of polymerized tubulin as $N_{tub} = I(c_{NP}, t = 110\ min)/I(c_{NP} = 0\ nM, t = 110\ min)$, as shown in Figure SI-XIV.6.

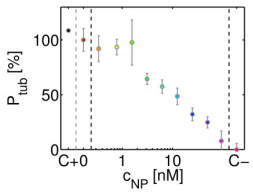

Figure SI-XIV.6: *Normalized amount of polymerized tubulin N_{tub} after 110 min of reaction in the presence of Au NPs. C+ is the positive control (paclitaxel) and C- is the $CaCl_2$ solution acting as negative control.*

The tubulin polymerization process was clearly inhibited as the concentration of Au NPs was increased, indicating Au NPs might destabilize microtubules. This correlates with the appearance of big holes among the tubulin network in HUVECs and HeLa cells at high concentration of Au NPs (*cf.* Figure SI-XIII.4 and Figure SI-XIII.5).

XV) In vivo cytotoxic effects using a zebrafish model

To assess the developmental hazard potential of the Au NPs *in vivo*, a toxicity study in zebrafish embryo was carried out. For t › experiments the sterile NPs in water were diluted in E3 medium (5 mM NaCl, 0.17 mM KCl, 0.33 mM $CaCl_2$, 0.33 mM $MgSO_4$) to form a 1:10 serial dilution series corresponding to c_{NP} = 700, 70, 7, 0.7, 0.07 and 0 nM. At 4 hours post fertilization, zebrafish embryo chorions were removed enzymatically, and the embryos were transferred to individual wells of a 96-well plate with 100 µL of the prepared test compound dilutions [28]. Exposure plates were sealed to prevent evaporation and wrapped with aluminum foil for photoprotection. The dilution series above was duplicated on each plate (colum 1-6 duplicated in columns 7-12) and 2 plates were run for the test compound. Thus, 32 embryos were exposed to each concentration. The static exposures were maintained at 28 °C until 24 hours post fertilization (hpf) when developmental progress, mortality, and photo-induced tail flexion were assessed. At 120 hpf, embryos were assessed for their photo-induced locomotor activity and their escape response to a gentle touch with a blunt probe to the head and tail region. Then they were euthanized by ricaine overdose and scored for mortality and morphological alformations. For malformation statistics, only embryos that survived until 120 hpf were included. 22 morphological endpoints were evaluated [29, 30]. Exposure to Au NPs was not associated with altered activity in the the 24 hpf photo-response test as it can be observed in Figure SI-XV.1.

a)

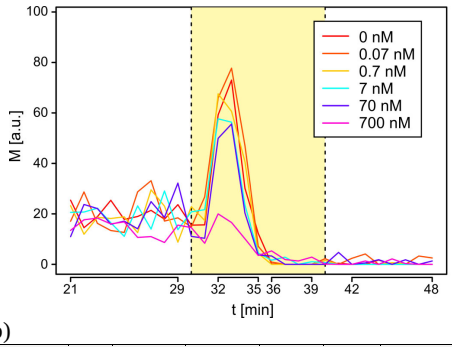

b)

c_{NP} [nM]	0	0. 07	0.7	7	70	700
Baseline phase	1	0.425	0.464	0.578	0.800	0.073
Excitatory phase 1	1	0.586	0.889	0.211	0.209	0.0000315
Excitatory phase 2	1	1	1	1	1	0.730
Refractory phase	1	1	1	1	1	1

Figure SI-XV.1: *Photo-induced tail flexion at 24 hpf associated with Au NPs exposure: a) The yellow area indicates the time of a single bright, visible light flash. The y-axis values are a unit less index of motion M (tail flexion) recorded as pixel changes between successive video frames. Embryos were placed 1 per well of a 96 well plate. b) P values indicate significant differences where $P < 0.01$(Kolmogorov-Smirnov test) in tail flexions per unit time from the vehicle (E3 medium) control group. No significant differences from the control group were observed. Dead or malformed embryos at 24 hpf were excluded from the analysis.*

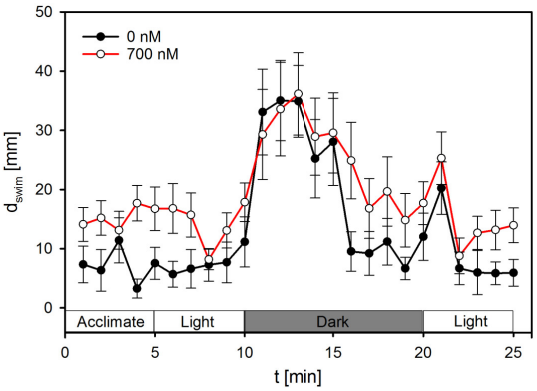

Figure SI-XV.2: *Total locomotor activity in terms of total swim distance d_{swim} under light/dark stimulation measured in 5 days post fertilization (dpf) zebrafish exposed from 6 hpf to 5 dpf to a Au NPs. Data were analyzed using a Mann-Whitney Rank Sum comparison of activity between*

treatment and control in each phase of the test (t =1-5 min = acclimation, minutes 6-10 = visible light, minutes 11 - 20 = dark (IR light), minutes 21-25 = visible light. The threshold for statistical significance was p < 0.05. Only the highest dose was reported because no other endpoints were significantly affected in the dose range used.

Other concentrations were not associated with behavioral abnormality at 120 h f. Exposure to Au NPs was not significantly associated with mortality or any morphological abnormality, *cf.* Figure SI-XV.3.

The results indicate that the Au NPs were not overtly toxic in the developmental zebrafish under the reported laboratory conditions and practices and, with the exception of the hyperactivity observed at 120 hpf, the hazard potential of this compound appears to be low.

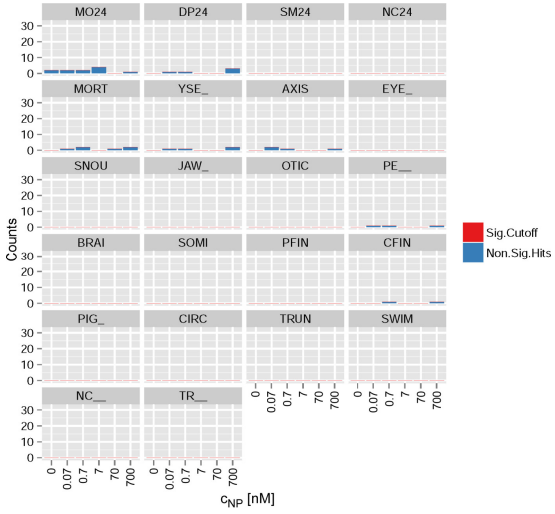

Figure SI-XV.3: *Endpoint incidence (binomial, presence/absence data) across all 24 replicates was plotted as stacked points, one point per observation. Any points at or above the threshold for statistical binomial significance would appear in red. The control incidence of all morphological and touch response endpoints was insignificant and within the 10 % tolerance limit. No significant responses were associated with exposure to Au NPs. Endpoint Key: Yolk sac edema (YSE), bent body axis (AXIS), eye defect EYE), snout malformed (SNOU), jaw malformed (JAW), ear malformed (OTIC), pericardial edema (PE), brain malformed (BRAI), muscle somite defect (SOMI), caudal fin defect (CFIN), pectoral fin(s) abnormal (PFIN), circulation slower/faster or less prevalent than normal (CIRC), pigmentation abnormal (PIG), body trunk length shorter than normal (TRUN), swim bladder not present or not inflated (SWIM), notochord curvy or otherwise abnormal (NC), and response to blunt probe gently touched to head or tail region without characteristic escape response (TR).*

XVI) References

[1] M. Brust, M. Walker, D. Bethell, D.J. Schiffrin, R. Whyman, J. Chem. Soc., Chem. Commun., 1 (1994) 801-802.

[2] F. Amin, D.A. Yushchenko, J.M. Montenegro, W.J. Parak, ChemPhysChem, 13 (2012) 1030-1035.

[3] D. Hühn, K. Kantner, C. Geidel, S. Brandholt, I. De Cock, S.J.H. Soenen, P. Rivera Gil, J.-M. Montenegro, K. Braeckmans, K. Müllen, G.U. Nienhaus, M. Klapper, W. Parak, ACS Nano, 7 (2013) 3253-3263.

[4] C.J.J. den Ouden, R.W. Thompson, J. Colloid Interface Sci., 143 (1991) 77-84.

[5] J. Fink, C.J. Kiely, D. Bethell, D.J. Schiffrin, Chem. Mater., 10 (1998) 922-926.

[6] M.T. Fernández-Argüelles, A. Yakovlev, R.A. Sperling, C. Luccardini, S. Gaillard, A.S. Medel, J.-M. Mallet, J.-C. Brochon, A. Feltz, M. Oheim, W.J. Parak, Nano Lett., 7 (2007) 2 3-2617.

[7] C.-A.J. Lin, R.A. Sperling, J.K. Li, T.-Y. Yang, P.-Y. Li, M. Zanella, W.H. Chang, W.J. Parak, Small, 4 (2008) 334-341.

[8] T. Pellegrino, L. Manna, S. Kudera, T. Liedl, D. Koktysh, A.L. Rogach, S. Keller, J. Rädler, G. Natile, W.J. Parak, Nano Lett., 4 (2004) 703-707.

[9] F. Zhang, E. Lees, F. Amin, P. Rivera_Gil, F. Yang, P. Mulvaney, W.J. Parak, Small, 7 (2011) 3113-3127.

[10] U.I. Tromsdorf, N.C. Bigall, M. Kaul, O.T. Bruns, M.S. Nikolic, B. Mollwitz, R.A. Sperling, R. Reimer, H. Hohenberg, W.J. Parak, S. Förster, U. Beisiegel, G. Adam, H. Weller, Nano Lett., 7 (2007) 2422-2427.

[11] Z. Ali, A.Z. Abbasi, F. Zhang, P. Arosio, A. Lascialfari, M.F. Casula, A. Wenk, W. Kreyling, R. Plapper, M. Seidel, R. Niessner, J. Knoll, A. Seubert, W.J. Parak, Anal. Chem., 83 (2011) 2877-2882.

[12] U. Kaiser, D.J.d. Aberasturi, R. Malinowski, F. Amin, W.J. Parak, W. Heimbrodt, Appl. Phys. Lett., 104 (2014) 41901-41904.

[13] E. Caballero-Díaz, C. Pfeiffer, L. Kastl, P. Rivera-Gil, B. Simonet, M. Valcárcel, J. Jiménez-Lamana, F. Laborda, W.J. Parak, Part. Part. Syst. Charact., 30 (2013) 1079-108

[14] T. Pellegrino, R.A. Sperling, A.P. Alivisatos, W.J. Parak, J. Biomed. Biotechnol., Article ID 26796 (2007) 1-9.

[15] R.A. Sperling, T. Liedl, S. Duhr, S. Kudera, M. Zanella, C.-A.J. Lin, W.H. hang, D. Braun, W.J. Parak, J. Phys. Chem. C, 111 (2007) 11552-11559.

[16] P. Rivera Gil, D. Jimene de Aberasturi, V. Wulf, B. Pelaz, P. del Pino, Y. Zhao, J. de la Fuente, I. Ruiz de Larramendi, T. Rojo, X.-J iang, W.J. Parak, Acc. Chem. Res., 46 (2013) 743-749.

[17] A. Carpenter, T. Jones, M. Lamprecht, C. Clarke, I. Kang, O. Friman, D. Guertin, J. Chang, R. Lindquist, J. Moffat, P. Golland, D. Sabatini, Genome Biology, 7 (2006) R100.

[18] Y. Liu, T. Jiang, C. Zhang, T.R. Jones, A. Carpenter, P. Golland, Voronoi-Based Segmentation of Cells on Image Manifolds, Computer Vision for Biomedical Image Applications, Springer Berlin Heidelberg2005, pp. 535-543.
[19] M. Sezgin, B.l. Sankur, J. Electron. Imaging, 13 (2004) 146-168.
[20] M.V. Boland, M.K. Markey, R.F. Murphy, Cytometry, 33 (1998) 366-375.
[21] R.M. Haralick, Proc. IEEE, 67 (1979) 786-804.
[22] M. Mahmoudi, A.M. Abdelmonem, S. Behzadi, J.H. Clement, S. Dutz, M.R. Ejtehadi, R. Hartmann, K. Kantner, U. Linne, P. Maffre, S. Metzler, M.K. Moghadam, C. Pfeiffer, M. Rezaei, P. Ruiz-Lozano, V. Serpooshan, M.A. Shokrgozar, G.U. Nienhaus, W.J. Parak, ACS Nano, 7 (2013) 6555-6562.
[23] J. O'Brien, I. Wilson, T. Orton, F.o. Pognan, Eur. J. Biochem., 267 (2000) 5421-5426.
[24] T. Mosmann, J. Immunol. Methods, 65 (1983) 55-63.
[25] A. Salic, T.J. Mitchison, Proc. Natl. Acad. Sci. U. S. A., 105 (2008) 2415-2420.
[26] G. Thoelking, B. Reiss, J. Wegener, H. Oberleithner, H. Pavenstaedt, C. Riethmuller, Nanotechnology, 21 (2010).
[27] B. Rothen-Rutishauser, D.A. Kuhn, Z. Ali, M. Gasser, F. Amin, W.J. Parak, D. Vanhecke, A. Fink, P. Gehr, C. Brandenberger, Nanomedicine, 9 (2014) 607-621.
[28] D. Mandrell, L. Truong, C. Jephson, M.R. Sarker, A. Moore, C. Lang, M.T. Simonich, R.L. Tanguay, J. Lab. Autom., 17 (2012) 66-74.
[29] L. Truong, S.L. Harper, R.L. Tanguay, Evaluation of embryotoxicity using the zebrafish model, Drug Safety Evaluation, Springer2011, pp. 271-279.
[30] L. Truong, D.M. Reif, L. St Mary, M.C. Geier, H.D. Truong, R.L. Tanguay, Toxicol. Sci., 137 (2014) 212-233.

nature nanotechnology

LETTERS

PUBLISHED ONLINE: XX XX 2015 | DOI: 10.1038/NNANO.2015.111

In vivo integrity of polymer-coated gold nanoparticles

Wolfgang G. Kreyling[1]*, Abuelmagd M. Abdelmonem[2], Zulqurnain Ali[2†], Alexander Wenk[1], Frauke Alves[3,4], Marianne Geiser[5], Stephanie Hirn[1†], Raimo Hartmann[2], Karsten Kantner[2], Nadine Haberl[1†], Dorleta Jimenez de Aberasturi[2,6,7], Gülnaz Khadem-Saba[1†], Jose-Maria Montenegro[2†], Joana Rejman[2], Teofilo Rojo[6], Idoia Ruiz de Larramendi[6], Roser Ufartes[3] and Wolfgang J. Parak[2,7]*

Inorganic nanoparticles are frequently engineered with an organic surface coating to improve their physicochemical properties, and it is well-known that their colloidal properties[1] may change upon internalization by cells[2,3]. While the stability of such nanoparticles is typically assayed in simple *in vitro* tests, their stability in a mammalian organism remains unknown. Here, we show that firmly grafted polymer shells around gold nanoparticles may degrade when injected into rats. We synthesized monodisperse radioactively labelled gold nanoparticles (^{198}Au)[4] and engineered an ^{111}In-labelled polymer shell around them[5]. Upon intravenous injection into rats, quantitative biodistribution analyses performed independently for ^{198}Au and ^{111}In showed partial removal of the polymer shell *in vivo*. While ^{198}Au accumulates mostly in the liver, part of the ^{111}In shows a non-particulate biodistribution similar to intravenous injection of chelated ^{111}In. Further *in vitro* studies suggest that degradation of the polymer shell is caused by proteolytic enzymes in the liver. Our results show that even nanoparticles with high colloidal stability can change their physicochemical properties *in vivo*.

Following internalization by cells, nanoparticles are typically localized inside highly acidic endosomes and/or lysosomes. They are often stabilized by negatively charged groups (such as COO^-) with pK_a values higher than the low pH values in the endosomes and lysosomes[6]. Internalization therefore leads to a loss of charge and, as a consequence, agglomeration[7]. A reduced pH can enhance the corrosion of nanoparticles[8], resulting in the release of toxic ions, as has been observed with CdSe[9,10] and Ag nanoparticles[11,12]. As well as changing the core properties of nano particles, uptake by cells can also lead to the removal of their surface capping both *in vitro*, as shown for polymer coated[3,13] and dextrane coated nanoparticles[14], and *in vivo*[15,16]. Intracellular enzymes may degrade the corona of adsorbed proteins[2], or may modify the surface chemistry of the nanoparticles[17,18]. To trace the fate of the different components of a nanoparticle that is, the inor ganic core, the organic surface capping and the protein corona each of these components needs to be labelled individually. To achieve this, we labelled the core and shell of monodisperse Au nanoparticles with radioisotopes[5] (Fig. 1) and followed their respective biodistributions *in vivo*. Equal biokinetics of both radiolabels would indicate *in vivo* stability of the nanoparticles, whereas different biodistributions would indicate partial degradation.

Au nanoparticles with ^{198}Au label in their core and ^{111}In in their shell were intravenously injected into rats, which were euthanized after 1 h or 24 h. Then complete organs of the rats were sampled, and the ^{198}Au and ^{111}In radioactivities originating from the different organs were measured[4,19]. The blood contents of the organs and the remaining body were calculated according to the methods of Oeff and co authors[20]. Figure 2a d and Supplementary Fig. 25 show the quantitatively balanced biodistributions (the sum of all ^{198}Au radioactivities and all ^{111}In radioactivities in all organs and tissues, the remaining carcass, and the total faecal and urinary excretion is 100%). For a detailed analysis of these data, the stability of the radioactive labels must be known. The ^{198}Au within a stable ^{197}Au matrix resulting from neutron activation of the original gold nanoparticles has been shown to dissolve negligibly out of the gold nanoparticle cores, in particular after the washing procedure during nanoparticle preparation[21]. Indeed, the gold nanoparticles are vir tually insoluble[21], so their biokinetics is indicated by the ^{198}Au label.

By calculating the ^{111}In to ^{198}Au ratio for each organ and tissue and each time point, major differences between the retentions of the two radioisotopes become evident (Fig. 2e,f). This differential be haviour indicates dissociation and removal of the ^{111}In label from the shell of the initial nanoparticle. To investigate the stability of the ^{111}In label with respect to its co localization with the polymer shell, we performed an auxiliary biokinetics studies in C57BL/6 mice. Soluble forms of the ^{111}In radioisotope (as free ions) and of a complex of ^{111}In with the chelator diethylene triamine pentaacetic acid (DTPA) were intravenously injected in order to distinguish the biodistribution of the soluble form (^{111}In ions) from the chelated form (^{111}In DTPA) and versus the particulate form (polymer coated Au nanoparticles with ^{111}In in the polymer shell, Fig. 2c, d). By using the same quantitative approach as used for the data in Fig. 2, data from Fig. 3 allow for distinguishing whether ^{111}In has been released from the Au cores in the form of free ions (that is, the shell label is lost) or in the chelated form (that is, as fragments from the polymer shell). In the case of the ionic form, ^{111}In is rapidly accumulated (time point 3 h) and retained (time point 24 h) in the liver (dark grey bars in Fig. 3, Supplementary Fig. 29).

[1]Institute of Lung Biology and Disease and Institute of Epidemiology 2, Helmholtz Zentrum München – German Research for Center for Environmental Health, Neuherberg/Munich 85764, Germany. [2]Fachbereich Physik, Philipps Universität Marburg, Marburg, Germany. [3]Department of Molecular Biology of Neuronal Signals, Max-Planck-Institut für Experimentelle Medizin, Göttingen 37075, Germany. [4]Department of Hematology and Oncology, University Medical Center Göttingen, Göttingen 37075, Germany. [5]Institute of Anatomy, University of Bern, Bern 3012, Switzerland. [6]Department of Inorganic Chemistry, UPV/EHU, Bilbao, Spain. [7]CIC Biomagune, San Sebastian, Spain; [†]Present addresses: Department of Physics, Air University, Sector E-9, Islamabad 44000, Pakistan (Z.A.); Walter Brendel Centre of Experimental Medicine, Ludwig-Maximilians-University, Munich 81377, Germany (S.H., N.H.); Department of Chemistry, Industrial Biocatalysis, Technische Universität München (TUM), Garching 85748, Germany (G.K-S.); Central Research Services, University of Malaga, Málaga 29071, Spain (J-M.M.). *e-mail: kreyling@helmholtz-muenchen.de; wolfgang.parak@physik.uni-marburg.de

LETTERS NATURE NANOTECHNOLOGY DOI: 10.1038/NNANO.2015.111

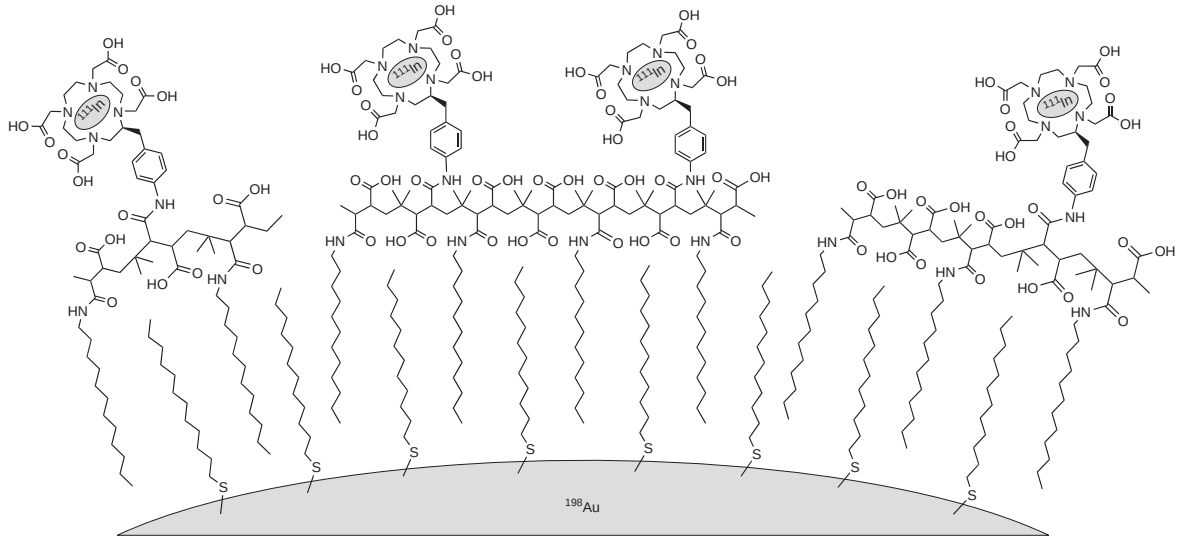

Figure 1 | Sketch of double-radiolabelled nanoparticles. Au cores were synthesized in the organic phase by reduction of Au^{3+}, and the resulting nanoparticles were stabilized by a ligand shell of dodecanethiol. Following neutron activation, some of the Au atoms were converted into the radioactive isotope ^{198}Au, to form the radiolabelled core. A shell of the amphiphilic polymer poly(isobutylene-alt-maleic anhydride)-graft-dodecyl was then wrapped around the Au core and rendered the nanoparticle water-soluble. DOTA was integrated into the polymer shell and was loaded with In (enriched with the radioactive isotope ^{111}In, which acted as the shell label). In this way, the nanoparticles core and shell were individually labelled by ^{198}Au and ^{111}In, respectively.

However, in the case of the chelated form, ^{111}In is efficiently excreted by urine (light grey bars in Fig. 3).

Most of the ^{111}In administered in particulate form is retained in the liver (Fig. 2c,d). Our data do not indicate whether the In in the liver is still attached to the polymer shell and thus the Au core, or is present in the form of free ions, as in both cases dominant retention occurs in the liver (Fig. 2a,b and dark grey bars in Fig. 3). On the other hand, the In excreted via urine is present in the chelated form, as this is the only efficient pathway for renal excretion (light grey bars in Fig. 3). Thus, in a likely scenario, parts of the polymer shell (with the chelated In) come off the Au cores in the liver, and these fragments are excreted by urine.

To probe where the polymer shell begins to separate from its Au core in the liver, where most nanoparticles are found, histology was performed (Fig. 2a d). Au cores with chelated In in their shell (without using radioisotopes) were intravenously administered to rats with the same protocols used for the biodistribution studies in Fig. 2. However, no Au nanoparticles were detected in tissue slices of the liver when imaged with transmission electron microscopy (TEM; Supplementary Figs 30 and 31). To double check these findings, fluorescence was also used for nanoparticle detection. For this purpose we used CdSe/ZnS quantum dots (QDs, emission at 605 nm) with the organic fluorophore DY636 (Dyomics, emission at 657 nm) in the polymer shell, which have colloidal properties similar to those of Au nanoparticles. The QDs were administered to rats with the same protocol, and tissue slices from the liver were imaged with optical microscopy. Again, no nanoparticle signal (either from the QD core or from the fluorophore labelled shell) could be detected above the autofluorescence background level (Supplementary Fig. 33). However, although the low nanoparticle doses of 10^{13} 10^{14} nanoparticles per animal did not allow the observation of individual nanoparticles in the liver slices used for TEM and fluorescence microscopy imaging, inductively coupled plasma mass spectrometry (ICP MS) analyses performed on the entire liver had enough sensitivity to detect the nanoparticles and clearly demonstrated their present in the liver (Supplementary Figs 32 and 35), confirming the data with radiolabelled nanoparticles.

Knowing, from the detection of radiolabels (Fig. 2a d) and ICP MS, that the nanoparticles are in fact dominantly retained in the liver, though at concentrations too low to allow for successful histology, we attempted to emulate the *in vivo* behaviour of the liver with *in vitro* investigation on cell lines representing different cell types in the liver. We selected Kupffer cells, which are specialized stellate macrophages in the liver, and human umbilical vein endothelial cells (HUVECs). First, the cellular uptake of polymer coated Au nanoparticles and QDs was quantified (by ICP MS) in terms of intracellular Au and Cd/Se, respectively. The nanoparticles are incorporated by both cell types (Supplementary Fig. 36), and the intracellular uptake of Au nanoparticles and QDs is similar (Fig. 4a,b and Supplementary Fig. 37). We attribute this to the similar surface chemistry of the Au nanoparticles and QDs, although time and concentration dependencies differ. Second, the intracellular location of the internalized Au nanoparticles and QDs (with a fluorescence label in their polymer shell) was determined by confocal microscopy via co localization with the lysosomal membrane marker LAMP 1 (Supplementary Fig. 38). The data demonstrate a time and concentration dependent rise in the localization of both types of nanoparticle in the lysosomes of both HUVECs (Fig. 4c,d and Supplementary Fig. 39) and Kupffer cells (Supplementary Fig. 40). Thus, our data indicate that nanoparticles retained in the liver are localized in the lysosomes of macrophages and of epithelial cells. Because of their similar surface chemistry, polymer coated QDs show a behaviour similar to that of polymer coated Au nanoparticles.

Figure 4e shows that incubating polymer coated QDs with a DY495 fluorescence label in their polymer shell with different proteolytic enzymes (trypsin, pronase, proteinase 3 and cathepsin G) leads to degradation of the polymer shell, as visualized by the removal of the integrated fluorescent label from the QDs. Thus, the presence of proteolytic enzymes leads to degradation of the polymer shell 'in test tube'. We hypothesized that the proteolytic lysosomal enzymes present in endosomes and lysosomes may be responsible for the *in vitro* degradation of the polymer shell. HUVECs and Kupffer cells were incubated with polymer coated QDs. Co localization analysis of the fluorescence originating from the QD core and the

NATURE NANOTECHNOLOGY DOI: 10.1038/NNANO.2015.111 LETTERS

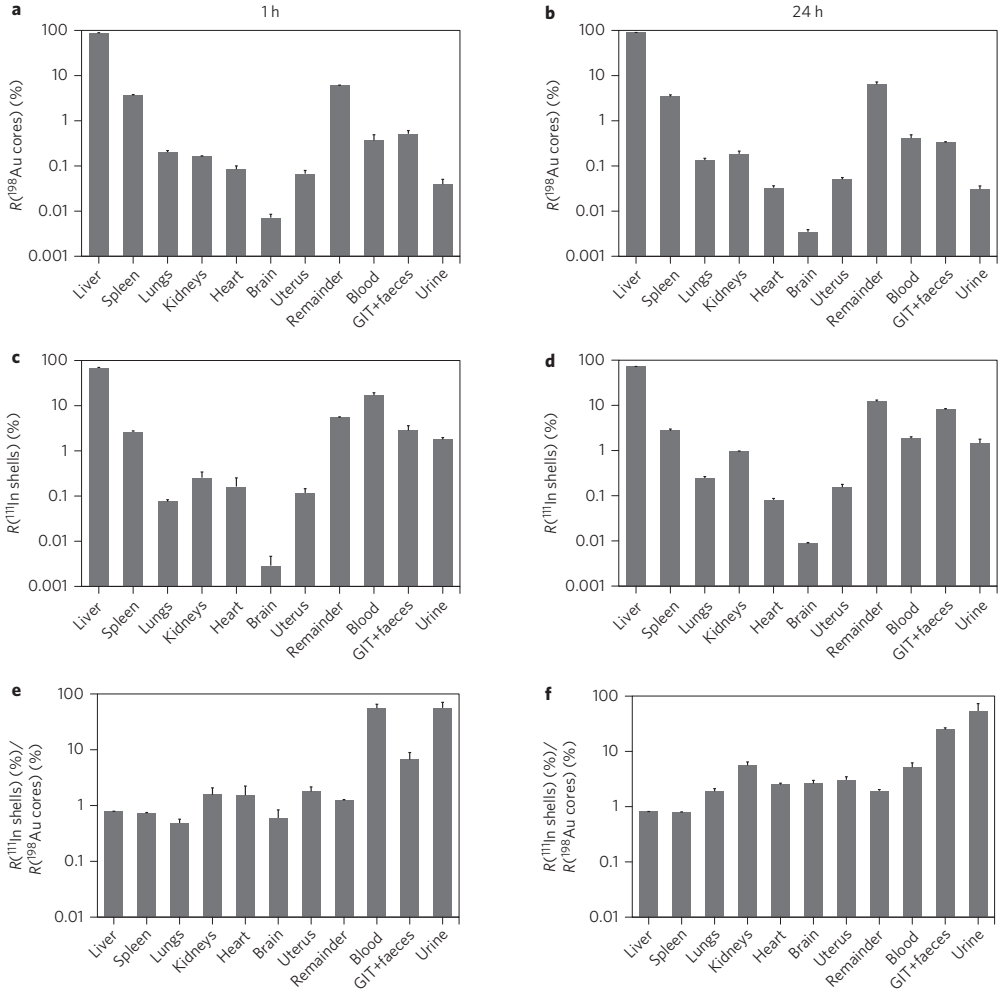

Figure 2 | Biodistribution of double-labelled nanoparticles. Au nanoparticles (core diameter $d_c = 4.8 \pm 0.9$ nm) with a ^{198}Au core radiolabel and a ^{111}In shell radiolabel were intravenously injected into the tail vein of Wistar–Kyoto rats and their radioactivities were determined in different organs. The graphs show the quantitative balance (that is, where the sum of all ^{198}Au or ^{111}In radioactivities over all organs and tissues, the remaining carcass and total faecal and urinary excretion is 100%) of the 1 h and 24 h biodistributions of double-labelled Au nanoparticles. The retentions *R*, given as mean data (±standard error of the mean, s.e.m.), are denoted as percent of the total radioactivity for the respective radio-isotope ($n = 4$ animals per data point). 'Remainder' represents radiolabels found in the rest of the carcass after sampling of organs (for example, soft tissues, skin and skeleton). 'GIT + faeces' represents the radiolabels found in the gastrointestinal tract and in faeces (note that after 1 h no radiolabels were found in faeces). 'Blood' represents the total content of radiolabels, as calculated from the measured content in the blood sample and the estimate of the total blood volume (see Methods). **a**,**b**, Biodistribution of the ^{198}Au nanoparticle core radiolabel at 1 h (**a**) and 24 h (**b**). **c**,**d**, Biodistribution of the ^{111}In shell radiolabel at 1 h (**c**) and 24 h (**d**). **e**,**f**, Ratio of ^{111}In shell to ^{198}Au nanoparticle radiolabel in each organ and tissue at 1 h (**e**) and 24 h (**f**). The data show that more ^{111}In shell labels than ^{198}Au core labels were detected in blood, urine, and GIT and faeces at any time point. Data are also plotted on a linear scale in Supplementary Fig. 25 and listed in Supplementary Tables 1 and 2.

fluorescence originating from the fluorescence of the DY495 label of the polymer shell indicate that after several hours the polymer shell label is partly displaced from the QD label, in agreement with the findings of others[3]. In the medium, the fluorescence of exocytosed QDs has a lower fraction of QD fluorescence compared to DY495 fluorescence, as is found for QDs inside cells that have been analysed after cell lysis. Our data also directly show that intracellular enzymatic degradation of internalized QDs can cause partial removal of either the DY495 labelled polymer shell or the DY495 label, which are subsequently exocytosed (as seen in Fig. 4f).

The 24 h biodistribution of the polymer coated ^{198}Au nanoparticles from the present study (Fig. 2b) is similar to that of 5 nm Au nanoparticles coated with triphenylphosphine sulphonate (TPPS) in previous studies[22,23] (Fig. 5). The protein corona plays a significant role in the determination of the biokinetics of the intravenously injected Au nanoparticles, so the similar patterns suggest that the protein coronas are very similar. For the virtually 'naked' TPPS coated Au nanoparticles it was shown that the coating is rather quickly removed in a cellular *in vitro* assay[24]. This is in agreement with our findings, in which the polymer coated Au nanoparticles lose parts of their polymer coating *in vitro* as *in vivo*. Thus, in both cases, the protein corona is formed on a partly 'naked' surface of the Au nanoparticles (that is, a surface partially stripped off the original organic coating). This is likely to be

LETTERS NATURE NANOTECHNOLOGY DOI: 10.1038/NNANO.2015.111

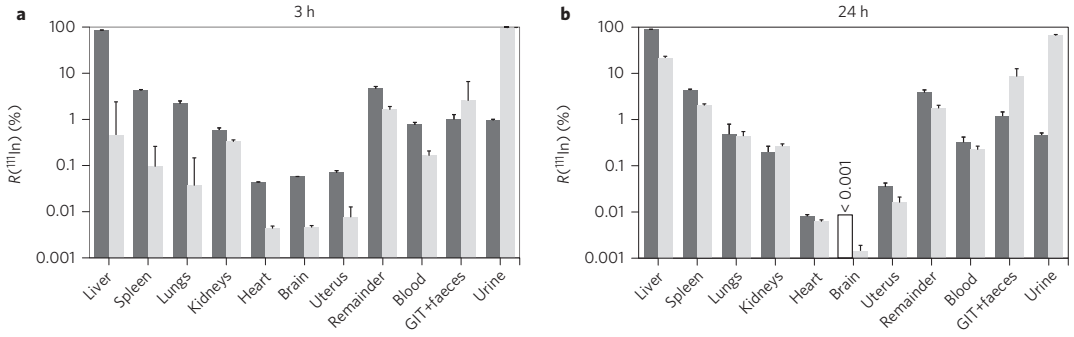

Figure 3 | Quantitative biodistribution of soluble free ^{111}In ions and ^{111}In–DPTA complexes. a,**b**, C57BL/6 mice were intravenously injected with free ^{111}In ions and chelated ^{111}In in the form of ^{111}In–DPTA complexes. Biodistribution was monitored at 3 h (**a**) and 24 h (**b**) by measuring the radioactivities of the different organs. The graph shows the percent retention *R* of ^{111}In for free (dark grey bars) and chelated (light grey bars) ^{111}In in whole organs and tissues, the remaining carcass without sampled organs, the GIT and total faeces 'GIT + faeces' and urinary excretion. Retentions *R* are given as mean data (±s.e.m.) and are denoted as percent of the total radioactivity for the respective radioisotope ($n = 4$ animals per data point). The data demonstrate that the biodistributions of ^{111}In ions and of ^{111}In–DPTA chelate complexes are different, in particular in the liver and urine.

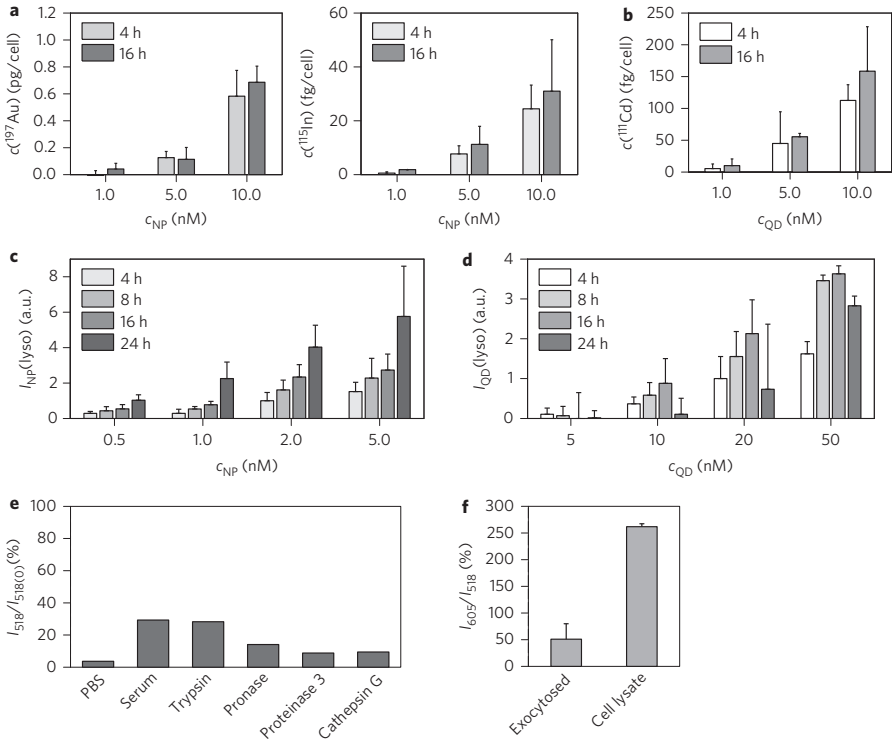

Figure 4 | Cellular internalization and degradation of polymer-coated Au nanoparticles and QDs by proteases 'in test tube' and *in vitro*. a,**b**, ICP-MS analysis of the uptake of Au nanoparticles with In in their polymer shell (**a**) and polymer-coated CdSe/ZnS QDs by HUVECs (**b**). The contents of Au, In (**a**) and Cd (**b**) are shown per cell after the indicated incubation times with different nanoparticle concentrations ($c_{NP} = 1$, 5 and 10 nM). **c**,**d**, Lysosomal enrichment of fluorescence-labelled Au nanoparticles (**c**) and CdSe/Zn QDs in HUVECs (**d**). The fluorescence intensity *I*(lyso) originating from the nanoparticles is given for different nanoparticle concentrations c_{NP}. **e**, Ratio $I_{518}/I_{518(0)}$ of the fluorescence intensity of DY495 label released from the shell around the QDs after 24 h 'in test tube' incubation with phosphate buffered saline (PBS, pH 7.4), in the presence of 10% fetal bovine serum (serum), trypsin (0.05%), pronase (0.2 units/ml), proteinase 3 (0.003 units/ml) and cathepsin G (13 units/ml). The ratio $I_{518}/I_{518(0)}$ was quantified by measuring the fluorescence I_{518} of DY495 (@518 nm) of the released DY495 label after separation from the QD core by ultrafiltration, as compared to the original fluorescence $I_{518(0)}$ of the DY495 label attached to the QDs. **f**, Ratio of QD and DY495 fluorescence intensities (I_{605}/I_{518}) for exocytosed QDs and QDs found inside Kupffer cells (cell lysate). Kupffer cells were incubated with the QDs for 22 h, followed by an additional 3 h incubation after removing the free QDs from the medium. All data are given as mean values ± standard deviation (s.d.). The data demonstrate partial removal of the polymer shell from the nanoparticle cores *in vitro*.

NATURE NANOTECHNOLOGY DOI: 10.1038/NNANO.2015.111 LETTERS

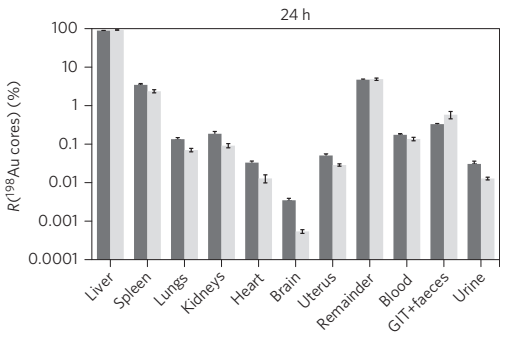

Figure 5 | Quantitative 24 h biodistribution of intravenously injected coated Au nanoparticles. Data obtained for monodisperse Au nanoparticles (d_c = 5 nm) coated with triphenylphosphine (TPPS) (dark grey bars; data taken from our previous study[22]) and of Au nanoparticles (d_c = 4.8 ± 0.9 nm) coated with a DOTA-modified polymer shell (light grey bars; data taken from Fig. 2b) in Wistar–Kyoto rats. For each time point, the retention *R* of the ^{198}Au cores is given in percent (mean ± s.e.m.; n = 4 animals) of the total radioactivity of each entire animal. The data demonstrate that the biodistributions of the Au nanoparticles with the two different surface coatings (TPPS versus polymer coating) are similar.

the reason behind the similar biodistributions of TTPS and polymer coated nanoparticles.

Conclusions

Using radio labelled Au cores and polymer shells, we have shown that the polymer shells of polymer coated Au nanoparticles are partially removed *in vitro* and *in vivo*. *In vivo*, the nanoparticles are mostly retained in the liver, and fragments of the organic shell are excreted through the kidneys. *In vitro* experiments show that nanoparticles internalized by HUVEC and Kupffer cells were localized in endosomal and lysosomal compartments. A partial separation of the organic shell from the inorganic core is caused by proteolytic enzymes present in these compartments. We believe *in vivo* degradation of the polymer shell is due to similar proteolytic digestion. Our findings indicate that the physicochemical properties and the integrity of nanoparticles can change dramatically following internalization by cells *in vitro* and *in vivo*. This may have potential consequences for drug targeting with nanoparticles.

Methods

Methods and any associated references are available in the online version of the paper.

Received 26 January 2013; accepted 21 April 2015; published online XX XX 2015

References

1. Rivera Gil, P. *et al.* The challenge to relate the physicochemical properties of colloidal nanoparticles to their cytotoxicity. *Acc. Chem. Res.* **46,** 743 749 (2013).
2. Chanana, M., Rivera Gil, P., Correa-Duarte, M. A., Parak, W. J. & Liz-Marzán, L. M. Physicochemical properties of protein-coated gold nanoparticles in biological fluids and cells before and after proteolytic digestion. *Angew. Chem. Int. Ed.* **52,** 4179 4183 (2013).
3. Chen, H. W., Zou, P., Connarn, J., Paholak, H. & Sun, D. X. Intracellular dissociation of a polymer coating from nanoparticles. *Nano Res.* **5,** 815 825 (2012).
4. Semmler-Behnke, M. *et al.* Biodistribution of 1.4- and 18-nm gold particles in rats. *Small* **4,** 2108 2111 (2008).
5. Ali, Z. *et al.* Multifunctional nanoparticles for dual imaging. *Anal. Chem.* **83,** 2877 2882 (2011).
6. Kreyling, W. G. *et al.* Interspecies comparison of phagolysosomal pH in alveolar acrophages. *Inhal. Toxicol.* **3,** 91 100 (1991).
7. Soenen, S. J. H. *et al.* Intracellular nanoparticle coating stability determines nanoparticle diagnostics efficacy and cell functionality. *Small* **6,** 2136 2145 (2010).
8. Levy, M. *et al.* Long term *in vivo* biotransformation of iron oxide nanoparticles. *Biomaterials* **32,** 3988 3999 (2011).
9. Derfus, A. M., Chan, W. C. W. & Bhatia, S. N. Probing the cytotoxicity of semiconductor quantum dots. *Nano Lett.* **4,** 11 18 (2004).
10. Kirchner, C. *et al.* Cytotoxicity of colloidal CdSe and CdSe/ZnS nanoparticles. *Nano Lett.* **5,** 331 338 (2005).
11. Kittler, S., Greulich, C., Diendorf, J., Koller, M. & Epple, M. Toxicity of silver nanoparticles increases during storage because of slow dissolution under release of silver ions. *Chem. Mater.* **22,** 4548 4554 (2010).
12. Caballero-Díaz, E. *et al.* The toxicity of silver nanoparticles depends on their uptake by cells and thus on their surface chemistry. *Part. Part. Syst. Charact.* **30,** 1079 1085 (2013).
13. Bose, K., Koch, M., Cavelius, C., Kiemer, A. K. & Kraegeloh, A. A correlative analysis of gold nanoparticles internalized by A549 cells. *Part. Part. Syst. Charact.* **31,** 439 448 (2014).
14. Lunov, O. *et al.* Lysosomal degradation of the carboxydextran shell of coated superparamagnetic iron oxide nanoparticles and the fate of professional phagocytes. *Biomaterials* **31,** 9015 9022 (2010).
15. Tietze, R. *et al.* Efficient drug-delivery using magnetic nanoparticles biodistribution and therapeutic effects in tumour bearing rabbits. *Nanomed. Nanotechnol.* **9,** 961 971 (2013).
16. Ducongé, F. *et al.* Fluorine-18-labeled phospholipid quantum dot micelles for *in vivo* multimodal imaging from whole body to cellular scales. *Bioconj. Chem.* **19,** 1921 1926 (2008).
17. Sée, V. *et al.* Cathepsin l digestion of nanobioconjugates upon endocytosis. *ACS Nano* **3,** 2461 2468 (2009).
18. Wang, F. *et al.* The biomolecular corona is retained during nanoparticle uptake and protects the cells from the damage induced by cationic nanoparticles until degraded in the lysosomes. *Nanomed. Nanotechnol.* **9,** 1159 1168 (2013).
19. Schleh, C. *et al.* Size and surface charge of gold nanoparticles determine absorption across intestinal barriers and accumulation in secondary target organs after oral administration. *Nanotoxicology* **6,** 36 46 (2012).
20. Oeff, K., Krentz, K. & Kessel, M. J-131-Clearance der normalen und pathologischen Magenschleimhaut. *Klin. Wochenschr.* **33,** 59 63 (1955).
21. Kreyling, W. G. *et al.* Air blood barrier translocation of tracheally instilled gold nanoparticles inversely depends on particle size. *ACS Nano* **8,** 222 233 (2014).
22. Lipka, M. *et al.* Biodistribution of PEG-modified gold nanoparticles following intratracheal instillation and intravenous injection. *Biomaterials* **31,** 6574 6581 (2010).
23. Hirn, S. *et al.* Particle size-dependent and surface charge-dependent biodistribution of gold nanoparticles after intravenous administration. *Eur. J. Pharm. Biopharm.* **77,** 407 416 (2011).
24. Pan, Y. *et al.* Gold nanoparticles of diameter 1.4 nm trigger necrosis by oxidative stress and mitochondrial damage. *Small* **5,** 2067 2076 (2009).

Acknowledgements

This work was supported by the Deutsche Forschungsgemeinschaft (DFG grant 'PA794/11-1' to W.J.P., grant 'SPP1313' to W.G.K.) and the European Commission Seventh Framework Programme (EC-FP7 grant 'ENPRA NMP4-SL-2009-228789' and 'Neuronano NMP4-SL-2008-214547' to W.G.K.). The authors would like to thank N. Senger, S. Kaidel, B. Kupferschmid and B. Krieger for technical assistance and to D. Hühn, R. Gill, M. Klapper and K. Dawson for scientific discussions.

Author contributions

W.G.K. and W.J.P. conceived the idea, designed and analysed the experiments, and mainly wrote the manuscript. All authors discussed the results, contributed to data analysis, and commented on the manuscript. A.M.A., Z.A., J.M.M., T.R. and I.R.d.L. prepared and characterized the nanoparticles. R.H., K.K., D.J.d.A. and J.R. preformed the *in vitro* experiments. A.W., N.H., S.H. and G.K.S. carried out *in vivo* experiments with radionucleotides. F.A. and R.U. carried out *in vivo* experiments with fluorescent nanoparticles. M.G. performed transmission electron microscopy measurements.

Additional information

Supplementary information is available in the online version of the paper. Reprints and permissions information is available online at www.nature.com/reprints. Correspondence and requests for materials should be addressed to W.G.K. and W.J.P.

Competing financial interests

The authors declare no competing financial interests.

LETTERS NATURE NANOTECHNOLOGY DOI: 10.1038/NNANO.2015.111

Methods

Nanoparticle preparation and characterization. Au nanoparticles (core diameter $d_c = 4.8 \pm 0.9$ nm, Supplementary Fig. 1) were neutron-activated, leading to conversion of parts of the Au atoms to the gamma-emitting isotope ^{198}Au (ref. 4). The Au cores were coated by an amphiphilic polymer (poly(isobutylene-alt-maleic anhydride)-*graft*-dodecyl), to which the In chelator 1,4,7,10-tetraazacyclododecane-1,4,7,10-tetraacetic acid (DOTA) had been integrated[5]. After addition of ^{111}In, the resulting double-labelled nanoparticles had a hydrodynamic diameter of $d_h = 13 \pm 1$ nm and a zeta-potential of 46 ± 16 mV (Supplementary Figs 14 and 15). The geometry of the nanoparticles is shown in Fig. 1 (for details see ref. 5). CdSe/ZnS QDs (core diameter of $d_c = 4.7 \pm 1$ nm, Supplementary Fig. 3) were synthesized according to the standard protocol. The QDs were coated with the same amphiphilic polymer as the Au nanoparticles, into which organic fluorophores were integrated. The QDs had a zeta-potential of 28 ± 4 mV (Supplementary Fig. 20). For details see ref. 5.

Animals. Healthy, female Wistar Kyoto rats (WKY/Kyo@Rj rats, Janvier, 8 10 weeks of age, bodyweight of ~250 g) were housed in pairs in humidity- and temperature-controlled ventilated cages on a 12 h day/night cycle. Rodent diet and water were provided *ad libitum*. All experiments were conducted under German federal guidelines for the use and care of laboratory animals and were approved by the Regierung von Oberbayern (Government of District of Upper Bavaria, approval no. 55.2-1-54-2531-26-10) and by the Institutional Animal Care and Use Committee of the Helmholtz Center Munich.

Nanoparticle administration and animal maintenance in metabolic cages. The entire administration has been described previously[4,19]. Briefly, the rats were anaesthetized by inhalation of 5% isoflurane until muscular tonus relaxed. Nanoparticle suspensions (50 70 µl, containing 1 10 µg of double-labelled gold nanoparticles) were administered to the animals via intravenous injection into the tail vein, then the rats were kept individually in metabolic cages for separate collection of total urine and faeces.

Sample preparation and radio analysis. One hour or 24 h post-injection, rats were anaesthetized and euthanized by exsanguination via the abdominal aorta. Radio analysis was performed on four rats for each time point according to previously published protocols[4,23]. Briefly, total organs, tissues, body fluids, the remaining carcass, and total urinary and faecal excretions were sampled and analysed γ-spectrometrically[4,19]. The ^{198}Au or ^{111}In radioactivities of all samples were measured without any further sample preparation by γ-spectroscopy. Small organ and tissue samples were analysed in a lead-shielded, 10 ml well type NaI(Tl) scintillation detector, while a lead-shielded, 1 l well type NaI(Tl) scintillation detector was used for large samples like the remaining carcass. Compton correction was carried out using the gamma acquisition analysis software Genie 2000 (Canberra Industries). Count rates were adjusted for physical decay and background radiation. The ^{198}Au or ^{111}In count rates were calibrated to either a ^{198}Au or ^{111}In reference source at a reference date in order to correlate ^{198}Au and ^{111}In radioactivities to the numbers and masses of the Au nanoparticles. Samples yielding net counts (that is, background-corrected counts) in the photo-peak region-of-interest of either the ^{198}Au or the ^{111}In γ-spectrum were defined to be below the detection limit when they were less than three standard deviations of the background counts of this region-of-interest. While dissecting, no organs were cut and all fluids were cannulated when necessary to avoid cross-contamination. We quantitatively determined the entire ^{198}Au and ^{111}In doses independently from each other in the entire animal by analysing for each radioisotope in each organ and tissue, and in the total excretion. Thus, for each radioisotope, a 100% balance of the biodistribution was performed.

Blood correction. The blood contents of the organs and the remaining body were calculated according to the findings of Oeff and colleagues[20], as described previously[22,23].

Calculations and statistical analysis. All calculated data are given as a percentage of the relevant integral radioactivity of all samples in each animal with the standard error of the mean (s.e.m.) for both radioisotopes.

Accompanying 'in test tube' and *in vitro* experiments with QDs. To support the *in vivo* observations obtained with polymer-coated Au nanoparticles with double radionucleotide labelling, additional 'in test tube' and *in vitro* experiments were performed with polymer-coated QDs with double fluorescence labelling (one colour for the inorganic nanoparticle core and one colour for the organic polymer shell). The QDs had similar geometry, surface chemistry and colloidal properties. 'In test tube' polymer-coated QDs were incubated with different proteolytic enzymes, and the resulting fragments of the DY495-labelled polymer shell/released DY495 were separated from the nanoparticles by filtration. The amount of released fluorescence label from the polymer coating was quantified with fluorescence spectroscopy. For *in vitro* experiments, HUVECs and Kupffer cells (which are relevant for nanoparticles present in the liver) were exposed to polymer-coated QDs labelled with different fluorophore labels in their polymer shell. Co-localization experiments between the QD core and the polymer shell label were performed. The fluorescence spectra of exocytosed QDs and QDs found in cell lysate were compared (Supplementary Figs 46 49).

Journal of Biomedical Optics 17(12), 126009 (December 2012)

Three-dimensional surface reconstruction within noncontact diffuse optical tomography using structured light

Kirstin Baum, Raimo Hartmann, Tobias Bischoff, Jan O. Oelerich, Stephan Finkensieper, and Johannes T. Heverhagen
Philipps University Marburg, Department of Radiology, Baldingerstraße, 35043 Marburg, Germany

Abstract. A main field in biomedical optics research is diffuse optical tomography, where intensity variations of the transmitted light traversing through tissue are detected. Mathematical models and reconstruction algorithms based on finite element methods and Monte Carlo simulations describe the light transport inside the tissue and determine differences in absorption and scattering coefficients. Precise knowledge of the sample's surface shape and orienta tion is required to provide boundary conditions for these techniques. We propose an integrated method based on structured light three dimensional (3 D) scanning that provides detailed surface information of the object, which is usable for volume mesh creation and allows the normalization of the intensity dispersion between surface and camera. The experimental setup is complemented by polarization difference imaging to avoid overlaying bypro ducts caused by inter reflections and multiple scattering in semitransparent tissue. [DOI: 10.1117/1.JBO.17.12.126009]

Keywords: diffuse optical tomography; 3 D surface reconstruction; structured light scanner.

Paper 12345P received Jun. 1, 2012; revised manuscript received Nov. 13, 2012; accepted for publication Nov. 13, 2012; published online Dec. 3, 2012.

1 Introduction

Using light for medical diagnostics and biomedical research has become increasingly popular over the last decades due to fast and noninvasive applications without the need for ionizing radiation.

In the range of near infrared light, the absorption coefficient of biological tissue components such as oxi/deoxihemoglobin, melanin, and water decreases. Therefore light can pass several centimeters through tissues.[1] A main field of research in this area is diffuse optical tomography (DOT). Most DOT systems detect transmitted light[2,3] and analyze the scattering and absorp tion differences to determine structural changes in tissues.[4,5] Interpreting these values with respect to experimentally obtained data for tissue parameters makes DOT suitable for breast cancer detection, small animal, or brain imaging and tracking of active pharmaceuticals.[2,6–9]

1.1 *Illumination and Light Capturing Methods*

In DOT systems different methods for illumination and light capturing have been established. In DOT systems, two different setups can be distinguished: the first type employs noncontact illumination and light capturing while the second system type uses optical fibers in direct contact to the tissue to inject and detect light.[6,7,10] The optical fiber applications are limited with respect to functionality due to the need of contact gel in suitable containers, inflexibility, and high maintenance require ments. Furthermore, an integrated real shape 3 D reconstruction of tissues or phantoms embedded in contact gel is difficult or even impossible.[8,11] In noncontact DOT, problems arise due to refraction at surfaces, reflection, and intensity variations caused by the irregularity of the objects geometry.

1.2 *Reconstruction of Inner Tissue Structure*

Mathematical models were developed to describe light transport inside tissue by employing finite element methods (FEM) or Monte Carlo simulations for image reconstruction and determin ing differences in absorption and scattering coefficients.[12–18] The use of such methods is strongly simplified due to the exis tence of highly sophisticated software toolboxes, e.g., TOAST (http://web4.cs.ucl.ac.uk/research/vis/toast/intro.html) or NIR FAST (http://www.dartmouth.edu/~nir/nirfast/), that offer a broad variety of adjustable parameters.[19] Current methods for mesh creation are mainly based on segmented pre MRI or CT scans, or rough approximations of the surface.[20–22] However, for a more accurate reconstruction, precise knowledge of the surface is inevitable.

1.3 *3-D Surface Scans and Reconstruction of the Object Shape*

In addition to the development of reconstruction software, dif ferent surface capturing methods have been employed. DOT systems with integrated 3 D cameras, holographic scanners, or photoluminescence plates were developed. Another method to capture the shape of the object is to process pre MRI or CT scans.[11,20–22] These systems have disadvantages regarding accu racy and/or handling, expenditure of time, availability and oper ating costs. For example, in semitransparent objects, 3 D cameras cannot distinguish between information from the sur face and light originating from the subsurface. Photolumines cence plates capture only a shadow image of the object disregarding fine details of the surface.[3,8,12,19] Structured light

Address all correspondence to: K. Baum, Philipps University Marburg, Department of Radiology, Baldingerstraße, 35043 Marburg, Germany. Tel: +4964215865933; Fax: +49(0)6421-58-68959; E-mail: baumk@med.uni-marburg.de

0091-3286/2012/$25.00 © 2012 SPIE

3 D scanners, which are widely used in a lot of industrial applications,[23–25] offer a cheap and flexible option for integration of a 3 D surface scanner into a DOT system. Libraries such as "Open Computer Vision" (open CV, http://opencv.willowgarage.com/wiki/) or "The Point Cloud Library" (PCL, http://pointclouds.org/) provide a multitude of suitable open source software components for utilization in optical imaging applications.[26]

In this paper we present an approach for 3 D surface reconstruction of semi transparent objects imaged by a DOT system, using a structured light projection setup in combination with polarization difference imaging (PDI). Combining these techniques allows for contactless image acquisition and also faster mesh generation for FEM based image reconstruction algorithms.

2 Theory and Methods

Within contactless image acquisition of objects in diffuse optical tomography, special care must be taken with regard to boundary surfaces, since the angle of refraction depends on the orientation of the surface normal and the refraction index of the medium.[11,27] To overcome this dilemma given an unknown object topology, multiple detectors are usually attached directly to the surface using a refraction index matching contact gel.[7]

For contactless image acquisition in transmission mode, the shape of an object has to be known for two reasons: first, the geometric information can be used for simple mesh creation to model diffuse light propagation in tissue employing FEM, like the one used by NIRFAST and TOAST. Second, the shape determines the direction of photons leaving the object and the intensity captured by the detector. These problems are illustrated in Fig. 1, where the surface shape influences the transmitted light intensity on the detector side. Assuming a Lambertian radiator at each node k of the FEM mesh on the object's surface, which is justified by the multiple scattering nature of light inside the tissue, the light intensity I_k as measured by the detector can be obtained from the surface shape and the transmitted intensity I_k^0 perpendicular to the surface by

$$I_k = I_k^0 \cdot \sin \beta_k, \quad k = 1, 2, 3. \tag{1}$$

The angles α_j with $j = 1, 2$ determine the amount of light reflected by the surface according to the Fresnel equations. However, since optical properties of the tissue are generally unknown, the incident laser beam should be kept perpendicular to the surface.

2.1 *Polarization Difference Imaging*

PDI is a relatively simple and fast technique, which allows the separation of light reflected by the real surface of an object from the signal originating from the subsurface.

In effect, in nonbirefringent media ballistic scattering does not alter the polarization state of light, while nonballistic scattering results in random polarization. By analyzing the polarization state of the reflected light, the real surface of the object can be extracted. Nevertheless, tissue penetration depth is correlated to multiple scattering events and inter reflections ultimately resulting in a loss of polarization.

If polarizer and analyzer are aligned in the same orientation, ballistic scattered photons are recovered. To decrease the noise caused by photons randomly polarized in the same manner as the incident light due to inelastic scattering, the analyzer is turned orthogonal to the polarizer and the measured signal is subtracted. The calculated intensity of ballistic photons is

$$I = |I_{||} - I_{\perp}|, \tag{2}$$

where $I_{||}$ is the intensity recorded during parallel alignment of polarizer and analyzer while $I_{\perp}$ is obtained after turning the analyzer at 90 deg.[1,28–30]

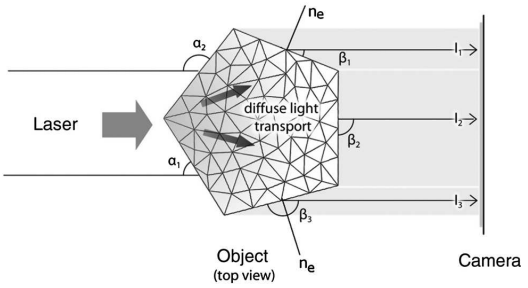

Fig. 1 The light intensities I_{1-3} measured by the camera depend on the surface orientation with respect to camera position and on the refractive index of object and ambient medium. The angles α_{1-2} show the orientation of the incident light to the surface segments, while β_{1-3} describe the angle between camera normal and the surface at the detector side ($I_k = I_k^0 \cdot \sin \beta_k$, $k = 1, 2, 3$). Note that n_k denotes the surface normal to the surface element number k.

2.2 *Structured Light 3-D Reconstruction*

A cloud of points on the object's surface is captured using ray plane intersection, which is then triangulated to obtain a discrete number of small surface elements. For the first step, gray coded fringe patterns are projected onto the object. In the camera plane, the stripes seem shifted and curved due to the topology of the object. Here every stripe in the projected image is identified in the captured image by its binary gray code.[31] Provided the positions of camera and projector are known, the 3 D object position within the coordinate system of the camera is obtained by calculating the intersection point of the plane given by a projector stripe and the light ray detected by the camera.[32] While examining tissue, it cannot be assumed that only direct surface reflections of fringe pattern are observed. Rather, photons originating from subsurface scattering must be accounted for. To this end, de scattering properties of phase shifting or PDI, which is used in this work, can be applied.[28]

By rotating the object and repeating the previous procedure, local 3 D reconstructions from different viewpoints are acquired and can be merged to obtain global surface information. This data is used to provide boundary information for FEM mesh creation on the one hand and to normalize images acquired during a DOT scan on the other hand (see Fig. 1).

An example for an experimental noncontact DOT setup with integrated PDI and structured light system is shown in Fig. 2.

2.3 *Workflow*

The workflow of a DOT system is illustrated in Fig. 3. In the first step, the object is rotated on a stage while fringe pattern image sequences are collected to reconstruct a 3 D surface model. The same detector is used subsequently to acquire images of the object trans illuminated by the laser. In the next step, the surface

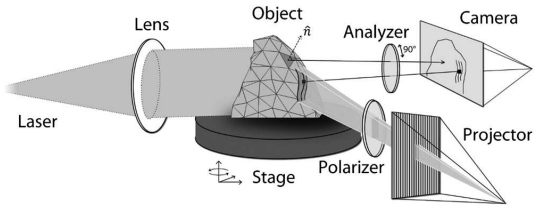

Fig. 2 Experimental setup for a noncontact DOT system with integrated PDI and structured light projection system (on the right hand side). The laser beam describes the transmitted light path of the system (left hand side). Transmitted light and fringe pattern can be captured by the same camera system. For 3 D surface shape reconstruction, the polarizer analyzer orientation can be adjusted between 0 and 90 deg, and the object can be illuminated with fringe patterns by the projector.

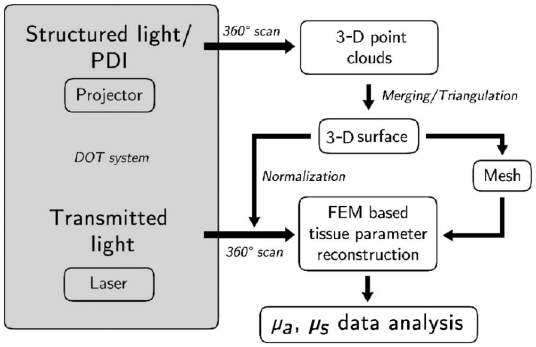

Fig. 3 Workflow of a DOT system with integrated PDI and structured light projection. Hardware control, image acquisition, data reconstruction, and data analysis can be performed within one software application.

model data is needed for mesh generation on the one hand and intensity normalization of the images, captured in trans illumination mode, on the other. Finally, the mesh is used for FEM based solving of the forward model of light propagation within the object.[19]

If the deviation between the solution of the forward model and the captured transmitted light data is minimized by parameter variation, the inversion of the forward problem can give an estimate for the distribution of the light absorption and scattering parameters μ_a and μ_s. All of the components are integrated in one experimental setup.

2.4 *From Point Clouds to Mesh*

In order to provide suitable information for tissue reconstruction applications like NIRFAST and TOAST, surface meshes have to be constructed out of the acquired point clouds. Such meshes usually consist of polygons, which in most cases form triangles for easier storage, rendering, and further processing of the data. Depending on the required accuracy, the density of points can be reduced first to reduce computing time. For the point cloud and surface reconstruction operations, the "Point Cloud Library"[26] is used. It provides implementations of several algorithms for both surface reconstruction and point cloud filtering/smoothing. For numerical iterative optimization purposes the "GNU Scientific Library" is used.[33]

3 Results

To specify and to validate the method, the following measurements were performed: both a nontransparent metallic cylinder and a semitransparent cylinder made of Agar Agar were scanned in order to determine the accuracy of the proposed method and demonstrate the advantages of PDI within the system.

Additional scans of more complex non and semitransparent objects were carried out. The resulting volume meshes are presented in Sec. 3.4.

3.1 *Accuracy of the Method for Nontransparent Objects*

To determine the accuracy of the 3 D scanning unit, a metallic cylinder of known radius $r_{cyl} = 7.7$ mm was scanned from different angles. The resulting point clouds were merged into a 360 deg surface cloud. The final point cloud is shown in Fig. 4. For this measurement, the cylinder was aligned so that its symmetry axis coincides with the system's rotation axis. Since the orientation of the rotation axis is known from

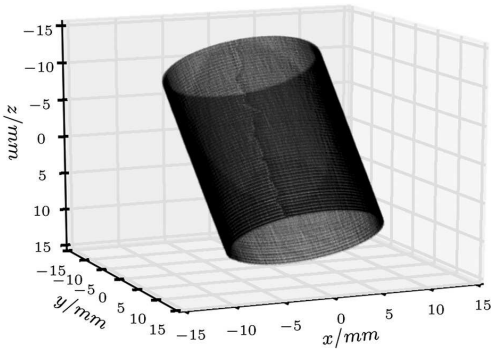

Fig. 4 Point cloud reconstruction of a metal cylinder with radius $r_{cyl} = 7.7$ mm.

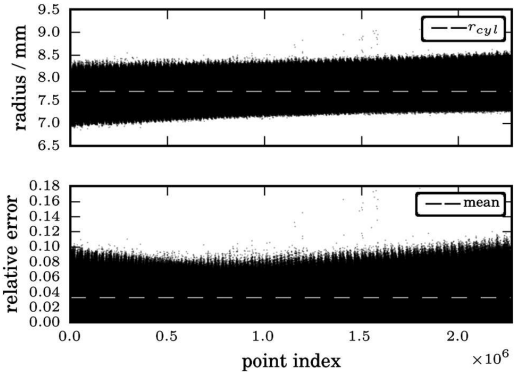

Fig. 5 Measurement of a test cylinder made of metal ($r_{cyl} = 7.7$ mm). The upper plot shows the computed radius for every point in comparison to the real cylinder radius, which is drawn as dashed line. The lower plot illustrates the relative error for every point. The mean error is 3.2% (dashed line) with a standard deviation of 2%. Note that the point indices are sorted by ascending z values.

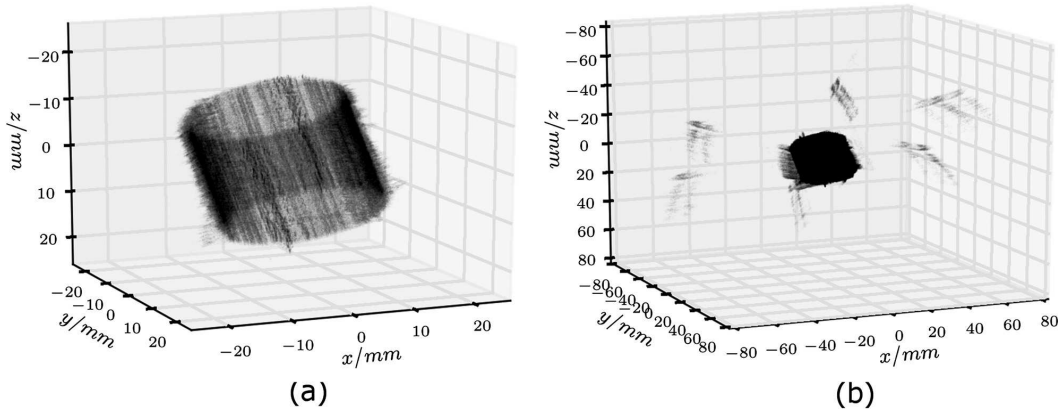

Fig. 6 (a) Point cloud reconstruction of an Agar Agar cylinder with a radius $r_{cyl} = 12.92$ mm using PDI technique. (b) Point cloud of the same cylinder measured without using PDI.

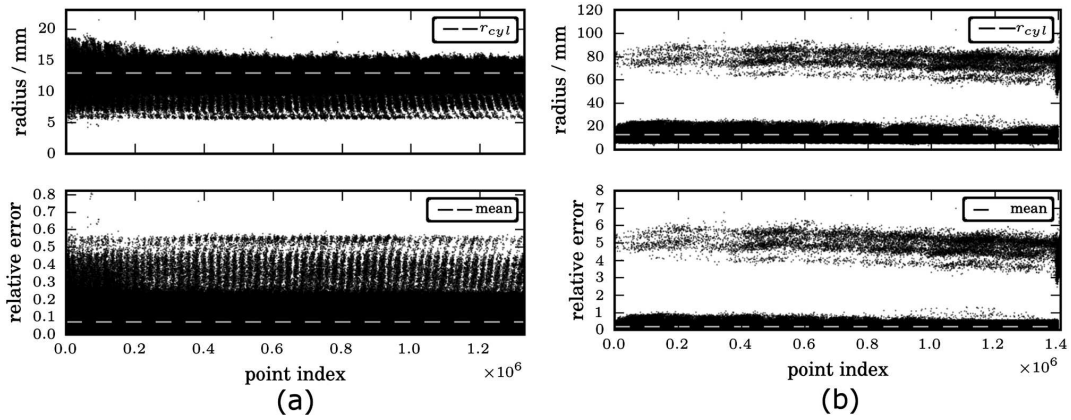

Fig. 7 Measurements of an Agar Agar cylinder ($r_{cyl} = 12.92$ mm) with and without PDI. The dashed lines indicate the ideal cylinder radius in the upper and the mean errors in the lower plots (a) PDI measurement of an Agar Agar cylinder. The mean error is 7.4% with a standard deviation of 7.9% (b) NonPDI measurement of the same cylinder. Here the mean error is 19.3% with a standard deviation of 60.5%. Note the different scaling of the y axis. Point indices are sorted by ascending z values in both cases.

the calibration procedure, it is possible to compare the distance of every point to the rotation axis with the actual cylinder radius.

As presented in Fig. 5, the computed point cloud is in good agreement with the real shape of the cylinder. The mean error is 3.2% with a standard deviation of 2%, which is a satisfying result.

3.2 *Accuracy of the Method for Semitransparent Objects*

Similar tests were performed on a semitransparent Agar Agar cylinder (2% Agar Agar Kobe I, Company Carl Roth GmbH Karlsruhe) of radius $r_{cyl} = 12.92$ mm. In order to determine the influence of PDI on the quality of the 3 D reconstruction, these measurements were carried out with and without using the PDI method. The following images illustrate the resulting point clouds of both measurements in comparison.

Figure 6 demonstrates that the absence of PDI leads to major reconstruction errors. This observation can be quantified by analyzing the cylinder radius as described in Sec. 3.1. As shown in Fig. 7(a), the usage of the PDI method suppresses most of the reconstruction errors. In addition, using PDI reduces the mean relative error from 19.3 to 7.4%. However, the errors still show a larger dispersion about the mean as compared to the metal cylinder. All the quantitative results are summarized in Table 1.

Table 1 Validation results.

	Metal Cylinder	Agar Agar cylinderwith PDI	Agar Agar cylinderwithout PDI
Mean relative error	3.2%	7.4%	19.3%
Standard deviation	2%	7.9%	60.5%

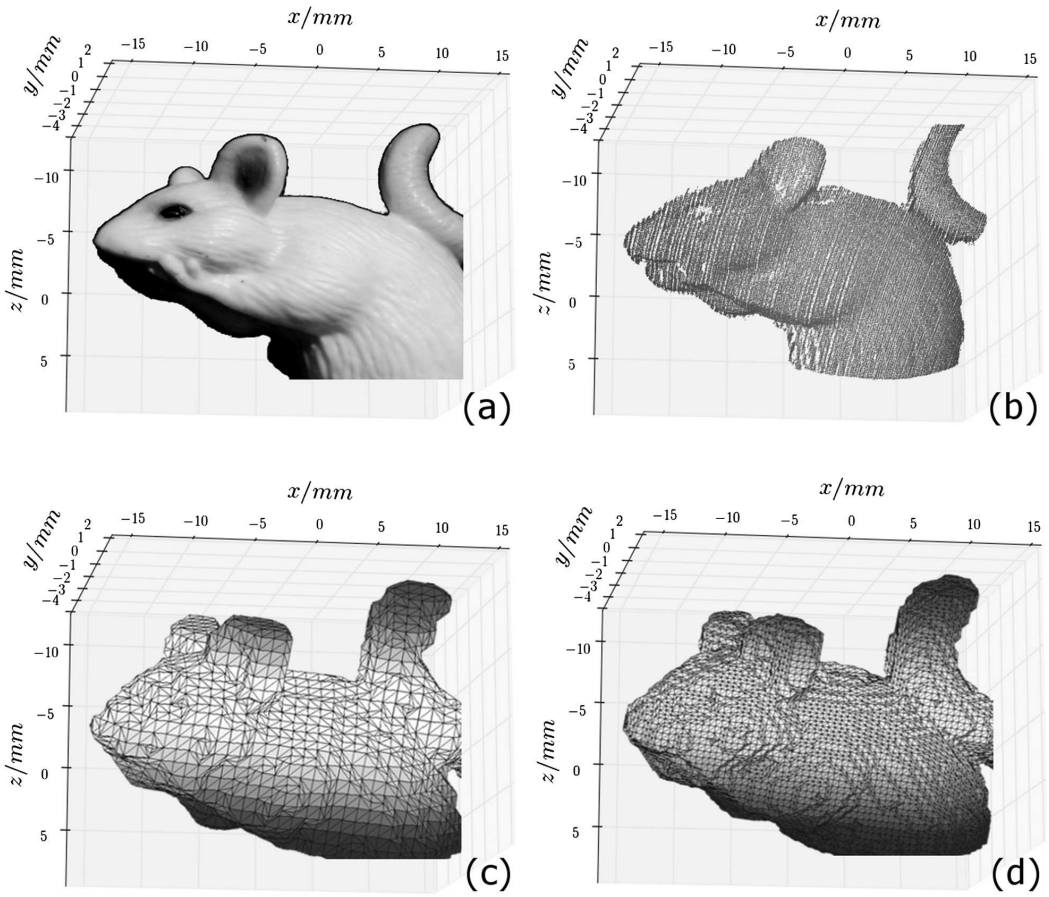

Fig. 8 (a) Photo of the phantom. (b) The point cloud image of the phantom. (c) and (d) Triangulated surface meshes with different node distances.

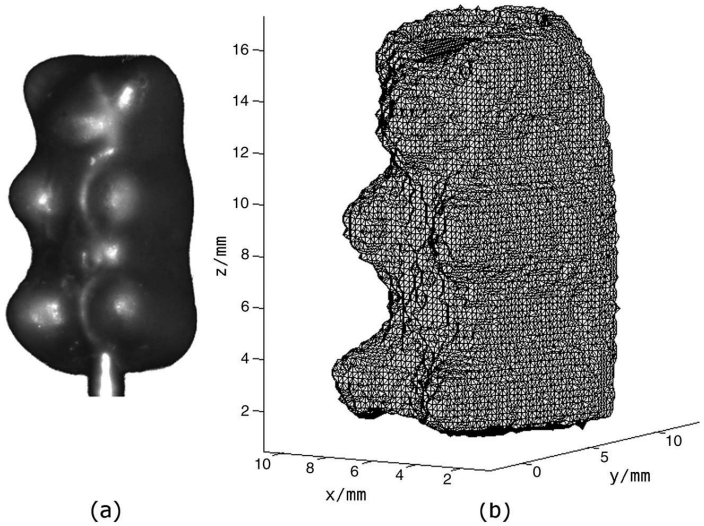

Fig. 9 (a) Photo of a typical HARIBO gold bear. (b) Volume mesh reconstructed from a PDI measurement of the same gold bear.

Based on these results, we conclude that the usage of PDI clearly improves the surface scans. However, our point cloud reconstructions of semitransparent objects do not reach the quality of nontransparent objects.

3.3 *Meshing of Nontransparent Objects*

Both a photography of a nontransparent object (here a plastic mouse phantom) and the corresponding point cloud captured with the introduced setup via structured light, are shown in Fig. 8(a) and 8(b), respectively.

Such surface point clouds captured from different angles were merged into a 360 deg surface point cloud of the sample. We then used a triangulation algorithm implemented in NIRFAST to find a 3 D volume mesh for further processing. Preliminary results are shown in Fig. 8(c) and 8(d) with different node distances.

3.4 *Meshing of Semitransparent Objects*

The main application of our approach is to handle tissue like and semi transparent objects using PDI. Figure 9(a) and 9(b) show both a photography of a typical HARIBO Gold bear (HARIBO of America, Inc., Baltimore, MD) and its corresponding mesh as calculated from point cloud data obtained with our setup. As shown in Sec. 3.2, the absence of PDI leads to significant recon struction errors and therefore the best results can be achieved by using PDI within a DOT system.

4 Conclusion

Our setup provides a quick and cost effective method to obtain a pure 3 D surface structure of an object within a DOT application concerning both hardware and software. Such surface scans including setup calibration, scanning and data processing can typically be finished within less than 10 min. Hardware compo nents like polarisation filters for PDI applications and a struc tured light pattern projector are added to an existing DOT system. It has to be mentioned that projector camera calibration is challenging for a camera field of view with sub centimeter size. The same detector is used for the transmitted and structured light image capturing. Furthermore, hardware control, image acquisition, data reconstruction, and data analysis are integrated into one software application. With our method, the images' intensities acquired through contactless trans illumination of tis sue can be corrected to simulate planar objects. Optical fibers and contact gel are not needed because photon propagation between object and detector can be calculated using the surface model data. Most importantly, the 3 D surface information can be used to generate a volume mesh to model the object for FEM based image reconstruction software like NIRFAST and to supersede MRI or CT analysis.

Acknowledgments

Supported by a research grant of the University Medical Center Gießen and Marburg (UKGM).

References

1. L. V. Wang and H.-I. Wu, *Biomedical Optics: Principles and Imaging*, John Wiley & Sons, Inc., New Jersey (2007).
2. A. H. Hielscher et al., "Near-infrared diffuse optical tomography," *Dis. Markers* **18**, 313 337 (2002).
3. R. B. Schulz, J. Ripoll, and V. Ntziachristos, "Noncontact optical tomography of turbid media," *Opt. Lett.* **28**(18), 1701 1703 (2003).
4. W. F. Cheong, S. A. Prahl, and A. J. Welch, "A review of the optical-properties of biological tissues," *IEEE J. Quant. Electron.* **26**(12), 2166 2185 (1990).
5. A. N. Bashkatov et al., "Optical properties of human skin, subcutaneous and mucous tissues in the wavelength range from 400 to 2000 nm," *J. Phys. Appl. Phys.* **38**(15), 2543 2555 (2005).
6. S. van de Ven et al., "Diffuse optical tomography of the breast: initial validation in benign cysts," *Mol. Imag. Biol.* **11**(2), 64 70 (2009).
7. H. Xu et al., "Near-infrared imaging in the small animal brain: optimization of fiber positions," *J Biomed. Opt.* **8**(1), 102 110 (2003).
8. N. Deliolanis et al., "Free-space fluorescence molecular tomography utilizing 360-deg geometry projections," *Opt. Lett.* **32**(4), 382 384 (2007).
9. V. Ntziachristos et al., "Looking and listening to light: the evolution of whole-body photonic imaging," *Nat. Biotechnol.* **23**, 313 320 (2005).
10. J. Ripoll et al., "Fast analytical approximation for arbitrary geometries in diffuse optical tomography," *Opt. Lett.* **27**(7), 527 529 (2002).
11. F. Nouizi et al., "3-D modeling for solving forward model of no-contact fluorescence diffuse optical tomography method," *Proc. SPIE* **7369**, 73690C (2009).
12. V. Ntziachristos and R. Weissleder, "Experimental three-dimensional fluorescence reconstruction of diffuse media by use of a normalized born approximation," *Opt. Lett.* **26**(12), 893 895 (2001).
13. S. Srinivasan et al., "A coupled finite element-boundary element method for modeling Diffusion equation in 3-D multi-modality optical imaging," *Biomed. Opt. Express* **1**(2), 398 413 (2010).
14. Q. Fang et al., "Nonlinear image reconstruction algorithm for diffuse optical tomography using iterative block solver and automatic mesh generation from tomosynthesis images," *Proc. SPIE* **6081**, 60810O (2006).
15. M. Chu et al., "Light transport in biological tissue using three-dimensional frequency-domain simplified spherical harmonics equations," *Phys. Med. Biol.* **54**(8), 2493 2509 (2009).
16. S. L. Jacques and B. W. Pogue, "Tutorial on diffuse light transport," *J. Biomed. Opt.* **13**(4), 041302 (2008).
17. P. Gonzalez-Rodriguez and A. D. Kim, "Comparison of light scattering models for diffuse optical tomography," *Opt. Express* **17**(11), 8756 8774 (2009).
18. J. Ripoll and V. Ntziachristos, "Iterative boundary method for diffuse optical tomography," *J. Opt. Soc. Am. A Opt. Image Sci. Vis.* **20**(6), 1103 1110 (2003).
19. H. Dehghani et al., "Near infrared optical tomography using NIRFAST: algorithm for numerical model and image reconstruction," *Comm. Numer. Meth. Eng.* **25**, 711 732 (2009).
20. B. Dogdas et al., "Digimouse: a 3-D whole body mouse atlas from CT and cryosection data," *Phys. Med. Biol.* **52**(3), 577 587 (2007).
21. B. W. Pogue and K. D. Paulsen, "High-resolution near-infrared tomographic imaging simulations of the rat cranium by use of a priori magnetic resonance imaging structural information," *Opt. Lett.* **23**(21), 1716 1718 (1998).
22. M. Schweigers and S. R. Arridge, "Optical tomographic reconstruction in a complex head model using a priori region boundary information," *Phys. Med. Biol.* **44**(11), 2703 2721 (1999).
23. S. S. Gorthi and P. Rastogi, "Fringe projection techniques: whither we are?," *Optic. Laser. Eng.* **48**(2), 133 140 (2010).
24. A. Kus, "Implementation of 3-D optical scanning technology for automotive applications," *Sensors* **9**(3), 1967 1979 (2009).
25. J. Burke et al., "Reverse engineering by fringe projection," *Proc. SPIE* **4778**, 312 324 (2002).
26. R. B. Rusu and S. Cousins, "3-D is here: Point Cloud Library (PCL)," in *IEEE International Conf. on Robotics and Automation (ICRA)*, Shanghai, China, pp. 1 4 (2011).
27. M. Born and E. Wolf, *Principles of Optics*, Cambridge University Press, Cambridge, United Kingdom (1998).
28. T. Chen et al., "Polarization and phase-shifting for 3-D scanning of translucent objects," in *IEEE Computer Society Conf. on Computer Vision and Pattern Recognition*, Minneapolis, pp. 1 8 (2007).
29. J. S. Tyo et al., "Target detection in optically scattering media by polarization-difference imaging," *Appl. Opt.* **35**(11), 1855 1870 (1996).

30. M. P. Rowe et al., "Polarization-difference imaging: a biologically inspired technique for observation through scattering media," *Opt. Lett.* **20**(6), 608 610 (1995).
31. J. Salvi, J. Pages, and J. Batlle, "Pattern codification strategies in structured light systems," *Pattern Recogn.* **37**(4), 827 849 (2004).
32. D. Lanman and G. Taubin, "Build your own 3-D scanner: 3-D photography for beginners," in *ACM SIGGRAPH 2009 Courses, 36th international Conf. and Exhibition on Computer Graphics and Interactive Techniques*, New Orleans, pp. 1 87 (2009).
33. M. Galassi et al., *GNU Scientific Library Reference Manual*, 3rd ed., Network Theory Limited, Bristol, United Kingdom (2009).

Journal of Materials Chemistry B

PAPER

View Article Online
View Journal

Cite this: DOI: 10.1039/c4tb02077d

Encapsulated enzymes with integrated fluorescence-control of enzymatic activity†

Pascal K. Harimech,‡[a] Raimo Hartmann,‡[a] Joanna Rejman,[a] Pablo del Pino,[b] Pilar Rivera Gil[a] and Wolfgang J. Parak*[ab]

Received 16th December 2014
Accepted 16th February 2015

DOI: 10.1039/c4tb02077d

www.rsc.org/MaterialsB

A fluorescence-based particle sensor for oxaloacetic acid is presented. In the presence of nicotinamide adenine dinucleotide as a cofactor, oxaloacetic acid is converted by malate dehydrogenase into L-malic acid. The progress of the reaction is monitored by sensing of proton consumption with an integrated pH sensor. The kinetics of this sensor are investigated on a single particle level. This work demonstrates the feasibility to detect analytes upon their enzymatic conversion into a product, which in turn can be sensed with a fluorophore responding to changes in the concentration of this product. Integration of enzymes and fluorophores into one carrier particle, as demonstrated here for the case of polyelectrolyte polymer capsules, allows the range of analytes that can be detected with fluorescence to be extended, as it enhances selectivity. This coupled system allows enzymatic activity, as well as the kinetics of malate dehydrogenase, to be monitored.

Introduction

Analyte-sensitive fluorophores are common tools for measuring the concentration of analytes in solution by means of fluorescence measurements.[1,2] Fluorophores which selectively respond to the presence of a large number of analytes have been reported in the literature and many of them are also commercially available,[3,4] such as Ru(ddp), FluoZin, tetraphenylethene-based diboronic acid, $[Ru(phen)3]^{2+}$, *etc.*[1,2,5,6] Selectivity to a target analyte however is often limited, as the presence of other (similar) analytes triggers an unwanted crosstalk response. In addition, for many analytes, no fluorophores which show a response upon their presence, have been described. One strategy to bypass these shortcomings is the use of enzymes. Enzymes are very selective to their target substrates. When fluorophores responsive to the enzymatic product are used, analytes which serve as a target for the enzyme can be selectively detected.[7 12] Ideally, enzymes and fluorophores (in addition to organic fluorophores and quantum dots and luminescent metal nanoclusters have also been used) should be coupled together into one entity, which is possible for example by linking both of them to colloidal particles. One convenient carrier particle system, which allows embedding of analyte-sensitive fluorophores,[13 16] as well as enzymes,[17 24] is polyelectrolyte capsules fabricated by layer-by-layer assembly.[25 27] The walls of the capsules can be made semi-permeable, which allows small analytes to diffuse inside the capsule to reach the embedded fluorophores and enzymes, while retaining the fluorophores and enzymes inside the cavity of the capsule. If the fluorophores are not retained due to their small size, they can be linked to larger molecules.[19] Combination of analyte-sensitive fluorophores and enzymes allows for selective detection of analytes/substrates.[28,29] For example, Kazakova *et al.* co-embedded urease and the pH-sensitive fluorophore seminaphtharhodafluor (SNARF-1) in polyelectrolyte capsules with the intention of designing an urea-selective fluorescence sensor.[29] Upon enzymatic processing of urea by urease, the local pH increases due to the production of ammonia, which is detected with the pH-sensitive fluorophore (*i.e.* consumption of protons). In principle, such enzyme-based fluorescence sensors could also be applied for intracellular sensing, similar to intracellular pH-sensing, which has been demonstrated to monitor cellular reactions.[30] In particular, this would be interesting for target molecules which are relevant for cellular function. Besides real-time determination of the intracellular concentrations of such target molecules, these capsules could be seen as theranostic devices. In cases where the concentration of an intracellular target is decreased by the enzymes delivered with the capsules, this decrease could be monitored directly by co-delivered fluorophores selective to one of the enzymatic products.

In this work, a proof-of-concept of such an encapsulated enzyme–fluorophore couple for a biologically relevant target analyte is demonstrated. Specifically, we encapsulated malate dehydrogenase, an enzyme involved in many metabolic pathways, including the Krebs cycle, which reversibly converts oxaloacetic acid (OAA) into L-malic acid:

[a]*Fachbereich Physik, Philipps Universitat Marburg, Marburg, Germany. E mail: wolfgang.parak@physik.uni marburg.de*

[b]*CIC Biomagune, San Sebastian, Spain*

† Electronic supplementary information (ESI) available. See DOI: 10.1039/c4tb02077d

‡ Both authors contributed equally to this work.

View Article Online

Journal of Materials Chemistry B

Paper

$$\text{OAA} + \text{NADH} + \text{H}^+ \rightleftharpoons \text{L malic acid} + \text{NAD}^+$$

This reaction requires nicotinamide adenine dinucleotide (NADH) as a cofactor. During the enzymatic reaction, protons are consumed/produced, depending on the direction of the reaction. Based on the response of the co-encapsulated pH-sensitive fluorophore, SNARF-1, the reaction can be monitored by pH-sensing, *cf.* Fig. 1. The kinetics of this combined system, and in particular that of its fluorescence read-out, are discussed in this work.

Materials and methods

Chemicals

Poly(sodium 4-styrenesulfonate) (PSS, $M_w \approx 70$ kDa, #243051), poly(allylamine hydrochloride) (PAH, $M_w \approx 56$ kDa, #283223), calcium chloride dehydrate ($CaCl_2$, #223506), sodium carbonate (Na_2CO_3, #S7795), ethylenediaminetetraacetic acid disodium salt dihydrate (EDTA disodium salt, #E5134), and mitochondrial malate dehydrogenase from porcine heart (#M2634) were purchased from Sigma-Aldrich (Germany). SNARF-1-dextran ($M_w \approx 70$ kDa, #D3304) from Life Technologies (Germany) was used. Sodium chloride (NaCl, #HN00.2), oxaloacetic acid (OAA, #4032.2), and β-nicotinamide adenine dinucleotide disodium salt (NADH, #AE12.1) were obtained from Roth (Karlsruhe, Germany). Phosphate buffered saline (PBS-Dulbecco, #L1825) was purchased from Biochrom (Berlin, Germany). Ultrapure double distilled water (ddH_2O) with a resistivity greater than 18.2 MΩ cm was used for all experiments.

Synthesis of polyelectrolyte sensor capsules

The synthesis of polyelectrolyte microcapsules was carried out as described previously,[14,15,30,31] with the following modifications: $CaCO_3$ microparticles were prepared at room temperature (RT) from solutions of $CaCl_2$ and Na_2CO_3 under vigorous stirring, in the presence of SNARF-1-dextran and malate dehydrogenase. 615 μL of an aqueous solution of $CaCl_2$ (0.33 M) with NaCl (1.33 M), 600 μL SNARF-1-dextran 70 kDa (1 mg mL^{-1}) and 100 μL malate dehydrogenase (11 mg protein per mL, 7700 U mL^{-1}) were mixed together in a glass vial. During magnetic stirring (1000 rpm), 615 μL of an aqueous solution of Na_2CO_3 (0.33 M) with NaCl (1.33 M) solution was added quickly. After 30 s the stirrer was turned off and particle growth was stopped after an additional 2 minutes by centrifugation. The particles were washed three times with ddH_2O and then directly used for the layer-by-layer assembly of polyelectrolytes. Alternating layers of negatively charged PSS (2 mg mL^{-1} in 0.5 M NaCl) and positively charged PAH (2 mg mL^{-1} in 0.5 M NaCl) were deposited onto the charged microparticles until four bilayers of the polyelectrolytes had been established ($CaCO_3$@(PSS/PAH)$_4$). For coating with each layer, the microparticles were suspended in 1 mL of polyelectrolyte solution, shaken gently for 10 minutes and washed three times with ddH2O. The dissolution of the cores was carried out by Ca^{2+} ion complexation with EDTA (1 mL, 0.2 M, pH 6) for several

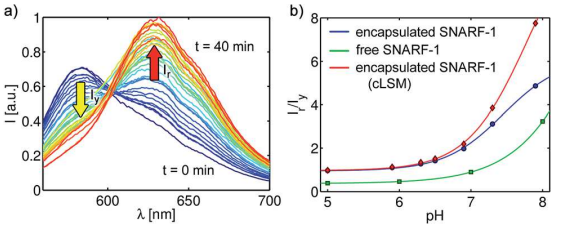

Fig. 2 (a) Changes in the emission spectra of free SNARF-1-dextran in a solution (initial pH 6) of OAA (10 mM), NADH (75 μM) and malate dehydrogenase in response to malate dehydrogenase activity. The emission of free SNARF-1-dextran shifts from the yellow (intensity I_y) to the red (intensity I_r) region, indicating a continuous increase in pH (after 40 min, pH 7.4). This is the result of proton consumption in the reaction OAA + NADH + H^+ → L-malic acid + NAD^+. (b) Comparison of the response I_r/I_y (pH) for free and encapsulated SNARF-1-dextran as obtained by spectrofluorimetry (blue and green curve) and cLSM (red).

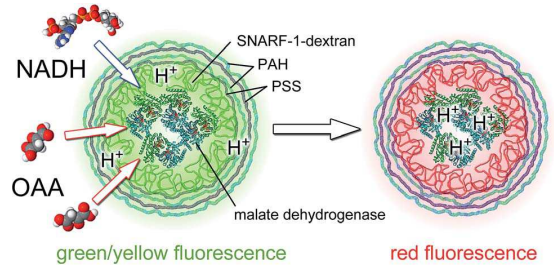

Fig. 1 Sensing principle: malate dehydrogenase and the pH-sensitive fluorescent dye, SNARF-1-dextran, are encapsulated inside hollow microcapsules made by depositing alternating layers of polystyrene sulfonate (PSS) and poly(allylamine hydrochloride) (PAH). The presence of oxaloacetic acid (OAA) or nicotinamide adenine dinucleotide (NADH) inside the cavity can be sensed by SNARF-1-dextran in response to the local decrease in proton concentration, caused by the enzymatic reaction OAA + NADH + H^+ → L-malic acid + NAD^+.

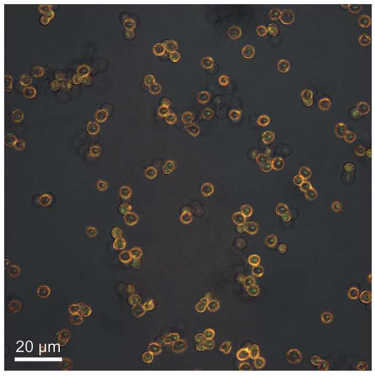

Fig. 3 Fluorescent micrograph of the sensor capsules. An overlay of the transmission and fluorescence channels (recorded with a cLSM) is shown in false colours (green: 560 615 nm, red: 615 750 nm). The scale bar corresponds to 20 μm.

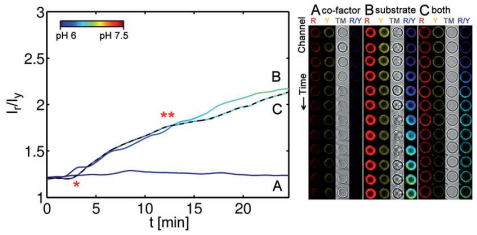

Fig. 4 Control system. Polyelectrolyte multilayer capsules without malate dehydrogenase were prepared. The capsules carrying SNARF-1-dextran were only exposed to OAA (500 μM) in the absence (B) or in the presence of NADH (50 μM, (C), dashed line). Lane A represents results obtained for the cofactor alone (500 μM). The substrate (OAA) was added at the time point indicated with an asterisk. The cofactor (NADH) was added at the time point marked with two asterisks. The reaction was followed for 25 minutes. The initial pH of all the solutions was adjusted to 6. The corresponding fluorescence images are shown on the right side, illustrating the response of a single capsule in the red (R) and yellow (Y) channel, in brightfield transmission mode (TM) and in a pseudo-coloured image (R/Y) corresponding to the I_r/I_y ratio per pixel (the same colour map as used in the plot window). The correlation of I_r/I_y to pH is shown in Fig. 2b, and is indicated by the colour code presented in the top panel.

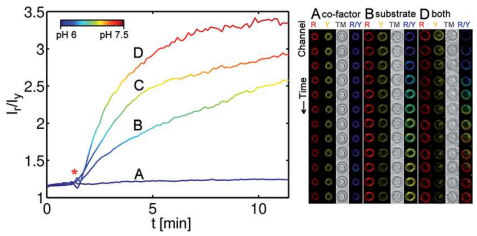

Fig. 5 Concentration-dependent changes in the emission spectra $I(\lambda)$ of encapsulated SNARF-1-dextran, reported as I_r/I_y (t), in response to malate dehydrogenase activity. The sensor capsules carrying malate dehydrogenase and SNARF-1-dextran were exposed to OAA (500 μM) in the absence (B) or presence of NADH (50 μM (C) or 100 μM (D)). The substrate and cofactor were added at the time point indicated with an asterisk. Lane A represents results obtained for the cofactor alone (500 μM). The reaction was followed for 12 min. The initial pH of all the solutions was adjusted to 6. The corresponding fluorescent images are shown on the right side, illustrating the response of a single capsule in the red (R) and yellow (Y) channel, in brightfield transmission mode (TM) and in a pseudo-coloured image (R/Y) corresponding to the I_r/I_y ratio per pixel (the same colour map as used in the plot window). The I_r/I_y ratio could be directly related to the corresponding pH values according to Fig. 2b, as displayed by the colour code in the panel.

minutes. The resulting SNARF-1 and malate dehydrogenase containing microspheres were washed three times with ultrapure water to remove excess EDTA and stored at 4 °C. The size of the resulting capsules ranged between 3 and 5 μm.

Fluorescence spectroscopy based sensing

To determine the response of SNARF-1 to the enzymatic activity of malate dehydrogenase in free solution, a reaction mixture of 10 mM OAA, 75 μM NADH, 1 μL malate dehydrogenase (11 mg protein per mL, 7700 U mL^{-1}) and 100 μg mL^{-1} SNARF-1 was

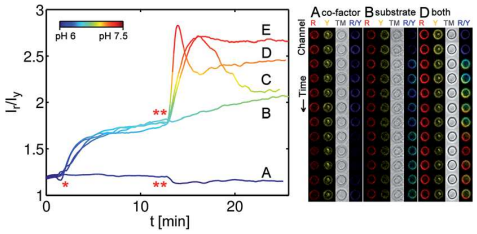

Fig. 6 Reaction kinetics response of sensor capsules to different concentrations of the substrate and cofactor. The sensor capsules carrying malate dehydrogenase and SNARF-1-dextran were exposed to different concentrations of OAA and NADH. A NADH (200 μM); B OAA (350 μM); C OAA (350 μM) + NADH (100 μM); D OAA (700 μM) + NADH (100 μM); E OAA (350 μM) + NADH (200 μM). The substrate (OAA) was added at the time point indicated with an asterisk. The cofactor (NADH) was added at the time point marked with two asterisks. The reaction was followed for 25 minutes. The initial pH of all the solutions was adjusted to 6. The corresponding fluorescent images are shown on the right side, illustrating the response of a single capsule in the red (R) and yellow (Y) channel, in brightfield transmission mode (TM) and in a pseudo-coloured image (R/Y) corresponding to the I_r/I_y ratio per pixel (the same colour map as used in the plot window).

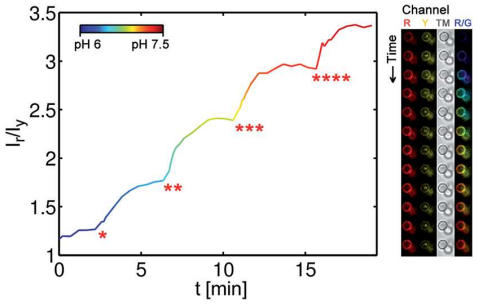

Fig. 7 Reaction kinetics response of the sensor capsules to stepwise addition of the cofactor. At (*) the substrate was added to the capsule solution to obtain an initial concentration of 500 μM (total volume: 50 L). Subsequently, 1 μL of the cofactor solution (350 μM) was added at each step (**) (****). The initial pH of all the solutions was adjusted to 6. The corresponding fluorescent images are shown on the right side, illustrating the response of a single capsule in the red (R) and yellow (Y) channel, in brightfield transmission mode (TM) and in a pseudo-coloured image (R/Y) corresponding to the ratio I_r/I_y per pixel (the same colour map as used in the plot window).

prepared. The pH of all stock solutions was adjusted to 6 with HCl and NaOH prior to use. Immediately after preparation, SNARF-1 was excited at 540 nm with a FluoroLog (Horiba, Japan) fluorescence spectrometer and the emission was recorded over time between 560–700 nm.

Fluorescence microscopy based sensing

A confocal laser scanning microscope (cLSM) was used (LSM 510 Meta, Zeiss) for local sensing of pH-changes with polyelectrolyte sensor capsules. Drops of capsule solution were examined on a glass slide (approximately 40 000 capsules per

View Article Online
Journal of Materials Chemistry B Paper

drop of reaction mixture). SNARF-1 was excited simultaneously at 488 nm and 543 nm. The fluorescence signal was recorded at ranges between 550–615 nm (channel 1) and 615–750 nm (channel 2). The ratio of the fluorescence intensity of channel 2 (intensity I_r)/channel 1 (intensity I_y) was calculated for all pixel pairs, where the intensity in both channels was above a threshold. The mean value for all pixel intensity ratios of one image (approximately 300 capsules) was calculated and used to determine the pH changes inside the capsule cavities caused by the enzymatic reaction catalyzed by malate dehydrogenase in the presence of the substrate OAA and the co-enzyme NADH. To determine the reaction kinetics, the fluorescence intensity of SNARF-1 in both channels was measured over time after the addition of OAA and coenzyme consecutively, if not stated otherwise. Image processing was performed with Matlab (Mathworks). All solutions used for the experiments were adjusted to pH 6 with HCl or NaOH immediately before the sensing process was performed. The reaction mixture was buffered with PBS (5%). The sensing experiments were always performed one day after capsule preparation.

Results and discussion

Four basic requirements have to be met in order to employ polyelectrolyte microcapsules for fluorescence sensing of products of enzymatic reactions. First, the enzymatic reaction itself should lead to a local change in the concentration of free ions. Second, an ion-sensitive fluorophore-sensor should be loaded together with the catalytically active molecules (*i.e.* enzymes). Third, the molecular size of the dye and the catalyst should be sufficiently large to retain them within the capsule cavity. Lastly, the substrate molecules should be small enough to penetrate through the capsule wall. Hereby, the precise molecular weight cut-offs depend on the capsule material and architecture.

In our experimental set-up we evaluated the sensing capacities of microcapsules carrying malate dehydrogenase (70 kDa, isoelectric point: 10) and the pH-sensitive dye, SNARF-1. SNARF-1 was coupled to dextran (70 kDa) to increase the molecular size of the fluorescent probe and to ensure that it is retained inside the capsule cavity.[15] The maximum of the emission spectrum of SNARF-1 shifts from 580 nm in acidic media to 640 nm in alkaline media. As described, the pK_a of the fluorophore might change in different environments. While the pK_a of the free dye is in accordance with the manufacturer's value of 7.50, it changes when encapsulated.[15,29] In the present case, while encapsulated together with malate dehydrogenase, the pK_a changes to about 6.80.

Malate dehydrogenase is an enzyme of the citric acid cycle. The molecular weight of the enzyme 70 kDa is sufficient to keep it inside the cavity. The conversion of L-malic acid into oxaloacetic acid is catalysed by the enzyme. This is accompanied by the reduction of the cofactor NAD^+ into NADH and the release of one hydrogen ion per reaction. The reaction constant of the enzyme depends on the concentration of the respective substrate, as well as on the pH of the solution. Depending on the initial conditions, the reaction can proceed in both directions. In the case of low pH-values (*i.e.* when many protons are available) and a low concentration of L-malic acid, the reaction runs to the right, protons are consumed, and thus the local pH increases (*cf.* Fig. 1): OAA + NADH + H^+ → L-malic acid + NAD^+. In the case of high pH values, the reaction runs to the left, protons are produced, and thus the local pH decreases: OAA + NADH + H^+ ← L-malic acid + NAD^+. Note that SNARF-1 is only sensitive to changes in pH around its pK_a value, and thus this fluorophore can be used to monitor the reaction in a certain pH range only. The reaction OAA + NADH + H^+ → L-malic acid + NAD^+ is favoured in the region where SNARF-1 responds most strongly to changes in pH.

In order to verify that the reaction ensures a significant impact on the pH, we first tested the reaction using free substrate (OAA), free cofactor (NADH), free enzyme (malate dehydrogenase), and free SNARF-1-dextran as a pH indicator in a solution of initial pH = 6. Upon addition of the substrate (10 mM OAA) and the cofactor (75 μM NADH) to the enzyme (7700 units per mL), a time-dependent change of fluorescence signal of the solution from dominant emission in the yellow region (580 nm) to dominant emission in the red region (640 nm) was observed, which indicates that the solution became more alkaline upon consumption of the protons, *cf.* Fig. 2a. A calibration curve, which allows the pH to be obtained from the ratio of red-to-yellow fluorescence (I_r/I_y), is shown in Fig. 2b. These data demonstrate that the reaction catalysed by malate dehydrogenase can be followed *in situ* by monitoring the pH.

In addition to the fluorescent pH indicator, SNARF-1-dextran, the pH indicator thymol blue was also utilized, which exhibits absorption spectrum changes in response to pH. Using UV/vis absorption spectroscopy allowed the pH during the reaction (by monitoring changes in the spectrum of thymol blue) to be measured, in addition to directly measuring the changes in the NADH concentration. Thymol blue changes its colour from blue (pH > 9) to yellow (pH < 7.4) (*cf.* Fig. S1†). The visual change is attributed to an increase in absorption at 430 nm and a decrease at 595 nm (*cf.* Fig. S2†). The change in absorption at 595 nm is more sensitive and shows the sigmoidal slope that is typical for a pH indicator. In contrast, the cofactor NADH shows two absorption bands at 260 nm and 340 nm, whilst the oxidized form NAD^+ absorbs only at 260 nm. Therefore, we analysed the change in NADH concentration in the solution by UV/vis absorption spectroscopy at 340 nm. This method is common in systems involving NAD^+/NADH for the determination of enzyme activities. These measurements cannot be performed in the presence of the dye, because of its absorption of UV light. The full set of data using UV/vis absorption spectroscopy is presented in the ESI.† In agreement with experiments involving SNARF-1-dextran, the data verify that the enzymatic activity of malate dehydrogenase can be followed by *in situ* pH measurements, in which a pH indicator and an enzyme are free in solution.

For the construction of a sensor system, we attempted to link both the enzyme and the pH-sensitive dye into one carrier particle. As there are multiple molecules in solution (in particular the carrier particles, which absorb and scatter light), we decided to use fluorescence instead of absorption spectroscopy

View Article Online
Paper Journal of Materials Chemistry B

as the most convenient read-out, and employed SNARF-1-dextran as a pH-sensitive reporter. Polyelectrolyte polymer capsules fabricated by layer-by-layer assembly were used as microreactor particles. To prepare the sensing microcapsules, malate dehydrogenase and SNARF-1-dextran were first co-precipitated in calcium carbonate particles. The particles were then coated with PSS and PAH using the well-described layer-by-layer technique.[32 34] In a final step, the $CaCO_3$ template was removed by re-dispersing the capsules in EDTA, which forms complexes with the Ca^{2+} ions. The resulting capsules, filled with the enzyme and SNARF-1-dextran, had a diameter of 3–5 μm. An image of such capsules is presented in Fig. 3. The capsules were spherical and well dispersed. The fluorescent dye, SNARF-1-dextran, was encapsulated and remained within the capsule after removal of the core. As reported in previous studies, the dye is not homogeneously distributed in the capsule cavity, and instead sticks to the inner capsule wall.[15] Because SNARF-1 molecules were coupled to 70 kDa dextran, which has the same molecular weight as the enzyme, it is reasonable to assume that the enzyme stays within the cavity as well, in agreement with previous studies,[19] though its presence cannot be concluded from the microscopy images.

Finally, we examined the combined system (enzyme and SNARF-1 encapsulated together) by recording the fluorescence intensities of SNARF-1-dextran at suitable wavelengths using a fluorescence microscope. The presence and activity of the enzyme can be proven by recording the changes in pH. Controls (capsules without the enzyme) were first investigated, *cf.* Fig. 4. The presence of the cofactor NADH has no impact on the I_r/I_y read-out of the dye, *cf.* Fig. 4A. Although in this case no enzymatic conversion can take place due to the lack of the enzyme, OAA already interacts with SNARF-1, as seen by the increasing I_r/I_y-values over time, independent of whether NADH is present or not, *cf.* Fig. 4B and C. OAA slowly decomposes in aqueous solution into pyruvic acid and CO_2, accompanied by an increase in pH. However, the rate of the alkalinizing effect of this decomposition was determined to be much slower than the observed phenomenon in Fig. 4B and C.

In the next set of experiments, capsules carrying malate dehydrogenase were exposed to their substrate OAA, in the presence of different concentrations of the cofactor NADH. The changes in SNARF-1-dextran fluorescence intensities were then recorded. As shown in Fig. 5, the initiation of the enzymatic reaction led to a decrease in the amount of free H^+ ions. This was visualised by the change in the I_r/I_y ratio of the fluorescence intensities of SNARF-1-dextran, as recorded in the range from 560–615 nm (I_y, yellow channel) to 615–750 nm (I_r, red channel), *cf.* Fig. 2a. The reaction only took place in the presence of the substrate (OAA). Without the substrate, the pH of the solution remained constant over time (*cf.* Fig. 5A), indicating that no reaction occurred. The presence of the cofactor increased the reaction rate. Saturation at high I_r/I_y values is caused by a decrease of the reaction rate and not by limited sensitivity of SNARF-1, as at $I_r/I_y > 3.5$, SNARF-1 is still responsive to changes in pH, *cf.* Fig. 2b.

To demonstrate the effect of the cofactor on the kinetics of the enzymatic reaction, the capsules carrying the enzyme were incubated with the substrate first, followed by the addition of NADH. As shown in Fig. 6, the more coenzyme was added, the higher the increase in fluorescence intensities of SNARF-1 in the red channel. Moreover, the sensor capsules showed no significant response to the cofactor alone (*cf.* Fig. 6A). Addition of the substrate caused a steady increase of the I_r/I_y ratio (*cf.* Fig. 6B), as already seen for the control particles without encapsulated enzymes, *cf.* Fig. 4B. The reaction could be enhanced by the addition of NADH (*cf.* Fig. 6C–E *versus* Fig. 6B). At an initial NADH concentration of 100 μM, the local pH strongly increased temporarily (*cf.* Fig. 6C and D). After a few minutes, the cofactor was used up and the pH inside the capsules became equilibrated with the outside value. For higher concentrations of the cofactor, the bulk pH was also increased by the sensing reaction (*cf.* Fig. 6E). Note that the I_r/I_y curves with OAA and with NADH lie on top of the curve with OAA, but without NADH. When small amounts of NADH were added (*cf.* Fig. 6C), after NADH has been consumed by the enzymatic reaction, the I_r/I_y curve approaches the curve in which NADH was not added (*cf.* Fig. 6B). The substrate can be enzymatically converted when the cofactor is present.

The data in Fig. 6C and D suggest that the continuance of the enzymatic reaction is limited by the amount of NADH present. Therefore, we tested whether it could be continued by supplying the system with additional NADH. To that end, the sensing capsules carrying malate dehydrogenase were first incubated with the substrate, followed by the addition of the cofactor. When the I_r/I_y ratio has reached a plateau value, additional NADH was added. Indeed, as seen in Fig. 7, this allowed the reaction to continue.

Conclusions

The synthesis and characterization of a particle bound sensor for the detection of OAA, based on enzymatic digestion followed by pH measurements has been demonstrated. As the enzymatic conversion of OAA is a continuous process, as long as the substrate and cofactor are available, this reaction needs to be monitored over time. This has been demonstrated with time lapse recordings of individual polyelectrolyte capsules, which serve as carrier particles for both enzymes and pH sensitive fluorophores. As the present work is a proof-of-concept study, no detailed analysis about selectivity and sensitivity is given. Instead, it is interesting to discuss the potential applications of such sensors for intracellular detection. It is well accepted that polyelectrolyte polymer capsules, as used here, are internalized by adherent cell lines *via* endocytosis, and that their final intracellular location is the lysosome.[31,35 37] This however involves general problems associated with particle based intracellular sensing.[16] Though some methods exist to release molecules from capsules (in the size range from *ca.* 150 nm[38] to 3–5 μm[39 41]) residing inside lysosomes into the cytosol, in a typical scenario, sensors will remain trapped inside lysosomes, which suggests sensing in the lysosome as the most facile application. Besides imposing a hostile environment to particles (lysosomal proteases, highly acidic pH), localization inside the lysosome imposes other limits to particle based intra-

lysosomal sensing. The sensing principle, as sketched in Fig. 1, relies on the detection of protons, which are consumed upon enzymatic digestion of the target molecule OAA. However, all pH-sensitive fluorophores have a limited range of operation, centred around their pK_a value. While the lysosomal pH can be highly acidic down to pH values of 3 (precise values depend on the cell line), the pK_a value of encapsulated SNARF-1-dextran, as used in this study, is 6.8. Thus, inside lysosomes, the pH-indicator SNARF-1 would be barely sensitive to small changes in pH upon digestion of OAA by malate dehydrogenase. In the data shown in this work, the pH of the starting solution was buffered on purpose to a value around 6, which sets an optimal range for observing the increase in pH upon the enzymatic reaction. In order to apply the sensing strategy for the intra-lysosomal detection of OAA, an alternative pH-indicator with a highly acidic pK_a value would be required. In the ESI†, thymol blue is presented as an example in this direction, though its pK_a value (*ca.* 1.7) would be too low for sensing inside lysosomes. It also needs to be pointed out, that the particle architecture could be improved. In our work, enzymes and analyte-sensitive fluorophores were co-localized in the cavity of polyelectrolyte polymer capsules. However, in principle, these capsules also allow for a multicompartment structure, in which enzymes and fluorophores could be placed at different locations.[42 47] Based on these considerations we suggest that further improvements could help to facilitate intracellular enzyme-based fluorescence sensing using polymer capsules as carrier systems. In addition to intracellular sensing, other potential applications which involve enzymatic or enzymatic-coupled reactions could be envisioned, such as enzymatic microreactors for chemical analysis (*e.g.* sensing of glucose, food contaminants, *etc.*), kinetic studies and catalysis. At any rate, it should be highlighted that inhomogeneous and/or variable loading of molecules in the capsules, as well as different diffusion limits of the molecules involved, hampers the application of the current coupled system for absolute detection of concentrations (be it for the proof-of-concept system described here or for other enzyme-based sensing systems). Nevertheless, the proof-of-concept system reported here demonstrates the feasibility of real time monitoring of enzymatic reactions (as well as kinetics) *in situ*. Further improvements of the material (*e.g.* homogeneous loading, development of new fluorescence probes, multicompartmental geometries, *etc.*) will strengthen the potential applications of enzyme-loaded capsules.

Acknowledgements

This work was supported by LOEWE (grant Synchembio to WJP). PRG acknowledges support from the MINECO (RYC-2012-10059 and CTQ2013-45433-P).

References

1 D. W. Domaille, E. L. Que and C. J. Chang, *Nat. Chem. Biol.*, 2008, **4**, 168–175.
2 L. Kazakova, L. Shabarchina, S. Anastasova, A. Pavlov, P. Vadgama, A. Skirtach and G. Sukhorukov, *Anal. Bioanal. Chem.*, 2013, **405**, 1559–1568.
3 A. S. Susha, A. Munoz Javier, W. J. Parak and A. L. Rogach, *Colloids Surf., A*, 2006, **281**, 40–43.
4 M. J. Ruedas-Rama, A. Orte, E. A. H. Hall, J. M. Alvarez-Pez and E. M. Talavera, *Analyst*, 2012, **137**, 1500–1508.
5 W. Qi, Z. Liu, J. Lai, W. Gao, X. Liu, M. Xu and G. Xu, *Chem. Commun.*, 2014, **50**, 8164–8166.
6 E. A. Lemke and C. Schultz, *Nat. Chem. Biol.*, 2011, **7**, 480–483.
7 M. J. Ruedas-Rama and E. A. H. Hall, *Anal. Chem.*, 2010, **82**, 9043–9049.
8 V. Pavlov, B. Shlyahovsky and I. Willner, *J. Am. Chem. Soc.*, 2005, **127**, 6522–6523.
9 R. Freeman and I. Willner, *Nano Lett.*, 2009, **9**, 322–326.
10 R. Freeman, L. Bahshi, T. Finder, R. Gill and I. Willner, *Chem. Commun.*, 2009, 764–766.
11 F. Khan, T. E. Saxl and J. C. Pickup, *Anal. Biochem.*, 2010, **399**, 39–43.
12 F. Wen, Y. Dong, L. Feng, S. Wang, S. Zhang and X. Zhang, *Anal. Chem.*, 2011, **83**, 1193–1196.
13 S. Hiller, A. Schnackel and E. Donath, *Cytometry, Part A*, 2005, **64**, 119.
14 M. Semmling, O. Kreft, A. Muñoz Javier, G. B. Sukhorukov, J. Käs and W. J. Parak, *Small*, 2008, **4**, 1763–1768.
15 L. L. del Mercato, A. Z. Abbasi and W. J. Parak, *Small*, 2011, **7**, 351–363.
16 K. Kantner, S. Ashraf, S. Carregal-Romero, C. Carrillo-Carrion, M. Collot, P. del Pino, W. Heimbrodt, D. J. De Aberasturi, U. Kaiser, L. I. Kazakova, M. Lelle, N. M. de Baroja, J. M. Montenegro, M. Nazarenus, B. Pelaz, K. Peneva, P. R. Gil, N. Sabir, L. M. Schneider, L. I. Shabarchina, G. B. Sukhorukov, M. Vazquez, F. Yang and W. J. Parak, *Small*, 2015, **11**, 896–904.
17 O. P. Tiourina, A. A. Antipov, G. B. Sukhorukov, N. L. Larionova, Y. Lvov and H. Mohwald, *Macromol. Biosci.*, 2001, **1**, 209–214.
18 N. G. Balabushevich, G. B. Sukhorukov and N. I. Larionova, *Macromol. Rapid Commun.*, 2005, **26**, 1168–1172.
19 M. Ochs, S. Carregal-Romero, J. Rejman, K. Braeckmans, S. C. De Smedt and W. J. Parak, *Angew. Chem., Int. Ed.*, 2013, **52**, 695–699.
20 C. S. Karamitros, A. M. Yashchenok, H. Moehwald, A. G. Skirtach and M. Konrad, *Biomacromolecules*, 2013, **14**, 4398–4406.
21 F. Caruso, D. Trau, H. Möhwald and R. Renneberg, *Langmuir*, 2000, **16**, 1485–1488.
22 M. Fischlechner, Y. Schaerli, M. F. Mohamed, S. Patil, C. Abell and F. Hollfelder, *Nat. Chem.*, 2014, **6**, 791–796.
23 A. M. Pavlov, G. B. Sukhorukov and D. J. Gould, *J. Controlled Release*, 2013, **172**, 22–29.
24 O. S. Sakr and G. Borchard, *Biomacromolecules*, 2013, **14**, 2117–2135.
25 E. Donath, G. B. Sukhorukov, F. Caruso, S. A. Davis and H. Möhwald, *Angew. Chem., Int. Ed.*, 1998, **37**, 2202–2205.

26 G. B. Sukhorukov, A. L. Rogach, B. Zebli, T. Liedl, A. G. Skirtach, K. Köhler, A. A. Antipov, N. Gaponik, A. S. Susha, M. Winterhalter and W. J. Parak, *Small*, 2005, **1**, 194–200.
27 M. F. Bedard, A. Munoz-Javier, R. Mueller, P. del Pino, A. Fery, W. J. Parak, A. G. Skirtach and G. B. Sukhorukov, *Soft Matter*, 2009, **5**, 148–155.
28 O. Kreft, M. Prevot, H. Mohwald and G. B. Sukhorukov, *Angew. Chem., Int. Ed. Engl.*, 2007, **46**, 5605–5608.
29 L. I. Kazakova, L. I. Shabarchina and G. B. Sukhorukov, *Phys. Chem. Chem. Phys.*, 2011, **13**, 11110.
30 P. Rivera Gil, M. Nazarenus, S. Ashraf and W. J. Parak, *Small*, 2012, **8**, 943–948.
31 R. Hartmann, M. Weidenbach, M. Neubauer, A. Fery and W. J. Parak, *Angew. Chem., Int. Ed.*, 2015, **54**, 1365–1368.
32 P. Rivera Gil, L. L. del Mercato, P. del Pino, A. Muñoz-Javier and W. J. Parak, *Nano Today*, 2008, **3**, 12–21.
33 J. W. Cui, M. P. van Koeverden, M. Mullner, K. Kempe and F. Caruso, *Adv. Colloid Interface Sci.*, 2014, **207**, 14–31.
34 S. De Koker, R. Hoogenboom and B. G. De Geest, *Chem. Soc. Rev.*, 2012, **41**, 2867–2884.
35 A. Muñoz Javier, O. Kreft, M. Semmling, S. Kempter, A. G. Skirtach, O. Bruns, P. d. Pino, M. F. Bedard, J. Rädler, J. Käs, C. Plank, G. Sukhorukov and W. J. Parak, *Adv. Mater.*, 2008, **20**, 4281–4287.
36 L. Kastl, D. Sasse, V. Wulf, R. Hartmann, J. Mircheski, C. Ranke, S. Carregal-Romero, J. A. Martínez-López, R. Fernández-Chacón, W. J. Parak, H.-P. Elsaesser and P. Rivera Gil, *ACS Nano*, 2013, **7**, 6605–6618.
37 Y. Yan, A. P. R. Johnston, S. J. Dodds, M. M. J. Kamphuis, C. Ferguson, R. G. Parton, E. C. Nice, J. K. Heath and F. Caruso, *ACS Nano*, 2010, **4**, 2928–2936.
38 J. Ruesing, O. Rotan, C. Gross-Heitfeld, C. Mayer and M. Epple, *J. Mater. Chem. B*, 2014, **2**, 4625–4630.
39 A. Muñoz Javier, P. del Pino, M. F. Bedard, A. G. Skirtach, D. Ho, G. B. Sukhorukov, C. Plank and W. J. Parak, *Langmuir*, 2008, **24**, 12517–12520.
40 S. Carregal-Romero, M. Ochs, P. Rivera Gil, C. Ganas, A. M. Pavlov, G. B. Sukhorukov and W. J. Parak, *J. Controlled Release*, 2012, **159**, 120–127.
41 C. Ganas, A. Weiß, M. Nazarenus, S. Rösler, T. Kissel, P. Rivera Gil and W. J. Parak, *J. Controlled Release*, 2014, **196**, 132–138.
42 O. Kreft, A. G. Skirtach, G. B. Sukhorukov and H. Mohwald, *Adv. Mater.*, 2007, **19**, 3142–3145.
43 L. L. del Mercato, A. Z. Abbasi, M. Ochs and W. J. Parak, *ACS Nano*, 2011, **5**, 9668–9674.
44 B. V. Parakhonskiy, A. M. Yashchenok, M. Konrad and A. G. Skirtach, *Adv. Colloid Interface Sci.*, 2014, **207**, 253–264.
45 R. Xiong, S. J. Soenen, K. Braeckmans and A. G. Skirtach, *Theranostics*, 2013, **3**, 141–151.
46 M. Delcea, H. Moehwald and A. G. Skirtach, *Adv. Drug Delivery Rev.*, 2011, **63**, 730–747.
47 M. Delcea, A. Yashchenok, K. Videnova, O. Kreft, H. Möhwald and A. G. Skirtach, *Macromol. Biosci.*, 2010, **10**, 465.

OPEN ACCESS
Submitted to S.T.A.M., DRAFT ONLY **1**

Focus Issue Paper

Cellular uptake and cell-to-cell transfer of polyelectrolyte microcapsules within a triple co-culture system representing parts of the respiratory tract

Dagmar A. Kuhn[1*], Raimo Hartmann[2*], Kleanthis Fytianos[1], Alke Petri-Fink[1], Barbara Rothen-Rutishauser[1†], Wolfgang J. Parak[2,3†]

[1] Adolphe Merkle Institute, Université de Fribourg, Fribourg, Switzerland
[2] Department of Physics, Philipps Universität Marburg, Marburg, Germany
[3] CIC Biomagune, San Sebastian, Spain

[*] both authors contributed equally
[†] corresponding authors: wolfgang.parak@physik.uni-marburg.de; barbara.rothen@unifr.ch

Received: 6 May 2015

Abstract
Polyelectrolyte multilayer microcapsules of around 3.4 micrometer in diameter were added to epithelial cells, monocyte-derived macrophages and dendritic cells *in vitro* and their uptake kinetics was quantified. All three cell types were combined in a triple co-culture model, mimicking the human epithelial alveolar barrier. Hereby, macrophages were separated in a three dimensional model from dendritic cells by a monolayer of epithelial cells. While passing of small nanoparticles has been demonstrated from macrophages to dendritic cells across the epithelial barrier in previous studies, for the micrometer-sized capsules this process could not be observed in significant amount. Thus, this barrier is a limiting factor for cell-to-cell transfer of micrometer-sized particles.

1. Introduction

The inhalation pathway is a promising entry portal for drug delivery. Due to the characteristics of the lung, *e.g.* huge internal surface of the lung parenchyma (*i.e.* alveoli and airways) of about 150 m^2 and millions of immune cells [1, 2], the uptake of particulate materials is favored. Hereby, the transfer from air to liquid, *e.g.* of particles, is controlled by structural as well as by cellular barriers, *i.e.* the human epithelial alveolar tissue barrier [3]. This barrier constitutes a complex system involving the interplay of several different types of cells. Still, essential features of the human epithelial alveolar barrier can be simulated with cellular model systems. A well-characterized three-dimensional (3D) model of this barrier has been established, which is composed of epithelial cells, human blood monocyte-derived macrophages (MDMs), and dendritic cells (MDDCs) [3]. With this triple cell co-cultures (TCCs) it has been demonstrated, that (nano)particles, in particular polystyrene particles with diameters of 0.1 - 1 µm, can be transferred across the lung barrier, by being passed from macrophages to dendritic cells [4]. While this process has been reported in several publications

OPEN ACCESS
Submitted to S.T.A.M., DRAFT ONLY

[4, 5], so far it remained unclear to which range of particle sizes this process applies. Potentially such a process could be harnessed for particle-based drug delivery applications. Particles in general are endocytosed by macrophages. Thus, targeting to the dendritic cells located underneath the epithelium could be achieved by active passing particles from macrophages across the epithelium to the dendritic cells.

We wanted to probe this concept for polyelectrolyte microcapsules (PEMs) [6-9], which are a universal delivery system. PEMs are fabricated by layer-by-layer assembly of charged polyelectrolytes around sacrificial templates [9] and can be readily used to encapsulate molecular cargo [10, 11]. Uptake of PEMs by cell lines and release of encapsulated cargo has been demonstrated with two-dimensional (2D) cell cultures [12-14]. While interaction of PEMs with cell lines is relatively well studied [15, 16], involving also the investigation of internalization pathways and cytotoxic effects [17, 18], most of these studies are based on 2D *in vitro* models. While there are several reports about *in vivo* applications, such as vaccination [19], the behavior of cells regarding PEMs in complex cellular scenarios is poorly understood. Thus, the objective of the present study was to investigate the interaction of PEMs with TCCs, and in particular to probe for their transfer across the lung barrier from macrophages to dendritic cells located underneath the epithelium. Such possible cell-to-cell transfer of PEMs could potentially be exploited for inhalation-based applications targeting dendritic cells, which are numerously distributed in the respiratory tract and the key antigen-presenting cells, orchestrating both, innate and adaptive immune functions [1]. PEMs composed out of biodegradable walls have been used to release pro-drug molecules inside cells, which are activated only after cellular internalization [20]. Due to the time delay of activation after incorporation, it might be possible that PEMs first are internalized by macrophages, and only after having been passed to dendritic cells their cargo is activated, which would allow for specific targeting. Whether such concepts can be realized however will strongly depend on the capability to transfer PEMs between macrophages and dendritic cells, which is the topic of the present study.

2. Experimental

1.1. Synthesis of polyelectrolyte microcapsules

Materials: Non-biodegradable PEMs made of poly(sodium 4-styrenesulfonate) (PSS) and poly(allylamine hydrochloride) (PAH), and biodegradable PEMs made of dextran sulfate (DextS) and poly-L-arginine (PLArg) were prepared as previously described [17, 20]. All chemicals used for PEM synthesis were obtained from Sigma-Aldrich (USA) except fluorescein isothiocyanate (FITC)-dextran 500 kDa and dequenching DQ-OVA (Life Technologies, USA).

Template core preparation: Either FITC-dextran or DQ-OVA was embedded into $CaCO_3$ template microparticles by co-precipitation. In the case of FITC-loaded particles, 10 mL of aqueous solution of $CaCl_2$ (0.33 M) and 10 mL FITC-dextran 500 kDa (0.25 mg/mL) were mixed in a glass vial. During magnetic stirring (1000 rpm) 3 mL of aqueous solution of Na_2CO_3 (0.33 M) was added quickly. After 30 s, the solution was transferred into two 15 mL centrifuge tubes and after 2 min, the particle growth was terminated by centrifugation. The particles were washed three times with double distilled water. In the case of QD-OVA, filled $CaCO_3$ template microparticles were synthesized using the same procedures, but with smaller amounts of materials: 615 µL of CaCl2 (0.33 M) solution, 770 µL DQ-OVA (50 µM) and 615 µL Na2CO3 (0.33 M), but elsewise the same procedures [21, 22].

Biodegradable capsules: Layer-by-Layer (LbL) assembly was carried out by adsorbing alternating layers of negatively charged DextS ($M_w \approx 40$ kDa, 2 mg/mL in 0.5 M NaCl) and positively charged PLArg ($M_w \approx$ 15-70 kDa, 1 mg/mL in 0.5 M NaCl) onto the template cores. For each coating step the microparticles were suspended in 1-5 mL of polyelectrolyte solution followed by three washing steps (centrifugation in ddH_2O). Finally, hollow FITC-dextran or DQ-OVA filled PEMs were obtained by dissolution of the $CaCO_3$ templates by Ca^{2+} ion complexion with ethylenediaminetetraacetic acid (EDTA, 0.2 M, pH 7) [17, 20].

Non-biodegradable capsules: Synthesis was performed analogously to that of the biodegradable PEMs with PSS ($M_w \approx$ 70 kDa) instead of DextS and with PAH ($M_w \approx$ 56 kDa) instead of PLArg [17, 20]. A summary of the prepared PEMs with

some of their physicochemical parameters is given in the Supporting Information (Supporting Information, Figure 1).

1.2. Cell culture techniques

Culture of cell lines: Human alveolar epithelial type II cells (A549) from American Tissue Type Culture Collection (ATTC #CCL-185), were cultured in Roswell Park Memorial Institute Medium (RPMI 1640, Gibco, Luzern, Switzerland) with 4-(2-hydroxyethyl)-1-piperazineethanesulfonic acid (HEPES, Gibco) supplemented with 10 % fetal bovine serum (FBS, heat inactivated, PAA Laboratories, Austria), 1 % L-glutamine (L-glut, Gibco, Luzern, Switzerland) and 1 % penicillin/streptomycin (P/S, Gibco, Luzern, Switzerland) and maintained at 37 °C and 5 % CO_2. A549 epithelial cells were sub-cultured twice per week using trypsin (0.05 % trypsin-EDTA, Gibco). 5 days prior to TCC preparation, A549 cells were seeded at a density of 2×10^5 cells/mL in the upper chamber of membrane inserts (BD Falcon, 0.3 cm^2 surface area, 3.0 µm pores, transparent PET-membrane) placed into growth medium-containing 24 well plates (Milian, Satigny, Switzerland) and grown to confluence. The growth medium was changed once before TCC preparation.

Isolation and monocyte differentiation: Monocytes were isolated from buffy coats from healthy donors (blood donation service, Bern, Switzerland) as previously described [4]. For differentiation into MDDCs, monocytes were cultured in RPMI 1640 medium supplemented with 10 % FBS (heat inactivated, PAA Laboratories, Austria), 1 % L-glut (Gibco, Luzern, Switzerland), 1 % penicillin/streptomycin (Gibco, Luzern, Switzerland), 10 ng/mL granulocyte macrophage colony-stimulating factor (GM-CSF, Miltenyi Biotech, Bergisch Gladbach, Germany) and 10 ng/mL interleukin-4 (IL-4, Miltenyi Biotech, Bergisch Gladbach, Germany). For differentiation into MDMs, no growth factors were added. Differentiation was performed in 6-well plates (10^6 cells/mL; 3 mL/well supplemented growth medium) for 6 days at 37 °C and 5 % CO_2. Differentiation and maturation into MDDCs and MDMs applying this culture conditions have been demonstrated in earlier studies [23, 24]. For the experiments, the primary cells were harvested after differentiation by off-scraping.

Cell preparation for live cell imaging: 1.2×10^5 MDMs/mL, 0.8×10^5 MDDCs/mL, or 2×10^5 A549 cells/mL, respectively, were grown inside 35 mm µ-dishes (Ibidi). After 24 h, the cells were placed inside an environmental module at 5 % CO_2 and 37 °C, DQ-OVA filled PEMs were added (15 PEMs/cell), and live imaging was performed.

Cell preparation for live cell imaging of bi-cultures: 1.2×10^5 MDMs/mL were grown inside 35 mm µ-dishes (Ibidi) and loaded with PEMs (15 PEMs/cell) for 2 h. Afterwards, 0.8×10^5 MDDCs/mL cells were added, which had been stained with tetramethylrhodamine-labeled wheat germ agglutinin (WGA, Life Technologies).

Cell preparation for live cell imaging of TCCs: A549 cells were fluorescently stained with CellTracker violet BMQC dye at a dilution of 1:1000 for 1 h at 37 °C followed by three washing steps with phosphate buffered saline (PBS). Simultaneously staining of mature MDDCs was performed inside the chambers of the 6 well plates which were used for differentiation. After triple washing, off-scraping and counting, MDDCs were added to the membrane inserts ($8.9 \times 10^3/cm^2$), containing stained A549 cells on the top side, to adhere at the bottom side by turning the insert upside down for 1 h. During the attachment process, MDMs were stained in the same way as MDDCs. Finally, 3.5×10^3 MDMs/mL were added on top of the A549 cells. PEMs were added into the upper well prior to image acquisition by confocal laser scanning microscopy (CLSM) and tracked over 24 h. In another approach MDMs were pre-incubated with PEMs for 24 h and then washed three times, scratched off and added to A549 cells and MDDCs being already attached to the insert.

Cell preparation for flow cytometry (FCM) measurements: MDMs were exposed to non-biodegradable PEMs (5 PEMs/cell) for 24 h. Afterwards, MDMs were washed three times, scraped off, re-suspended in fresh medium and spun down for 3 min at 500 rcf. Simultaneously, MDDCs were prepared for bi-culture. MDMs and MDDCs (1.25×10^6 cells/mL; 1:1 ratio), respectively, were co-exposed in a new chamber of a 6 well plate another for 24 h for possible cell-to-cell PEM transfer to take place. On day 7, the cells were washed three times, scraped off, re-

suspended in PBS and spun down for 3 min at 500 rcf. The supernatant was replaced by fragment crystallizable blocking receptor reagent (Fc-Block, Miltenyi Biotech #130059901) for 10 min in order to reduce nonspecific binding. Then, cells were resuspended in 1 mL of FCM buffer (1 % bovine serum albumin (Sigma Aldrich, St. Louis, Missouri, USA) and 0.1 % NaN_3 (Sigma Aldrich, St. Louis, Missouri, USA) in PBS, (Life technologies, California, USA) and stained with the following antibodies: CD1c-Pacific Blue (Biolegend #331507) for MDDCs and CD14-Brilliant Violet (Biolegend #301830) for MDMs. Finally, cells were washed and FCM analysis was performed.

1.3. Analysis techniques

Confocal fluorescence microscopy: Cells were kept in an environmental module at 5 % CO_2 and 37 °C. Image acquisition was carried out with a CLSM 710 Meta setup (Zeiss, Germany/Switzerland) equipped with lasers for excitation at 405 nm, 488 nm or 543 nm. In the case of observing the individual cells types separately for obtaining the kinetics of PEM uptake, images were acquired at a temporal resolution of 5 min using a Plan-Apochromat 20x/0.8 M27 objective. Fluorescence of DQ-OVA was excited at 488 nm and 543 nm and the emission was collected between 500-540 nm (green channel) and 560-750 nm (red channel). PEMs were counted based on the time-lapse image series using CellProfiler [25], whereby internalized PEMs were identified by their increased fluorescence in the green channel upon contact with digestive enzymes after engulfment. In the case of bi-cultures and TCCs, analysis was performed using a 25x objective with a numerical aperture of 1.4 and an immersion oil lens. After TCC imaging, cellular and morphological information was retrieved using Imaris (Bitplane 7.4, Zürich, Switzerland). The spots module was applied and set to 5 µm in order to track the PEMs throughout the TCCs. Further, the cells morphology was restored in 3D by surface rendering of smoothed data using the same software.

Flow cytometry: FCM was carried out with a BD-LSR Fortessa machine. The entire procedure was performed on ice and 10,000 events were recorded. The obtained data were analyzed with FlowJo (Tree Star). Representative gating strategies are shown in the Supporting Information.

3. Results

1.4. Uptake of biodegradable capsules

In order to investigate whether PEMs or fragments of digested PEMs can be passed from MDMs to MDDCs, DQ-OVA labeled with boron-dipyrromethene (BODIPY) was encapsulated into biodegradable DextS/PLArg PEMs as described previously [20]. The green fluorescence of the dye BODIPY is almost completely self-quenched due to the close proximity of the dye molecules inside non-fragmented ovalbumin [26]. At high dye concentrations as occurring inside PEMs slightly red fluorescent excimers are formed. After enzymatic degradation during uptake by cells, the green fluorescence intensity of BODIPY is dramatically increased and internalized PEMs and potentially released and passed fragments of DQ-OVA become visible [20].

For recording of the uptake kinetics of PEMs in MDMs, MDDCs, and A549 epithelial cells, all types of cells were exposed to DQ-OVA filled PEMs and the ratio N_{int}/N_{tot} of internalized to total PEMs was calculated over time. Hereby, N_{tot} refers to the total number of capsules and N_{int} to the number of internalized PEMs present in a randomly chosen area recorded by CLSM (size of recorded areas ≈ 0.2 mm^2). The change in color from red to green fluorescence of BODIPY-labeled DQ-OVA allowed for distinguishing between internalized PEMs and PEMs outside cells (Figure 1B). MDMs showed the faster kinetics of internalization (green curve in Figure 1A), followed by MDDCs (red curve in Figure 1A), and A549 cells (blue curve in Figure 1A). In contrast to MDMs, MDDCs are highly mobile. Thus, they were able to take up much more PEMs present over time, whereas MDMs could only reach and internalize PEMs in close proximity and a certain fraction of non-internalized PEMs always remained, depending on the cell density. Immediately after uptake, intracellular degradation of encapsulated DQ-OVA was observable by a partial release of BODIPY dye into the cytosol of both, MDMs and MDDCs (Figure 1). In A549 cells only degradation inside the cavities of the capsules but no release of encapsulated material was

OPEN ACCESS
Submitted to S.T.A.M., DRAFT ONLY

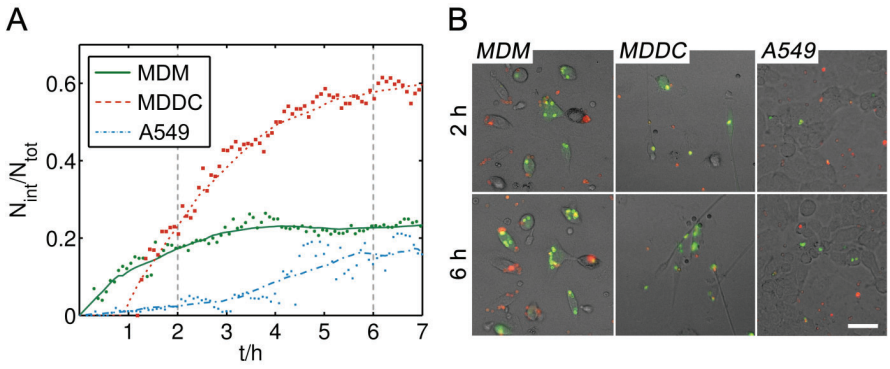

Figure 1. A: Kinetics of PEM uptake for the different types of cells used for the experiments. Cells were exposed to DextS/PLArg PEMs filled with BODIPY-labeled DQ-OVA. By investigating the color change from red to green emission due to enzymatic digestion upon uptake, the fraction of internalized PEMs N_{int}/N_{tot} over time was quantified were N_{int} represents the number of internalized and N_{tot} represents the total number of PEMs visible in a randomly chosen area. B: Example fluorescence micrographs for the time points 2 h and 6 h are shown. Non-internalized PEMs appear red. Green fluorescence is associated with digested and released DQ-OVA. The scale bar corresponds to 50 µm.

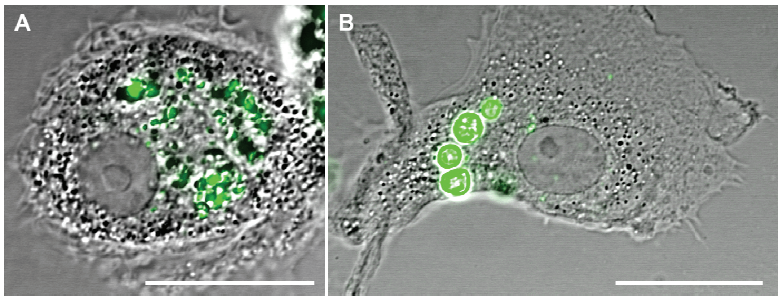

Figure 2. Biodegradable PEMs (A) and non-biodegradable PEMs (B) engulfed by MDMs at 1 hour of exposure. Cells are shown in differential interference contrast (DIC; grey) and PEMs are shown in green. The scale bar corresponds to 20 µm. More images are shown in Figure SI-2.

visible. Within 24 h, fragmentation of the capsules could be already detected in MDMs as shown by CLSM (Figure 2). In bi-cultures of capsule-loaded MDMs and MDDCs, one possible transfer of PEM-released BODIPY-labeled DQ-OVA fragments from one MDM to a MDDC could be witnessed (Figure 3) during excessive imaging. When triple cell co-cultures composed of epithelial cells (A549), MDMs on top as well as MDDCs at the bottom of the membrane inserts were exposed to biodegradable DextS/PLArg capsules, PEMs were engulfed by MDMs in a time frame of 30 minutes and a partial release of DQ-OVA into the cytosol occurred similarly than observed in monocultures (Figure 1). Some fluorescence signals of the degraded PEMs could be detected in MDDCs on the bottom side of the membrane (Figure 4). Additionally, F-actin protrusions of MDDCs from the lower chamber have been observed to penetrate the pores of the insert membrane reaching the upper side of the chamber. During live cell imaging the visualization of transfer events of released BODIPY-labeled DQ-OVA from MDMs to MDDCs was not possible because of the rather long time-intervals between acquisitions of the single 3D-stacks. In bi-cultures of MDMs and MDDCs only one possible transfer event was observed during excessive imaging (Figure 3, t = 130 min). Thus, a direct passing of digested PEM fragments from MDMs to MDDCs in bi- as well as in triple cell co-cultures was difficult to track and almost not observable by CLSM within several time-lapse recordings of live cells. Uptake of non-biodegradable capsules

Instead of imaging the cargo (BODIPY) of biodegradable capsules as described above, we probed the possible detection of full PEM-transfer events. For this purpose cells exposed to non-degradable PEMs based on PSS/PAH were

OPEN ACCESS
Submitted to S.T.A.M., DRAFT ONLY

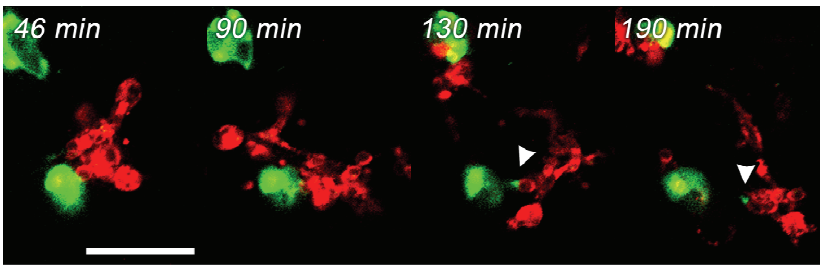

Figure 3. Possible MDM-to-MDDC transfer of PEM-released BODIPY-labeled DQ-OVA fragments in MDM/MDDC bi-culture. MDMs (appearing in green due to engulfed PEMs) were loaded with biodegradable DextS/PLArg PEMs filled with BODIPY-labeled DQ-OVA for 2 h. Subsequently, MDDCs marked with fluorescently-labeled wheat germ agglutinin (red) were added. PEMs appear as yellow spots, while digested DQ-OVA exhibits bright green fluorescence. The transfer of released DQ-OVA is marked with white arrows. The scale bar corresponds to 50 µm.

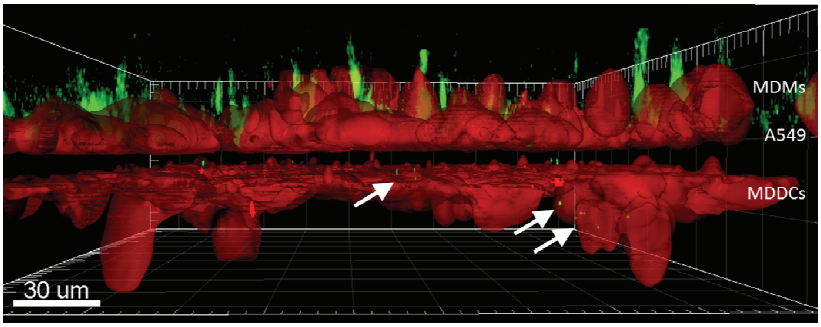

Figure 4. Lateral view of a TCC model exposed to biodegradable DexS/PLArg PEMs containing BODIPY-labeled DQ-OVA after 4.5 h of incubation (surface rendering). Capsules were added on top of the MDM cells and can be seen by the green fluorescence of DQ-OVA. Fluorescence signals of BODIPY (green) on the bottom side of the insert are highlighted by white arrows. Cellular plasma membranes are shown in red. The dark gap between the two red cell layers represents the membrane of the insert.

recorded in both, CLSM and high content screening experiments realized with FCM. Uptake of PEMs in TCCs was analyzed with CLSM first. Hereby, the PEMs were added on top of the membrane inserts, *i.e.* to the upper chamber in which the MDMs were grown. As CLSM allows for lateral resolution (in contrast to FCM) these measurements can help to retrieve more details about the F-actin protrusions being continuously formed by MDDCs grown in the lower chamber towards the upper chamber of the inserts. In contrast to data shown in Figure 4, in this experiment, only MDDCs were stained with CellTracker violet BMQC dye (Figure 5).

Again persistent "grabbing" of MDDCs for the PEMs was observed, but no PEMs were "pulled down", *i.e.* no transfer of PEMs from the upper to the lower chamber could be observed. F-Actin protrusions formed by MDDCs occurred similarly as observed in the previous exposure experiments with biodegradable PEMs. Also, in case MDMs were pre-incubated with PEMs for 24 h before adding them to the bi-culture system, the PEMs were not detected in MDDCs. Thus, CLSM data did not indicate transfer of PEMs from MDMs to MDDCs across the epithelial barrier formed by A549 cells.

As "grabbing" of MDDCs towards PEM-loaded MDMs was observed in the TCC model possible PEM transfer events were investigated also by FCM within bi-cultures of MDMs and MDMs. MDMs were pre-loaded with non-biodegradable PSS/PAH PEMs filled with fluorescein isothiocyanate (FITC) and added to cultures of MDDCs. After 24 h, cells were analyzed by FCM (Figure 6). In 87 % of all MDMs fluorescence signals of the PEMs could be found, and 66 % of all MDDCs were fluorescent after 24 h of co-culturing. Comparing the two primary cell types, the standard deviation for MDDCs is much larger than the standard deviation for MDMs (Figure 6).

OPEN ACCESS
Submitted to S.T.A.M., DRAFT ONLY

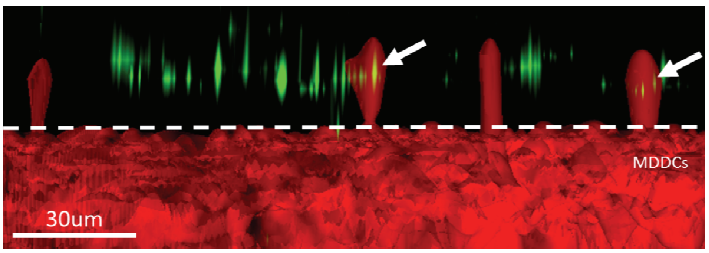

Figure 5. Side view of a TCC (3D surface rendering) exposed to non-biodegradable PSS/PAH PEMs filled with BODIPY-labeled DQ-OVA (green) after 1 h. For clarification, only MDDCs were fluorescently stained (red). White arrows indicate F-actin protrusions of MDDCs through the pores of the membrane insert (white dotted line). A549 and MDMs are not visible in this representation.

4. Discussion

To investigate uptake and possible cell-to-cell transfer of released material from PEMs or whole PEM transfer events between two different types of immune cells, *i.e.* from MDMs to MDDCs, two different types of PEMs were used. Biodegradable PEMs were prepared to trace released fluorescent molecules, whereas non-biodegradable PEMs seemed reasonable to trace whole PEM cell-to-cell transfer events acting as control in case transfer of released material from biodegradable PEMs would have been occurred in high frequency. Qualitative CLSM as well as quantitative FCM analysis was applied. The application of live cell imaging for visualization of TCCs is very challenging, since the thickness of the whole tissue barrier is about 50-80 µm. In addition, especially MDDCs are highly motile, and thus, live imaging requires a high temporal resolution to resolve cell-to-cell interactions. In this case, image acquisition cannot be realized by conventional CLSM, but would need spinning-disc techniques. However, with our set-up we could show that the process of uptake and ingestion of biodegradable PEMs by MDMs was very fast, *i.e.* within 30-45 minutes, as also shown by others [27]. In experiments with TCCs, signals of biodegradable PEMs were detected inside MDDCs on the bottom side of the chamber after 4.5 h. Capsule fragments were possibly transferred directly from MDMs to MDDCs *via* tight junctions through the epithelium. This process has been observed for polystyrene particles with 1 µm in diameter in case of MDM/MDDC co-cultures by Blank *et al.* [4, 5]. However, since intracellular release of DQ-OVA from PEMs in MDMs starts taking place immediately after uptake (Figure 1), it could also be possible that MDDCs came into contact with exocytozed PEM fragments. These fragments might have been secreted either by MDMs or A549 cells into the surrounding medium or could have been directly transmitted from MDMs/A549 cells to MDDCs. Another possibility could be that the released PEM fragments from the MDMs have passed through the 3 µm-sized membrane pores (either directly or *via* A549 cells) followed by subsequent active uptake by MDDCs. Even internalized but non-fragmented capsules should be able to pass the pores of the membrane once internalized, although they are larger in size: They are rather elastic (mechanical stiffness < 2 Nm^{-1}) [27] and, according to previous studies, can be deformed and compressed by cells easily [27, 15, 28]. As the capsules are slightly larger than the pore size, passive diffusion from the top to the bottom side of the insert can almost be excluded. Hence, capsules being present on the MDDC side must have actively been transferred by cells.

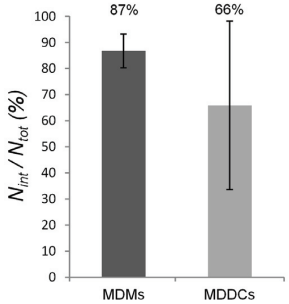

Figure 6. Investigation of PEM transfer events within 24 h from initially PEM-loaded MDMs to MDDCs in bi-culture, as observed by FCM. The y-axis represents the frequency N_{int}/N_{tot} (%) of MDMs and MDDCs having internalized non-degradable PEMs. Hereby, N_{int} corresponds to the number of cells with internalized PEMs and N_{tot} to the total number of cells (the gating strategy can be found in the Supporting Information, Figure SI-3). MDMs were marked with CD14 and MDDCs with CD1c antibodies. Experiments were performed in triplicates and results are given as mean ± SD.

In order to confirm the exact route of the released capsules/capsule fragments from MDMs towards the bottom side of the membrane insert in the two-chamber system it would be necessary to do more observations with microscopy techniques that allow a higher temporal resolution. The non-biodegradable PEMs were not transmitted to MDDCs residing at the bottom side of the insert at any conditions. We assume that this is a matter of size, since it was shown that 1 µm polystyrene beads were detected inside MDDCs on the bottom side of the insert in TCCs after initial exposure of MDMs with the particles [24, 29, 4]. For both architectures of PEMs cellular F-actin protrusion from MDDCs were detected throughout the exposure. These protrusions were well visualized when applying image restoration. It is known that F-actin filament growth occurs within microseconds [29] and is a prerequisite for cells to move, grow, scan and sense their surrounding environment [30, 31]. Since F-actin protrusions were observed to occur throughout the measurement, the cells seem to try to reach out for capsules persistently without any success.

Whereas live cell imaging allows for the analysis of whole TCCs, in additionally performed FCM measurements only bi-cultures were examined. Although the two approaches of live cell imaging and FCM differed in their sample preparation and detection, the findings coincided in terms of no observed capsule transmission from MDMs to MDDCs. In a supplementary performed FCM-based control experiment capsule transmission from MDMs to epithelial A549 cells, instead of MDDCs, was probed. Similar results were observed, *i.e.* capsules could be detected inside A549 cells with the same frequency than inside MDDCs, hence, FCM experiments could neither verify PEM transfer from MDMs to MDDCs. This indicates that in these bi-cultures PEM uptake most probably derived from the free PEMs in the surrounding medium. Although validation is required, non-phagocytic A549 cells seemed to be a good control, since their function as barrier forming cells is far different than the function of immune cells, which perform phagocytosis and crosstalk with other cells. Thus, based on the FCM data, we could not confirm any cell-to-cell transfer of PEMs between MDMs and MDDCs.

1.5. Acknowledgements

Parts of this work were supported by LOEWE (grant Synchembio to WJP). The authors acknowledge technical discussions and input from Dr. Pilar Rivera Gil in the initial state of this project. This study was also supported by grants of the Deutsche ForschungsGemeinschaft (DFG, SPP1313), the NRP64 program of the Swiss National Science Foundation (#406440-131266/1), by the Swiss National Science foundation through the National Centre of Competence in Research Bio-Inspired Materials, and the Adolphe Merkle Foundation.

1.6. References

[1] C. von Garnier, B. Rothen-Rutishauser and F. Blank, *Nanoparticles in the Respiratory Tract: Modulation of Antigen-Presenting Cell Function*, Journal of Environmental Immunology and Toxicology, 1 (2013), pp. 140-149.

[2] L. Müller, A. D. Lehmann, B. D. Johnston, F. Blank, P. Wick, A. Fink and B. Rothen-Rutishauser, Inhalation Pathway as a Promising Portal of Entry: What Has to Be Considered in Designing New Nanomaterials for Biomedical Application? Handbook of Nanotoxicology, Nanomedicine and Stem Cell Use in Toxicology, John Wiley & Sons, Ltd, 2014, pp. 205.

[3] B. Rothen-Rutishauser, F. Blank, C. Mühlfeld and P. Gehr, *Nanoparticle-Cell Membrane Interactions*, Informa Healthcare, 2009.

[4] F. Blank, M. Wehrli, A. Lehmann, O. Baum, P. Gehr, C. von Garnier and B. M. Rothen-Rutishauser, Macrophages and Dendritic Cells Express Tight Junction Proteins and Exchange Particles in an in Vitro Model of the Human Airway Wall, Immunobiology, 216 (2011), pp. 86-95.

[5] F. Blank, B. Rothen-Rutishauser and P. Gehr, *Dendritic Cells and Macrophages Form a Transepithelial Network against Foreign Particulate Antigens*, American Journal Of Respiratory Cell And Molecular Biology, 36 (2007), pp. 669-677.

[6] E. Donath, G. B. Sukhorukov, F. Caruso, S. A. Davis and H. Möhwald, *Novel Hollow Polymer Shells by Colloid-Templated Assembly of Polyelectrolytes*, Angewandte Chemie International Edition, 37 (1998), pp. 2202-2205.

[7] P. Rivera Gil, L. L. del Mercato, P. del Pino, A. Muñoz-Javier and W. J. Parak, *Nanoparticle-Modified Polyelectrolyte Capsules*, Nano Today, 3 (2008), pp. 12-21.

[8] B. G. De_Geest, S. De Koker, G. B. Sukhorukov, O. Kreft, W. J. Parak, A. G. Skirtach, J. Demeester, S. C. De Smedt and W. E. Hennink, *Polyelectrolyte Microcapsules for Biomedical Applications*, Soft Matter, 5 (2009), pp. 282-291.

[9] J. Borges and J. F. Mano, Molecular Interactions Driving the Layer-by-Layer Assembly of Multi-

layers, Chemical Reviews, 114 (2014), pp. 8883.
[10] L. L. del Mercato, P. Rivera Gil, A. Z. Abbasi, M. Ochs, C. Ganas, I. Zins, C. Sönnichsen and W. J. Parak, *Lbl Multilayer Capsules: Recent Progress and Future Outlook for Their Use in Life Sciences*, Nanoscale, 2 (2010), pp. 458-467.
[11] P. Rivera_Gil and W. J. Parak, *Composite Nanoparticles Take Aim at Cancer*, ACS Nano, 2 (2008), pp. 2200-2205.
[12] A. Muñoz Javier, P. del Pino, M. F. Bedard, A. G. Skirtach, D. Ho, G. B. Sukhorukov, C. Plank and W. J. Parak, *Photoactivated Release of Cargo from the Cavity of Polyelectrolyte Capsules to the Cytosol of Cells*, Langmuir, 24 (2008), pp. 12517-12520.
[13] M. F. Bedard, A. Munoz-Javier, R. Mueller, P. del Pino, A. Fery, W. J. Parak, A. G. Skirtach and G. B. Sukhorukov, *On the Mechanical Stability of Polymeric Microcontainers Functionalized with Nanoparticles*, Soft Matter, 5 (2009), pp. 148-155.
[14] C. Ganas, A. Weiß, M. Nazarenus, S. Rösler, T. Kissel, P. Rivera_Gil and W. J. Parak, *Biodegradable Capsules as Non-Viral Vectors for in Vitro Delivery of Pei/Sirna Polyplexes for Efficient Gene Silencing*, J. Control. Release, 196 (2014), pp. 132-138.
[15] A. Muñoz_Javier, O. Kreft, M. Semmling, S. Kempter, A. G. Skirtach, O. Bruns, P. d. Pino, M. F. Bedard, J. Rädler, J. Käs, C. Plank, *et al.*, *Uptake of Colloidal Polyelectrolyte Coated Particles and Polyelectrolyte Multilayer Capsules by Living Cells*, Advanced Materials, 20 (2008), pp. 4281-4287.
[16] U. Reibetanz, D. Halozan, M. Brumen and E. Donath, Flow Cytometry of Hek 293t Cells Interacting with Polyelectrolyte Multilayer Capsules Containing Fluorescein-Labeled Poly(Acrylic Acid) as a pH Sensor, Biomacromolecules, 8 (2007), pp. 1928-1933.
[17] L. Kastl, D. Sasse, V. Wulf, R. Hartmann, J. Mircheski, C. Ranke, S. Carregal-Romero, J. A. Martínez-López, R. Fernández-Chacón, W. J. Parak, H.-P. Elsaesser, *et al.*, *Multiple Internalization Pathways of Polyelectrolyte Multilayer Capsules into Mammalian Cells*, ACS Nano, 7 (2013), pp. 6605-6618.
[18] C. Kirchner, A. M. Javier, A. S. Susha, A. L. Rogach, O. Kreft, G. B. Sukhorukov and W. J. Parak, *Cytotoxicity of Nanoparticle-Loaded Polymer Capsules*, Talanta, 67 (2005), pp. 486-491.
[19] B. G. De Geest, M. A. Willart, H. Hammad, B. N. Lambrecht, C. Pollard, P. Bogaert, M. De Filette, X. Saelens, C. Vervaet, J. P. Remon, J. Grooten, *et al.*, *Polymeric Multilayer Capsule-Mediated Vaccination Induces Protective Immunity against Cancer and Viral Infection*, ACS Nano, 6 (2012), pp. 2136-2149.
[20] P. Rivera_Gil, S. D. Koker, B. G. De_Geest and W. J. Parak, *Intracellular Processing of Proteins Mediated by Biodegradable Polyelectrolyte Capsules*, Nano Letters, 9 (2009), pp. 4398-4402.
[21] G. Sukhorukov, L. Dähne, J. Hartmann, E. Doanth and H. Möhwald, *Controlled Precipitation of Dyes into Hollow Polyelectrolyte Capsules Based on Colloids and Biocolloids*, Advanced Materials, 12 (2000), pp. 112-115.
[22] A. A. Antipov and G. B. Sukhorukov, *Polyelectrolyte Multilayer Capsules as Vehicles with Tunable Permeability*, Advances in Colloid and Interface Science, 111 (2004), pp. 49-61.
[23] A. Lehmann, B. Ch., F. Blank, P. Gehr and B. Rothen-Rutishauser, *A 3D Model of the Human Epithelial Airway Barrier*, Methods in Bioengineering: Alternative Technologies to Animal Testing (2010), pp. 239-260.
[24] B. M. Rothen-Rutishauser, S. G. Kiama and P. Gehr, *A Three-Dimensional Cellular Model of the Human Respiratory Tract to Study the Interaction with Particles*, American Journal Of Respiratory Cell And Molecular Biology, 32 (2005), pp. 281-289.
[25] A. Carpenter, T. Jones, M. Lamprecht, C. Clarke, I. Kang, O. Friman, D. Guertin, J. Chang, R. Lindquist, J. Moffat, P. Golland, *et al.*, *Cellprofiler: Image Analysis Software for Identifying and Quantifying Cell Phenotypes*, Genome Biology, 7 (2006), pp. R100.
[26] M. K. Mansour, E. Latz and S. M. Levitz, Cryptococcus Neoformans Glycoantigens Are Captured by Multiple Lectin Receptors and Presented by Dendritic Cells, Journal of Immunology, 176 (2006), pp. 3053-3061.
[27] R. Hartmann, M. Weidenbach, M. Neubauer, A. Fery and W. J. Parak, *Stiffness-Dependent in Vitro Uptake and Lysosomal Acidification of Colloidal Particles*, Angewandte Chemie International Edition, 54 (2015), pp. 1365-1368.
[28] R. Palankar, B.-E. Pinchasik, S. Schmidt, B. G. De Geest, A. Fery, H. Möhwald, A. Skirtach and M. Delcea, Mechanical Strength and Intracellular Uptake of Caco 3-Templated Lbl Capsules Composed of Biodegradable Polyelectrolytes: The Influence of the Number of Layers, Journal of Materials Chemistry B, 1 (2013), pp. 1175-1181.
[29] B. Rothen-Rutishauser, C. Mühlfeld, F. Blank, C. Musso and P. Gehr, Translocation of Particles and Inflammatory Responses after Exposure to Fine Particles and Nanoparticles in an Epithelial Airway Model, Part. Fibre Toxicol., 4 (2007), pp. 9.
[30] J. R. Kuhn and T. D. Pollard, Real-Time Measurements of Actin Filament Polymerization by Total Internal Reflection Fluorescence Microscopy, Biophysical journal, 88 (2005), pp. 1387-1402.
[31] R. Ananthakrishnan and A. Ehrlicher, *The Forces Behind Cell Movement*, International journal of biological sciences, 3 (2007), pp. 303.

1

Cellular uptake and cell-to-cell transfer of polyelectrolyte microcapsules within a triple co-culture system representing parts of the respiratory tract

SUPPORTING INFORMATION

Type	Encapsulated cargo	Polyelectrolytes		N_{bi}	Diameter/µm	Fig
		-	+			
PEMs for flow cytometry	FITC-Dextran 500kDa	PSS	PAH	4	3.3 ± 0.3	A
PEMs for release/transport experiments	BODIPY-labeled DQ-OVA			4	4.7 ± 0.4	B
		DextS	PLArg	4	4.0 ± 0.5	C

Table SI-1. *Characteristics of polyelectrolyte multilayer capsules (PEMs) used for the experiments (Figure SI-1). N_{bi} describes the number of bilayers of which the capsule shell is composed. The size distributions (mean value ± standard deviation, capsules were assumed to be circular) where derived computer-aided from confocal fluorescence micrographs, such as the ones presented in Figure SI-1. More than 800 capsules were analyzed per sample. Details about the capsule segmentation procedure can be found in the supporting information of Hartmann et al*[1].

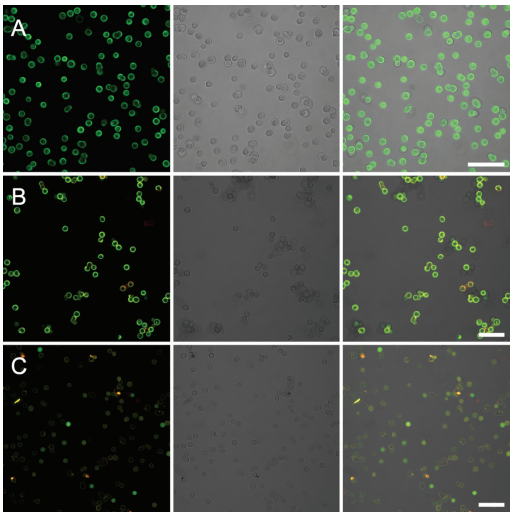

Figure SI-1. *Fluorescence micrographs (left: green channel, middle: brightfield image, right: composition) of polyelectrolyte multilayer capsules used for the experiments. The labels A-C correspond to the samples listed in Table SI-1 (last column). The scale bar corresponds to 20 µm.*

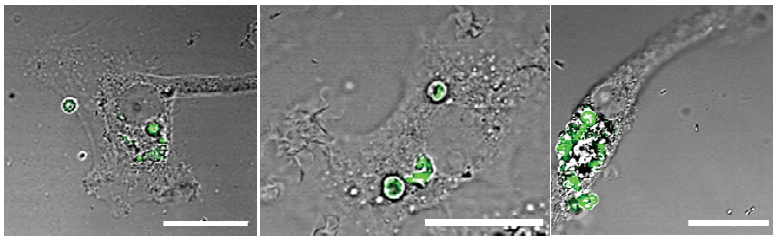

Figure SI-2. *Biodegradable PEMs engulfed by MDMs at 1 hour of exposure. Cells are shown in differential interference contrast (DIC) and PEMs are shown in green. The scale bar corresponds to 20 µm.*

[1] R. Hartmann, M. Weidenbach, M. Neubauer, A. Fery and W. J. Parak, *Stiffness-dependent in vitro uptake and lysosomal acidification of colloidal particles*, Angewandte Chemie International Edition, 54 (2015), pp. 1365-1368.

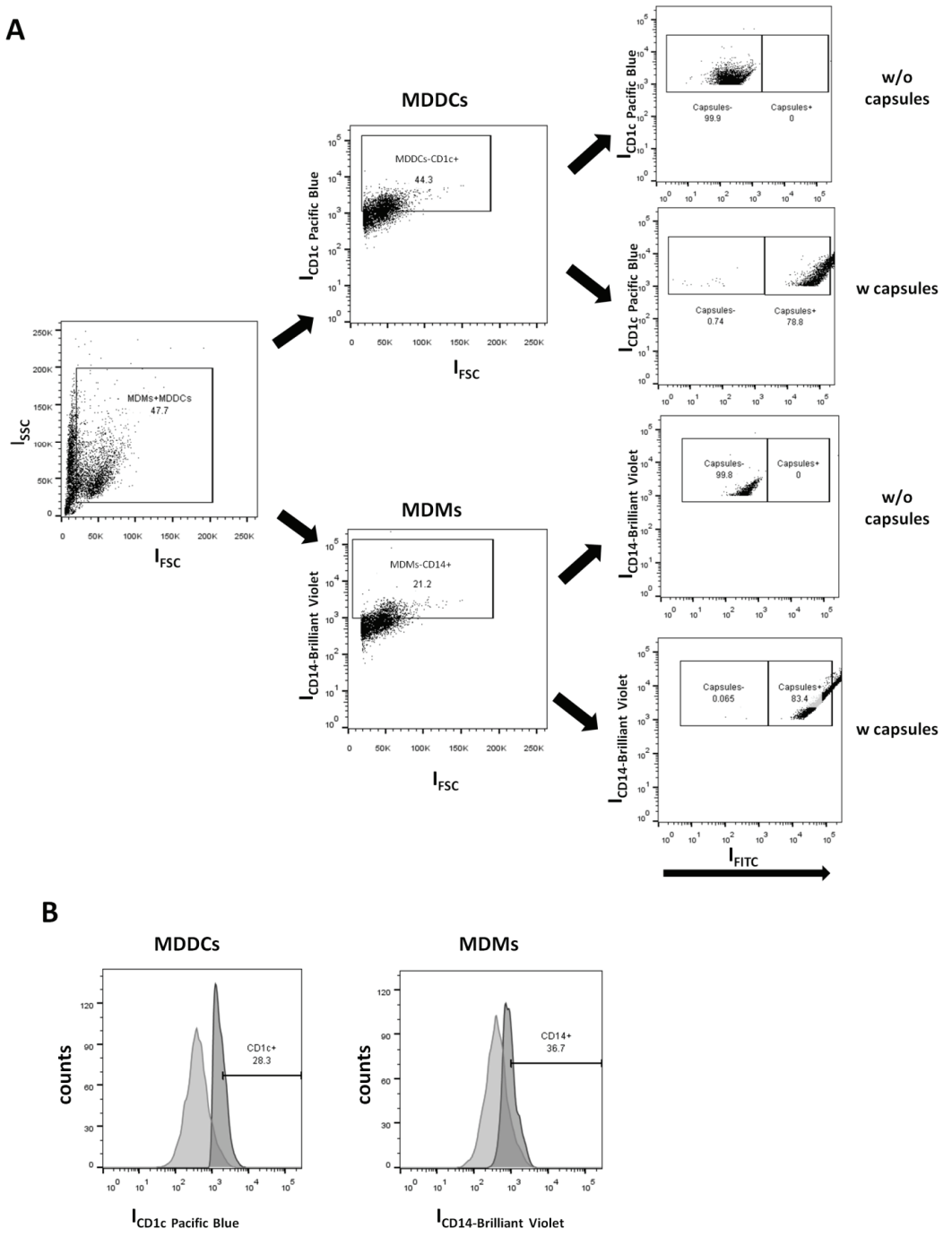

Figure SI-3. *Flow cytometry gating strategy for the bi-cultures. (A) Identification of the different cell populations in MDMs-MDDCs bi-cultures. The cells were stained with specific surface markers (MDDCs: CD1c-Pacific Blue; MDMs: CD14-Brilliant Violet). Initially, unspecific gating was applied (FSC vs. SSC) in order to exclude cellular debris. Afterwards, the populations were identified according to the fluorescence intensity of each specific marker. Finally, the FITC intensity was utilized to determine capsule uptake. Each experiment was repeated three times (n=3) and cells from different cell cultures were used. Capsule-: samples without capsules; Capsule+: samples treated with capsules. (B) % Frequencies of the different cell populations in the bi-cultures; light grey: unstained control; dark grey: stained sample. The entire procedure was performed at 4 °C. The numbers represent the cells expressing the markers.* $I_{CD1c\text{-}Pacific\ Blue}$ *and* $I_{CD14\text{-}Brilliant\ Violet}$ *correspond to the fluorescence intensity of the MDDC and MDM marker, respectively.*

9.2. Curriculum Vitae

Entfernt.

9.3. Acknowledgements

This thesis and the underlying publications would not have been completed without the help and support of my colleagues and friends from the Philipps-University of Marburg and from my family and friends in "the real world"!

First of all, I want to thank to Wolfgang J. Parak, my supervisor, for help and guidance, for involving me in many interesting projects, and also for letting me work independently on topics of particular interest to me. Then, I want to express my appreciation for Dr. Pilar Rivera Gil's support in the early stage of my PhD and her commitment for the cooperation with Dr. Loretta del Mercato from Italy.

I would like to thank all collaboration partners for their helpful and valuable cooperation. I am thankful to Prof. Dr. Itamar Willner for the opportunity to be a guest in his group at the Hebrew University in Jerusalem and in particular the students of his entire research group for the enjoyable time during my stay. I also want to mention Philipp Nold and Prof. Dr. Cornelia Brendel from the Division of Hematology at the University Medical Center in Marburg, who targeted mesenchymal stem cell with gold nanoparticles, Martin Neubauer from Bayreuth, who helped with characterizing the elasticity of polymer capsules, and Dagmar Kuhn from Fribourg in Switzerland, who was testing polymer capsules on a 3D cell culture model.

Certainly, I enjoyed the great company of all the colleagues I shared the office with during the last years. Thank you, Andrea, Christian, Christiane, Jana, Jonas, Lena, Maximilian, Moritz, Verena, and Xiang for the good time!

In addition, I would like to express my thanks to all past and present members of the Biophotonics research group for the friendly and supportive environment and the after-work activities, which were always a lot of fun!

I would also like to thank Julia, Colleen, Kirsten and, again, my parents for proofreading of the manuscript.

Last but not least I am very thankful to Julia for always supporting and patiently waiting for me to finish this thesis!

9.4. Erklärung

Hiermit versichere ich gemäß § 10(c) der Promotionsordnung, dass ich meine Dissertation „Examining Uptake of Nanomaterials by Eukaryotic Cells with Digital Image Cytometry" selbständig ohne unerlaubte Hilfe angefertigt und mich dabei keiner anderen als der von mir ausdrücklich bezeichneten Quellen und Hilfen bedient habe. Ich habe alle vollständig oder sinngemäß übernommenen Zitate als solche gekennzeichnet und die Dissertation in der jetzigen oder einer ähnlichen Form noch bei keiner anderen in- oder ausländischen Hochschule anlässlich eines Promotionsgesuchs oder zu einem anderen Prüfungszweck eingereicht.

Name, Vorname: Hartmann, Raimo

Marburg, 24.07.2015 Unterschrift: